

# Convection, dissipation, and rotation in simulations of stellar and planetary interiors and atmospheres

Simon Robert White Lance

Submitted by Simon Robert White Lance to the University of Exeter as a thesis for the degree of Doctor of Philosophy in Physics, March, 2023.

This thesis is available for Library use on the understanding that it is copyright material and that no quotation from the thesis may be published without proper acknowledgement.

I certify that all material in this thesis which is not my own work has been identified and that no material has previously been submitted and approved for the award of a degree by this or any other University.

Signed: .....

Simon Robert White Lance

Date: .....

## Abstract

A wide range of fluid flows occur within astrophysical bodies such as stars and planets. In particular, convective flows are dominant throughout a significant portion of the structure of these objects, playing a key role in the transport of heat throughout their interiors. In a steady state, this convection must be maintained against any viscous and Ohmic dissipation that is present. Prior numerical studies on the nature of this dissipation have often lacked key physical components of the convection, such as the influence of rotation and stratification. Additionally, in planetary atmospheres the influence of the underlying interior convection zone on the resulting surface circulation has historically been underrepresented. This thesis examines idealised convective systems in an attempt to understand some of these influences. We present the first systematic numerical study of viscous dissipation and convection in a Cartesian layer in the highly stratified, rotating regime, and mixed fixed-entropy and fixed-flux boundary conditions. We find that while the influence of rotation does not affect the total amount of dissipation within the layer, the spatial distribution varies considerably as a result of the change in dynamical structure in the rotationally constrained cases. The obtained heat transport scalings show good agreement with those obtained in prior Boussinesq calculations and we define a new parameter  $z_{diss}$  which quantifies the spatial distribution of the dissipation and appears to provide a good indicator for whether a given system follows the rotationally constrained scalings or not. We also use the globally averaged value of dissipative heating to place constraints on the maximum (negative) value of the kinetic energy flux. Lastly, this thesis presents preliminary results on the influence of more physically motivated convective parameterisations on the atmospheric circulation of highly irradiated tidally locked exoplanets. Initial results show a significant weakening of the eastward equatorial jet, with an accompanying acceleration of the westward midlatitude jets. The thesis then concludes with a discussion of future work, along with accompanying proof-of-concept results.

# Contents

<b>1</b>	<b>Introduction</b>	<b>1</b>
1.1	Fluid flow in Stars and Planets . . . . .	1
1.1.1	Convection in Stars . . . . .	3
1.1.1.1	Surface granulation . . . . .	3
1.1.1.2	Convective interiors . . . . .	6
1.1.2	Planetary atmospheres . . . . .	9
1.1.2.1	Atmospheric dynamics . . . . .	10
1.1.2.2	Radius inflation and the interior heat flux . . . . .	14
1.2	Structure of the thesis: Flow from Stars to Planets . . . . .	15
<b>2</b>	<b>Theoretical Background</b>	<b>18</b>
2.1	Fundamentals of Fluid Flow . . . . .	18
2.1.1	The continuity equation . . . . .	18
2.1.2	Anelastic approximation . . . . .	20
2.1.3	The momentum equation . . . . .	21
2.1.4	An energy equation . . . . .	22
2.1.5	The induction equation . . . . .	23
2.1.6	Convective instability . . . . .	24
2.2	Non-dimensional numbers . . . . .	26
2.2.1	Non-dimensionalisation . . . . .	26
2.2.2	Rayleigh number . . . . .	28
2.2.3	Prandtl Number . . . . .	29
2.2.4	Stratification . . . . .	30

---

2.2.5	Taylor Number . . . . .	30
2.2.6	Rossby Number . . . . .	31
2.2.7	Reynolds Number . . . . .	32
2.2.8	Magnetism . . . . .	32
2.3	An overview of convective scaling relations . . . . .	33
2.3.1	Early convective experiments . . . . .	34
2.3.2	The influence of rotation . . . . .	37
2.3.3	Compressible convective theory . . . . .	41
2.4	Chapter summary . . . . .	43
<b>3</b>	<b>Numerical Modelling</b>	<b>44</b>
3.1	Linear convection code . . . . .	44
3.1.1	Model setup . . . . .	45
3.1.2	Spectral method . . . . .	48
3.1.3	Finite difference method . . . . .	50
3.1.4	Tridiagonal solver . . . . .	51
3.1.5	Timestepping . . . . .	53
3.1.6	Linear reduction . . . . .	54
3.1.7	Finding the critical Rayleigh number . . . . .	56
3.2	Dedalus . . . . .	58
3.2.1	Introduction to Dedalus . . . . .	58
3.2.1.1	Writing a Dedalus code . . . . .	59
3.2.2	Calculating the critical Rayleigh number (EVP) . . . . .	63
3.2.3	Convection modelling (IVP) . . . . .	67
3.3	Global Circulation Models: The Unified Model . . . . .	70
3.3.1	Governing equations of the dynamical core . . . . .	70
3.3.2	Internal heat flux . . . . .	74
3.3.3	Latitude dependence . . . . .	77
3.4	Chapter summary . . . . .	78
<b>4</b>	<b>Simulations of stellar convection: Basic setup and diagnostics</b>	<b>79</b>
4.1	Model Setup . . . . .	79

4.1.1	Domain Geometry . . . . .	79
4.1.2	2.5D approximation . . . . .	80
4.1.2.1	Equation set . . . . .	82
4.2	Fluxes . . . . .	86
4.3	An aside on timescales . . . . .	90
4.4	Flux balance . . . . .	92
4.5	Convective structure . . . . .	93
4.5.1	Varying Prandtl number . . . . .	97
4.5.2	Stratification . . . . .	99
4.5.3	Varying Taylor number . . . . .	105
4.6	Chapter summary . . . . .	108
<b>5</b>	<b>Viscous Dissipation and Dynamics in Rotating, Stratified Convection</b>	<b>109</b>
5.1	Introduction . . . . .	109
5.1.1	Prior work - Energetics of dissipation . . . . .	111
5.1.2	Bounds and constraints on dissipative heating . . . . .	115
5.1.3	Convective penetration . . . . .	117
5.2	Model Setup . . . . .	120
5.2.1	Domain Geometry . . . . .	120
5.2.2	Governing equations . . . . .	121
5.3	Overview of resulting dynamics . . . . .	122
5.4	The magnitude and spatial distribution of viscous dissipation . . . . .	125
5.4.1	The maximum value of viscous dissipation at high Ra . . . . .	125
5.4.2	The spatial distribution of dissipation . . . . .	130
5.5	Links between dynamics, heat transport, and dissipation . . . . .	138
5.5.1	Energy balances and transport . . . . .	139
5.5.2	Entropy profiles and Nusselt number scalings . . . . .	143
5.5.3	Flow amplitudes . . . . .	149
5.5.4	Boundary layers and the link to dissipation . . . . .	152
5.5.5	Predicting the kinetic energy flux from the viscous dissipation . . . . .	156
5.6	Chapter summary . . . . .	158

<b>6 Influence of the interior convective heat flux on planetary atmospheres</b>	<b>163</b>
6.1 Basic simulations of hot Jupiters and brown dwarfs . . . . .	163
6.1.1 An introduction to radius inflation in hot Jupiters . . . . .	164
6.1.2 A typical numerical simulation of a hot Jupiter atmosphere . . . . .	165
6.2 Varying the magnitude of the internal heat flux . . . . .	170
6.2.1 Motivation . . . . .	170
6.2.2 Numerical simulations . . . . .	171
6.3 Latitudinal dependence of the internal heat flux . . . . .	175
6.4 Chapter summary . . . . .	179
<b>7 Conclusions and discussion of future work</b>	<b>180</b>
7.1 Conclusion . . . . .	180
7.2 Future Work . . . . .	186
7.2.1 Magnetohydrodynamics . . . . .	187
7.2.2 3D geometry . . . . .	189
7.2.3 Development of the bottom boundary in hot Jupiter simulations .	190
<b>The Appendices</b>	<b>194</b>
<b>A Dedalus input equations - 3d Anelastic (rotating)</b>	<b>195</b>
A.1 Non-dimensionalisation . . . . .	195
A.2 Equation Expansion . . . . .	199
A.3 2.5D approximation . . . . .	206
<b>Bibliography</b>	<b>209</b>

# List of Figures

1.1	A cartoon schematic of a possible zeroth, first, and second order approximations of star or planet. Under the most simple approximation, these bodies are large spheres of fluid. To a higher degree of detail, there may exist a solid surface or a fluid layer with a considerably different structure.	2
1.2	The typical structure of stellar interiors as a function of mass ( $M$ ) in units of solar mass ( $M_{\odot}$ ). Stars with a mass, $M \lesssim 0.35M_{\odot}$ are fully convective throughout their entire interior, those with mass $0.35M_{\odot} \lesssim M \lesssim 1.5M_{\odot}$ have radiative cores and an overlying convective envelopes, and those with $M \gtrsim 1.5M_{\odot}$ have convective cores and radiative envelopes. Image credit: <a href="https://en.wikipedia.org/wiki/File:Star_types.svg">https://en.wikipedia.org/wiki/File:Star_types.svg</a>	4
1.3	An image of the surface of the Sun taken by the Swedish 1m Solar Telescope in 2017 showing distinct convective cells of order 1-2Mm in width. These structures develop on a typical timescale of order 10 minutes. Image credit: Institute for Solar Physics, Sweden.	5
1.4	Doppler imaging of the sun obtained by MDI instrument onboard the SOHO satellite. Image credit: SOHO/MDI/ESA (Rincon and Rieutord 2018)	5
1.5	Angular velocity profiles of the sun as a function of radius from helioseismology. (a) Shows the full latitude and radial dependence of $\Omega$ from Schou et al. (1998) (b) Shows radial cuts of the $\Omega$ profile for a range of latitudes from Miesch and Toomre (2009).	7

---

1.6	Figure taken from Miesch et al. (2008), Figure 1. Numerical outputs of the radial velocities for giant cell convection at (a) $r = 0.98R_{\odot}$ , and (b) $r = 0.95R_{\odot}$ , where $r$ is the radius and $R_{\odot}$ is the solar radius. The figure uses a Mollweide projection such that all $360^{\circ}$ of longitude can be seen. The dashed lines represent constant latitude of $0^{\circ}$ , $\pm 30^{\circ}$ , and $\pm 60^{\circ}$ , and lines of constant longitude of $0^{\circ}$ and $\pm 90^{\circ}$ . . . . .	8
1.7	The gas giant Jupiter (a) and its Earth-sized storm, the Great Red Spot (b). Image credits: NASA's Hubble Space Telescope on Aug. 25, 2020 (a) and NASA's Juno orbiter on Jul. 10, 2017 (b). . . . .	10
1.8	Figure taken from Louden and Wheatley (2015), Figure 1. Model of how the relative flux of the leading and trailing limbs of a transiting hot Jupiter exoplanet can be separated. . . . .	11
1.9	Panel (a) shows the predicted decay profile of Jupiter's 1 bar zonal flows as a function in depth as presented in Kaspi et al. 2018, Figure 4a. This profile is obtained from a minimum cost optimisation process using high resolution gravity measurements from Juno. Panels (b) and (c) show the zonal and temporal mean profiles of the zonal wind ( $ms^{-1}$ ) as a function of latitude $\phi$ and pressure. . . . .	12
1.10	Figure taken from Hammond and Lewis (2021), Figure 10. A schematic of the three main components of the circulation present in a hot Jupiter atmosphere. An overturning circulatory pattern (blue) can be seen rising at the substellar point, diverging almost isotropically towards the night side before descending. Rotational circulation is then divided into a large-scale zonal jet and a stationary wave component. . . . .	13
1.11	Figure taken from Baraffe et al. (2010), Figure 2. A mass-radius diagram for transiting exoplanets. The black line represents theoretical predictions of radius as a function of mass from a 1D stellar evolution with solar metallicity values (Baraffe et al. 2008). The full black circles labeled, J, S, and N, represent the solar system objects Jupiter, Saturn, and Neptune respectively.	14

2.1	Figure adapted from Glatzmaier 2013, Figure 1.1 and Figure 1.2. The top panel (a) demonstrates the effect on a parcel of fluid raised from position (1) to position (2) adiabatically in a fluid with a subadabatic vertical profile. The bottom panel (b) shows the same process however for a superadabatic vertical profile. . . . .	25
2.2	Figure taken from Grossmann and Lohse 2000, Table 1. Power-law exponents $\gamma$ for $\text{Nu} \sim \text{Ra}^\gamma$ for a range of convective experiments at different $\text{Ra}$ and $\text{Pr}$ . . . . .	37
2.3	Figure taken from Grossmann and Lohse 2000, Figure 2. A phase diagram in $\text{Ra} - \text{Pr}$ space showing the different scaling regimes that exist depending on where the boundary layers or the bulk dominate the global thermal or viscous dissipation. Regimes <i>I</i> and <i>II</i> are those in which the thermal dissipation is boundary-layer dominated with viscous dissipation dominating in the boundary and the bulk for <i>I</i> and <i>II</i> respectively. Regimes <i>III</i> and <i>IV</i> therefore represent bulk dominated thermal dissipation with again boundary and bulk dominated viscous dissipation in <i>III</i> and <i>IV</i> respectively. Subscripts <i>l</i> and <i>u</i> denote the lower and upper $\text{Pr}$ regimes. . . . .	38
2.4	Figure taken from King et al. 2012, Figure 3. Nusselt number plotted against Rayleigh number for a range of Ekman number taken from both laboratory experiments (solid symbols) and direct numerical simulations (open symbols) of no-slip, Boussinesq convection. Symbol size corresponds to $\text{Pr}$ value, whereas the shape and colour correspond to Ekman number, $\text{Ek}$ (smaller $\text{Ek}$ means faster rotation rate). The dashed black line demonstrates a $\text{Nu} \sim \text{Ra}^{2/7}$ scaling whereas the solid blue line shows the $\text{Nu} \sim \text{Ra}^3$ scaling for $\text{Ek} = 10^{-5}$ . Lastly the '+' and 'x' symbols correspond to non-rotating and rotating laboratory experiments from Rossby (1969), respectively. . . . .	40
2.5	Figure taken from Julien et al. 2012, Figure 2. $(\text{Nu} - 1)\text{R}^{-3/2}$ as a function of $\text{R}$ , where $\text{R} = \text{Ra}\text{Ek}^{4/3} \sim \text{Ra}/\text{Ra}_c$ . The horizontal dashed lines at constant $(\text{Nu} - 1)\text{R}^{-3/2}$ correspond to regime paths in which the scaling law in equation (2.53) is valid. . . . .	41

3.1	Values of the globally averaged temperature perturbation as a function of time for a range of Rayleigh number, Ra, for a given Prandtl number, Pr and aspect ratio $\alpha$ . These cases are initialised with a globally averaged temperature perturbation of 0.5, and so initially present a decay before subsequently growing (or decaying further). . . . .	58
3.2	Figure taken from the Dedalus project tutorial pages showing the grid-spacing of Chebyshev polynomials with multiple scalings. Image credit: <a href="https://dedalus-project.readthedocs.io">https://dedalus-project.readthedocs.io</a> . . . . .	60
3.3	Grid of calculated growth rates from the EVP solver in the given Ra, $k_x$ space. This is for a case of stratified, anelastic convection with $N_p = 1$ , $Pr = 1$ using the governing equations and boundary conditions as described in Section 4.1. . . . .	66
3.4	Calculated growth rates grid from the EVP solver in the given Ra, $k_x$ space as shown in Figure 3.3, overplotted with the critical Rayleigh number $Ra_c$ as a function of $k_x$ space. . . . .	67
3.5	Schematic of UM's geometric domain. A simulated atmospheric spherical shell of height $h$ situated on top of an unsimulated convective interior of radius $R_p$ . The influence of the convective interior is then parameterised by an internal heat flux as detailed in Section 3.3.2. . . . .	71
3.6	Schematic of the energy balance present at the planetary "surface". The "SW" and "LW" labels represent the radiative heating from shortwave and longwave radiation respectively, while the $\sigma T_{int}^4$ represents the internal heating from the convective heat flux. From the energy balance of these components we then calculate a surface temperature $T_s$ . . . . .	75
4.1	A schematic view of the location of our cartesian layer on a rotating sphere. . . . .	80
4.2	Vertical profiles of $L_{diss}$ taken from a typical non-rotating convective simulation, with $Ra = 1e5$ , $Pr = 1$ , $Ta = 0$ , $N_p = 1$ . Each is averaged over $0.2 \tau_v$ at a range of points during the simulation. The plot is split across two panels for ease of x-axis scaling. . . . .	91

- 4.3 Vertical profiles of  $L_{cond}$  taken from a typical non-rotating convective simulation.  $\text{Ra} = 1\text{e}5$ ,  $\text{Pr} = 1$ ,  $\text{Ta} = 0$ ,  $N_\rho = 1$ . Each is averaged over  $0.2 \tau_\kappa$  at a range of points during the simulation. The plot is split across two panels for ease of x-axis scaling. . . . . 91
- 4.4 An example plot of a equilibrated flux plot is shown for non-rotating convection with,  $\text{Ra}/\text{Ra}_c = 10^3$ ,  $N_\rho = 1.4$ , and  $\text{Pr} = 1$ . . . . . 92
- 4.5 A snapshot of the convective structure for a non-rotating, unstratified fluid with  $\text{Ra}/\text{Ra}_c = 10^2$ ,  $N_\rho = 0$ , and  $\text{Pr} = 1$ . The first panel shows the total entropy structure of the fluid domain with the direction of the fluid motion indicated with streamline arrows. The second and third panels show the individual horizontal and vertical components of the velocity fields respectively. As the horizontal boundaries are periodic, the plots have been horizontally re-scaled so that the main features of the convection are centralised. . . . . 94
- 4.6 Values of mean Reynolds number for a range of non-rotating ( $\text{Ta} = 0$ ), unstratified ( $N_\rho = 0$ ,) convective simulations at  $\text{Pr} = 1$  and a range of  $\text{Ra}/\text{Ra}_c$ . Increasing the supercriticality shows a clear trend in increasing the resulting Reynolds number, that is, the flow becomes less laminar and more turbulent in nature. . . . . 95
- 4.7 Vertical profiles of the horizontally averaged total entropy (top), the convective flux (middle), and conductive flux (bottom), in non-rotating ( $\text{Ta} = 0$ ), unstratified ( $N_\rho = 0$ ,) convective simulations at  $\text{Pr} = 1$  and a range of supercriticality. The convective and conductive flux profiles have been overplotted (black dotted) with the bulk values expected from sufficiently stratified convection (1 and 0 respectively). . . . . 96
- 4.8 Values of mean Reynolds number for a range of non-rotating convective simulations with  $\text{Ra} = 1\text{e}5$ ,  $N_\rho = 1$ ,  $\text{Ta} = 0$ , for a range of  $\text{Pr}$ . Increasing Prandtl number shows a clear trend away from turbulent flows and towards more laminar convection. . . . . 98

- 4.9 A comparison plot of the flux balance for four different non-rotating convective simulations with  $\text{Ra}/\text{Ra}_c = 1.78 \times 10^3$ ,  $\text{Pr} = 1$ , and values of  $N_\rho = 0.5, 1.0, 1.4$ , and  $2.0$ . The solid colour, dotted, and dashed lines represent the convective, conductive, and "other" energy transport terms where  $L_{\text{other}}$  is given by  $L_{\text{other}} = L_{\text{diss}} + L_{\text{buoy}} = L_p + L_{KE} + L_{visc}$  and encapsulates the additional transport terms present due to the influence of stratification. The solid black line represents the overall sum of all energy transport terms,  $L_{\text{tot}}$ . . . . . 101
- 4.10 A comparison plot of the horizontally averaged entropy profiles for four different non-rotating convective simulations with  $\text{Ra}/\text{Ra}_c = 1.78 \times 10^3$ ,  $\text{Pr} = 1$ , and values of  $N_\rho = 0.5, 1.0, 1.4$ , and  $2.0$ . . . . . 102
- 4.11 A comparison of the full fields of the total entropy, vertical component of the velocity, and horizontal component of the velocity (top, middle, and bottom rows respectively) for non-rotating convective simulations with  $\text{Ra}/\text{Ra}_c = 1.78 \times 10^3$ ,  $\text{Pr} = 1$ , and values of  $N_\rho = 0.5$  (left column) and  $1.0$  (right column). . . . . 103
- 4.12 A comparison of the full fields of the total entropy, vertical component of the velocity, and horizontal component of the velocity (top, middle, and bottom rows respectively) for non-rotating convective simulations with  $\text{Ra}/\text{Ra}_c = 1.78 \times 10^3$ ,  $\text{Pr} = 1$ , and values of  $N_\rho = 1.4$  (left column) and  $2.0$  (right column). . . . . 104
- 4.13 A two panel plot showing different velocity profiles for four different non-rotating convective simulations with  $\text{Ra}/\text{Ra}_c = 1.78 \times 10^3$ ,  $\text{Pr} = 1$ , and values of  $N_\rho = 0.5, 1.0, 1.4$ , and  $2.0$ . The first panel shows the column averaged vertical component of the velocity fields. The solid lines represent the actual values of  $w$  whereas the dashed lines represent the peak value and its negative mirror for the purpose of highlighting the asymmetry in the peak velocity values of the upflows and downflows. The second panel shows a slice of the horizontal component of the velocity,  $v$ , taken at the middle of a convective cell ( $y = 1$ ) with the dashed black line representing zero horizontal motion. . . . . 106

4.14 Results of the EVP outputs of $\text{Ra}_c$ for increasing $\text{Ta}$ at $N_\rho = 0, 1, 2$ in blue, red, and green respectively. The circles are the exact outputs from the EVP with the lines representing linear regression fits with corresponding Pearson correlation coefficients of 0.9998, 0.9998, and 0.9999 for $N_\rho = 0, 1, 2$ respectively. . . . .	107
5.1 Plot taken from Jarvis and McKenzie (1980), Figure 15. This shows the values of viscous dissipation normalised by the flux passing through the layer as a function of supercriticality for infinite Prandtl number. The solid black lines represents the thermodynamical upper limit provided by Hewitt et al. 1975. The simulation D1 is of particular note due to having a value of $E = \frac{\Phi}{L} > 1$ . . . . .	113
5.2 Plot taken from Anders et al. (2022) showing how the depth of the penetrative region, or rather, specifically the 50% departure point $\delta_{0.5}$ varies with increasing values of $f$ , the fraction of the buoyancy work that is being dissipated within the convective region. . . . .	119
5.3 Example dynamics of four cases sampling different parameter regimes. Shown are entropy $s$ , vertical velocity $w$ , and horizontal velocity $v$ for four different cases. The top two rows are for non-rotating cases at $\text{Ra} = 10^4 \text{Ra}_c$ showing both lightly and heavily stratified regimes with $N_\rho = 0.2$ and $1.4$ respectively. The bottom two rows show rotating cases at two different degrees of rotational influence where $N_\rho = 1.4$ , $\text{Ta} = 10^8$ , $\text{Ra} = 1.78 * 10^2 \text{Ra}_c$ and $N_\rho = 1.4$ , $\text{Ta} = 10^{11}$ , $\text{Ra} = 100 \text{Ra}_c$ . Note the bottom case has a different aspect ratio of 1.075. . . . .	124
5.4 Calculated values for $E$ at a range of stratifications and supercriticalities for some non-rotating (black) and rotating cases (blue). Values of $N_\rho = 0.5$ (circles), $1.4$ (stars and squares), and $2.0$ (pluses) are used. The horizontal black lines represent the value of equation 5.1 for a given value of $N_\rho$ . It is of note that due to the effect of rotation on the critical Rayleigh number, the rotating cases have considerably larger values of $\text{Ra}$ for a given stratification.	126

5.5	The maximum value of E achieved for a given $N_\rho$ . The blue line represents the upper bound limit presented in equation 5.1. The values of E for $N_\rho = 3$ and 4 appear much lower than the asymptotic limit having not yet been performed at the required supercriticality. . . . .	128
5.6	The values of E for a range of rotation rates. All cases have a fixed supercriticality of $Ra/Ra_c = 10^2$ , and are shown at two different stratifications of $N_\rho = 0.5$ and 1. The black labels at the highest and lowest values of Ta for each stratification show the value of the convective Rossby number $Ro_c$ . . .	129
5.7	Comparison snapshots demonstrating the different dynamical flows present in two simulations of $Ra = 10^2 Ra_c$ , $N_\rho = 1$ , at $Ta = 10^5$ , $Ro_c = 3.81$ (top row) and at $Ta = 10^9$ , $Ro_c = 0.703$ . From left to right the plots show the total entropy of the fluid, and the vertical and horizontal velocities. . . . .	129
5.8	Local dissipative heating and vertical velocities in a sample of cases. Left panels show $Q_{diss}$ , right panels $w$ . Top row shows a non-rotating case at $Ra = 10^6 Ra_c$ ; the other rows all consider cases at $Ta = 10^8$ , at varying supercriticalities ( $Ra = 1.78 \times 10^2 Ra_c$ in the middle two rows; $Ra = 10^4 Ra_c$ in the bottom row) and latitudes (at the pole in the first rotating example; at 45 degrees in the bottom two). . . . .	131
5.9	Dissipative heating integrated from 0 to $z$ , $L_{diss}(z)$ , and integrated buoyancy work $L_{buoy}$ for a sample of non-rotating cases (top panel) and rotating ones. Solid lines represent $L_{diss}$ and $Q_{diss}$ in the left and right columns respectively, whereas dashed lines represent $L_{buoy}$ and $Q_{buoy}$ . The non-rotating cases sample a range of $Ra$ ; the rotating cases are those shown in the previous figure. As can be seen in the rotationally constrained cases in the bottom right panel, the more dynamically complex flow structure requires significantly longer time averages to smooth out. . . . .	133
5.10	Vertical profiles of $L_{diss}$ and $L_{buoy}$ for a non-rotating stratified case with $N_\rho = 1.4$ , and $Ra = 10^4 Ra_c$ . . . . .	135
5.11	Values of $z_{diss}$ for a range of non-rotating and rotating simulations at a range of stratifications, $N_\rho$ . . . . .	137

5.12 Values of $z_{diss}$ for a range of simulations at fixed supercriticality, $\text{Ra} = 10^2 \text{Ra}_c$ for stratifications of $N_\rho = 0.5$ (red circles) and 1.4 (blue crosses) and a range of $\text{Ta}$ . . . . .	138
5.13 Fluxes of energy provided by different transport terms in the total energy equation (left panels) and internal energy equation (right panels), for example 2D cases at varying $\text{Ra}$ , $N_\rho$ , and $\text{Ta}$ . . . . .	141
5.14 Specific entropy, $s$ , as a function of depth in a variety of non-rotating and rotating cases at a range of stratifications, and $\text{Ra}_F$ . The top panel shows non-rotating cases with $N_\rho = 1.4$ at a range of supercriticalities, the middle panel shows non-rotating cases at fixed supercriticality but varying $N_\rho$ , and the bottom panel shows rotating cases with $\text{Ta} = 10^8$ and $N_\rho = 1.4$ at varying supercriticality. . . . .	145
5.15 Calculated values of the Nusselt number, $\text{Nu}$ , as a function of $\text{Ra}_F$ for a wide sample of both non-rotating and rotating calculations at a range of different $N_\rho$ and latitudes. . . . .	148
5.16 Values of the non-dimensionalised velocity (the Reynolds number, $\text{Re}$ ) as a function of $\text{Ra}_F$ for a wide sample of both non-rotating and rotating calculations at a range of different $N_\rho$ and latitudes. The top panel is plotted against $\text{Ra}_F/\text{Ra}_c$ whereas the bottom panel is plotted against $\text{Ra}_F$ . . . . .	151
5.17 Properties of top and bottom boundary layers at varying $\text{Ra}_F$ , $N_\rho$ , and $\text{Ta}$ shown as a function of supercriticality. The top panel shows the predicted values of the ratio top and bottom boundary layer entropy gradients, compared to those calculated from convective simulations. The bottom panel shows how the depth of the top and bottom boundary layers $\delta_{BL}$ , overplotted with $\text{Ra}_F^{1/4}$ and $\text{Ra}_F^{1/4}$ scalings. . . . .	154
5.18 A plot of KE flux magnitudes for varying $N_\rho$ at asymptotically high $\text{Ra}_F$ , compared to simulations at finite $\text{Ra}_F$ . . . . .	159
6.1 A latitude-longitude global map of the temperature at the top of the atmosphere for an evolved HD 209458 b atmosphere at $t = 1150\text{days}$ . The white star marker indicates the position of the sub-stellar point. . . . .	165

---

6.2	A latitude-longitude global map of the zonal wind at the top of the atmosphere for an evolved HD 209458 b atmosphere at $t = 1150$ days. The white star marker indicates the position of the sub-stellar point. . . . .	167
6.3	Figure taken from Showman and Polvani 2011, Figure 12. A latitude-longitude global map of the temperature (colour scale, K) and wind speed (arrows) at 30 mbar pressure of the shallow-water solar-metallicity model of HD 189733b. . . . .	167
6.4	Vertical profiles of the latitudinally averaged temperature plotted against atmospheric height (first panel) or pressure (second panel) at 4 different longitudes corresponding to the sub-stellar point (green), the anti-sub-stellar point (blue), and the two terminators (yellow and red) . . . . .	168
6.5	Zonal (top panel) and meridional (bottom panel) wind profiles averaged in longitude, and plotted as a function of latitude and atmospheric height (first panel) or pressure (second panel). The simulation is of an evolved HD 209458 b atmosphere at $t = 1150$ days. . . . .	169
6.6	Figure adapted from Thorngren et al. 2019, Figure 1 & 4. The top panel (a) shows intrinsic temperatures calculated from equation (6.2) using two different heating models Thorngren and Fortney 2019. For the "HD 209458 b"-like planet being studied within this chapter, such a relation yields $T_{int}$ values in excess of 500K. The bottom panel (b) shows radiative-convective boundary pressures as a function of $T_{eq}$ for a range of surface gravities. HD 209458 b has a surface gravity of $9.4\text{ms}^{-2}$ . . . . .	172
6.7	Longitudinally averaged zonal (left) and meridonal (right) flow profiles for a $T_{int} = 100\text{K}$ (top) and $T_{int} = 500\text{K}$ (middle) case. The bottom row shows the difference between these two cases ( $(u, v)_{T=500\text{K}} - (u, v)_{T=100\text{K}}$ ) . . . . .	173
6.8	The top two panels show zonal wind profiles for both the $T_{int} = 100\text{K}$ (left) and $T_{int} = 500\text{K}$ (right) cases as a function of longitude and latitude. These are accompanied by longitudinally averaged zonal profiles for both cases (middle) and the difference between them (bottom). These profiles are for a horizontal slice at $p = 3.68 \times 10^4$ Pa which encapsulates both the eastward equatorial jet and the westward mid-latitude jets at a moderate atmospheric depth. . . . .	174

6.9	Latitudinal profiles of the bottom boundary intrinsic heat flux $T_{int}$ for the original spatially invariant case, and the two latitude dependent cases. . .	177
6.10	Longitudinally averaged zonal (left) and meridonal (right) flow profiles for a constant surface temperature forcing with $T_{int} = 100\text{K}$ (top) and variable forcing as given by equation 6.5, with $T_{int} = 100\text{K}$ , $\alpha = 0.2$ (middle). The bottom row shows the difference between these two cases (constant flux minus variable flux). . . . .	178
7.1	Four different plots showing outputs from a preliminary MHD convective simulation at $\text{Ra}_F = 3.8 \times 10^7$ , $N_p = 1$ , $Q = 10$ , and $\text{Pr} = \text{Pm} = 1$ . A vertical background magnetic field of strength $B_0$ exists, with both the top and bottom boundary conditions such that the field is purely vertical at boundaries. The top two panels show the two flux decompositions previously discussed, showing the additional magnetic terms $L_{ohm}$ and $L_{lor}$ given by equations (7.4) and (7.5) respectively. The bottom left panel shows the value of total value of $E$ , as well as the ohmic and viscous components, for both a magnetic and non-magnetic case of comparable $\text{Ra}_F$ . The bottom right panel shows the time-averaged entropy structure over which lines of constant magnetic potential (magnetic field lines) are plotted. . . . .	188
7.2	Comparison between the internal energy flux decomposition (left) and the horizontally averaged vertical entropy profiles (right) of two non-rotating, stratified, simulations within the same parameter regime of $\text{Ra}_F = 100\text{Ra}_c$ and $N_p = 1/4$ . Differences in the overall flux balances are negligible, with the largest deviation in $L_{tot}$ between the 2D and 3D cases being $\sim 0.05\%$ and the overall entropy contrast across the domain varying by $3.04\%.$ . . .	190
7.3	Figure adapted from Amundsen et al. 2014, Figure 4. Heating rates as a function of atmospheric pressure obtained from the radiation scheme used within the UM (green and cyan) compared to the 1D radiative-convective equilibrium code ATMO (black). The dotted blue line shows heating rates from using band-averaged mean absorption coefficents. The flaws of using these mean absorption coefficents is discussed in more depth in Section 4.4 of Amundsen et al. (2014). . . . .	192

## **Declaration**

Chapter 5 was adapted from "Viscous Dissipation in Simulations of Rotating, Strongly Stratified Planar Convection", a paper being prepared for publication in collaboration with Matthew Browning and Laura Currie who both have contributed to its development.

# Acknowledgements

Firstly, I wish to thank my two supervisors: Matthew Browning and Nathan Mayne. I cannot thank you both enough for your guidance and mentorship throughout the course of my PhD, and I genuinely could not have asked for a better pair of supervisors. In the same vein, I wish to show my gratitude to Laura Currie for her continued help and support throughout the course of my PhD. A large portion of the success of this thesis can be attributed to the supervision and support of these three people, and words cannot express how grateful I am for your time and energy.

I must also acknowledge the members of the Exeter Exoplanet Theory Group (EETG). A special mention goes to Duncan Christie, as without you I doubt I could have ever deciphered the amalgamation of Fortran that calls itself the Unified Model. A real highlight of my PhD, and of what was a truly difficult time for everyone across the world, was the continued EETG social zoom calls that we held as group (with the sole exception of certain objectively false opinions in one of our online quizzes regarding which premiership rugby team is the best). The commitment to the costumes in a certain murder mystery night was truly something to be remembered. To the wider Astrophysics group here at Exeter, the appreciation I have for you all could fill a whole extra chapter of this thesis. Members past and present, I owe you all thanks. Specifically to Laura and Freddy, I am genuinely at a loss for what to say, although I hope you already know. Thank you.

I truly would never have completed my undergraduate degree, let alone my PhD, without the love and support of my family. George, you have been an ever-present role model and I could not have asked for a better brother. Your success has always been an inspiration to me, and I cannot thank you enough for always being there. To my best friend and partner, Federica. I could not have gotten through these past few months without your

continued love and support, you are the absolute rock of my life. Finally, I owe it all to my mum, Karen. Words cannot express my appreciation for what you've done for me, not only throughout my PhD but throughout my life, and for that, I dedicate this thesis to you.

Simon Robert White Lance

Exeter, U.K.

4<sup>th</sup> March 2023

# Chapter 1

## Introduction

This chapter will introduce some of the fundamental background of fluid flows in astrophysics, specifically those found within stars and planets. Section 1.1 will begin by giving an overview of the types of fluid flows present in astrophysics, specifically those relevant to this thesis such as interior convection (relevant to Chapters 4 and 5) and large scale atmospheric circulation (relevant to Chapter 6). It will then provide an overview of some of the outstanding puzzles that are present within these fields both in theory, and in observations. There will be a particular focus on interior stellar convection, as well as the observed anomalously high radius of many close orbiting, tidally-locked, gas giant planets. Lastly Section 1.2 will provide a breakdown of the overall structure of this thesis.

### 1.1 Fluid flow in Stars and Planets

Fluid dynamical flows are ubiquitous within astrophysics, ranging from the large scale outflows from active galactic nuclei (King and Pounds 2015), to the collapse of giant molecular clouds into densely interacting star forming regions (Girichidis et al. 2020), down to the study of cryolava fluid flows on the surface of Saturn’s moon Titan (Bodin and Cordier 2022). Direct observation of these flows is difficult, in some cases impossible, and so to study these fluid dynamical phenomena we must turn to numerical simulations and to theory.

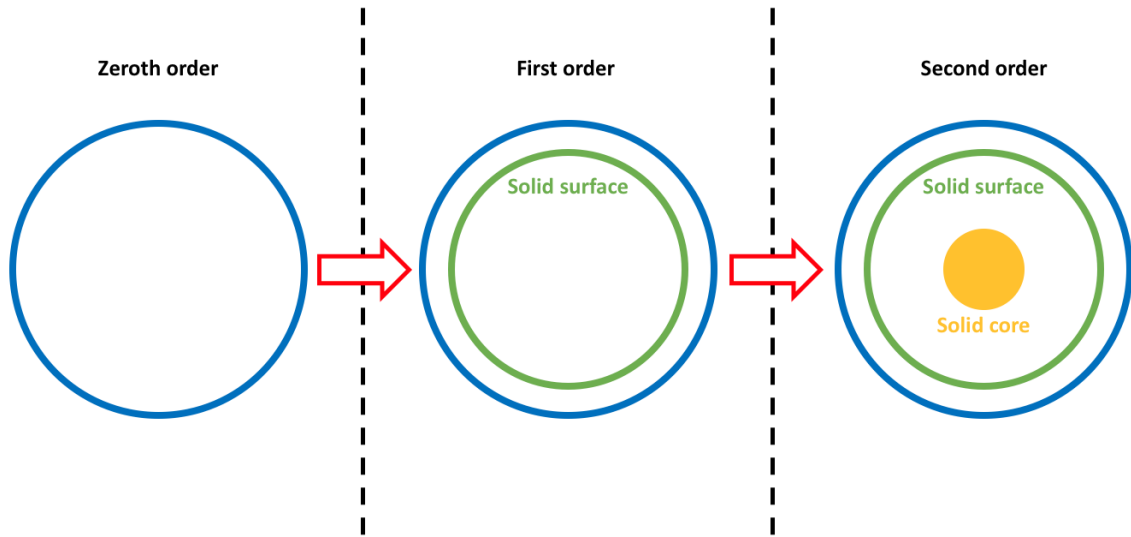


**Figure 1.1:** A cartoon schematic of a possible zeroth, first, and second order approximations of star or planet. Under the most simple approximation, these bodies are large spheres of fluid. To a higher degree of detail, there may exist a solid surface or a fluid layer with a considerably different structure.

In the case of stars and planets, to a most basic zeroth order approximation, they are large spheres of fluid. In the case of terrestrial planets, an ever-so-slightly more complex first order approximation might include a solid boundary, or surface, at some point on the planet, and then a second order approximation might include a solid inner core of some radius (see Figure 1.1). Using the Earth as an example, as much as 75% of the planetary radius can be described and studied as a fluid. While this might seem trivial with the zeroth, first, and second order distinctions being somewhat arbitrary, the purpose of this figure is to emphasize how much of these objects can be treated as a fluid, and as such can be studied by some extension of the governing equations of fluid dynamics (see Chapter 2). The different regions in these objects are distinctly different, that is, the Earth's interior mantle is clearly physically different to the Earth's atmosphere, however they are still both describable as fluids, and often exhibit the same dynamical phenomena. See, for example, the study of convection in the Earth's mantle (Ricard et al. 2022), its oceans (Kovalevsky et al. 2020), and its atmosphere (Stevens 2005). The physical properties such as viscosity, density, and temperature vary considerably between these three different regions resulting in distinctly different fluids, but they all exhibit convection. We shall see in our study of interior convection that as the typical flow velocities are sufficiently subsonic, certain approximations can be made to filter out sound waves and simplify the governing equations that describe the fluid flow (see Ogura and Phillips (1962), Gough (1969) and

discussion in Section 2.1.2). In some other regimes, for example, high in planetary atmospheres, these approximations may break down, leading many authors to turn to fully compressible models instead. Both of these fluid regimes exist within a hot Jupiter for example.

The following two sections will delve deeper into the sorts of fluid flows that are present in stars (Section 1.1.1) and planets (Section 1.1.2) building towards introducing some of the current problems.

### 1.1.1 Convection in Stars

The two primary forms of heat transport within stars are via radiation and convection. Which of these dominates the heat transport at a given radius is dependent on the overall mass of the star. As can be seen in Figure 1.2, low mass stars with  $M \lesssim 0.35M_{\odot}$  where  $M$  is the stellar mass, and  $M_{\odot}$  is the mass of the Sun, are fully convective throughout their interiors, stars with mass  $0.35M_{\odot} \lesssim M \lesssim 1.5M_{\odot}$  have radiative cores and convective envelopes, and those with  $M \gtrsim 1.5M_{\odot}$  have convective cores and radiative envelopes (Kippenhahn et al. 2013). Considering that fully-convective low-mass stars make up > 70% of the stellar population of the Milky Way (Chabrier and Baraffe 1997), and convective motions dominate the majority of their interiors, it is clear that understanding convection is of crucial importance to understanding these objects.

#### 1.1.1.1 Surface granulation

Observations of our closest star, the Sun, reveal a surface covered in convective granules that are present within the Sun's photosphere (see Figure 1.3). This granular convection is believed to be driven primarily by the non-adiabatic radiative cooling of the fluid within a thin thermal boundary layer (Stein and Nordlund 1998). This is formed by the strongly superadiabatic region that exists at the depth where the optical depth of the fluid is unity (Nordlund et al. 2009). Above this point, the fluid is optically thin and therefore radiative cooling from the surface becomes important. Doppler measurements of the Sun also reveal a larger scale cellular flow structure of order 30 Mm known as supergranulation (see Figure 1.4). These structures have much longer dynamical timescales when compared

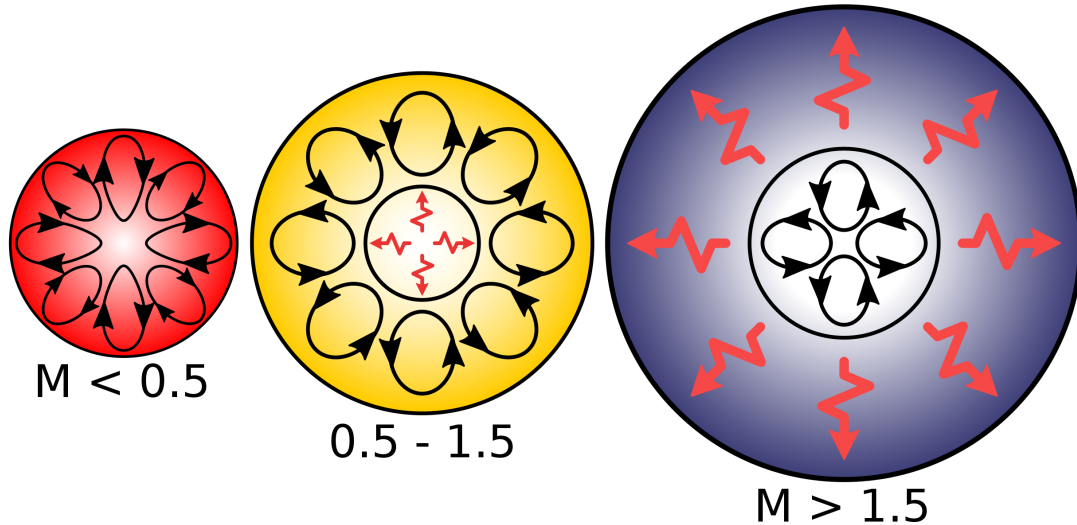
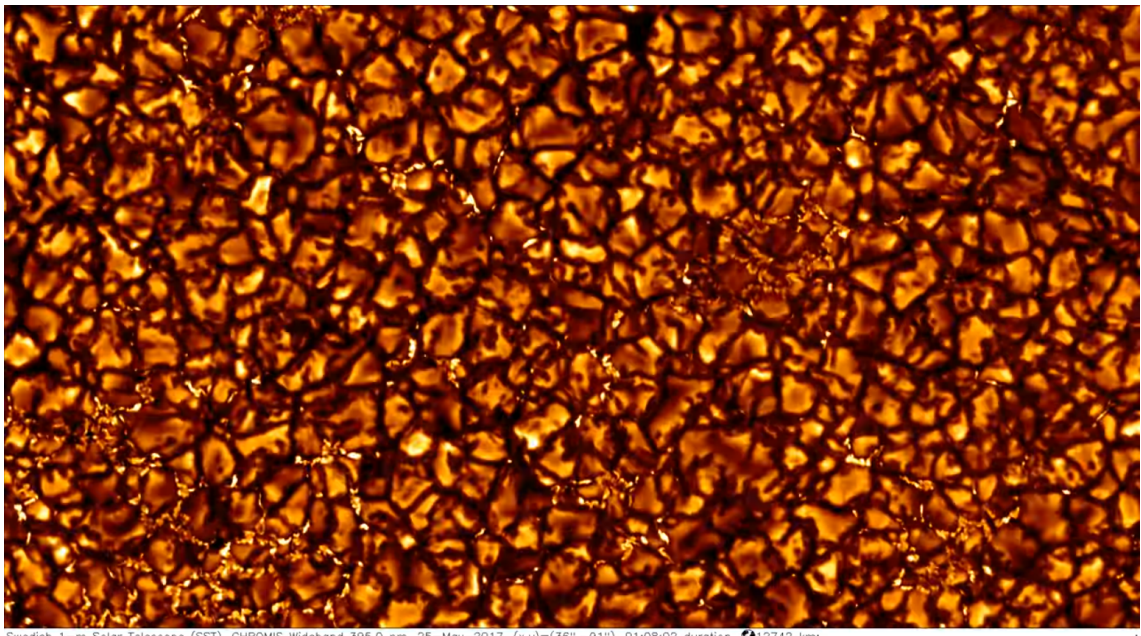


**Figure 1.2:** The typical structure of stellar interiors as a function of mass ( $M$ ) in units of solar mass ( $M_{\odot}$ ). Stars with a mass,  $M \lesssim 0.35M_{\odot}$  are fully convective throughout their entire interior, those with mass  $0.35M_{\odot} \lesssim M \lesssim 1.5M_{\odot}$  have radiative cores and an overlying convective envelopes, and those with  $M \gtrsim 1.5M_{\odot}$  have convective cores and radiative envelopes. Image credit: [https://en.wikipedia.org/wiki/File:Star\\_types.svg](https://en.wikipedia.org/wiki/File:Star_types.svg)

to typical surface granulation (existing for somewhere in the order of 1-2 days) and they consist of strong horizontal flows with rms velocities in the range of  $300\text{-}400\text{ ms}^{-1}$ , an order of magnitude larger than their vertical components. This can again be seen clearly in Figure 1.4 where the Doppler signal at the center of the disc is at a minimum, representative of a primarily horizontal flow pattern.

This surface convection is of particular interest to those wishing to detect long-period, low-mass exoplanets through radial velocity measurements. These convective motions produce their own radial velocity signals as a result of the asymmetries in the granular structure. The wide, upwelling, motions produce a larger signal than the narrow downwelling intergranular lanes. This is further enhanced by the flux difference due to the larger upwelling signal being hotter, and therefore brighter, than the narrow downwelling fluid (Liebing et al. 2021). The suppression of convective motions as a result of magnetic activity results in a decrease in the observed convective blueshift and introduces variability to the observed radial velocity measurements (Dravins et al. 1981). This is one of the main obstacles facing the detection, confirmation, and characterisation of Earth- and Neptune-mass planets in long-period orbits via the radial velocity method (Crass et al. 2021), although recent progress has been made in removing the noise from such sig-



Swedish 1-m Solar Telescope (SST), CHROMIS Wideband 395.0 nm, 25-May-2017, (x,y)=(36°,-91°), 01:08:02 duration 12742 km

**Figure 1.3:** An image of the surface of the Sun taken by the Swedish 1m Solar Telescope in 2017 showing distinct convective cells of order 1-2Mm in width. These structures develop on a typical timescale of order 10 minutes. Image credit: Institute for Solar Physics, Sweden.

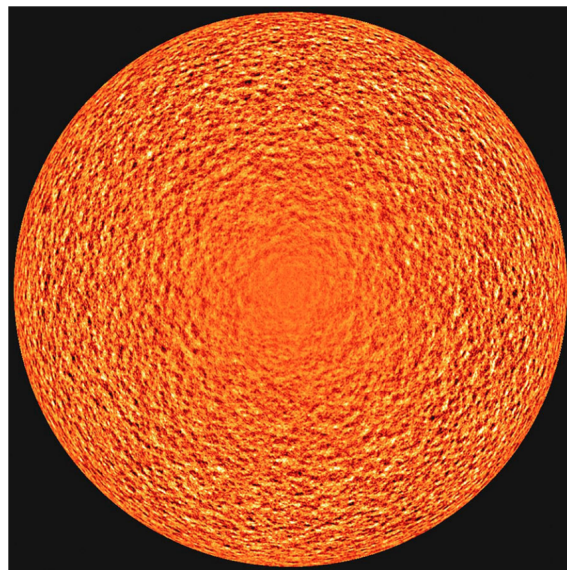


**Figure 1.4:** Doppler imaging of the sun obtained by MDI instrument onboard the SOHO satellite. Image credit: SOHO/MDI/ESA (Rincon and Rieutord 2018)

nals through the use of surface activity proxies (Haywood et al. 2022) or deep learning algorithms (de Beurs et al. 2022). Of more interest to the work contained in this thesis however, is the study of giant cell convection in the interiors of these objects.

### 1.1.1.2 Convective interiors

As previously mentioned, direct observations of these types of astrophysical fluid flows are difficult. As a result, large scale numerical simulations are regularly employed to study the convective interiors of stars. One stellar interior that can be observationally constrained however, is the Earth's closest star, the Sun. It has been known for more than a century that the surface of the Sun rotates differently at different latitudes, with the equator experiencing a rotating rate of  $\sim 25$  days, and the mid-latitudes experiencing a period of  $\sim 33$  days (Miesch and Toomre 2009). The advent of helioseismology allowed for the investigation of the solar interior by studying the oscillations of sound waves (known as p-modes) as they propagate through Sun (Gough and Toomre 1991). Such methods resulted in direct observations of angular velocity ( $\Omega$ ) profiles of the Sun's interior, and revealed features such as a uniformly rotating deep interior (below  $\sim 0.7R_\odot$ , the boundary known as the tachocline between the radiative interior and the convective envelope). Above the tachocline lines of near constant  $\Omega$  with respect to radius for a given latitude can be seen, and a radial shear layer is visible at the surface (see Figure 1.5). To study these regions further, we are required to turn to numerical simulations.

All global numerical simulations of sufficient depth develop large scale convective flows, commonly referred to as giant-cell convection (Rast 2020). Despite neglecting the surface granulation and instead evoking more simplistic impermeable upper boundary conditions, these simulations have had remarkable success at reproducing the gross features of the solar differential rotation profile (Brun and Toomre 2002, Karak et al. 2015 and others) and studying components of dynamo action (Browning et al. 2006, Nelson and Miesch 2014 for example). Figure 1.6 from Miesch et al. (2008) demonstrates the typical convective structure formed within the upper portion of the convective regime at two radial heights of  $r = 0.98R_\odot$  and  $r = 0.95R_\odot$ , where  $r$  is the radius and  $R_\odot$  is the solar radius. Large asymmetries between the hot, upward and cold, downward flows can be seen

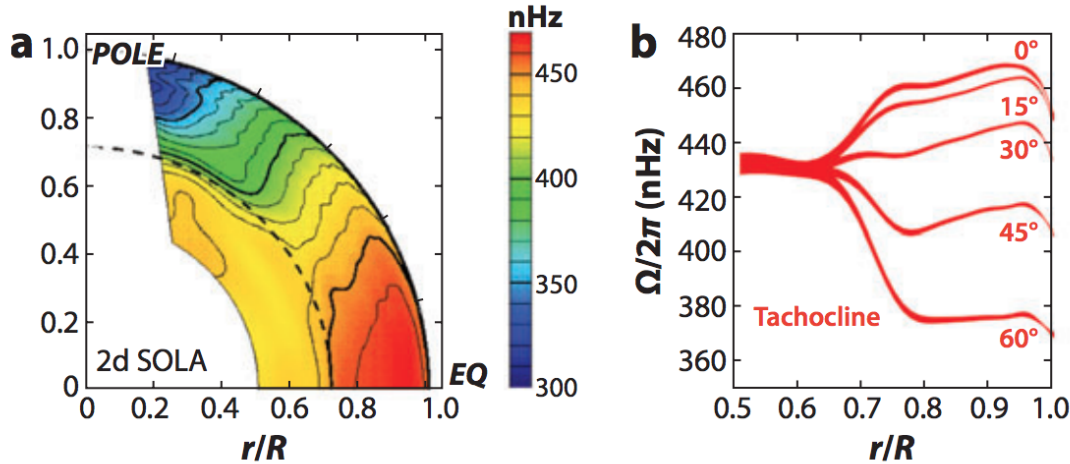


**Figure 1.5:** Angular velocity profiles of the sun as a function of radius from helioseismology. (a) Shows the full latitude and radial dependence of  $\Omega$  from Schou et al. (1998) (b) Shows radial cuts of the  $\Omega$  profile for a range of latitudes from Miesch and Toomre (2009).

as a result of the density stratification and are a known feature of compressible convection (Stein and Nordlund 1989).

However, as modellers moved to more higher resolution, and thus more resolved turbulent convection, they have encountered what is referred to as the *convective conundrum*. Simulations by Brun and Toomre (2002) had produced results in reasonable agreement with helioseismic measurements, that is, a fast rotating equator with a corresponding angular velocity drop of  $\sim 30\%$  from the equator to the pole. The higher resolution models (which resolved more of the previously unresolved turbulence) explored in Miesch et al. (2008) showed a reduced contrast in the latitudinal differential rotation – specifically 50% lower than that observed in the lower resolution case of Brun and Toomre (2002). When the diffusivities were lowered even further at fixed rotation rate, often the simulations were found to "flip" to an anti-solar differential rotation profile. Gastine et al. (2013), following the pioneering work of Gilman (1977) links this transition from strong solar-like differential rotation to anti-solar behaviour (rapidly rotating poles and a slow equator) to a transition in the relative strengths of the inertial and Coriolis force (encapsulated by the Rossby number,  $Ro$ ). Similar results have been shown by Featherstone and Miesch (2015) in which rotationally constrained flows (low  $Ro$ ) correspond to solar-like rotation profiles, whereas weakly rotationally constrained flows develop anti-solar rotation as a result of angular momentum transport by convective Reynolds stresses establishing single cell

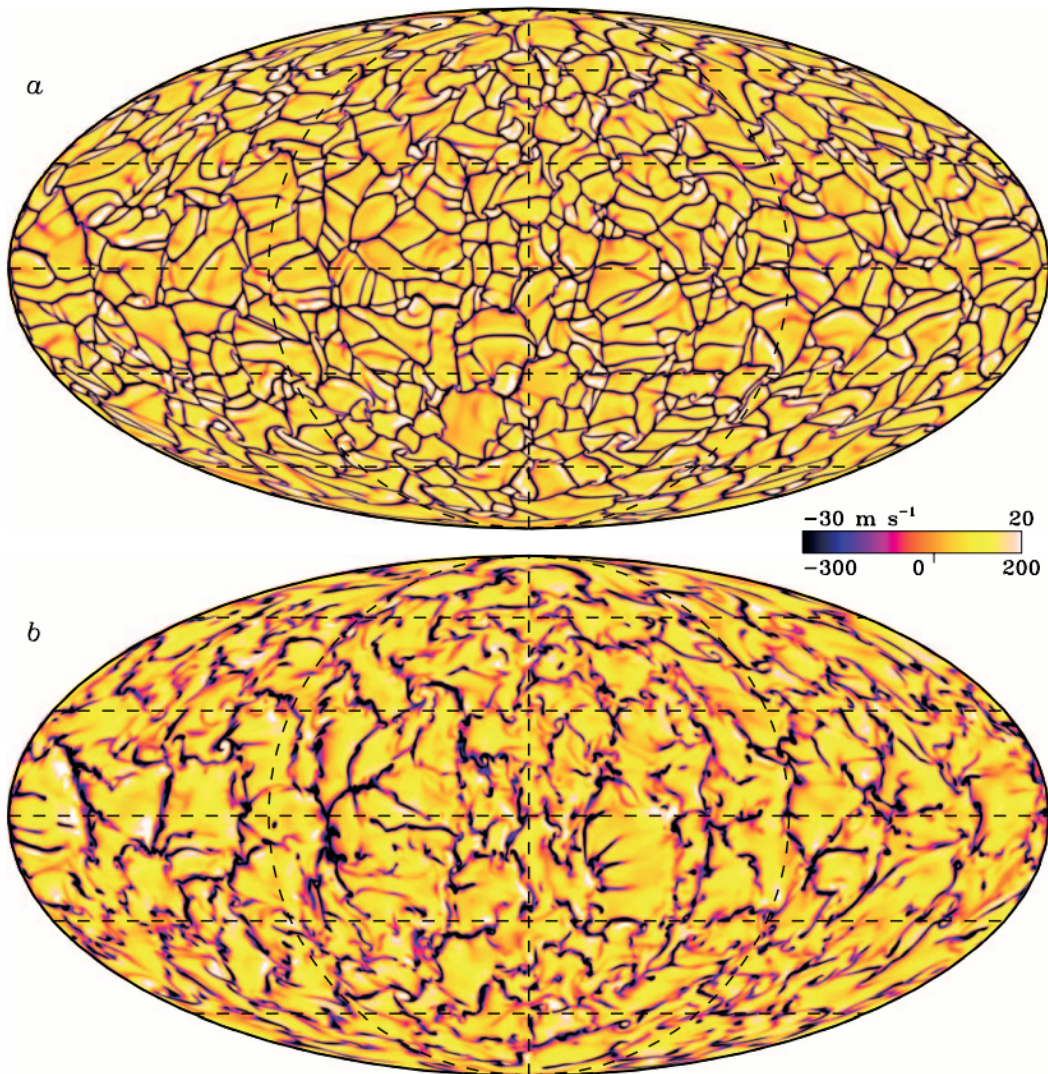


**Figure 1.6:** Figure taken from Miesch et al. (2008), Figure 1. Numerical outputs of the radial velocities for giant cell convection at (a)  $r = 0.98R_{\odot}$ , and (b)  $r = 0.95R_{\odot}$ , where  $r$  is the radius and  $R_{\odot}$  is the solar radius. The figure uses a Mollweide projection such that all  $360^\circ$  of longitude can be seen. The dashed lines represent constant latitude of  $0^\circ, \pm 30^\circ$ , and  $\pm 60^\circ$ , and lines of constant longitude of  $0^\circ$  and  $\pm 90^\circ$ .

meridional circulations.

Furthermore, disagreement between helioseismic measurements, numerical simulations and theory regarding the amplitude and structure of the convection still exist. Hanasoge et al. (2012) demonstrated that helioseismic observations of the convective amplitudes that are present in the Sun are much smaller (several orders of magnitudes lower) than those obtained in numerical simulations. Greer et al. (2015) apply a different helioseismology method (ring-diagram, instead of time-difference in Hanasoge et al. (2012)) to recover convective amplitudes considerably closer to those produced by numerical simulations. This disagreement remains unresolved. Vasil et al. (2021) propose that the solar convective zone is rotationally constrained almost everywhere beneath the near-surface shear layers and that this rotation acts to decrease the length scale at which the convection occurs and suppress giant cell convection. They also argue that the observations of Hanasoge et al. (2012) are due to a scale effect and not due to an actual small velocity.

In conclusion, there is considerable evidence that our knowledge of the large-scale convective flows that occur within the solar interior is incomplete. Current numerical models do not accurately predict the convective velocities we observe via helioseismology and therefore it is entirely possible that we are similarly getting other key mechanisms, such as the treatment of dissipation, wrong. Many authors have previously pointed to various key components of the convection that are missing from our numerical simulations, with the influences of rotation and stratification arguably chief among them (Vasil et al. 2021). By considering idealised convective systems, as done in Chapters 4 and 5 we aim to explore the influence of rotation and stratification on the resulting dissipation, heat transport, and overall dynamics of the convection.

### 1.1.2 Planetary atmospheres

As discussed in 1.1, to a zeroth order approximation a planet is largely just a large sphere of fluid. This picture is somewhat distorted in the case of terrestrial planets, however with the exception of this chapter these planets will not be discussed within this thesis. The focus of this work will be on gas giant planets, and while physically these are clearly different objects from stars, they are analogous in that they can be treated largely as fluids.

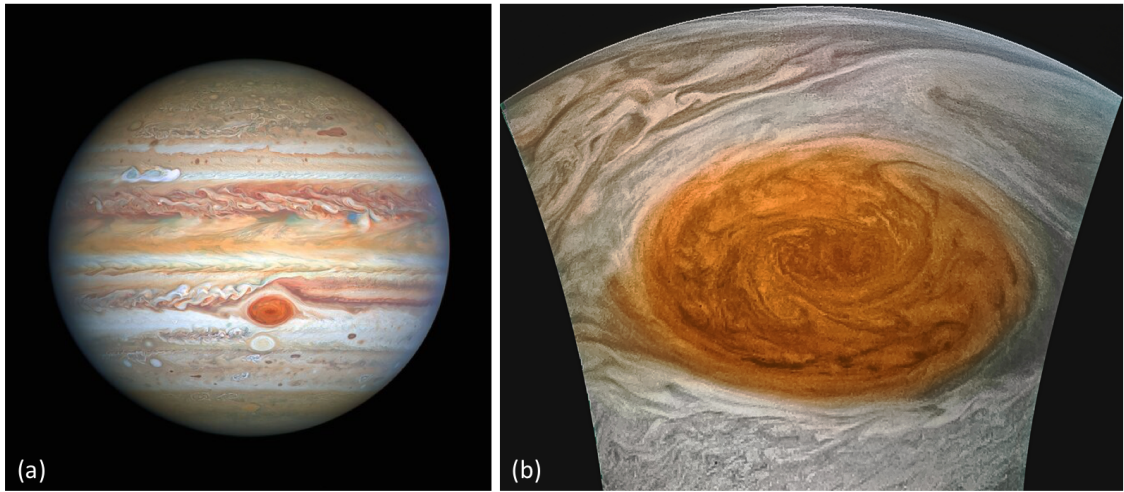


**Figure 1.7:** The gas giant Jupiter (a) and its Earth-sized storm, the Great Red Spot (b). Image credits: NASA's Hubble Space Telescope on Aug. 25, 2020 (a) and NASA's Juno orbiter on Jul. 10, 2017 (b).

### 1.1.2.1 Atmospheric dynamics

The most studied gas giant to date is Earth’s own neighbour, Jupiter (see Figure 1.7). Due to its proximity and long term study (with the naked eye from as early as the 8th century BCE, and telescope observations from the 17th century) it has received a considerable amount of attention and is without a doubt the most heavily studied example of a gas giant planet. Its banded structure and Great Red Spot were observed as early as the 17th century and Giovani Cassini measured its differential rotation in 1692 (Beebe 1996). These dynamical features are abundant in Jupiter’s atmosphere, with large-scale zonal jets extending around its entire circumference generating many turbulent eddies at the interfaces between counter-rotating jets as a product of Kelvin-Helmholtz instabilities (formed by velocity shear in two adjacent regions of fluid). Recent observations of Jupiter’s polar regions by the Juno spacecraft also revealed stable and long-lasting cyclone structures (Mura et al. 2022).

Extending outwards towards gas giant exoplanets it is not unreasonable to expect a similar abundance of dynamical features. This is especially the case for “hot Jupiters”, which are Jupiter mass planets in extremely close and short orbits of their host star. These planets are so close that they are in fact tidally locked, meaning their rotation period is equal to their orbital period. Such planets have one side of the planet in permanent day and the other in permanent night. This results in two distinct regions, a very heavily

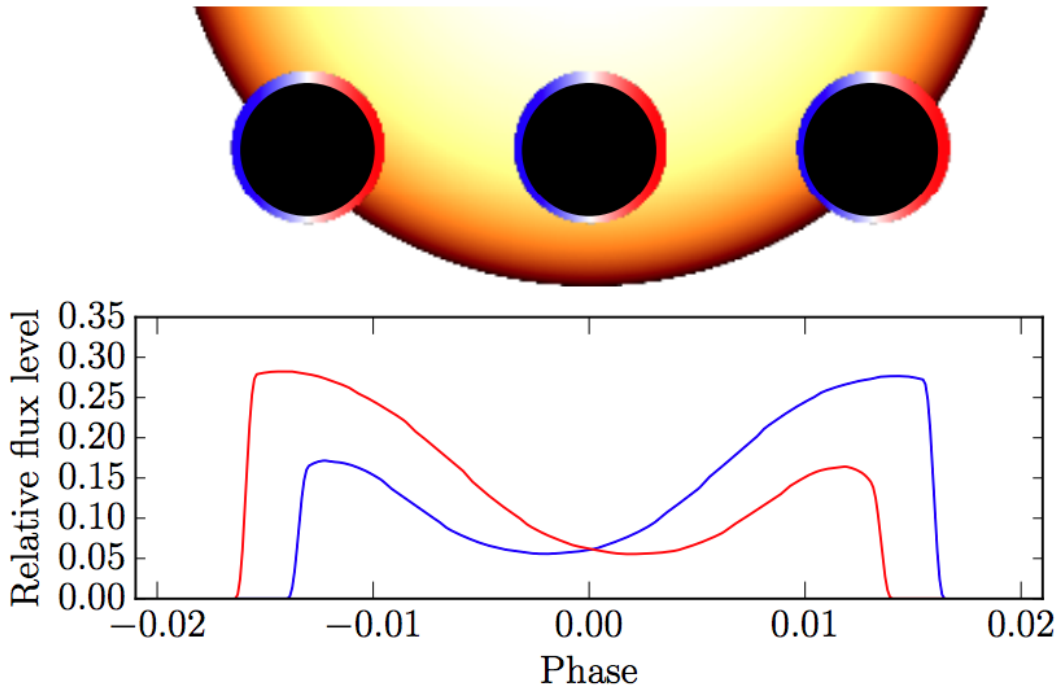


**Figure 1.8:** Figure taken from Louden and Wheatley (2015), Figure 1. Model of how the relative flux of the leading and trailing limbs of a transiting hot Jupiter exoplanet can be separated.

irradiated and hot side, and a dark, cold side. This establishes a significant temperature gradient across the day-night terminators and is believed to establish considerable zonal jets. It is these types of planets that are the focus of Chapter 6.

The closest hot Jupiter to Earth is HD 189733 b, and at a distance of 64.5 light years away, it is of order  $10^6$  times further away than Jupiter. It understandable then that these objects are much harder to observe in detail, and so use of numerical simulations is important to try and understand the dynamics of the atmospheres of these objects. As previously mentioned, one of the commonly predicted dynamical features of these types of exoplanets is a strong equatorial zonal jet established due to the day-night temperature gradient. Attempts to measure such dynamical features have been ongoing with the detection of a net blue shift of sodium absorption signals in the transmission spectra of the hot Jupiters HD 209458 b (Snellen et al. 2010), and HD 189733 b (Wytttenbach et al. 2015). The work presented by Louden and Wheatley (2015) (see Figure 1.8) however managed to spatially resolve and isolate excess velocity shifts to the leading and trailing limbs of HD 189733 b. After assuming the exoplanet is rotating at a fixed rate for a tidally locked orbit of 2.22 days, and adjusting for the resulting systematic red and blue shifts on the leading and

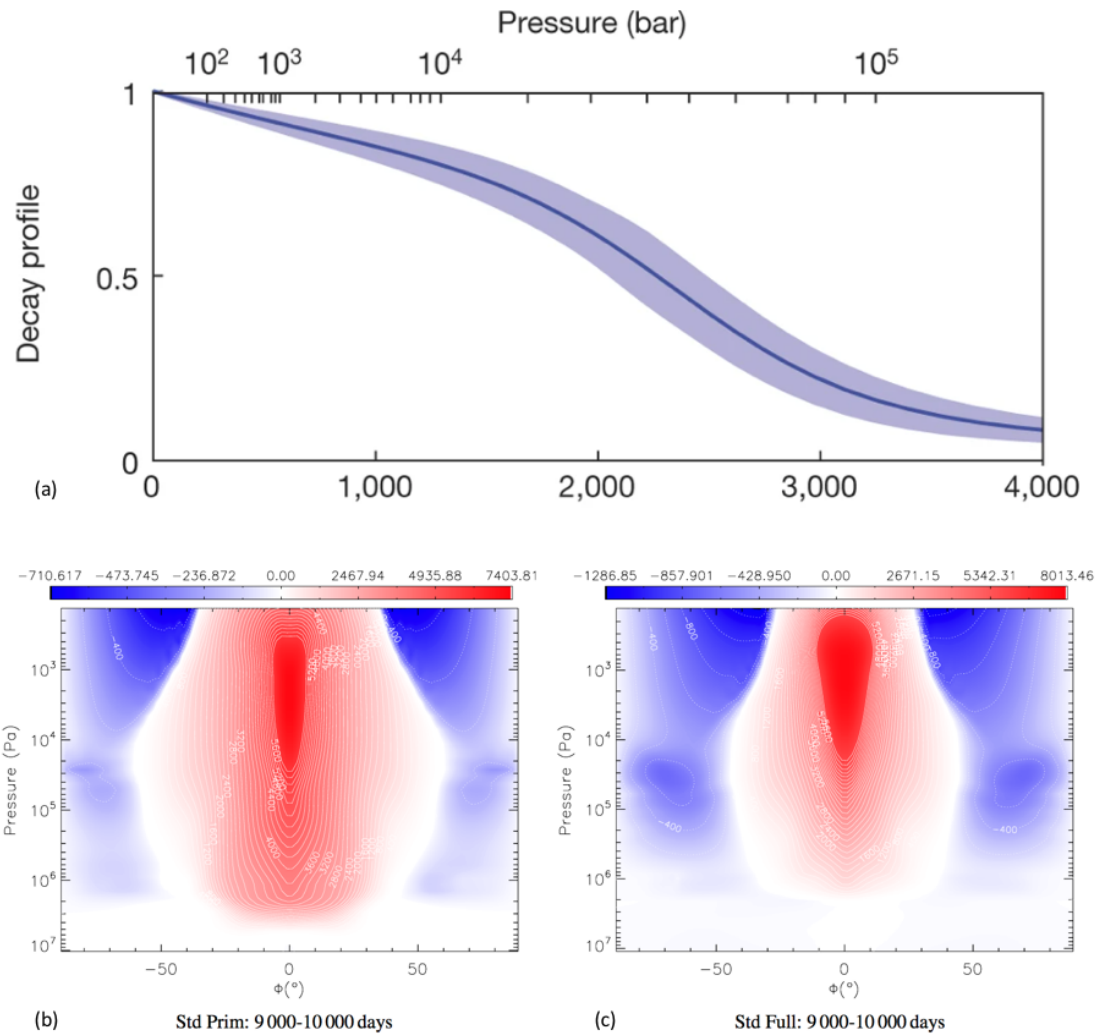


**Figure 1.9:** Panel (a) shows the predicted decay profile of Jupiter’s 1 bar zonal flows as a function in depth as presented in Kaspi et al. 2018, Figure 4a. This profile is obtained from a minimum cost optimisation process using high resolution gravity measurements from Juno. Panels (b) and (c) show the zonal and temporal mean profiles of the zonal wind ( $m s^{-1}$ ) as a function of latitude  $\phi$  and pressure.

trailing limbs respectively, a net blue shift is observed on the trailing limb, suggestive of an eastward equatorial zonal jet. From this excess Louden and Wheatley (2015) proceed to measure the wind velocities of such a jet, and thus produce the first spatially resolved measurement of the atmospheric dynamics of an exoplanet.

Another prominent dynamical feature is the presence of deep planet-wide zonal flows that extend down towards the interior of these planets. Juno observations of Jupiter’s gravitational field indicate that the observed zonal flows present at its “surface” extend thousands of kilometers deep into the interior of the planet as seen in Figure 1.9 from Kaspi et al. 2018. While still only a small fraction of Jupiter’s radius, this is consider-

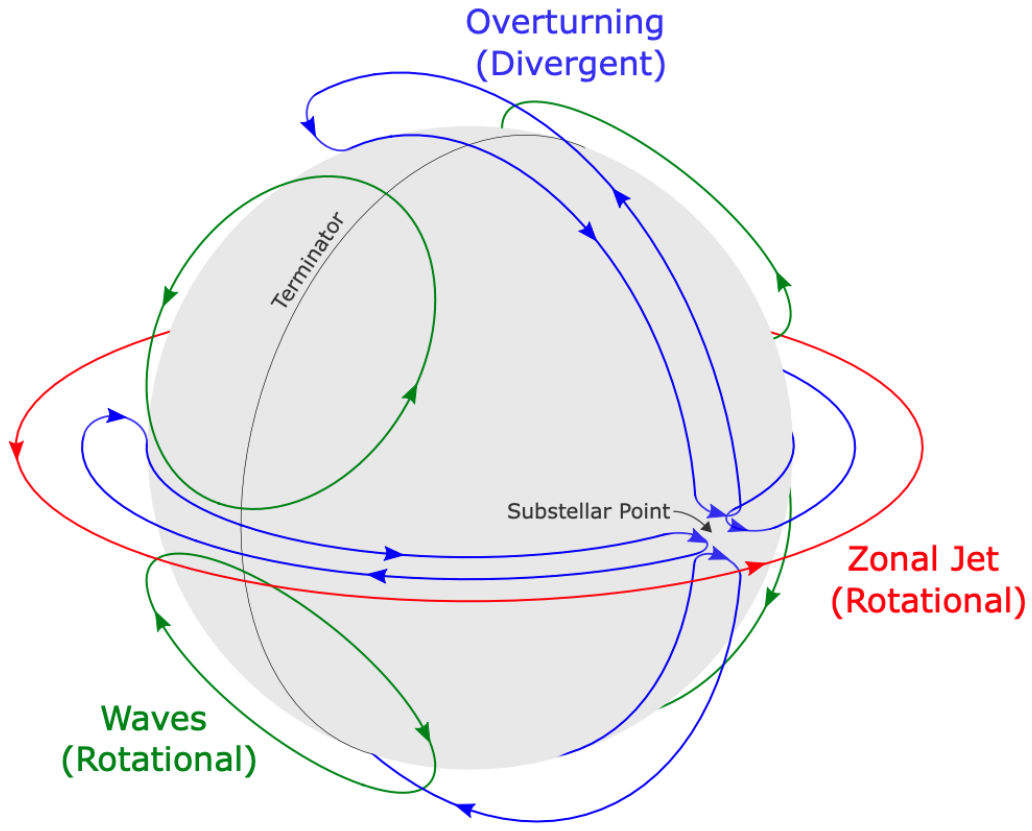


**Figure 1.10:** Figure taken from Hammond and Lewis (2021), Figure 10. A schematic of the three main components of the circulation present in a hot Jupiter atmosphere. An overturning circulatory pattern (blue) can be seen rising at the substellar point, diverging almost isotropically towards the night side before descending. Rotational circulation is then divided into a large-scale zonal jet and a stationary wave component.

able deeper than most numerical simulations resolve. Similar measurements have been made in the study of Saturn, in both planets these supposed higher depth flows exist in a regime where the magnetic field is large enough that Ohmic effects will play a key role in damping such flows (Kaspi et al. 2020). Numerical models of hot Jupiters also suggest that their large scale zonal flows extend the full vertical extent of the simulated domain (as seen and discussed in Chapter 6). Another way to view the various components of the atmospheric circulation is presented in Figure 1.10 from Hammond and Lewis (2021). They show the total flow structure can be decomposed into rotational (divergence-free) and divergent (vorticity-free). For a numerical simulation of a hot Jupiter, Hammond and Lewis (2021) demonstrate that the divergent flow can be responsible for up to  $\sim 50\%$  of the heat transport between the day and the night side.

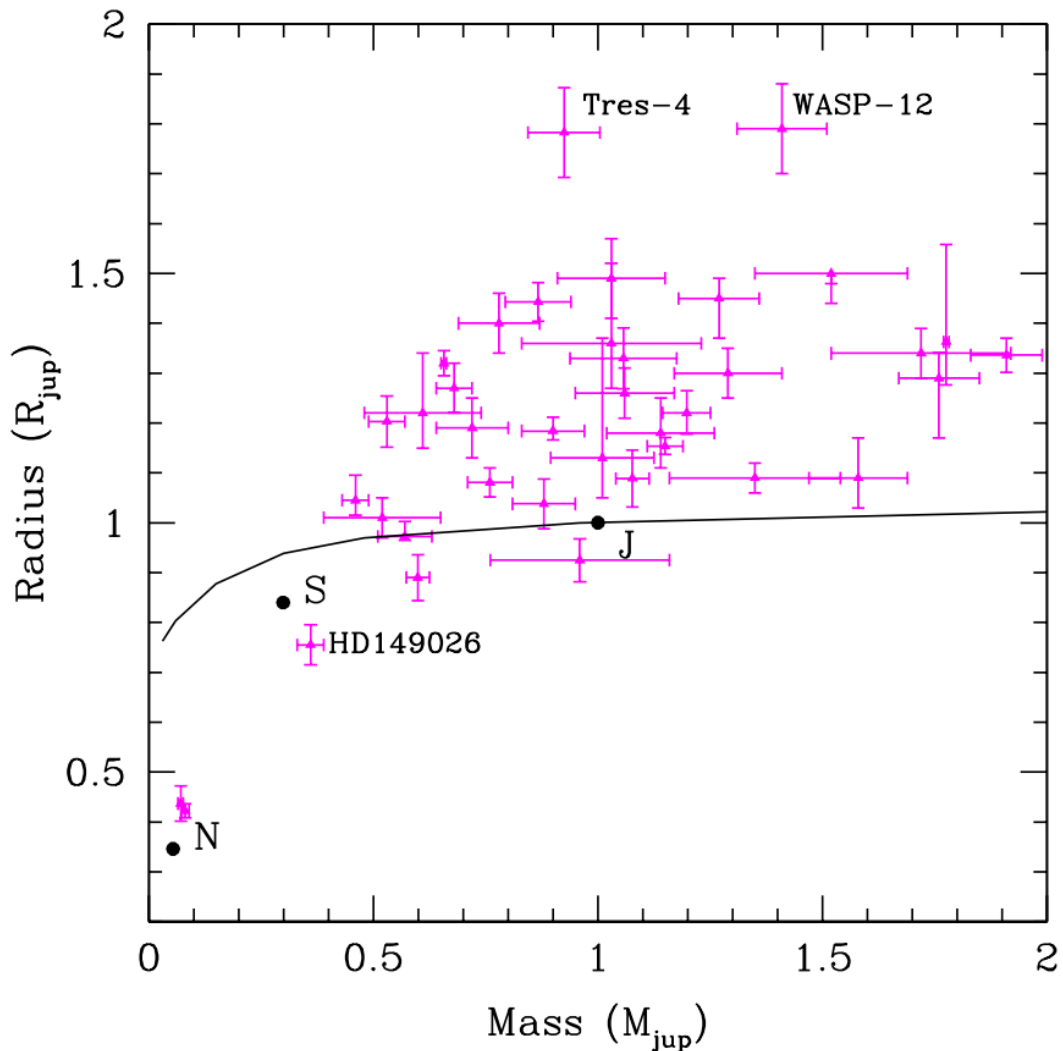


**Figure 1.11:** Figure taken from Baraffe et al. (2010), Figure 2. A mass-radius diagram for transiting exoplanets. The black line represents theoretical predictions of radius as a function of mass from a 1D stellar evolution with solar metallicity values (Baraffe et al. 2008). The full black circles labeled, J, S, and N, represent the solar system objects Jupiter, Saturn, and Neptune respectively.

### 1.1.2.2 Radius inflation and the interior heat flux

A long standing problem in the field of exoplanet studies since the discovery of HD 209458 b (Brown et al. 2001) is the anomalously inflated radii of highly irradiated, tidally locked gas giant planets. As can be seen Figure 1.11, a significant fraction of transiting exoplanets appear to have inflated radii compared to theoretical values obtained from 1D stellar evolution calculations (Baraffe et al. 2010).

Several mechanisms have been proposed in an attempt to explain the inflation of these exoplanets radii (see Baraffe et al. 2010; Baraffe et al. 2014; Fortney and Nettelmann

2010 for reviews) however as of now there does not appear to be a satisfactory resolution to the problem. A promising mechanism is in the form of an additional source of energy being deposited within the planet's interior resulting in a hotter interior adiabat and therefore a larger planetary radius. Both Lubow et al. (1997) and Bodenheimer et al. (2001) propose mechanisms for this missing energy in the form of tidal synchronisation and circularisation of an eccentric orbit, however also acknowledge the inadequacies of these explanations. Specifically, the timescales on which these processes are likely to occur ( $\sim 10^5$  years in Lubow et al. (1997),  $10^8$  in Bodenheimer et al. (2001)) are too short to provide the answer.

Observational evidence of a correlation between the observed inflated radii, and stellar irradiance that these planets receive (Demory and Seager 2011; Laughlin et al. 2011; Weiss et al. 2013 for example) suggest that this missing energy source is in fact the high levels of incident stellar flux absorbed by these planets. Numerical work provided by Showman and Guillot (2002) showed that only a fraction of this incident flux ( $\sim 1\%$ ) needs to be dissipated within the interior to reproduce the observed radius of HD 209458 b. Complimentary numerical evidence appears to provide a robust mechanism for this energy transport in the form of the vertical advection of potential temperature (Tremblin et al. 2017; Sainsbury-Martinez et al. 2019; Sainsbury-Martinez et al. 2021).

If, as outlined above, these inflated radii are the result of additionally interior heating due to the planets increased irradiance, then on some timescale (potentially as short as tens of megayears Thorngren and Fortney 2018) the interior will achieve some thermal equilibrium with this incident flux. Then what is the effect of these hotter interiors on the typical atmospheric circulation patterns of these hot Jupiters?

## 1.2 Structure of the thesis: Flow from Stars to Planets

This chapter has provided an introduction to the types of fluid flow that exist in stars and planets. Particular interest has been given to interior convection, and the atmospheric circulation of highly irradiated and tidally-locked, gas giant planets, and some of the current puzzles and open questions within the study of these fields have been discussed. The rest

of this thesis will be dedicated towards trying to help answer these questions.

Chapter 2 will begin by providing the mathematical framework and theory that underpins the study of astrophysical fluid dynamics, and introducing the governing equations of fluid dynamics. After detailing the process by which convective instabilities arise, and introducing the array of non-dimensional parameters used to study them, it will finish with an overview of the current literature of convective theory, focusing on how such non-dimensional parameters influence and scale with one another. Chapter 3 will then provide an overview of the numerical methods required, and that are subsequently used throughout this thesis. In particular it will outline the development of a "proof-of-concept" linear convection code for the purpose of calculating the point of convective onset, before introducing the Python framework Dedalus and detailing how it has been used to construct both a linear solver for the critical Rayleigh number,  $Ra_c$ , and a 2.5D compressible, rotating, non-linear convection code. Lastly the chapter will introduce the UK Met Office's Unified Model (the UM), highlighting parts of particular interest. These first three chapters will have provided the motivation, mathematical rigour, and numerical methods required for the study of an astrophysical fluid dynamical system. Chapter 4 will then utilise these to present a suite of convective simulations using the non-linear, anelastic, and rotating convection code detailed in the previous chapter. Features of interest that will be discussed here are the breaking of vertical symmetry in response to the introduction of stratification, and the stabilising effects of rotation against convection.

Chapter 5 will then provide an introduction to dissipation in a convective layer, giving an overview of the existing literature. The chapter will then continue by characterising the dynamics of the flow in both the non-rotating, and rotationally constrained regimes, before discussing how these different dynamical regimes affect both the magnitude, and spatial distribution of the viscous dissipation. This will be followed by a discussion of the energy balances that occur within these different regimes and will lead into a comparison of the resultant vertical entropy profiles that develop. Non-dimensional measures of the heat transport and convective flow amplitudes will then be compared to the various literature scalings introduced in Chapter 2, before exploring how the boundary layers vary with stratification and turbulent forcing. Lastly the chapter finishes with a discussion of

how the viscous dissipation can be used to constrain the resulting kinetic energy flux.

The thesis will then conclude with Chapter 6 investigating the effects of introducing hotter, shallower, and more physically realistic convective parameterisations on the bottom boundary of numerical simulations of hot Jupiter atmospheres. Specifically it will present preliminary results of the effects on the developed atmospheric circulation. Chapter 7 will then conclude by summarising the main results of this work, and outline relevant future work.

## Chapter 2

# Theoretical Background

This chapter will provide an overview of much of the mathematics and theory behind the study of astrophysical fluid dynamics, with a specific focus on the process of developing convective instabilities and the study of the resulting flow. Considering a range of non-dimensional parameters representing the relative influence of particular components of the fluid flow and the forces involved allows for particular "regimes" to be defined and studied. In particular, the way these parameters influence and scale with one another, specifically how the heat transport, and velocity amplitudes scale with the buoyancy driving, forms a significant part of convective theory and will form the main conclusions of this chapter.

## 2.1 Fundamentals of Fluid Flow

### 2.1.1 The continuity equation

Consider first, a parcel of fluid of fixed volume  $V$  that is contained within some surface  $S$ . Any net fluid flow into this parcel must be matched by either a corresponding flow out of the parcel or by a change in the density of the fluid remaining. In the case where there is a net gain or loss of fluid inside the fixed volume the density must change to compensate. Mathematically this is expressed as,

$$\int_S \rho \cdot \mathbf{u} \, dS = \int_V -\frac{\partial \rho}{\partial t} \, dV, \quad (2.1)$$

where  $\rho$  is the density,  $\mathbf{u}$  is the fluid velocity,  $t$  is time, and  $S$  is the enclosing surface. As we have assumed a fixed volume (and thus does not vary in time), we can move the time derivative inside the volume integral. When the left-hand side (LHS) of equation (2.1) is positive, it represents a net outward fluid flow from the fixed volume,  $V$ , and corresponds to a decrease in the density. Applying the divergence theorem to the LHS and then rearranging the following is obtained,

$$\int_V \left[ \frac{\partial \rho}{\partial t} + \nabla \cdot (\rho \mathbf{u}) \right] dV = 0, \quad (2.2)$$

and as this applies to any arbitrary volume  $V$ , the integrand must also be equal to zero, that is,

$$\frac{\partial \rho}{\partial t} + \nabla \cdot (\rho \mathbf{u}) = 0. \quad (2.3)$$

This is the continuity equation, one of the primary governing equations included in the study of fluid dynamics. It encapsulates the nature of mass conservation inside a fixed volume. Any fluid flow into such a volume must be matched by either some equal outward flow or a corresponding change in density. When appropriate, various approximations can be applied to this equation to simplify the terms that are contained within it, making such fluid systems easier to study both analytically and numerically.

In the simplest case where the density is taken to be constant, then  $\frac{\partial \rho}{\partial t} = 0$ , and  $\nabla \cdot (\rho \mathbf{u}) = \rho(\nabla \cdot \mathbf{u})$ , resulting in simply,

$$\nabla \cdot \mathbf{u} = 0. \quad (2.4)$$

That is, for an incompressible fluid any flow into a fixed volume is matched exactly by a

corresponding fluid flow outwards. This is the form the equation takes under the Boussinesq approximation, which in essence ignores any and all density perturbations with the exception of those that are multiplied by the gravitational acceleration,  $g$ , e.g. in the buoyancy term of the momentum equation (see section 2.1.3). Applying such an approximation however does, by necessity, result in an unstratified system. Many astrophysical flows, and in particular flows that this thesis is interested in studying, that is, stellar convection, span multiple density and temperature scale heights and as such the Boussinesq approximation falls short at encapsulating their complete nature. Note that the scale heights defined here (and used again in our discussion in Section 2.2.4) is the distance at which the relevant quantity has dropped by a factor of  $e$ . A solution to this comes in the form of the anelastic approximation.

## 2.1.2 Anelastic approximation

The anelastic approximation was first proposed by Ogura and Phillips 1962 in order to filter out sound waves of a fluid system without assuming hydrostatic balance. It is an approximation of the fully-compressible equations of motion that is valid provided flows are sufficiently sub-sonic and is analogous to sound-waves traveling at an infinite speed, that is, any perturbation in density is known at all points within the domain instantaneously. Additionally, it requires that all deviations to thermodynamic variables are sufficiently small when compared to their nearly adiabatic background reference state (a case often realised in stellar convection). This is of particular importance in the application of the Lantz-Braginsky-Roberts (LBR) approximation (Lantz 1992; Braginsky and Roberts 1995) which makes further assumptions regarding the buoyancy term in obtaining equation 3.50. Put more practically, the anelastic equation set neglects the time derivative of density within the continuity equation, that is equation (3.51) reduces to,

$$\nabla \cdot (\rho \mathbf{u}) = 0. \quad (2.5)$$

One of the main advantages of the anelastic approximation is that it is computationally much faster and therefore cheaper than solving for fully-compressible flows. This is due

to the fact that by removing the need to resolve sound waves it allows for considerably larger timesteps. When calculating the size of the timestep that can be used for numerical stability, one measure that must be considered is the CFL criterion, that is,

$$\nabla t_{max} = \frac{\nabla x}{u_f} \quad (2.6)$$

where  $\nabla x$  is our grid spacing, and  $u_f$  is the fastest relevant velocity that is present in our system. In the case of fully compressible flows the presence of sound waves requires us to consider the speed of sound in the context of the CFL criterion. For typical convective flows, the speed of sound is a factor of  $10^5$  larger than the fluid velocity and so would require us to constrain the timestep to be a factor of  $10^5$  smaller than it would otherwise need to be. There are methods to avoid limiting the timestep as heavily as this in fully compressible flows, such as ramping up the luminosity with a "boost factor" to lessen the difference between the fluid velocity and the speed of sound, however such methods are outside the scope of this work (see Baraffe et al. 2021 for a discussion of this method).

### 2.1.3 The momentum equation

Consider a given fluid mass of arbitrary volume  $V$ . The momentum per unit volume is given by  $\rho\mathbf{u}$  and so it follows that the total momentum is given by this quantity's volume integral. The rate of change of the total momentum for this fluid mass is then given by its material derivative, and from Newton's second law this is balanced by the force acting upon it. That is,

$$\frac{D}{Dt} \int_V \rho\mathbf{u} \, dV = \int_V \mathbf{F} \, dV, \quad (2.7)$$

where  $\frac{D}{Dt}$  is the material derivative of a fluid, and  $\mathbf{F}$  is the force per unit volume acting upon said mass. That material derivative is defined as

$$\frac{DA}{Dt} = \frac{\partial A}{\partial t} + (\mathbf{u} \cdot \nabla A), \quad (2.8)$$

where  $A$  is some fluid property, and represents a Lagrangian view of the fluid, that is, the change in  $A$  following some fluid parcel. It considers the fact that the fluid property  $A$  at a given position can change both as a result of a local change in  $A$  with time,  $\frac{\partial A}{\partial t}$ , and as a result of some contribution due to neighbouring fluid motions, namely advection,  $(\mathbf{u} \cdot \nabla)A$ . Using the following expression,

$$\frac{D}{Dt} \int_V \rho A \, dV = \int_V \rho \frac{DA}{Dt} \, dV, \quad (2.9)$$

(see, for example, Vallis 2006 for more details on the origin of this equality, and for more on the material derivative in general) for the fluid velocity  $\mathbf{u}$ , substituting this into equation (2.7) and expanding the material derivative out using equation (2.8) it follows that,

$$\int_V \rho \frac{Du}{Dt} \, dV = \int_V \rho \left( \frac{\partial \mathbf{u}}{\partial t} + \mathbf{u} \cdot \nabla \mathbf{u} \right) \, dV = \int_V \mathbf{F} \, dV. \quad (2.10)$$

Once again the choice of volume is arbitrary, and so with a final bit of rearranging the following momentum equation can be obtained,

$$\frac{\partial \mathbf{u}}{\partial t} + \mathbf{u} \cdot \nabla \mathbf{u} = \frac{1}{\rho} (-g - \nabla P + \nabla \cdot \tau_{i,j} - 2\Omega \times \mathbf{u} + \mathbf{j} \times \mathbf{B}), \quad (2.11)$$

where  $\mathbf{F}$  has been expanded to show the various forces acting upon the fluid parcel. Those included here are gravity,  $\mathbf{g}$ , pressure,  $\nabla P$  where  $P$  is the fluid pressure, viscosity  $\nabla \cdot \tau_{i,j}$ , where  $\tau_{i,j}$  is the viscous stress tensor, rotation,  $2\Omega \times \mathbf{u}$  where  $\Omega$  is the angular velocity, and magnetism,  $\mathbf{j} \times \mathbf{B}$ , where  $\mathbf{j}$  is the electric current and  $\mathbf{B}$  is the magnetic field strength.

#### 2.1.4 An energy equation

The last addition required to complete this description of a general hydrodynamical system (along with specifying an appropriate equation of state) is obtained by considering the internal energy of the fluid.

For the work contained within Chapters 4 and 5, the anelastic equations under

the Lantz-Braginsky-Roberts approximation (LBR) are used (Lantz 1992; Braginsky and Roberts 1995). The resulting system therefore diffuses entropy instead of temperature and the energy equation takes the form,

$$\bar{\rho}\bar{T} \left( \frac{\partial S}{\partial t} + (\mathbf{u} \cdot \nabla)S \right) = \nabla \cdot (\kappa \bar{\rho}\bar{T} \nabla S) + \tau_{i,j} \frac{\partial u_i}{\partial x_j} + \frac{j^2}{\sigma} + H, \quad (2.12)$$

where  $S$  is the entropy of the fluid,  $\kappa$  is the thermal diffusivity,  $\sigma$  is the conductivity, and  $H$  is the rate of internal heat generation. The bar terms represent the nearly adiabatic reference state. Entropy diffusion is commonly used in numerical simulations of anelastic convection (see Jones et al. 2011 for example). More on the differences between temperature and entropy diffusion can be seen in Lecoanet et al. 2014.

The LHS of equation (2.12) is similar to equation (2.11) in that it has two terms describing the change in the entropy of fluid at a given point as a result of local heating (that is, as a result of the terms on the RHS) and advection. The RHS terms correspond (from left to right respectively) to entropy diffusion, viscous heating, Ohmic heating, and any internal energy generation.

### 2.1.5 The induction equation

We have so far retained a magnetic field in our equations. For a charged fluid (or plasma) in the presence of a magnetic field the momentum equation (2.11) and energy equation (2.12) depend on the field strength  $\mathbf{B}$  in the form of the Lorentz force and Ohmic dissipation respectively. Additionally the motion of a plasma results in the generation of a magnetic field via induction. To incorporate this evolving magnetic field into the system the following equation is used,

$$\frac{\partial \mathbf{B}}{\partial t} = \nabla \times (\mathbf{u} \times \mathbf{B}) + \eta \nabla^2 \mathbf{B}, \quad (2.13)$$

where  $\eta$  is the magnetic diffusivity. This is the induction equation and encapsulates the balance between the generation of magnetic fields via induction, versus their decay via

diffusion (Kulsrud 2005). The work contained within this thesis however is isolated to the hydrodynamical case where  $B = 0$  and therefore both the Lorentz force and Ohmic dissipation are identically zero (apart from a proof-of-concept calculation as described in Section 7.2.1).

### 2.1.6 Convective instability

Convection is the process by which energy is transported through fluid motions due to the presence of a supercritical vertical temperature gradient. Consider first a layer of fluid in hydrostatic equilibrium, meaning the weight of the fluid as a result of some downward-pointing gravitational field is balanced by the pressure force. Now consider a parcel of fluid that is perturbed vertically upwards in such a way that no heat transfer occurs - i.e. it moves adiabatically, however still remains in pressure equilibrium with the surrounding fluid. The parcel will now find itself at a lower pressure than it began. For an ideal gas where  $P \propto \rho T$ , with the parcel pressure equal to fluid pressure,  $P_p = P_f$ , if the temperature of the parcel now finds itself lower than the surroundings,  $T_p < T_f$ , then the parcel will be over-dense compared to the surroundings,  $\rho_p > \rho_f$ , and as such will experience a negative buoyancy force causing the parcel to accelerate back towards its initial position (see panel a of Figure 2.1). The parcel will then pass its initial position, find itself with  $T_p > T_f$  and  $\rho_p < \rho_f$ , and experience a buoyancy force to once again accelerate it towards its initial position. This oscillatory behaviour is known as an internal gravity wave and is a common feature of convectively stable layers of fluid. These oscillations occur if the vertical temperature gradient of the fluid being such that it is less steep than the adiabatic temperature profile,

$$\frac{\partial T_f}{\partial z} < \left. \frac{\partial T}{\partial z} \right|_{ad}, \quad (2.14)$$

or in terms of entropy,

$$\frac{\partial S_f}{\partial z} > 0. \quad (2.15)$$

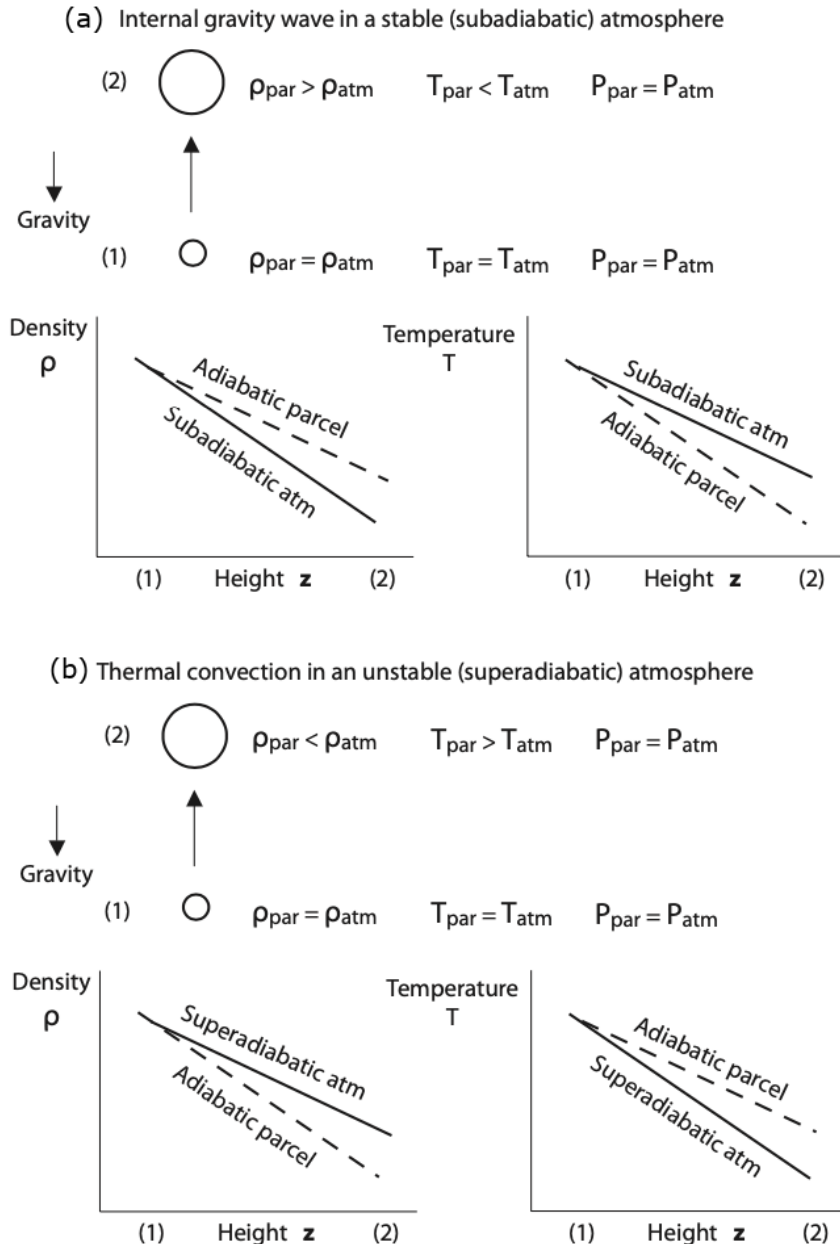


**Figure 2.1:** Figure adapted from Glatzmaier 2013, Figure 1.1 and Figure 1.2. The top panel (a) demonstrates the effect on a parcel of fluid raised from position (1) to position (2) adiabatically in a fluid with a subadabatic vertical profile. The bottom panel (b) shows the same process however for a superadabatic vertical profile.

If, however, the temperature gradient is steeper than the adiabatic gradient, that is,

$$\frac{\partial T_f}{\partial z} > \left. \frac{\partial T}{\partial z} \right|_{ad}, \quad (2.16)$$

or in terms of entropy,

$$\frac{\partial S_f}{\partial z} < 0, \quad (2.17)$$

then after the initial perturbation and resulting temperature and density changes the parcel will find itself at still a higher temperature and therefore lower density than its surroundings,  $T_p > T_f$  and  $\rho_p < \rho_f$ , and as such will feel a positive buoyancy force that will act to accelerate the parcel further upwards from its initial position (see panel b of Figure 2.1). This is the essence of convective instability, that is, the formation of buoyancy driven vertical motions as a result of a superadiabatic temperature gradient.

## 2.2 Non-dimensional numbers

Throughout this thesis, and specifically in the work contained within Chapters 4 and 5 the governing equations are non-dimensionalised and as a result a variety of non-dimensional numbers appear in the equations. This section will first briefly detail the non-dimensionalisation that has been applied and will then provide an overview of these non-dimensional numbers and their physical representations.

### 2.2.1 Non-dimensionalisation

The convective system studied here is non-dimensionalised in time by the viscous timescale,  $t \sim d^2/\nu$ , and in distance by the depth of the convective layer  $d$ . This leads to the following substitutions that are used to non-dimensionalise equations (2.5), (2.11), and (2.12),

$$\frac{\partial}{\partial t} = \frac{\nu}{d^2} \frac{\partial}{\partial \hat{t}} \quad \nabla = \frac{1}{d} \hat{\nabla} \quad \mathbf{u} = U \hat{\mathbf{u}} = \frac{\nu}{d} \hat{\mathbf{u}} \quad \tilde{p} = \frac{\nu^2}{d^2} \hat{p}. \quad (2.18)$$

Additionally, the thermodynamic quantity of choice, entropy, is non-dimensionalised by,

$$s = \frac{Fd}{\kappa \rho_0 T_0} \hat{s}, \quad (2.19)$$

where  $F$  is the flux passing through the layer and  $\rho_0$  and  $T_0$  is the density temperature at the bottom of our domain. The  $\hat{\cdot}$  notation indicates a non-dimensional version of the given variable. For cases that include them, the angular velocity and magnetic field strength are non-dimensionalised by,

$$\Omega = \Omega \hat{\Omega} \quad B = B_0 \hat{B}, \quad (2.20)$$

where  $\Omega$  and  $B_0$  are appropriate angular velocity and magnetic field strength scales. Upon applying these non-dimensionalisations a collection of non-dimensional numbers appear as factors to various terms which can then be used to quantify various flow regimes. For example, the Prandtl number  $\text{Pr}$  as will be discussed in section 2.2.3 quantifies the relative strengths of viscous to thermal diffusivities. In the regime of very high  $\text{Pr}$  the viscous timescale is much smaller than the thermal timescale, and so for fluid regimes in which this is the case, a  $\text{Pr} \sim \infty$  approximation can be used to simplify the equation set (Jarvis and McKenzie 1980).

The resulting equation set is discussed in more detail in Section 4.1.2.1, however for completeness, the fully non-dimensionalised equations for a non-rotating, stratified system in the absence of a magnetic field is given by,

$$\begin{aligned} \frac{\partial \hat{u}}{\partial \hat{t}} + (\hat{u} \cdot \hat{\nabla}) \hat{u} &= -\hat{\nabla} \hat{p} + \frac{\text{Ra}}{\text{Pr}} \hat{s} \hat{e}_z \\ &+ \left[ \frac{1}{\hat{\rho}} \frac{\partial}{\partial \hat{x}_j} \left( \hat{\rho} \left( \frac{\partial \hat{u}_i}{\partial \hat{x}_j} + \frac{\partial \hat{u}_j}{\partial \hat{x}_i} \right) \right) - \frac{2}{3\hat{\rho}} \frac{\partial}{\partial \hat{x}_i} \left( \hat{\rho} \frac{\partial \hat{u}_j}{\partial \hat{x}_j} \right) \right], \end{aligned} \quad (2.21)$$

$$\hat{\nabla} \cdot (\hat{\rho} \hat{u}) = 0, \quad (2.22)$$

$$\text{Pr}\hat{\rho}\hat{T}\left(\frac{\partial\hat{s}}{\partial\hat{t}} + (\hat{u} \cdot \hat{\nabla})\hat{s}\right) = \hat{\nabla} \cdot (\hat{\rho}\hat{T}\hat{\nabla}\hat{s}) + \frac{\text{Pr}^2\theta}{\text{Ra}}\hat{\tau}_{ij}\frac{\partial\hat{u}}{\partial\hat{x}_j}, \quad (2.23)$$

where  $\tau_{i,j}$  is the non-dimensional viscous stress tensor. The following sections will define the resulting non-dimensional parameters Ra, Pr, and  $\theta$ , and discuss their physical interpretations.

## 2.2.2 Rayleigh number

A key parameter in the study of convection or buoyancy driven flow is the Rayleigh number, Ra. The Rayleigh number represents the ratio of the destabilising effect of the buoyancy force to the stabilising effects of viscosity (Kundu 1990). Thus for a fluid with a sufficiently high Rayleigh number buoyancy driven flow can develop. For a system in which the negative entropy gradient across a fluid layer provides the forcing (consider a slab of fluid heated from below and cooling on its surface), the Rayleigh number may be defined as,

$$\text{Ra} = \frac{gd^3\Delta S}{c_p\nu\kappa}, \quad (2.24)$$

where  $g$  is the gravitational acceleration,  $\Delta S$  is the entropy difference across the fluid layer,  $d$  is the depth of the layer,  $c_p$  is the specific heat capacity at constant pressure,  $\kappa$  is the thermal diffusivity, and  $\nu$  is the viscous diffusivity (Duarte et al. 2016). Similarly, for a Boussinesq fluid the Rayleigh number can be expressed in terms of temperature, as will be used in Section 3.1,

$$\text{Ra} = \frac{\alpha gd^3\Delta T}{\nu\kappa}, \quad (2.25)$$

where  $\alpha$  is the coefficient of thermal expansion, and  $\Delta T$  is the temperature drop across the convective layer. For the scenario where the forcing for this buoyancy driven flow is provided by some supplied flux at the bottom of the fluid layer instead of an entropy difference, it is often more helpful to define a flux-based Rayleigh number. Typically this

is given as

$$\text{Ra}_F = \text{Ra}\text{Nu}, \quad (2.26)$$

where  $\text{Nu}$  is the Nusselt number, a measure of the relative strength of the heat transport terms, given in this case as the ratio of the total flux to the conductive flux, that is

$$\text{Nu} = \frac{Fd}{\kappa\rho T\Delta S}. \quad (2.27)$$

where  $F$  is the flux passing through the layer,  $\rho$  is the density,  $T$  is the temperature, and  $\Delta S$  is once again the entropy drop across the layer. As a result, the flux-based Rayleigh number can be expressed as,

$$\text{Ra}_F = \frac{gFd^4}{\kappa\nu^2\rho T c_p}. \quad (2.28)$$

This thesis will primarily use the flux based Rayleigh number,  $\text{Ra}_F$ , as our measure of buoyancy driving and so unless otherwise stated it should be assumed that all future references to  $\text{Ra}$  in the context of the numerical simulations are of this form. An exception to this is Section 2.3.

### 2.2.3 Prandtl Number

As briefly discussed at the start of this section, the Prandtl number,  $Pr$  is defined simply as the ratio of the viscous and thermal diffusivities, that is,

$$Pr = \frac{\nu}{\kappa} \quad (2.29)$$

Thus it clearly follows that for  $Pr \ll 1$  the thermal diffusivity dominates while for  $Pr \gg 1$  viscous diffusion dominates. For the majority of the work contained within this thesis, specifically in Chapters 4 and 5,  $Pr$  is simply taken as 1 to allow for a more

direct comparison to prior work. That is, the diffusivities are equal.

Similarly, a magnetic Prandtl number,  $Pm$ , can be defined from the ratio of the viscous to magnetic diffusivities,

$$Pm = \frac{\nu}{\eta}, \quad (2.30)$$

where  $\eta$  is the magnetic diffusivity,

#### 2.2.4 Stratification

Another commonly used parameter within this thesis is the measure of the degree of stratification for the given fluid layer. In this work this is encapsulated by the number of density scale heights across said layer,

$$N_p = -m \ln(1 - \beta d), \quad (2.31)$$

where  $m$  is the polytropic index and  $\beta$  is the inverse temperature scale height, where again a scale height is the distance at which the given quantity has decreased by a factor of  $e$ . The parameter  $\theta$  is a non-dimensional version of this and frequently appears in the form,

$$\theta = \beta d = \frac{gd}{c_{p,0}T_0}. \quad (2.32)$$

Note that to satisfy the conditions of the anelastic approximation, our background reference state is taken to be a polytropic atmosphere with  $m = 1.5$ .

#### 2.2.5 Taylor Number

When rotational effects are included the Taylor number appears as a factor to the Coriolis force term that appears in equation (2.11). The Taylor number,  $Ta$ , (and the directly related Ekman number,  $Ek$ ) is a relevant non-dimensional number in the context of a fluid dynamical system that is undergoing rotation. It is a measure of the strength of the Cori-

olis force due to rotation about a given axis compared to viscous effects. Considering first these two terms and their respective dimensional scalings, that is  $\mathbf{u} \sim \frac{\nu}{d}$ , where  $\nu$  is the viscous diffusivity and  $d$  is the layer depth,

$$2\Omega \times \mathbf{u} \sim \frac{2\Omega\nu}{d}, \quad (2.33)$$

$$\frac{1}{\rho} \nabla \cdot \tau_{i,j} \sim \frac{\nu^2}{d^3}. \quad (2.34)$$

Taking the ratio of these, that is, dividing through equation (2.34) by equation (2.33) gives the following,

$$\frac{\frac{1}{\rho} \nabla \cdot \tau_{i,j}}{2\Omega \times \mathbf{u}} \sim \frac{\nu^2/d^3}{2\Omega\nu/d} = \frac{\nu}{2\Omega d^2} = \text{Ek} \quad (2.35)$$

The Ekman number is directly related to the Taylor number by simply  $\text{Ta} = \text{Ek}^{-2}$ , and so we obtain the following expression for  $\text{Ta}$  which will appear frequently in the discussion of Chapter 5,

$$\text{Ta} = \frac{4\Omega^2 d^2}{\nu^2}. \quad (2.36)$$

Large values of  $\text{Ta}$  are indicative of rapidly rotating systems whereas  $\text{Ta} = 0$  defines a non-rotating system.

### 2.2.6 Rossby Number

Another non-dimensional number of particular interest to rotating regimes, is the Rossby number. This is the ratio of inertial to Coriolis forces. For some flow of velocity scale  $U$ , the inertial and Coriolis terms scale as  $\mathbf{u} \cdot \nabla \mathbf{u} \sim U^2/d$  and  $2\Omega \times \mathbf{u} \sim 2\Omega U$ , therefore the resulting ratio is,

$$\text{Ro} = \frac{U}{2\Omega d}. \quad (2.37)$$

Flows with  $Ro \ll 1$  can be considered rotationally constrained whereas those with  $Ro \gg 1$  can be considered to be dominated by inertial forces. A useful version of the Rossby number in the study of convective flows is that first proposed by Gilman (1977), the convective Rossby number,

$$Ro_c = \sqrt{\frac{Ra}{PrTa}}, \quad (2.38)$$

which is a measure of the buoyancy driving to the Coriolis force. For the model established and described in Chapters 3, 4, and 5,  $Ro_c$  depends only upon the given input parameters and so it serves as a useful prior estimate of the degree of rotational constraint. The discussion at the end of Chapter 4 discusses the differences between these various rotational parameters in more depth.

### 2.2.7 Reynolds Number

The Reynolds number,  $Re$ , is defined as the ratio of the inertial and viscous forces operating within our fluid. That is, for some flow of velocity scale  $U$ , the inertial and viscous terms scale as,  $\mathbf{u} \cdot \nabla \mathbf{u} \sim U^2/d$  and  $\frac{1}{\rho} \nabla \cdot \tau_{i,j} \sim \frac{Uv}{d^2}$ ,

$$Re = \frac{Ud}{v}. \quad (2.39)$$

It is a measure of how turbulent the fluid is with low Reynolds numbers resulting in highly viscous flows and high Reynolds numbers resulting in small scale turbulent eddies.

### 2.2.8 Magnetism

When considering magnetism, a moving, charged fluid has an associated current that interacts with the underlying magnetic field, and generates a Lorentz force given by  $\mathbf{j} \times \mathbf{B}$ . The Chandrasekhar number,  $Q$  is defined as the ratio of this Lorentz to any viscous forces present. That is, for some magnetic field of scale  $B \sim B_0$ , the Chandrasekhar number is defined as,

$$Q = \frac{B_0^2 d^2}{\mu_0 \rho v \eta}. \quad (2.40)$$

In the absence of a magnetic field this parameter is identically zero and the problem reduces to a non-magnetic system. Much like the Prandtl number and Reynolds number discussed in Sections 2.2.3 and 2.2.7 respectively, there are accompanying "magnetic" versions of these parameters, suitably named the magnetic Prandtl number,  $Pm$ , and magnetic Reynolds number,  $Rm$ , that are measured relative to the magnetic diffusivity,  $\eta$ . That is,

$$Pm = \frac{v}{\eta}, \quad (2.41)$$

and

$$Rm = \frac{Ud}{\eta}. \quad (2.42)$$

## 2.3 An overview of convective scaling relations

The array of non-dimensional numbers presented in the previous section provide a useful way of quantifying a variety of features of the resulting dynamics present in a convective system. A primary motivation of convective theory is to understand how the temperature forcing across a convective layer is related to the heat transport. This relationship in terms of non-dimensional parameters is encapsulated in the so called Nusselt-Rayleigh scaling,  $Nu(Ra)$ , that is, how the ratio of the total flux to the conductive flux,  $Nu$ , changes in relation to a measure of the buoyancy forcing,  $Ra$ . A few things are worthy of note here. Firstly, the simulations contained with Chapters 4 and 5 are done using a flux-based Rayleigh number,  $Ra_F = RaNu$ , as discussed in Section 2.2.2. As such, quoted scalings in terms of  $Ra$  differ from those expected in this thesis. However, the relationship between the two is straightforward, that is, if  $Nu \sim Ra^\gamma$ , this implies

$$\text{Nu} \sim \text{Ra}_F^{\frac{\gamma}{\gamma+1}}. \quad (2.43)$$

Additionally, there is often some variation as to whether Nu or Nu – 1 is presented. In the simple case of Boussinesq convection, the total heat flux is given by  $F_{total} = F_{cond} + F_{conv}$ . The Nusselt number can then be written as,

$$\text{Nu} = \frac{F_{total}}{F_{cond}} = \frac{F_{cond} + F_{conv}}{F_{cond}} = 1 + \frac{F_{conv}}{F_{cond}} \quad (2.44)$$

$$\text{Nu} - 1 = \frac{F_{conv}}{F_{cond}}. \quad (2.45)$$

It is convenient however that this difference is negligible in sufficiently turbulent convection where  $\text{Nu} \gg 1$ .

This Nu(Ra) scaling has been a significant area of interest in the development of convective theory throughout the past century and this section will give a brief overview of the history of these so called scaling laws and the resulting dynamical regimes that are proposed to exist. The introduction contained within Grossmann and Lohse 2000 provides a review of the earlier development of these various scaling laws however for completeness a similar review will be presented here.

### 2.3.1 Early convective experiments

As summarised in Davis (1922), early studies of convection in enclosed air cells, covering the parameter space of Prandtl number,  $\text{Pr} \sim 1$ , and Rayleigh number,  $\text{Ra} \lesssim 10^8$  demonstrated a power-law scaling between the Nusselt number, Nu, and Ra, of  $\text{Nu} \sim \text{Ra}^\gamma$  where  $\gamma = 1/4$ . Later experiments presented by Malkus (1954a) on convection in distilled water ( $\text{Pr} \sim 7$ ) noted that there is a transition that occurs from a "laminar boundary layer" regime to a "turbulent boundary layer" regime with increasing Ra. An accompanying theoretical investigation into the scaling of heat transport, Malkus (1954b), established this scaling as the classical Malkus scaling,

$$\text{Nu} \sim \text{Ra}^{1/3}. \quad (2.46)$$

Further experiments by Heslot et al. (1987) at  $\text{Pr} \sim 1$  observed three convective regimes relating to boundary layer formation and dynamics. These were referred to (in order of increasing  $\text{Ra}$ ) as an initial "chaotic" state, a middle "soft-turbulence" state, and then a high  $\text{Ra}$  "hard-turbulence state". The scaling law found in this soft-turbulence regime was characterised by the formation of a laminar boundary layer with the transition to the hard-turbulence regime relating to the formation of a turbulent boundary layer. These two scaling regimes corresponded to  $\gamma \sim 1/3$  and  $\gamma \sim 2/7$  respectively. Interestingly, there was a disparity between the classical  $\text{Nu} \sim \text{Ra}^{1/3}$  scaling law for the turbulent boundary layer regime and the  $\text{Nu} \sim \text{Ra}^{2/7}$  scaling presented by Heslot et al. (1987). This is discussed further in Castaing et al. (1989) in which the difference is attributed to the their individual treatment of the boundary layer stability, specifically the inclusion of the destabilising effect of shear flows in the case of the  $\text{Nu} \sim \text{Ra}^{2/7}$  scaling. Extension of the Castaing et al. (1989) theory to incorporate a  $\text{Pr}$  dependence is provided by Cioni et al. (1997), along with a corresponding scaling law for the Reynolds number,  $\text{Re}$ , that is,

$$\text{Nu} \sim \text{Ra}^{2/7} \text{Pr}^{2/7}, \quad (2.47)$$

$$\text{Re}_f \sim \text{Ra}^{3/7} \text{Pr}^{-4/7}. \quad (2.48)$$

Note that the  $\text{Re}$  scaling in equation 2.48 is for the velocity fluctuations (denoted by the subscript  $f$ ) and not the large scale flow. Shraiman and Siggia (1990) proposed an alternative theory in the form of a nested thermal boundary layer lying within the turbulent boundary layer. These produce,

$$\text{Nu} \sim \text{Ra}^{2/7} \text{Pr}^{-1/7}, \quad (2.49)$$

$$\text{Re} \sim \text{Ra}^{3/7} \text{Pr}^{-5/7}. \quad (2.50)$$

They recover the same dependence on Ra however obtain different dependencies on Pr. It is of note that while the two theories provide different Pr scalings, it has been shown that equation 2.47 is appropriate for small Pr whereas equation 2.49 is more appropriate in the large Pr regime (Zaleski 2000).

Further study of the Pr dependence on Nu revealed multiple points in which the established value of the Rayleigh numbers exponent,  $\gamma = 2/7$ , began to break down. A particularly significant finding was that  $\gamma$  itself appeared to have a slight Pr dependence as demonstrated in Figure 2.2 where a range of exponents between 1/2 and 1/3 have been found. In multiple studies (Cioni et al. 1997 for example) the  $\gamma = 2/7$  scaling also broke in the regime of very high Ra.

Alternatively, Spiegel (1963) applied mixing-length theory (MLT) arguments by considering a convective layer consisting of plumes that transport energy at nearly the buoyancy free-fall speed. In this regime they showed that an "ultimate" scaling of,

$$\text{Nu} \sim (\text{RaPr})^{1/2}, \quad (2.51)$$

was followed. Kraichnan (1962) similarly obtained this  $\gamma \sim 1/2$  MLT, albeit with an additional factor of  $\ln(\text{Ra})^{-\frac{3}{2}}$ , and this scaling is often referred to as the asymptotic Kraichnan regime. It corresponds to a regime in which the convective heat flux is not limited by transport across the thermal boundary layers as in the classical Malkus scaling but by transport across the bulk of the fluid (Doering 2020).

Grossmann and Lohse 2000 used these arguments to motivate a re-evaluation of the various scaling laws of thermal convection and the parameter regimes in which they operated. They suppose that by simply considering whether the bulk or the boundary layers dominate the thermal and viscous dissipation (denoted by labels *I* through *IV*) and whether the given Pr is small or large (denoted by subscripts *l* and *u* respectively) it can

Reference	fluid	$Pr$	$Ra$ range	$\gamma$
Ashkenazi & Steinberg (1999)	SF <sub>6</sub>	1–93	$10^9$ – $10^{14}$	$0.30 \pm 0.03$
Garon & Goldstein (1973)	H <sub>2</sub> O	5.5	$10^7$ – $3 \times 10^9$	0.293
Tanaka & Miyata (1980)	H <sub>2</sub> O	6.8	$3 \times 10^7$ – $4 \times 10^9$	0.290
Goldstein & Tokuda (1980)	H <sub>2</sub> O	6.5	$10^9$ – $2 \times 10^{11}$	$\frac{1}{3}$
Qiu & Xia (1998)	H <sub>2</sub> O	$\approx 7$	$2 \times 10^8$ – $2 \times 10^{10}$	0.28
Lui & Xia (1998)	H <sub>2</sub> O	$\approx 7$	$2 \times 10^8$ – $2 \times 10^{10}$	$0.28 \pm 0.06$
Shen <i>et al.</i> (1996)	H <sub>2</sub> O	$\approx 7$	$8 \times 10^7$ – $7 \times 10^9$	$0.281 \pm 0.015$
Threlfall (1975)	He	0.8	$4 \times 10^5$ – $2 \times 10^9$	0.280
Castaing <i>et al.</i> (1989)	He	0.7–1	$\lesssim 10^{11}$	$0.282 \pm 0.006$
Wu & Libchaber (1991)	He	0.6–1.2	$4 \times 10^7$ – $10^{12}$	0.285
Chavanne <i>et al.</i> (1997)	He	0.6–0.73	$3 \times 10^7$ – $10^{11}$	$\frac{2}{7}$
Davis (1922)	air	$\approx 1$	$\lesssim 10^8$	0.25
Rossby (1969)	Hg	0.025	$2 \times 10^4$ – $5 \times 10^5$	0.247
Takeshita <i>et al.</i> (1996)	Hg	0.025	$10^6$ – $10^8$	0.27
Cioni <i>et al.</i> (1997)	Hg	0.025	$5 \times 10^6$ – $5 \times 10^8$	$0.26 \pm 0.02$
Cioni <i>et al.</i> (1997)	Hg	0.025	$4 \times 10^8$ – $2 \times 10^9$	0.20
Glazier <i>et al.</i> (1999)	Hg	0.025	$2 \times 10^5$ – $8 \times 10^{10}$	$0.29 \pm 0.01$
Horanyi <i>et al.</i> (1998)	Na	0.005	$\lesssim 10^6$	0.25

TABLE 1. Power-law exponents  $\gamma$  of the power law  $Nu \sim Ra^\gamma$  for various experiments. The experiments were done with different aspect ratios; however, no strong dependence of the scaling exponent  $\gamma$  on the aspect ratio is expected (in contrast to the prefactors, which do have an aspect ratio dependence as found by Wu & Libchaber 1992).

**Figure 2.2:** Figure taken from Grossmann and Lohse 2000, Table 1. Power-law exponents  $\gamma$  for  $Nu \sim Ra^\gamma$  for a range of convective experiments at different Ra and Pr.

be seen which scaling law the convection follows. The phase diagram shown in Figure 2.3 shows these different regimes in Ra and Pr space.

The work of Grossmann and Lohse 2000 and others discussed above have been primarily developed for non-stratified, Boussinesq convection with no-slip boundary conditions. This is a system quite physically distant from the desired regime of stellar-like convective zones. Additionally the parameter regimes in Ra-Pr space that are currently able to be probed by both experiments and numerical simulations are significantly distant from those likely to exist within the Sun's convection zone. This is clearly therefore an unfinished, and ongoing field of study.

### 2.3.2 The influence of rotation

Rapidly rotating regimes ( $Ro < 1$ ) in which the dynamics of the flow are significantly influenced by rotation are common within the field of astrophysical fluid dynamics. In particular, a particularly prevalent and immediate effect on the resulting dynamics of the fluid is the Taylor-Proudman effect in which the fluid motions become aligned with the rotation axis (Taylor 1923). This acts to change the nature of the heat transport across the thermal boundaries and convective bulk, and results in  $Nu \sim Ra^\gamma$  scalings with consider-

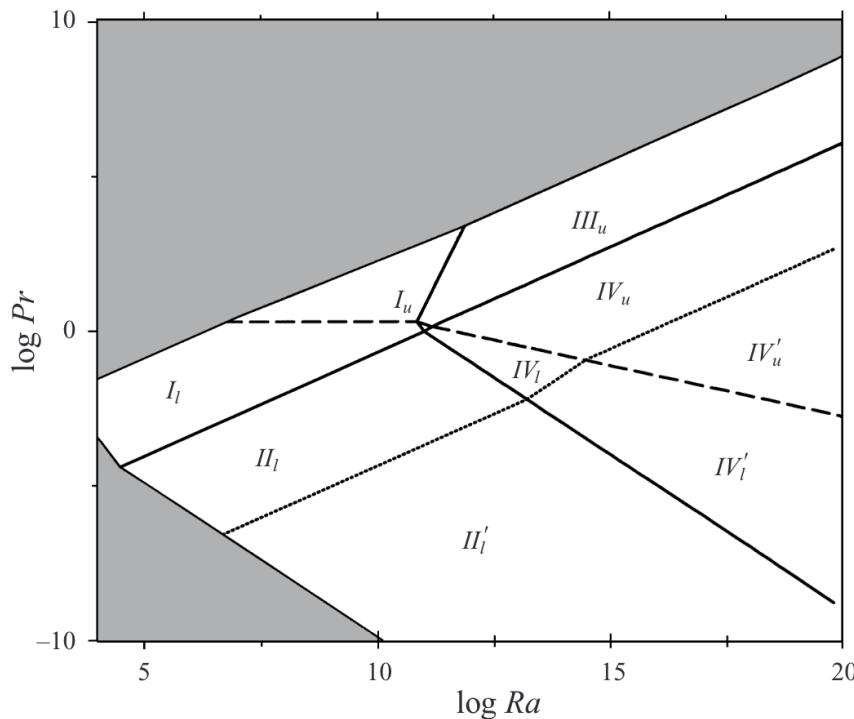


**Figure 2.3:** Figure taken from Grossmann and Lohse 2000, Figure 2. A phase diagram in  $\text{Ra} - \text{Pr}$  space showing the different scaling regimes that exist depending on where the boundary layers or the bulk dominate the global thermal or viscous dissipation. Regimes  $I$  and  $II$  are those in which the thermal dissipation is boundary-layer dominated with viscous dissipation dominating in the boundary and the bulk for  $I$  and  $II$  respectively. Regimes  $III$  and  $IV$  therefore represent bulk dominated thermal dissipation with again boundary and bulk dominated viscous dissipation in  $III$  and  $IV$  respectively. Subscripts  $l$  and  $u$  denote the lower and upper Pr regimes.

ably different values of  $\gamma$  than the non-rotationally constrained cases ( $\text{Ro} > 1$ ). There is still some debate as to what form these scaling laws will take. King et al. (2012) present similar arguments to those used to obtain the classical Malkus scaling for non-rotating convection of  $\gamma = 1/3$ . They consider the stability criterion of two boundary layers across which most of the temperature drop occurs ( $\Delta T \approx 2\Delta T_\delta$ , where  $\delta$  is the width of the boundary layer and  $\Delta T_\delta$  indicates the temperature change across said boundary layers) and obtain the scaling relation,

$$\text{Nu} \approx \left( \frac{\text{Ra}}{\text{Ra}_c} \right)^3 \approx 0.0023 \text{Ra}^3 \text{Ek}^4, \quad (2.52)$$

where  $\text{Ra}_c = 7.6 \text{Ek}^{-4/3}$  Chandrasekhar (1961). Figure 2.4 shows the scalings found for both new and old experiments (Rossby 1969) and supporting numerical simulations of Boussinesq convection with no-slip boundary conditions. They show reasonable agreement with this proposed scaling in the rotationally influenced regime before transitioning onto the previously seen  $\text{Nu} \sim \text{Ra}^{2/7}$  scaling with increasing Rayleigh number as the system transitions towards a non-rotating system. Additionally, the delayed onset of convection at increasing rotation rates, that is, the dependence of  $\text{Ra}_c$  on  $\text{Ek}$  can be seen clearly by noting the point where  $\text{Nu} = 1$  at each value of  $\text{Ek}$ .

Numerical work on rotating convection with stress free boundary conditions (Schmitz and Tilgner 2009) find instead that while  $\text{Nu}$  does scale more steeply with  $\text{Ra}$  than the non-rotating cases, it does so more in line with  $\text{Nu} \sim \text{Ra}^{6/5} \text{Ek}^{8/5}$ . Julien et al. 2012 demonstrate in the, inviscid, low Ekman number regime (highly rotationally constrained), that the efficiency of the bulk turbulence determines the  $\text{Nu}(\text{RaEk})$  scaling and present,

$$\text{Nu} - 1 \approx C_1 \text{Pr}^{-1/2} \text{Ra}^{3/2} \text{Ek}^2, \quad (2.53)$$

where  $C_1$  is a constant prefactor given as  $C_1 = 0.04 \pm 0.00025$ . Once again, for a given  $\text{Ek}$  the scaling law breaks down in the high  $\text{Ra}$  regime at the point in which the local Rossby number of the thermal boundary layer becomes approximately unity and loses its rotational constraints. At this point the scaling law once again transitions to nonrotating

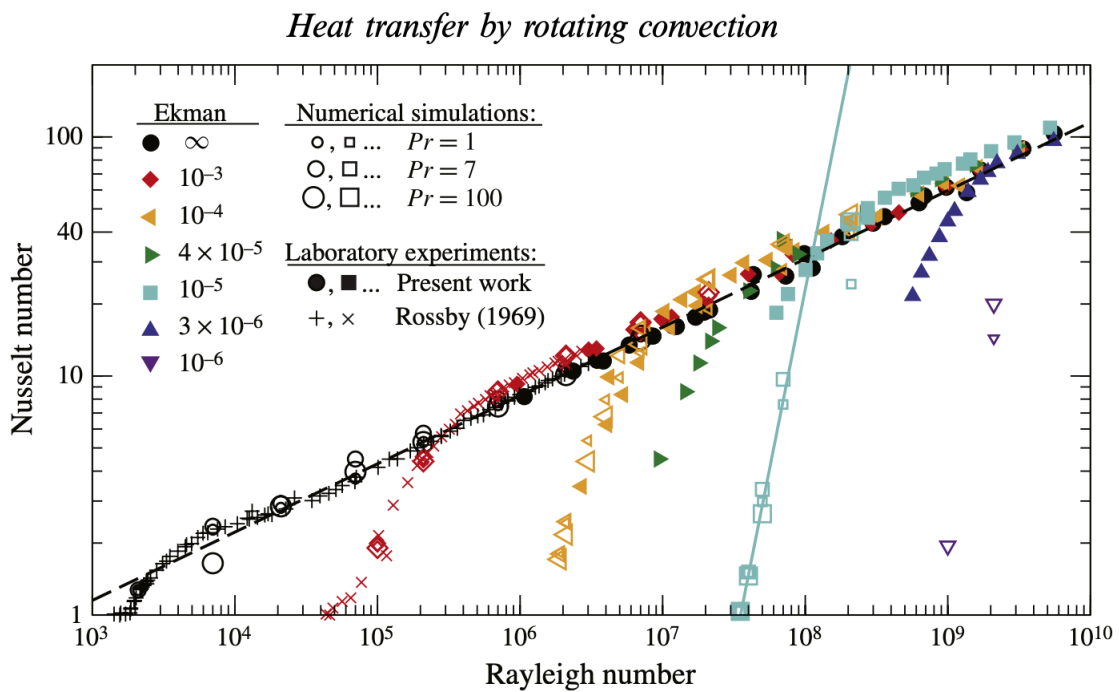


**Figure 2.4:** Figure taken from King et al. 2012, Figure 3. Nusselt number plotted against Rayleigh number for a range of Ekman number taken from both laboratory experiments (solid symbols) and direct numerical simulations (open symbols) of no-slip, Boussinesq convection. Symbol size corresponds to  $\text{Pr}$  value, whereas the shape and colour correspond to Ekman number,  $\text{Ek}$  (smaller  $\text{Ek}$  means faster rotation rate). The dashed black line demonstrates a  $\text{Nu} \sim \text{Ra}^{2/7}$  scaling whereas the solid blue line shows the  $\text{Nu} \sim \text{Ra}^3$  scaling for  $\text{Ek} = 10^{-5}$ . Lastly the '+' and 'x' symbols correspond to non-rotating and rotating laboratory experiments from Rossby (1969), respectively.

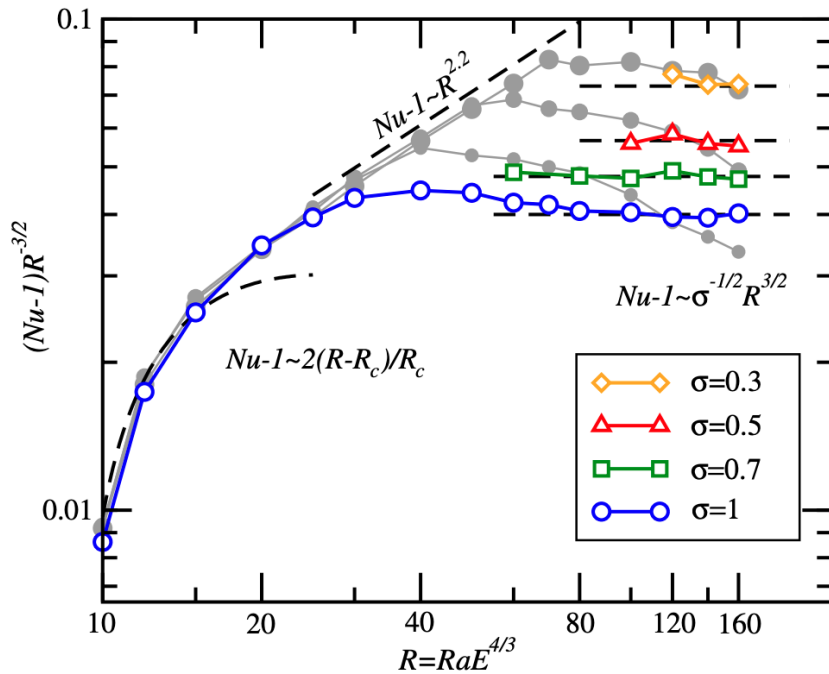


**Figure 2.5:** Figure taken from Julien et al. 2012, Figure 2.  $(\text{Nu} - 1)R^{-3/2}$  as a function of  $R$ , where  $R = \text{Ra}E^{4/3} \sim \text{Ra}/\text{Ra}_c$ . The horizontal dashed lines at constant  $(\text{Nu} - 1)R^{-3/2}$  correspond to regime paths in which the scaling law in equation (2.53) is valid.

result of  $\gamma \sim 2/7$ , that is, the regime in which the efficiency of the heat transport is being determined by the boundary layers and not the bulk turbulence. As can be seen in Figure 2.5, taken from Julien et al. 2012, their numerical simulations show a good agreement with the  $3/2$  scaling to within 6% in the rotational constrained regime.

### 2.3.3 Compressible convective theory

Expanding in complexity towards a compressible, anelastic regime comes with a number of crucial differences in the resulting dynamics. These will be explored in more depth in Chapter 4 however to briefly summarise here, the two main developments are the breaking of vertical dynamical symmetry and the resulting sizes of the convective upflows and downflows, and the relative contributions of the viscous heating and buoyancy work to the overall heat transport through the system. Jones et al. (2022) extends the study of these convective scalings numerically to the anelastic regime by exploring the validity of the previously established non-compressible scalings provided by the Grossman & Lohse theory (GL theory) in anelastic convection with no-slip boundary conditions. They focus specifically on the cases where the thermal dissipation is boundary-layer dominated (GL

regimes *I* and *II*) as these are regimes in which current numerical capabilities are likely to be able to probe. The cases in which the thermal dissipation is bulk dominated (GL regimes *III* and *IV*) occur at significantly higher  $Ra$  values, and as such are numerically inaccessible.

Under the basis that fully evolved turbulent convection produces a well mixed, isentropic interior with thin boundary layers, they derive scaling relations for Nu and Re. Much the same as the Boussinesq GL theory, Jones et al. (2022) find different scaling laws for both the high and low Pr regimes, depending on whether the viscous dissipation is primarily bulk, or boundary layer dominated. Equations 6.13 and 6.14 in Jones et al. (2022) provide scaling laws for  $\text{Nu}(RaPr\Gamma)$  where  $\Gamma$  is defined as the ratio of the temperatures at the top and bottom boundaries, and provides a measurement of the fluid stratification. As discussed in section 2.2.4, in the following chapters the degree of stratification will be quantified by  $\theta = \frac{gd}{c_p,0T_0}$ , a non-dimensionalised inverse scale height and  $N_\rho$ , the number of density scale heights across the fluid layer. These are related to  $\Gamma$  by,

$$\Gamma = \frac{T_B}{T_T} = \frac{1}{1 - \theta} = e^{N_\rho/m}, \quad (2.54)$$

where  $T_B$  and  $T_T$  and the temperature at the top and bottom boundaries respectively. The regime of  $\Gamma \rightarrow 1$  ( $N_\rho \rightarrow 0$ ) is the Boussinesq limit and in this limit the scaling relations of Jones et al. (2022) recover those of GL regime *I*. They similarly recover the scaling of GL regime *II* for the bulk-dominated viscous dissipation regime in the theory presented in their Appendix B.

A primary difference in the stratified regime is that the vertical asymmetries introduced by the presence of stratification develop considerably different upper and lower boundary layers. In particular, the upper boundary layer becomes increasingly thick compared to the lower boundary with increasing stratification as a result of this asymmetry. The scaling laws proposed by Jones et al. (2022) are dependent on the assumption that the boundary layers are sufficiently thin, and so as the system becomes increasingly stratified it is required that the convection is similarly increasingly turbulent (that is, at higher values of Ra) to ensure the upper boundary is sufficiently narrow that the derivation of these

scalings is still valid.

## 2.4 Chapter summary

In this chapter, we have aimed to provide a brief overview of some of the basic theory, terminology, and prior work that underpins our investigations in Chapter 5. Section 2.1 provided an overview of the fundamental mathematical equations required for the study of a fluid system, and in particular it describes the basic physics involved in the development of a convective instability and the resulting formation of turbulent convection. Section 2.2 then defined a range of non-dimensional numbers that are used to quantify the importance and relative strengths of different fluid properties / forces. The chapter finished with a brief introduction to the prior and current understanding of convective theory (and its resulting scaling laws) in Section 2.3.

Chapter 3 will move on to introducing the various numerical methods utilised within this thesis and the study of convection and fluid dynamical phenomenon more generally, which will then be applied to the study of rotating, stratified convection in Chapters 4 and 5.

## Chapter 3

# Numerical Modelling

Now that Chapter 2 has established the underlying mathematical framework needed for the study of astrophysical fluids, this chapter will concern itself with detailing the numerical methods required, which are utilised extensively throughout the proceeding chapters. Section 3.1 begins by detailing the development of a proof-of-concept linear convection code largely following that of Glatzmaier (2013), introducing the numerical methods involved, and ending with the calculation of the critical Rayleigh number  $\text{Ra}_c$  indicating convective onset. Section 3.2 then provides an initial overview of the python framework Dedalus, before detailing how this can be utilised to solve both an initial value problem (which is later used for a rotating, stratified, convective code as presented in Chapters 4 and 5) and an eigenvalue problem (for the purpose calculating the required  $\text{Ra}_c$  values). Lastly, Section 3.3 introduces the UK Met Office’s Unified Model (UM), and highlights parts of particular interest and relevance to the work in Chapter 6.

### 3.1 Linear convection code

As discussed in Chapter 2, in the study of convection an important parameter to know a priori is the point of convective onset. This is best described by the critical Rayleigh number,  $\text{Ra}_c$ . To reiterate, this is the Rayleigh number (equation (2.25)) at which an instability occurs such that a small perturbation of a parcel of fluid would result in said parcel experiencing a buoyancy force that would cause the perturbation to exponentially grow with

time. Knowledge of such a parameter in advance allows one to perform calculations of known supercriticalities, often a more informative metric of the resulting turbulent nature of the fluid flow.

### 3.1.1 Model setup

Consider a layer of fluid contained between a hot bottom boundary and a cold upper boundary where  $L$  is the horizontal extent of our box, and  $d$  is the depth of the fluid layer. The aspect ratio is then defined as  $a = L/d$ . All boundaries are taken to be impermeable. The Boussinesq equations of motion that describe the fluid are as follows:

$$\nabla \cdot \mathbf{u} = 0, \quad (3.1)$$

$$\frac{\partial \mathbf{u}}{\partial t} + (\mathbf{u} \cdot \nabla) \mathbf{u} = -\frac{\nabla p}{\rho_0} + \alpha g T \hat{z} + \nu \nabla^2 \mathbf{u}, \quad (3.2)$$

$$\frac{\partial T}{\partial t} + (\mathbf{u} \cdot \nabla) T = \kappa \nabla^2 T, \quad (3.3)$$

where  $\mathbf{u}$  is the fluid velocity,  $p$  is the pressure perturbation,  $\rho_0$  is the density,  $\alpha$  is the coefficient of thermal expansion,  $g$  is gravity, and  $\nu$  and  $\kappa$  are the viscous and thermal diffusivities respectively. As discussed more extensively in Spiegel and Veronis 1960, the buoyancy term of equation 3.2 is an essential part of the convective system.  $T$  is the temperature perturbation and its presence in this term results from the fact that the contribution of pressure perturbations to the buoyancy are insignificant compared to thermal contributions (to order  $d/H$ , where  $d$  is the depth of the fluid, and  $H$  is the scale height, recalling that for Boussinesq cases  $d \gg H$ .)

This model setup is as shown in Glatzmaier (2013) and a full derivation can be seen there. The length, time, and temperature are scaled by the depth of the box ( $d$ ), the thermal diffusion time ( $d^2/\kappa$ ), and the temperature difference between our two boundaries ( $\Delta T$ ) respectively, and the pressure scale is defined as  $\rho_0 \kappa^2 / d^2$ . Multiplying (3.2) by  $d^2/\kappa$  and

(3.3) by  $d^2/\kappa\Delta T$ , non-dimensional forms of the equation set above can be obtained:

$$\nabla \cdot \mathbf{u} = 0, \quad (3.4)$$

$$\frac{\partial \mathbf{u}}{\partial t} + (\mathbf{u} \cdot \nabla) \mathbf{u} = -\nabla p + \text{RaPr}T\hat{z} + \text{Pr}\nabla^2\mathbf{u}, \quad (3.5)$$

$$\frac{\partial T}{\partial t} + (\mathbf{u} \cdot \nabla) T = \nabla^2 T, \quad (3.6)$$

Non-dimensionalising the system in this way yields two of the non-dimensional numbers previously introduced in Chapter 2, the Rayleigh and Prandtl numbers (equations (2.25) and (2.29) respectively). It is convenient for a system such as this to use a vorticity-streamfunction formulation which can be obtained by taking the curl of equation (3.5) with  $\omega \equiv \nabla \times \mathbf{u}$ . At this stage we assume a 2D geometry such that  $u_y = 0$  and  $\partial/\partial y = 0$  and as a result the vorticity equation only has a component in the y-direction. The two components of the momentum equation (3.5) for the velocity components,  $u_x$  and  $u_z$ , are replaced by a single scalar equation for the y-component of the vorticity,

$$\frac{\partial \omega}{\partial t} + (\mathbf{u} \cdot \nabla) \omega = -\text{RaPr} \frac{\partial T}{\partial x} + \text{Pr} \nabla^2 \omega. \quad (3.7)$$

We then define a streamfunction  $\psi$ , such that it obeys,

$$\mathbf{u} \equiv \nabla \times (\psi \hat{y}) = -\frac{\partial \psi}{\partial z} \hat{x} + \frac{\partial \psi}{\partial x} \hat{z}, \quad (3.8)$$

from which the individual velocity components can be recovered,

$$(u_x, u_z) = \left( -\frac{\partial \psi}{\partial z}, \frac{\partial \psi}{\partial x} \right), \quad (3.9)$$

that itself is obtained from the definition of the vorticity,

$$\omega = -\nabla^2 \psi. \quad (3.10)$$

It may not be immediately clear why this reformulation is advantageous. To start, by utilising a streamfunction we automatically satisfy the mass conservation equation (3.1), as  $\nabla \cdot (\nabla \times \mathbf{A}) = 0$  for any vector  $\mathbf{A}$ . Additionally contours of  $\psi$  act as streamlines for the fluid flow. This is because,

- $\nabla \psi \cdot \mathbf{u} = 0$ , and therefore  $\psi$  contours are tangential to the velocity.
- $\nabla \psi$  has the same amplitude as  $\mathbf{u}$  and so  $\psi$ -contour density is proportional to the amplitude of velocity.

Lastly, and somewhat more importantly, it is computationally more efficient as instead of needing to apply a time integration scheme to two momentum equations (the  $x$  and  $z$ -components of the fluid velocity), instead only a single equation for the  $y$ -component of vorticity needs to be solved. The streamfunction can then be calculated at each new timestep from the Poisson equation (3.10) using a tridiagonal solver. While an additional equation was also added in the form of equation (3.10), there is no longer the need to solve for the mass continuity equation (3.1) as this is automatically satisfied by the use of a streamfunction,  $\psi$ .

To summarise, the system is therefore fully described by the set of prognostic equations (3.7), (3.10), and (3.3). The boundaries are taken to be impermeable, and so require that the vertical component of velocity,  $u_z$  vanishes at  $z = 0, d$  and that the horizontal component of velocity,  $u_x$ , vanishes at  $x = 0, L$ . These boundaries are also taken to be stress-free, such that parallel flows are uninhibited by viscous forces from said boundary. Mathematically this translates to perpendicular gradients of this flow vanishing at these boundaries. That is,  $\partial u_x / \partial z = 0$  at  $z = 0, d$  and  $\partial u_z / \partial x = 0$  at  $x = 0, L$ . For our thermal boundary conditions we define them such that temperature perturbations are fixed to be zero and  $\Delta T$  at the  $z = 0, d$  respectively and the horizontal boundaries are taken to be insulating. As there can be no advective heat flux due to their impermeability, it is

then simply required that the horizontal gradients in temperature,  $\partial T / \partial x$  vanish at these boundaries. Note that these are different boundary conditions to those used in the calculations performed in Chapters 4 and 5. Now that the geometry and governing equations of our system have been sufficiently defined, we will now discuss the numerical methods used to solve these equations.

### 3.1.2 Spectral method

We utilise spectral methods to evaluate spatial derivatives with the aid of Fourier series expansions. This is advantageous for a number of reasons. Firstly, by treating these functions as periodic the discrete horizontal variable  $x_i$ , which is defined only on a finite set of horizontal grid points,  $i$ , can be converted to a generalised function defined for all values of  $x$ . Additionally, the computational error in calculating the derivatives decreases exponentially with  $N$ , the number of periodic terms used in the expansion, and so for large values of  $N$  spectral methods become considerably more accurate than traditional finite difference methods. Note that such Fourier expansions are orthogonal, that is to say,

$$\int_0^a \sin\left(\frac{n_1\pi x}{a}\right) \sin\left(\frac{n_2\pi x}{a}\right) dx = \begin{cases} \pm a/2 & \text{if } n_1 = \pm n_2 \\ 0 & \text{if } |n_1| \neq |n_2| \end{cases} \quad (3.11a)$$

$$\int_0^a \cos\left(\frac{n_1\pi x}{a}\right) \cos\left(\frac{n_2\pi x}{a}\right) dx = \begin{cases} a/2 & \text{if } n_1 = \pm n_2 \\ 0 & \text{if } |n_1| \neq |n_2| \end{cases} \quad (3.11b)$$

Expanding the temperature, vorticity, and streamfunction as a series of cosine and sine periodic functions, the following is obtained,

$$T(x, z, t) = \sum_{n=0}^N T_n(z, t) \cos\left(\frac{n\pi x}{a}\right), \quad (3.12)$$

$$\omega(x, z, t) = \sum_{n=1}^N \omega_n(z, t) \sin\left(\frac{n\pi x}{a}\right), \quad (3.13)$$

$$\psi(x, z, t) = \sum_{n=1}^N \psi_n(z, t) \sin\left(\frac{n\pi x}{a}\right). \quad (3.14)$$

Note that due to the specified horizontal boundary conditions the temperature is only defined by cosine expansions and the vorticity and streamfunction are only defined by sine expansions. Additionally the  $n = 0$  mode vanishes for sine expansions and so expansions for  $\psi$  and  $\omega$  begin from the  $n = 1$  mode.

We can then substitute these expressions into equations (3.6), (3.7), and (3.10), calculating the various spatial derivatives of equations (3.12), (3.13), and (3.14) and then apply the orthogonality rules in equation (3.11) to obtain the following,

$$\frac{\partial T_n}{\partial t} + [(\mathbf{u} \cdot \nabla) T]_n = \left( \frac{\partial^2 T_n}{\partial z^2} - \left(\frac{n\pi}{a}\right)^2 T_n \right), \quad (3.15)$$

$$\frac{\partial \omega_n}{\partial t} + [(\mathbf{u} \cdot \nabla) \omega]_n = \text{RaPr} \left( \frac{n\pi}{a} \right) T_n + \text{Pr} \left( \frac{\partial^2 \omega_n}{\partial z^2} - \left(\frac{n\pi}{a}\right)^2 \omega_n \right), \quad (3.16)$$

$$\omega_n = - \left( \frac{\partial^2 \psi_n}{\partial z^2} - \left(\frac{n\pi}{a}\right)^2 \psi_n \right). \quad (3.17)$$

A clarification of note is that while the non-linear advection terms in equations (3.15) and (3.16) are labelled with a subscript  $n$ , there's terms are actually made of up interactions between multiple modes (see Glatzmaier (2013) for more on this). We now have a system of equations of which the solutions are the  $z$  and  $t$  dependent coefficients to the Fourier expansions seen in (3.12), (3.13), and (3.14). To solve this system, a finite-difference method can be applied.

### 3.1.3 Finite difference method

The system of equations outlined above depend upon the vertical coordinate,  $z$ , and time,  $t$ . We approximate the vertical derivatives within these equations by discretising the vertical domain into  $N_z$  grid points, with a constant grid-spacing of  $\Delta z \equiv (N_z - 1)^{-1}$ . Using the vorticity,  $\omega$ , as an example, let the subscripts denote the value of  $\omega$  at each vertical grid-point, that is  $\omega_i$  represents the value of  $\omega$  at the  $i$ -th gridpoint  $z_i$ ,  $\omega_{i+1}$  at  $z_{i+1}$ , and so on. The Taylor expansion of  $\omega$  at  $z = z_{i+1}$  is given by,

$$\omega(z_{i+1}) = \omega(z_i) + \Delta z \left( \frac{\partial \omega}{\partial z} \right)_i + (\Delta z)^2 \frac{1}{2} \left( \frac{\partial^2 \omega}{\partial z^2} \right)_i + \dots . \quad (3.18)$$

This shows that continuous derivatives can be approximated by discrete values by considering only the first two terms of the above equation, and disregarding terms of order  $(\nabla z)^2$  and higher),

$$\left( \frac{\partial \omega}{\partial z} \right)_i = \frac{\omega(z_{i+1}) - \omega(z_i)}{\Delta z}. \quad (3.19)$$

This method is the most basic explicit numerical integration method for solving differential equations and is known as the Euler-forward scheme (Iserles 1996). It is a first-order method with an accompanying global truncation error of order  $\Delta z$ . By considering instead the Taylor series expansion at  $z = z_{i-1}$ ,

$$\omega(z_{i-1}) = \omega(z_i) - \Delta z \left( \frac{\partial \omega}{\partial z} \right)_i + (\Delta z)^2 \frac{1}{2} \left( \frac{\partial^2 \omega}{\partial z^2} \right)_i + \dots , \quad (3.20)$$

then a similar approximation for the first derivative can be obtained,

$$\left( \frac{\partial \omega}{\partial z} \right)_i = \frac{\omega(z_i) - \omega(z_{i-1})}{\Delta z}. \quad (3.21)$$

This is also a first-order numerical method and is known as the Euler-backward scheme. A more sophisticated numerical method can be obtained by utilising both the Taylor expan-

sions about  $z = z_{i+1}$  and  $z = z_{i-1}$ , specifically subtracting equation (3.20) from equation (3.18). Doing so obtains a first-order scheme numerical scheme,

$$\left( \frac{\partial \omega}{\partial z} \right)_i = \frac{\omega(z_{i+1}) - \omega(z_{i-1})}{2\Delta z}. \quad (3.22)$$

This method of utilising Taylor expansions at different grid points can be generalised and it is easy to see how one can extend this formulation to higher orders by simply considering more neighbouring grid points to increase the accuracy of the scheme. By considering the expansions of  $\omega(z_{i-2})$ ,  $\omega(z_{i-1})$ ,  $\omega(z_{i+1})$ , and  $\omega(z_{i+2})$ , a fourth-order accurate central difference scheme with a truncation error of  $(\Delta z)^4$  can be obtained,

$$\left( \frac{\partial \omega}{\partial z} \right)_i = \frac{-\omega(z_{i+2}) + 8\omega(z_{i+1}) - 8\omega(z_{i-1}) + \omega(z_{i-2})}{12\Delta z}. \quad (3.23)$$

For the aforementioned work a second order scheme is sufficient. We can similarly approximate the second derivative by considering this time the sum of equations (3.18) and (3.20) and disregarding terms of order  $(\nabla z)^3$  and higher),

$$\left( \frac{\partial^2 \omega}{\partial z^2} \right)_i = \frac{\omega(z_{i+1}) - 2\omega(z_i) + \omega(z_{i-1})}{(\Delta z)^2}. \quad (3.24)$$

Using the above in conjunction with equation (3.22) we have obtained a way to approximate the first and second derivatives in equation (3.16) using only the values of the function at the two closest grid points. Ordinarily we would be required to modify this scheme at the top and bottom grid points as here grid points  $z_{i+1}$  and  $z_{i-1}$  respectively would be undefined. However due to our choice of boundary conditions fixing the values of  $\omega$  at these grid points such a modification is not required. The same arguments apply for the temperature and the streamfunction.

### 3.1.4 Tridiagonal solver

The methods outlined in the previous section allow for the calculation of  $T(z, t)$  and  $\omega(z, t)$ , leaving only equation (3.17) left to be solved so that the streamfunction can be updated

at each timestep. Using the finite-difference method outlined in Section 3.1.3 to calculate the second derivative we can rewrite equation (3.17) as

$$\omega_i = - \left( \frac{\psi_{i+1} - 2\psi_i + \psi_{i-1}}{(\Delta z)^2} - \left( \frac{n\pi}{a} \right)^2 \psi_i \right). \quad (3.25)$$

To reiterate, at this point in the calculation at some time  $t$ , time derivatives of  $T_t$  and  $\omega_t$ , have been expressed as a function of known quantities, with the exception of the streamfunction. We obtain this by way of a tridiagonal matrix algorithm, that is, for system such that,

$$a_i x_{i-1} + b_i x_i + c_i x_{i+1} = d_i, \quad (3.26)$$

then a matrix equation of rank  $N_z$  where  $N_z$  is the number of vertical gridpoints used in our system can be defined as,

$$\begin{bmatrix} b_1 & c_1 & & & \\ a_2 & b_2 & c_2 & & \\ \ddots & \ddots & \ddots & & \\ & a_{i-1} & b_{i-1} & c_{i-1} & \\ & a_i & b_i & & \end{bmatrix} \begin{bmatrix} x_1 \\ x_2 \\ \vdots \\ x_{i-1} \\ x_i \end{bmatrix} = \begin{bmatrix} d_1 \\ d_2 \\ \vdots \\ d_{i-1} \\ d_i \end{bmatrix} \quad (3.27)$$

rewriting then equation (3.25) in the form of equation 3.26,

$$\left( \frac{-1}{(\Delta z)^2} \right) \psi_{i-1} + \left[ \left( \frac{n\pi^2}{a} \right) + \frac{2}{(\Delta z)^2} \right] \psi_i + \left( \frac{-1}{(\Delta z)^2} \right) \psi_{i+1} = \omega_i, \quad (3.28)$$

from which,

$$a_i = c_i = \left( \frac{-1}{(\Delta z)^2} \right), \quad (3.29)$$

$$b_i = \left[ \left( \frac{n\pi^2}{a} \right) + \frac{2}{(\Delta z)^2} \right]. \quad (3.30)$$

The details of how this algorithm works in practice can be seen in Glatzmaier (2013), however in short the value of  $\psi$  at each gridpoint can be calculated given the values of  $\omega$ . We now have all the tools required to take a system of with known variable  $T_t$ ,  $\omega_t$ , and  $\psi_t$  and calculate their values at some point  $\Delta t$  later have now been shown. The following section will outline how we do this.

### 3.1.5 Timestepping

We have outlined in Section 3.1.2 how spectral methods can be used to reduce the problem down to one where the functions being solved for only depend on the vertical and temporal coordinates, such as  $T(z, t)$ . Section 3.1.3 demonstrates how we approximate the spatial derivatives in  $z$  that remain, and how we recover the value of  $\psi$  from equation (3.17) using a tridiagonal matrix formulation in section 3.1.4. The only remaining step is to evolve the system forward in time.

There are multiple different methods and timestepping schemes that can be used; here we employ an Adams-Bashforth second-order technique (Iserles 1996). We start with equation 3.15 which has been rearranged to leave the temporal derivative of  $T$  alone on the left-hand side,

$$\frac{\partial T_n}{\partial t} = -[(\mathbf{u} \cdot \nabla) T]_n + \left( \frac{\partial^2 T_n}{\partial z^2} - \left( \frac{n\pi}{a} \right)^2 T_n \right). \quad (3.31)$$

Dropping the  $n$  notation for clarity, and instead using the subscripts  $t - \delta t$ ,  $t$ , and  $t + \delta t$  to indicate the the value of the variable at the previous, current, and future timestep respectively, we can approximate the time derivative as,

$$\frac{T_{t+\Delta t} - T_t}{\Delta t} = \frac{3}{2}f_t - \frac{1}{2}f_{t-\Delta t}, \quad (3.32)$$

where  $f$  is the right hand side of equation (3.31). By some simple rearranging, we can

then calculate  $T_{t+\Delta t}$  using values from the current, and previous timestep. That is,

$$T_{t+\Delta t} = T_t + \frac{\Delta t}{2} (3f_t - f_{t-\Delta t}). \quad (3.33)$$

As this is a second-order timestepping scheme information is required from both the current and previous timesteps. Analogous to how higher order numerical schemes for approximating the spatial derivatives require more neighbouring information to achieve higher accuracy, higher order time-stepping techniques require more prior timesteps. This obviously cannot be used for the very first time step as there exists no "previous" step and so for the very first iteration a lower accuracy first-order method must be used, that is,

$$T_{t+\Delta t} = T_t + \Delta t f_t. \quad (3.34)$$

It is worth noting that this is the same as the Euler method briefly introduced in Section 3.1.3. After this initial step we then use equation (3.33) for the rest of our timestepping.

### 3.1.6 Linear reduction

In the previous sections we have used the non-linear form of the governing equations, however, to achieve the initial goal of calculating the critical Rayleigh number,  $\text{Ra}_c$ , it is easier to first consider the linear versions of equations (3.15), (3.16), and (3.17) as opposed to their full non-linear versions. Completely neglecting the  $[(\mathbf{u} \cdot \nabla) T]_n$  and  $[(\mathbf{u} \cdot \nabla) \omega]_n$  terms however results in a rather uninteresting and trivial result. The resulting linear thermal equation would become independent of  $\omega$  and  $\psi$  and so any initial temperature perturbation, and then with it any  $\omega$  and  $\psi$ , would decay away to zero.

For our linear problem then, the horizontally averaged temperature is taken to be some time-independent background temperature,  $T(z)$  (Chandrasekhar 1961). To achieve this we take the  $n = 0$  mode of the Fourier expansion of temperature,  $T_0(z)$ , so the linear thermal equation simply becomes,

$$\frac{\partial^2 T_0}{\partial z^2} = 0, \quad (3.35)$$

and recalling our boundary conditions we obtain both,

$$\frac{\partial T_0}{\partial z} = -1, \quad (3.36)$$

and

$$T_0(z) = 1 - z. \quad (3.37)$$

For the linear problem this background conductive temperature gradient is assumed to be large relative to any  $n > 0$  perturbations and so can approximate the non-linear advection term  $[(\mathbf{u} \cdot \nabla) T]_n$  to be a linear term dominated by the  $n = 0$  temperature gradient (equation (3.36)). That is,

$$[(\mathbf{u} \cdot \nabla) T]_n = \left[ u_z \frac{\partial T_0(z)}{\partial z} \right]_n = (-u_z)_n, \quad (3.38)$$

and utilising equation 3.9,

$$[(\mathbf{u} \cdot \nabla) T]_n = \left( \frac{\partial \psi}{\partial x} \right)_n = \left( \frac{n\pi}{a} \right) \psi_n. \quad (3.39)$$

Note that these above equations are technically incorrect. They do not equal  $[(\mathbf{u} \cdot \nabla) T]_n$  exactly, but instead they equal the coefficients of its cosine expansion. The cosines then drop upon substitution back into the original equation. With this approximation we can then obtain a linear set of equations,

$$\frac{\partial T_n}{\partial t} = \left( \frac{n\pi}{a} \right) \psi_n + \left( \frac{\partial^2 T_n}{\partial z^2} - \left( \frac{n\pi}{a} \right)^2 T_n \right), \quad (3.40)$$

$$\frac{\partial \omega_n}{\partial t} = \text{RaPr} \left( \frac{n\pi}{a} \right) T_n + \text{Pr} \left( \frac{\partial^2 \omega_n}{\partial z^2} - \left( \frac{n\pi}{a} \right)^2 \omega_n \right), \quad (3.41)$$

$$\omega_n = - \left( \frac{\partial^2 \psi_n}{\partial z^2} - \left( \frac{n\pi}{a} \right)^2 \psi_n \right), \quad (3.42)$$

with the associated boundary conditions

$$T_n = \omega_n = \psi_n = 0 \quad \text{for } z = 0 \text{ and } 1. \quad n > 0 \quad (3.43)$$

Finally some initial conditions are required for the system. A simple choice is for the fluid to be taken as initially at rest, that is  $\omega_n = \psi_n = 0$ , with a prescribed temperature perturbation that is zero at the boundaries  $T_n = \sin(\pi z)$ .

### 3.1.7 Finding the critical Rayleigh number

For a given  $\text{Ra}$ ,  $\text{Pr}$ , and  $a$  we can now solve this linear system of equations numerically. These solutions approximate the initial growth that occurs when a convective instability is present. Once this initial growth has occurred in a full nonlinear case, the amplitudes of the solutions quickly become large enough that the nonlinear advection terms act to stop the exponential growth caused by the instability. The purpose of excluding these terms is to perform a linear stability analysis on this initial growth (or decay) that occurs at the start of the simulation.

To do this we select values of  $\text{Pr}$  and  $a$  for which we wish to calculate the critical Rayleigh number,  $\text{Ra}_c$ , and then calculate solutions for a range of  $\text{Ra}$  values. For cases where  $\text{Ra} > \text{Ra}_c$  the solution will be supercritical (see Section 2.1.6) and  $T_n(z, t)$ ,  $\omega_n(z, t)$ , and  $\psi_n(z, t)$  will exponentially grow with time. Cases where  $\text{Ra} < \text{Ra}_c$  are referred to as subcritical and will result in solutions that decay to zero. We then calculate solutions for a range of  $\text{Ra}$  values and find the values of  $\text{Ra}$  where the solution transitions from subcritical to supercritical. These two values are now the new upper and lower limits for  $\text{Ra}_c$  and a new range of solutions can be obtained for  $\text{Ra}$  values between these two limits. This method can then be continued to further bracket the  $\text{Ra}_c$  until we obtain the desired level of accuracy.

With the benefit of knowing the solution ahead of time (as some formulations of this type of system can be solved analytically) the following is a typical workflow for finding the value of  $\text{Ra}_c$  for a case of  $a = \sqrt{2}$  (Chandrasekhar 1961).  $\text{Ra}_c$  is independent of  $\text{Pr}$  for this system. Beginning with a range of 10  $\text{Ra}$  values of 100, 200, ... 900, 1000, the solutions for the first 6 cases (up to and including  $\text{Ra} = 600$ ) would be subcritical and decay away to zero. For the cases of  $\text{Ra} = 700$  and higher the solutions would be supercritical and would exponentially grow. See Figure 3.1 for an example of this. Thus we know  $600 < \text{Ra}_c < 700$ . We can then repeat this for another range of  $\text{Ra}$  values between our new limits. Doing so would eventually tend towards the known value of  $\text{Ra}_c = 657.5$ . The limiting factor here is that as the precision of  $\text{Ra}_c$  is increased, each solution must be run for longer before it can be determined whether it is in fact growing or decaying. Typically we would repeat the above calculation for a few iterations and then once a sufficient level of accuracy has been obtained, take an average of the final two limits as the approximate  $\text{Ra}_c$  value.

What has been outlined in this section is a numerical solver for approximating the value of  $\text{Ra}_c$  in a 2D Boussinesq fluid, contained within four impermeable and stress free boundaries, with fixed temperature perturbations at  $z = 0, d$  and that are insulating ( $\frac{\partial T}{\partial x} = 0$ ) at  $x = 0, L$ . The disadvantage of such a method is that this calculation is inflexible. That is, we have made considerable assumptions throughout the derivation of this numerical code which while are appropriate to the system defined here, may not be appropriate for a different set of boundary conditions. In short, the code that we have just discussed does

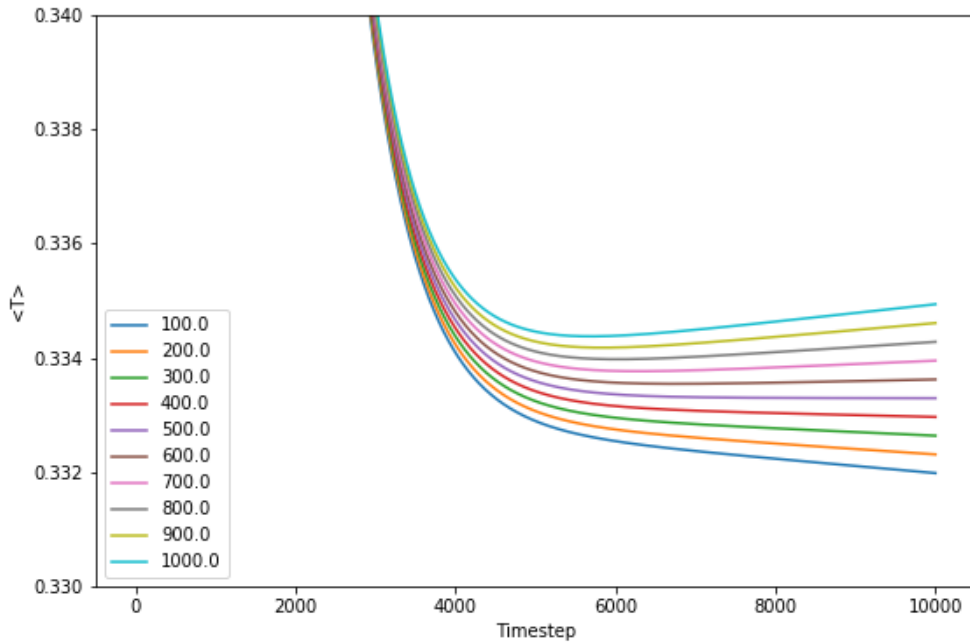


**Figure 3.1:** Values of the globally averaged temperature perturbation as a function of time for a range of Rayleigh number,  $\text{Ra}$ , for a given Prandtl number,  $\text{Pr}$  and aspect ratio  $a$ . These cases are initialised with a globally averaged temperature perturbation of 0.5, and so initially present a decay before subsequently growing (or decaying further).

an excellent job at solving the system that was defined, however may require significant changes for a comparatively slight change in the problem setup.

An alternative, and more flexible method would be to employ a numerical setup to solve for arbitrary fluid flows and boundary conditions. To this end, in the next section we turn to the Python framework Dedalus.

## 3.2 Dedalus

### 3.2.1 Introduction to Dedalus

The Dedalus Project is an open-sourced computational framework for solving partial differential equations. By utilising symbolic equation entry, the code can parse plain text equations and boundary conditions from which a numerical solver is then constructed. The same framework can also be used to create custom analysis tasks and outputs. The work contained in Chapters (4) and (5) have all been performed using version 2 of the

psuedo-spectral code Dedalus (Burns et al. 2020). A beneficial feature of Dedalus is that it is heavily parallelisable with minimal input from the user. As a result all calculations shown within this thesis that have utilised Dedalus have been run across multiple cores.

### 3.2.1.1 Writing a Dedalus code

While a more full and rigorous tutorial of how to setup and run an initial Dedalus code can be found within the Dedalus Project documentation, in this section I will briefly outline the key points and walk through how an initial value problem (IVP) solver can be setup. Generally Dedalus supports N-dimensional problems where N-1 domains employ spectral methods (see Section 3.1.2) and the final dimension utilises Chebyshev methods (see Iserles 1996). Given however, that the context of this work is the study of applied fluid dynamics, and specifically, the study of convection, the problem dimensions will be limited to 3D, corresponding to our spatial domain. Spectral bases are used for the horizontal coordinates with Chebyshev polynomials representing being the vertical coordinate,  $z$ . This domain can be established easily with the following setup,

```
x_basis = de.Fourier('x', nx, interval=(0,Lx), dealias=3/2)
y_basis = de.Fourier('y', ny, interval=(0,Ly), dealias=3/2)
z_basis = de.Chebyshev('z', nz, interval=(0,Lz), dealias=3/2)
domain = de.Domain([x_basis, y_basis, z_basis], grid_dtype=np.float64)
```

Here "de" is the Dedalus library import, "nx", "ny", and "nz", is the domain resolution, and "Lx", "Ly", and "Lz" is the physical extent of each base. The x and y dimensions use the "Fourier" basis which utilise cosine and sine expansions, whereas our z dimension uses the "Chebyshev" basis which makes the vertical coordinate into a discrete grid. The Chebyshev grid is not equidistant, and instead grid point density increases quadratically closer to the boundaries  $z = 0, Lz$ . An example of such spacings can be seen in Figure 3.2).

Once domain has been defined, the problem type needs to be chosen. Dedalus can solve initial value, eigenvalue, and boundary value problems however we will only be covering the first two in this thesis. To initialise an initial value problem the following is done,

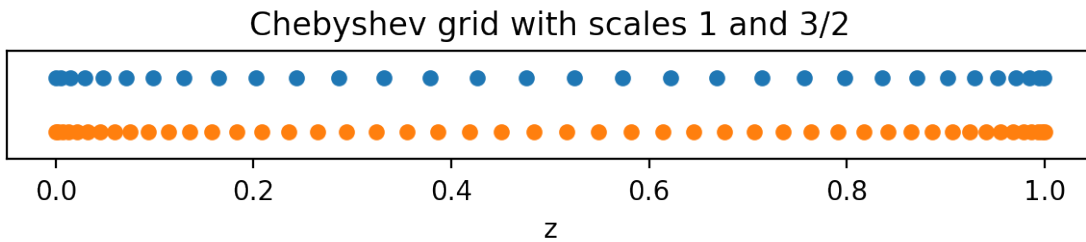


**Figure 3.2:** Figure taken from the Dedalus project tutorial pages showing the grid-spacing of Chebyshev polynomials with multiple scalings. Image credit: <https://dedalus-project.readthedocs.io>

```
variables=['u', 'v', 'w', 'T', 'uz', 'vz', 'wz', 'Tz']
problem = de.IVP(domain, variables)
```

where we need to provide the domain and any variables we are solving for. In this example these are the three components of the velocity, "u", "v", and "w", and the temperature, "T". The additional variables of "uz", "vz", "wz", and "Tz" represent their vertical derivative.

We have established our "problem" object and now the process is straightforward for adding our boundary conditions and governing equations. For example, the lines

```
problem.add_bc("left(u) = 0")
problem.add_bc("right(u) = 0")
```

add boundary conditions to "u" where the functions "left" and "right" apply to the first and last values of our Chebyshev coordinate, which in this case is the bottom and top of our vertical domain. We enter our governing equations in much the same way utilising the symbolic equation entry that Dedalus provides. For example, implementation of the equation (3.3) into the Dedalus solver as one of our governing equations would require the following. Fully expanding out the advection and diffusion terms we obtain,

$$\frac{\partial T}{\partial t} + u \frac{\partial T}{\partial x} + v \frac{\partial T}{\partial y} + w \frac{\partial T}{\partial z} = \kappa \left( \frac{\partial^2 T}{\partial x^2} + \frac{\partial^2 T}{\partial y^2} + \frac{\partial^2 T}{\partial z^2} \right). \quad (3.44)$$

To add this equation to our Dedalus solver we enter the following python code,

```
problem.add_equation( "dt(T) - kappa*( dx(dx(T)) +
+ dy(dy(T)) + dz(dz(Tz)) ) =
```

$$- u^*dx(T) - v^*dy(T) - w^*Tz'' )$$

where "problem" is a python class used by Dedalus. The second derivatives of  $\frac{\partial^2 T}{\partial x^2}$  and  $\frac{\partial^2 T}{\partial y^2}$  are represented by "dx(dx(T))" and "dy(dy(T))" while  $\frac{\partial^2 T}{\partial z^2}$  is represented by "dz(Tz)". This is because our Dedalus solver requires our equations to be reduced to first-order in the Chebyshev domain. This is why the additional "uz", "vz", "wz", and "Tz" variables are included in the initial problem declaration. These are then defined as additional equations in the form,

```
problem.add_equation("uz - dz(u) = 0")
problem.add_equation("vz - dz(v) = 0")
problem.add_equation("wz - dz(w) = 0")
problem.add_equation("Tz - dz(T) = 0")
```

An issue with this current implementation of the temperature diffusion equation is that we have not at any point in told Dedalus what  $\kappa$  is. This can be achieved by creating a parameter object,

```
problem.parameters["kappa"] = K
```

where the "K" on the right hand side of the equation is simply a previously defined python variable for our thermal diffusivity. If instead of a constant we wanted a non-constant coefficient, we can use the same process of defining a parameter object along with a few extra steps. Let us assume some arbitrary linear function for our thermal diffusivity such that its value drops by up to 20% across our vertical domain starting from a maximum value of  $K$  at the bottom boundary, that is  $\kappa = K(1 - 0.2z)$ ,

```
kappa = domain.new_field(name="kappa")
kappa["g"] = K*(1 - 0.2*z)
kappa.meta["x","y"]["constant"]
problem.parameters["kappa"] = kappa
```

where we have defined a new field, given it values, set some additional meta-data telling Dedalus the value is constant in the horizontal, and then finally constructed the parameter object. Alternatively an equivalent result can be obtained by doing a simple substitution,

---

```
problem.substitutions["kappa"] = K*(1 - 0.2*z)
```

which is telling Dedalus to "replace all instances of 'kappa' with ' $K * (1 - 0.2 * z)$ '". These parameter and substitution definitions should be done prior to adding any equations or boundary conditions.

Another important detail is about how Dedalus interprets and then solves our equation set. In the `problem.add_equation()` command, the advection and diffusion terms have switched which side of the equals sign they are on. This is because all of our diffusion terms are linear (they only depend on a singular variable,  $T$ ) whereas our advection terms are non-linear (they depend on both a component of the velocity,  $u$ ,  $v$ , and  $w$ , and the temperature,  $T$ ). The left-hand side is then parsed into a sparse matrix formulation whereas the non-linear right-hand side is evaluated explicitly (see Burns et al. 2020 for more detail on the numerical methods used by Dedalus).

Finally we can choose a time-stepping regime and build our solver object,

```
ts = de.timesteppers.RK443
solver = problem.build_solver(ts)
```

where "RK443" refers to a third-order Runge Kutta integration scheme (details of which can be seen in Ascher et al. 1997, section 2.8). Other timestepping regimes like the Adams Bashforth scheme outlined in section 3.1.5 are also available for use. Additionally, as discussed in Section 2.1.2 we are required to limit our time step based on the magnitude of our velocities, that is, we need to adjust our timestep in accordance with the CFL criterion (see (2.6)). To do this we use a part of Dedalus called `flow_tools`.

```
CFL = flow_tools.CFL(solver, initial_dt=dt, cadence=10, safety=0.5,
                      max_change=1.5, min_change=0.5, max_dt=rpf.max_dt)
CFL.add_velocities(('u', 'v', 'w'))
```

A useful feature of Dedalus is the ability to create custom built analysis tasks that will be performed and outputted at varying frequencies, for example,

```
snapshots = solver.evaluator.add_file_handler("snapshots", iter=100)
```

---

```
snapshots.add_system(solver.state)
```

This has created a `snapshots` output which with the `solver.add_system(solver.state)` command has then added the entire state of the problem at that point in time to the output. The parameters `iter` defines how often to output (in number of iterations) the data.

```
analysis = solver.evaluator.add_file_handler("analysis", iter=5)
analysis.add_task(" integ( integ( integ(
    0.5*(u*u + v*v + w*w),
    'x')/Lx, 'y')/Ly, 'z')/Lz",
    layout='g', name='KE')
```

This has created an `analysis` output where we have used the `add_task` command to write a custom built analysis task, in this case, the globally averaged kinetic energy making use again of the symbolic equation entry. These custom built analysis tasks allow for the user to easily add and remove new analysis tasks as easily as they declare the governing equations and boundary conditions.

Lastly the code is then iterated over until the given stop condition is met, in this example we use a simple maximum number of iterations.

```
solver.stop_iteration = 5000
while solver.ok:
    dt = CFL.compute_dt()
    solver.step(dt)
```

where the `CFL.compute_dt()` function calculates the new timestep size as previously described.

### 3.2.2 Calculating the critical Rayleigh number (EVP)

As discussed in Chapter 2 and reiterated at the start of Section 3.1, it is advantageous to have knowledge of the critical Rayleigh number prior to performing a full convective calculation. The linear calculation outlined in 3.1 is a perfectly valid method for obtaining  $\text{Ra}_c$ , however is not a particularly flexible method. The code we outlined is very specific to

the problem setup and somewhat rigid to any larger changes we might wish to implement. This is one of the significant advantages to Dedalus. If we instead turn to solving an eigenvalue problem for the value of  $\text{Ra}_c$  using Dedalus it can then be adapted with relative ease to include additional physics such as rotation, magnetism, etc. The following is a outline of how to build such a code for a 2D convective simulation. Much like with the initial value example outlined above, a more thorough tutorial can be found within the Dedalus Project documentation.

The initial setup is largely the same as with an IVP however there are some significant changes. Firstly when constructing the domain object we only need to provide a vertical basis, that is,

```
z_basis = de.Chebyshev('z', Nz, interval=(0, Lz))
d = de.Domain([z_basis], comm=MPI.COMM_SELF)
z = z_basis.grid()
```

We also need to provide a parameter space grid over which we which are going to search. What the code will do is produce an output which informs us where for a given horizontal mode,  $k_x$ , at which value of  $\text{Ra}$  the perturbation switches from decaying to growing. That is, at a given  $k_x$  at what  $\text{Ra}$  does a convective instability occur. To setup such a grid we do the following,

```
Ra_vals, kx_vals = 60, 60
mins = np.array((18000, 2))
maxs = np.array((35000, 13))
nums = np.array((Ra_vals, kx_vals))
```

where `Ra_vals` and `kx_vals` represent the resolution of our parameter grid and `mins` and `maxs` are the minimum and maximum values of  $\text{Ra}$  and  $k_x$  respectively.

Next we setup a problem object similar to the IVP case with the addition of defining what our eigenvalue is called,

```
variables = ['p', 's', 'u', 'v', 'w', 'sz', 'uz', 'vz', 'wz']
problem = de.EVP(d, variables, eigenvalue='omega')
```

When defining our initial problem parameters we are required to provide values for  $Ra$  and  $k$  however these will be overwritten once the solver begins producing our growth rate grid. This "eigenvalue" input is then used in some important substitutions; along with any other problem parameters that are needed, we require the following,

```
problem.parameters['Ra'] = 1000
problem.parameters['k'] = 1
problem.substitutions['dt(A)'] = 'omega*A'
problem.substitutions['dx(A)'] = '1j*k*A'
```

The values of  $Ra$  and  $k$  here are largely irrelevant, and we can simply choose something sensible. The rest of the problem setup, defining non-constant coefficients, defining the governing equations, and adding the boundary conditions, follows the same method as the IVP. Once this is done we utilise the "eigentools" Dedalus package to create an Eigenproblem object,

```
from eigentools import Eigenproblem, CriticalFinder
EP = Eigenproblem(rayleigh_benard, sparse=True)
```

We use this in conjunction with the `CriticalFinder` function to generate a grid of growth rates,

```
cf.grid_generator(mins, maxs, num_s)
```

The results of this calculation can be seen in Figure 3.3 where the colour indicates the value of the growth rate as a function of  $Ra$  and  $k_x$ . If required this grid can be saved as a .h5 data file and similarly, previously calculated growth rates can be loaded. We can then use two more eigentools functions to find  $Ra_c$  for a given wavenumber,  $k_x$ , and then find the overall  $Ra_c$  for all  $k_x$ . These are,

```
cf.root_finder()
crit = cf.crit_finder()
```

The first function `cf.root_finder()` simply interpolates the growth rates in  $Ra$  space and finds the value of  $Ra$  at which the growth rate is equal to zero. At this point we

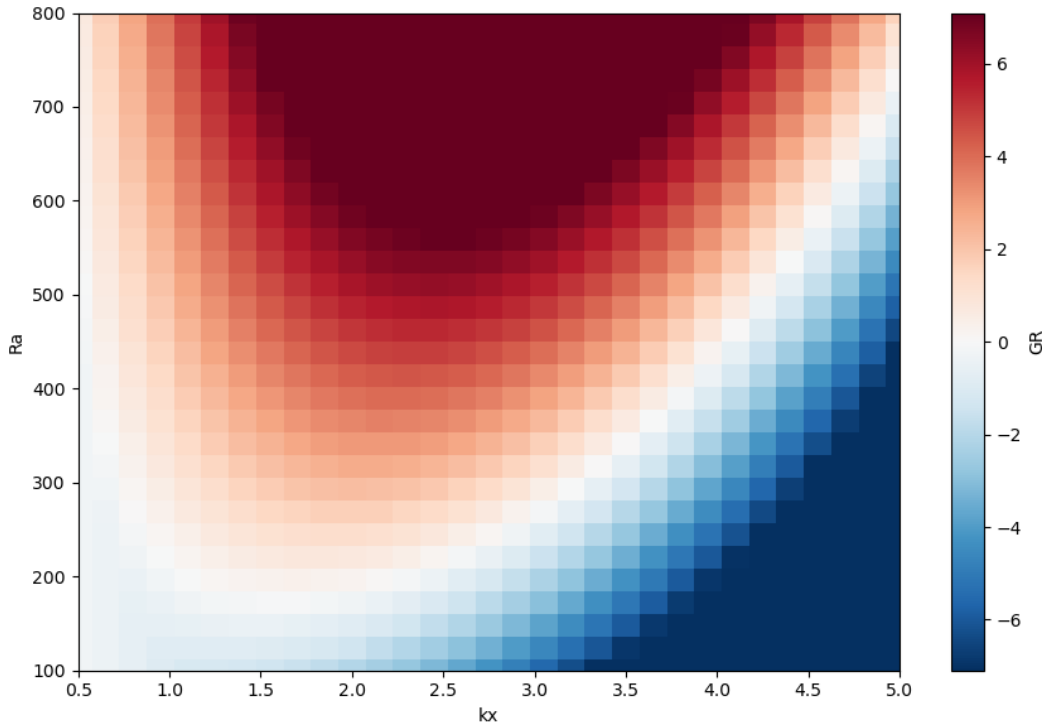


**Figure 3.3:** Grid of calculated growth rates from the EVP solver in the given  $\text{Ra}$ ,  $k_x$  space. This is for a case of stratified, anelastic convection with  $N_\rho = 1$ ,  $\text{Pr} = 1$  using the governing equations and boundary conditions as described in Section 4.1.

have the values of  $\text{Ra}_c$  for each discrete  $k_x$ . The second function `cf.crit_finder()` then interpolates across  $k_x$  space to find an overall minimum value of  $\text{Ra}_c$  and returns the critical wavenumber,  $k_{x,c}$ , and the corresponding critical Rayleigh number,  $\text{Ra}_c$ . The output of these two functions can be seen more clearly in Figure 3.4 which shows the previously shown calculated growth rates overplotted with the critical Rayleigh number as a function of  $k_x$ .

Lastly we need to consider the horizontal extent of our domain. Note that previously in Section 3.1 we used  $a$  to indicate the horizontal extent of the domain to remain consistent with that of Glatzmaier (2013). However, for the work contained in later chapters, in particular that of Chapter 5,  $L_x$  and  $L_y$  are instead used. For consistency with the rest of this thesis the latter notation will now be adopted. For a given horizontal extent  $L_x$ , only wavenumbers equal to  $k_{x,r}$  can fit in our domain, where  $k_{x,r}$  is defined as,

$$k_{x,r} = n \frac{2\pi}{L_x}. \quad (3.45)$$

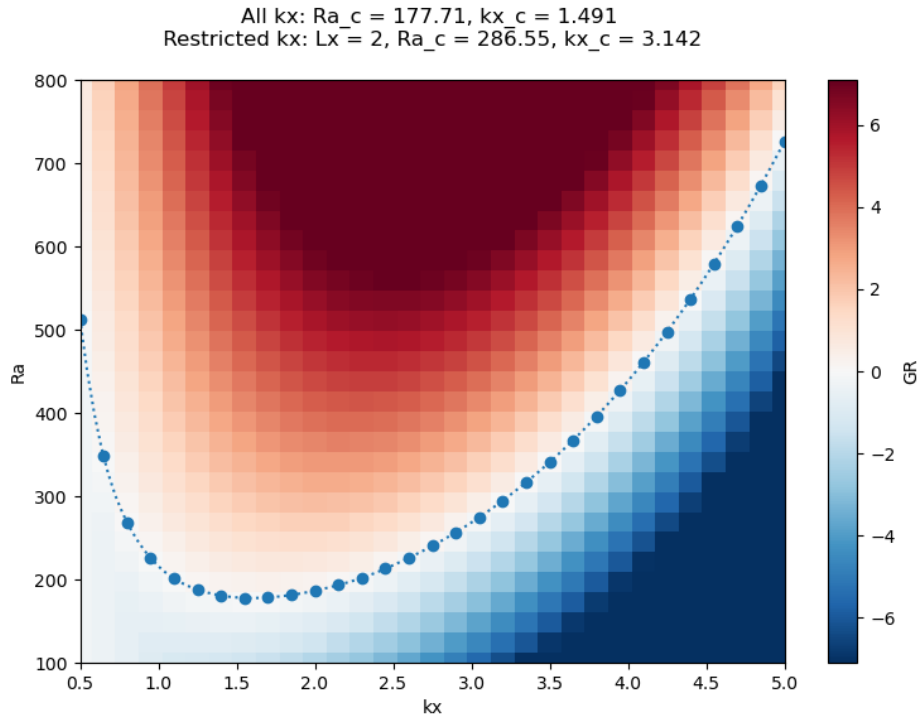


**Figure 3.4:** Calculated growth rates grid from the EVP solver in the given  $\text{Ra}, k_x$  space as shown in Figure 3.3, overplotted with the critical Rayleigh number  $\text{Ra}_c$  as a function of  $k_x$  space.

We can then extract the value of  $\text{Ra}_c$  for the allowed  $k_{x,r}$  values corresponding to the horizontal extent of our domain.

### 3.2.3 Convection modelling (IVP)

With the understanding of how to build our convective code from Section 3.2.1.1, and the ability to calculate the relevant values of  $\text{Ra}_c$  from Section 3.2.2, we can proceed to lay out the governing equations that define the convective code used extensively in Chapters 4 and 5.

Consider first a volume of convective fluid,  $V$ , enclosed between two impenetrable, stress-free boundaries with an associated magnetic field  $\mathbf{B}$ . By local conservation of energy, the rate of change of total energy is equal to the sum of the net inward flux of energy, and the rate of internal heat generation (by radioactivity, nuclear reactions etc.) This implies,

$$\frac{\partial}{\partial t} \left( \rho e + \frac{1}{2} \rho u^2 + \frac{B^2}{2\mu_0} - \rho \psi \right) = -\nabla \cdot \left( \rho \left( e + \frac{1}{2} u^2 - \psi \right) \mathbf{u} + \frac{(\mathbf{E} \times \mathbf{B})}{\mu_0} + P \mathbf{u} - \boldsymbol{\tau} \cdot \mathbf{u} - k \nabla T \right) + H \quad (3.46)$$

where  $\rho$  is the fluid density,  $e$  is the internal energy of the fluid,  $\psi$  is the gravitational potential that satisfies  $\mathbf{g} = \nabla \psi$ ,  $P$  is the pressure,  $\tau_{ij}$  is the contribution to the total stress tensor from irreversible processes,  $k$  is the thermal conductivity,  $T$  is the temperature,  $H$  is the rate of internal heat generation, and  $\frac{\mathbf{E} \times \mathbf{B}}{\mu_0}$  is the Poynting flux ( $\mathbf{E}$  is the electric field, and  $\mu_0$  is the permeability of free space).

We can also consider the internal energy equation:

$$\rho \left( \frac{\partial e}{\partial t} + (\mathbf{u} \cdot \nabla) e \right) = \nabla \cdot (k \nabla T) - P (\nabla \cdot \mathbf{u}) + \tau_{ij} \frac{\partial u_i}{\partial x_j} + \frac{j^2}{\sigma} + H \quad (3.47)$$

where  $\sigma$  is the conductivity of the fluid. We examine only cases where there is no internal heat generation, and thus  $H = 0$ , and instead drive convection by imposing a fixed flux,  $F$  at the bottom boundary. Integrating over  $V$ , assuming a steady state, and recalling that our boundaries are impermeable, equation 3.47 becomes,

$$\int_V (\mathbf{u} \cdot \nabla) P dV + \Phi = 0 \quad (3.48)$$

where here,

$$\Phi = \int_V \tau_{ij} \frac{\partial u_i}{\partial x_j} + \frac{j^2}{\sigma} dV \quad (3.49)$$

is the total dissipative heating rate including viscous and Ohmic heating terms.

For the case of no magnetic field (that is  $\mathbf{B}$ , and therefore  $\mathbf{j}$ , equal to zero), our governing equations are as follows:

$$\frac{\partial \mathbf{u}}{\partial t} + (\mathbf{u} \cdot \nabla) \mathbf{u} = -\nabla \tilde{p} + \frac{g^s}{c_p} \hat{\mathbf{e}}_z + \nu \left[ \frac{1}{\bar{\rho}} \frac{\partial}{\partial x_j} \left( \bar{\rho} \left( \frac{\partial u_i}{\partial x_j} + \frac{\partial u_j}{\partial x_i} \right) \right) - \frac{2}{3\bar{\rho}} \frac{\partial}{\partial x_i} \left( \bar{\rho} \frac{\partial u_j}{\partial x_j} \right) \right] \quad (3.50)$$

$$\nabla \cdot (\bar{\rho} \mathbf{u}) = 0 \quad (3.51)$$

$$\bar{\rho} \bar{T} \left( \frac{\partial s}{\partial t} + (\mathbf{u} \cdot \nabla) s \right) = \nabla \cdot (\kappa \bar{\rho} \bar{T} \nabla s) + \tau_{ij} \frac{\partial u_i}{\partial x_j} \quad (3.52)$$

where  $\mathbf{u}$  is the fluid velocity,  $\tilde{p} = \frac{p}{\bar{\rho}}$  is the modified pressure,  $g$  is the acceleration due to gravity,  $s$  is the specific entropy,  $c_p$  is the specific heat capacity at constant pressure,  $\nu$  is the kinematic viscosity, and  $\kappa$  is the thermal diffusivity. The system is anelastic and we have applied the LBR approximation so that we are diffusing entropy as opposed to temperature (see discussion in Section 2.1.2). Barred variables denote the polytropic ideal gas reference state described in more detail in Section 4.1.2.1. In short, the LBR approximation is valid when the reference state is approximately adiabatic, and so by defining our reference state as a  $m = 1.5$  polytrope (where  $m$  is the polytropic index) we satisfy this condition. We also assume a constant  $\nu$  and  $\kappa$ . Additionally,

$$\tau_{ij} = \nu \bar{\rho} \left( \frac{\partial u_i}{\partial x_j} + \frac{\partial u_j}{\partial x_i} - \frac{2}{3} \delta_{ij} \nabla \cdot \mathbf{u} \right) \quad (3.53)$$

is the viscous stress tensor.

Taking our vertical boundaries to be stress-free and assuming fixed entropy and fixed flux boundary conditions at the top and bottom respectively, we can begin to input this into Dedalus. A more detailed coverage of this system can be seen in Chapter 4 and the full version of equations expanded into a Dedalus-compatible format (e.g. the reduction to first order and reorganisation between the left and right hand sides) can be seen in Appendix A.

The numerical methods outlined above in Sections 3.2.2 and 3.2.3 will be used extensively in the following chapters, namely Chapters 4 and 5. For the study of the atmospheric circulation of exoplanets in Chapter 6 we turn to a fully global, 3D general circulation model developed by the UK Met Office, the Unified Model.

### 3.3 Global Circulation Models: The Unified Model

The Unified Model (UM) is a 3D general circulation model (GCM) that simulates atmospheric flows that has been in continued development by the UK Met Office for the past three decades (Walters et al. 2019). While originally developed for weather and climate forecasting it has recently been applied to the study of a variety of exoplanet atmospheres such as hot Jupiters (Mayne et al. 2014a; Amundsen et al. 2016; Tremblin et al. 2017; Drummond et al. 2020; Zamyatina et al. 2023), mini-Neptunes/super Earths (Drummond et al. 2018; Lines et al. 2019), and terrestrial planets (Mayne et al. 2014b; Boutle et al. 2017; Sergeev et al. 2020; Eager-Nash et al. 2023). The dynamical core at the heart of the UM, ENDGame (Wood et al. 2014), numerically solves the fully compressible, non-hydrostatic equations of motion with semi-Lagrangian advection and semi-implicit time stepping. A variety of smaller scale processes such as convection and radiation are included in the form of sub-grid scale parameterizations.

#### 3.3.1 Governing equations of the dynamical core

The UM models a spherical shell of atmosphere of height  $h$ , situated above an unsimulated planetary interior of radius  $R_p$ , visualised in figure 3.5. The governing equations that are solved by the ENDGame dynamical core are the momentum equations for the zonal, meridional, and vertical wind velocities, the continuity equation, and then the thermodynamic equation. This equation set is then fully closed with an equation of state. These are as follows,

$$\frac{\partial u}{\partial t} + \frac{u}{r \cos \phi} \frac{\partial u}{\partial \lambda} + \frac{v}{r} \frac{\partial u}{\partial \phi} + w \frac{\partial u}{\partial r} = \frac{uv \tan \phi}{r} - \frac{uw}{r} + fv - f'w - \frac{c_p \theta}{r \cos \phi} \frac{\partial \Pi}{\partial \lambda} + D(u) \quad (3.54)$$

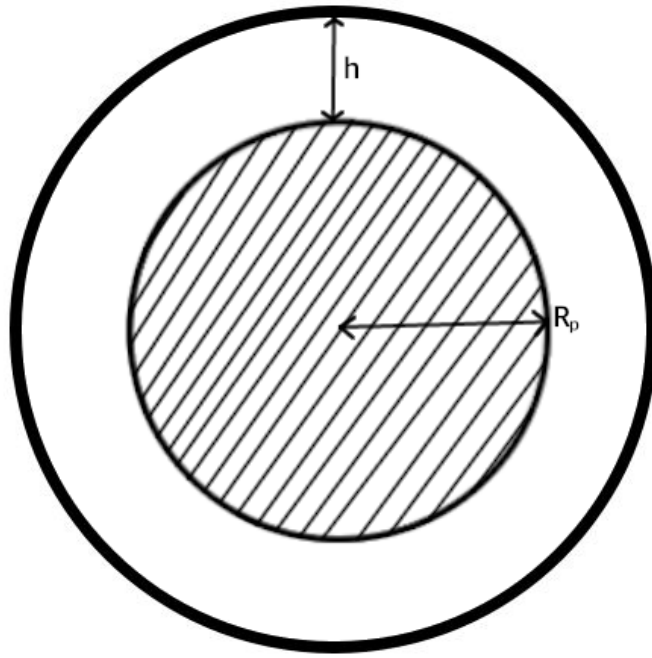


**Figure 3.5:** Schematic of UM's geometric domain. A simulated atmospheric spherical shell of height  $h$  situated on top of an unsimulated convective interior of radius  $R_p$ . The influence of the convective interior is then parameterised by an internal heat flux as detailed in Section 3.3.2.

$$\frac{\partial v}{\partial t} + \frac{u}{r \cos \phi} \frac{\partial v}{\partial \lambda} + \frac{v}{r} \frac{\partial v}{\partial \phi} + w \frac{\partial v}{\partial r} = -\frac{u^2 \tan \phi}{r} - \frac{vw}{r} - fu - \frac{c_p \theta}{r} \frac{\partial \Pi}{\partial r} + D(v) \quad (3.55)$$

$$\frac{\partial w}{\partial t} + \frac{u}{r \cos \phi} \frac{\partial w}{\partial \lambda} + \frac{v}{r} \frac{\partial w}{\partial \phi} + w \frac{\partial w}{\partial r} = \frac{u^2 + v^2}{r} + f'u - g(r) - c_p \theta \frac{\partial \Pi}{\partial r} \quad (3.56)$$

$$\frac{\partial \rho}{\partial t} + \frac{u}{r \cos \phi} \frac{\partial \rho}{\partial \lambda} + \frac{v}{r} \frac{\partial \rho}{\partial \phi} + w \frac{\partial \rho}{\partial r} = -\rho \left[ \frac{1}{r \cos \phi} \frac{\partial u}{\partial \lambda} + \frac{1}{r \cos \phi} \frac{\partial (v \cos \phi)}{\partial \phi} + \frac{1}{r^2} \frac{\partial (r^2 w)}{\partial r} \right] \quad (3.57)$$

$$\frac{\partial \theta}{\partial t} + \frac{u}{r \cos \phi} \frac{\partial \theta}{\partial \lambda} + w \frac{\partial \theta}{\partial r} = \frac{Q}{\Pi} + D(\theta) \quad (3.58)$$

$$\Pi^{\frac{\bar{R}}{c_p} - 1} = \frac{\bar{R}\rho\theta}{P_0} \quad (3.59)$$

Where as before  $\rho$  is our density and  $\mathbf{u}$  is the velocity vector with components  $u$ ,  $v$ , and  $w$ , in the longitudinal ( $\lambda$ ), latitudinal ( $\phi$ ), and radial ( $r$ ) directions respectively.  $c_p$  is the specific heat capacity,  $\bar{R}$  is the specific gas constant,  $Q$  is fluid heating rate,  $D$  is our diffusion operator. Rotation is included by defining two Coriolis parameters  $f$  and  $f'$  that are functions of the rotation rate  $\Omega$  and the latitude  $\phi$ . These are given by,

$$\begin{aligned} f &= 2\Omega \sin \phi \\ f' &= 2\Omega \cos \phi, \end{aligned} \quad (3.60)$$

In the case when the mass of the atmosphere  $M_{atmo}(r) = M(r) - M(R_p)$ , is insignificant compared to the mass of the interior, a height-dependent gravity can be obtained such that,

$$g(r) = g_p \left( \frac{R_p}{r} \right)^2, \quad (3.61)$$

where  $g_p$  is the surface gravity. However, this may not be the case in gas giant planet simulations. More formally,

$$g(r) = \frac{GM(r)}{r^2}, \quad (3.62)$$

therefore the gravitational acceleration at the bottom boundary is given by,

$$g_p = \frac{GM_p}{R_p^2}, \quad (3.63)$$

$$g(r) = \frac{G}{r^2} [M_p + M_{atmo}(r)], \quad (3.64)$$

$$g(r) = g_p \left( \frac{R_p}{r} \right)^2 + \frac{GM_{atmo}(r)}{r^2}, \quad (3.65)$$

which approximates to equation 3.61 if at a given radial height  $r$ ,  $M_{atmo}(r) \ll M_p$ . Lastly, we define a potential temperature and a non-dimensional pressure known as the Exner pressure, and these are given by,

$$\theta = T \left( \frac{p_0}{p} \right)^{\frac{\bar{R}}{c_p}}, \quad (3.66)$$

and

$$\Pi = \left( \frac{p}{p_0} \right)^{\frac{\bar{R}}{c_p}} = \frac{T}{\theta} \quad (3.67)$$

The potential temperature is a type of "dynamical temperature". It is the temperature a parcel of fluid would have if it was displaced from a pressure  $p$  to some reference pressure  $p_0$ . As a result this is a good measure of vertical stability. In the UM, both  $\theta$  and  $\Pi$  are prognostic variables. The gradient of potential temperature is analogous to the gradient of specific entropy as seen in Section 2.1.6, where

$$\frac{\partial \theta}{\partial z} > 0 \quad (3.68)$$

results in a stability stratified atmosphere which acts to suppress vertical motions whereas

$$\frac{\partial \theta}{\partial z} < 0 \quad (3.69)$$

results in an unstable atmosphere and convection. It is worth specifying that planetary

atmosphere cases presented here consider dry atmospheres, that is, neglect the presence of water vapour and the influence of its resulting phase transitions. On Earth for example, water vapour can play a significant role in atmospheric convective energy transport. In temperature regimes more applicable to say hot Jupiters, the evaporation and formation of silicate clouds have similar influences (Gao et al. 2020). This condensation and evaporation acts analogously to ‘sources’ and ‘sinks’ of energy as a result of the latent heat required for such phase changes. Subsequent advection of these substances can then act as a form of energy transport via. the mechanism of ‘removing’ energy from the atmosphere as a result of evaporation, and then ‘supplying’ it upon condensation. Considering the presence of convection is heavily influenced by other competing energy transport terms, the inclusion (or omission) of such phase changes are of note.

### 3.3.2 Internal heat flux

As briefly discussed in Section 1.1.2.2 highly irradiated tidally-locked exoplanets are likely to have hotter interiors than those predicted from 1D structural evolution models as a result of the increased incident stellar flux that they receive. However Figure 3.5 shows that the interior is not resolved in the simulations performed using the UM. The section will introduce the vertical boundary conditions used by the UM and detail the parameterisation of the convective interior.

Both vertical boundaries are taken to be rigid and impermeable to conserve energy and mass (Wood and Staniforth 2003). A nonphysical side effect of these rigid boundaries is that any vertically propagating waves such as gravity or sound waves can be artificially reflected back into the domain. This is typically only significant during the spin-up period of the simulation where the initial adjustment of the atmospheric mass generates a significant gravity wave activity. This is mitigated at the upper boundary by the introduction of a sponge layer which acts to dampen any vertical velocity perturbations (see Melvin et al. 2010). At the lower boundary the density of the fluid is high enough to not require any additional dampening. In the hot Jupiter cases this sponge layer extends low enough that it has the potential to alter the atmospheric flow, however tests performed in Mayne et al. (2017) demonstrated that this does not significantly effect the dynamics.

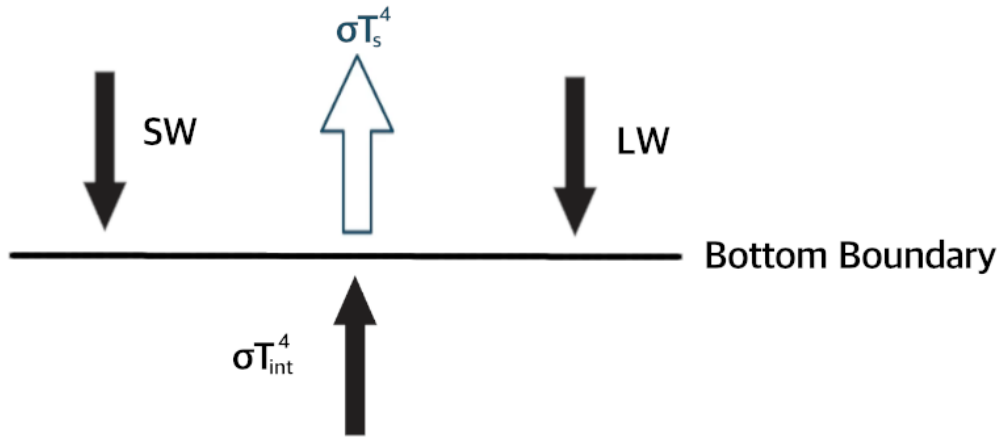


**Figure 3.6:** Schematic of the energy balance present at the planetary "surface". The "SW" and "LW" labels represent the radiative heating from shortwave and longwave radiation respectively, while the  $\sigma T_{int}^4$  represents the internal heating from the convective heat flux. From the energy balance of these components we then calculate a surface temperature  $T_s$ .

For terrestrial planets the lower boundary is simply defined as our physical surface, however for gaseous planets such as hot Jupiters there exists no convenient solid surface and so instead we impose a frictionless inner boundary at the planetary radius  $R_p$ . The UM uses a fixed surface temperature,  $T_s$ , that radiates as a black-body, however as previously mentioned gas giant planets do not have a clearly defined surface, and so also do not have a convenient surface temperature to select. Therefore, in order to explore the impact of the interior convection regions on the outer atmosphere we require a more sophisticated boundary convection, more realistically capturing the energy released. The UM (along with other GCMs) achieve this by introducing an intrinsic temperature,  $T_{int}$ , an effective temperature in the absence of radiation. This intrinsic temperature captures the residual heat that remains from the initial gravitational collapse of the planetary formation stages that is then typically supplied to our atmosphere from the interior via the convective motions that lie beneath the simulated domain.

In the absence of any convective heat flux from the interior (consider  $T_{int} = 0$ ), the surface temperature can be calculated from a radiative balance calculation of the surface fluxes, that is,

$$\epsilon \sigma T_s^4 = F = \epsilon L + S, \quad (3.70)$$

where  $\epsilon$  is the emissivity of the surface, a value between 0 and 1 describing how like a black-body the emitter is,  $\sigma$  is the Stefan-Boltzmann constant,  $F$  is the total flux absorbed at the surface, and lastly  $L$  and  $S$  are the downwelling longwave and net absorbed shortwave fluxes respectively. Hence

$$T_s = \left[ \frac{\epsilon L + S}{\epsilon \sigma} \right]^{1/4}. \quad (3.71)$$

With the addition of an intrinsic convective heat flux we can obtain a new expression for  $T_s$  as follows, beginning with the intrinsic flux at the top of the atmosphere we have,

$$F_{int} = \sigma T_{int}^4, \quad (3.72)$$

and so the total energy output at the top of the atmosphere is,

$$L_{int} = 4\pi(R_p + h)^2 \sigma T_{int}^4, \quad (3.73)$$

where  $R_p$  is the radius of the planet up to the bottom of our domain, and then  $h$  is the additional height of the atmosphere that we are directly simulating. If we then consider the energy transport through the surface,  $L_s = 4\pi R_p^2(F_s^+ - F_s^-)$ , where the subscript  $s$  denotes surface values, and the superscripts + and - denote upwelling and downwelling fluxes respectively. Assuming radiation is the primary mechanism for vertical energy transport (that is, there is no advection of energy across the boundary), equate this to  $L_{int}$  we obtain the following,

$$4\pi(R_p + h)^2 \sigma T_{int}^4 = 4\pi R_p^2(F_s^+ - F_s^-) \quad (3.74)$$

which with some tidying becomes,

$$F_s^+ = \frac{(R_p + h)^2}{R_p^2} \sigma T_{int}^4 + F_s^- \quad (3.75)$$

where  $F_s^- = \epsilon L + S$ . Typically the radius of the planet is multiple orders of magnitude larger than the height of our atmospheric shell, that is  $R_p \gg h$ . We can therefore obtain an equation for  $T_s$  of the form,

$$T_s = \left( T_{int}^4 + \frac{\epsilon L + S}{\sigma} \right)^{1/4} \quad (3.76)$$

In many previous studies  $T_{int}$  has been set at the value assumed for Jupiter itself, that is,  $T_{int} = 100\text{K}$  (Amundsen et al. 2016) however as will be shown in Section 6 this is likely to be incorrect. In the context of young gas giant planets or brown dwarfs their interiors are likely to be much hotter and therefore have higher values of  $T_{int}$ . Additionally there has been increasing observational evidence to suggest a correlation between inflated planetary radii and stellar irradiation (Demory and Seager 2011; Laughlin et al. 2011; Weiss et al. 2013). As will be discussed more in Section 6, we can derive an equilibrium relation between the effective temperature (a function of stellar irradiance) and this intrinsic temperature  $T_{int}$  (see Thorngren et al. 2019 for details). This suggests that values of  $T_{int} > 100\text{K}$  are more physically realistic.

### 3.3.3 Latitude dependence

In real planets this interior convection likely does not supply a homogeneous convective heat flux at all latitudes and longitudes, and is not constant with time. Some prior work has explored the differences in the resulting circulation between a hot and cold interior (Komacek et al. 2022), and others have explored spatial and temporal effects of a "plume-like" overshooting convective boundary in a reduced, "shallow-water" system (Zhang and Showman 2014), however no extensive study has yet been performed in the fully compressible regime. Let this additional heat flux being supplied to our atmospheric layer at its bottom boundary be given by the parameter  $Q_{int}$  such that currently,

$$Q_{int} = \sigma T_{int}^4 \quad (3.77)$$

We can introduce an initial latitude dependence to the parameterised internal heat flux in two ways:

This latitude dependence can be introduced to the parameterised internal heat flux in two ways:

- Case A: Allow  $Q$  to decrease with distance from the equator,

$$Q_{int} = \sigma [T_{int} (1 - \alpha[1 - \cos(\phi)])]^4. \quad (3.78)$$

- Case B: Allow  $Q$  to increase with distance from the equator,

$$Q_{int} = \sigma [T_{int} (1 - \alpha \cos(\phi))]^4. \quad (3.79)$$

where  $\alpha$  is a scaling factor for the extent at which  $Q$  varies with latitude.

### 3.4 Chapter summary

This chapter has provided an overview of the numerical methods that will be used throughout the remainder of this thesis. The numerical methods introduced in Section 3.2 will be utilised extensively in Chapters 4 and 5. Chapter 6 will then use the Unified Model described in Section 3.3 to explore variations on the interior convection parameterisations and their influence on the atmospheric dynamics.

## Chapter 4

# Simulations of stellar convection: Basic setup and diagnostics

With the theoretical background discussed in Chapter 2, and the numerical frameworks laid out in Chapter 3, this chapter will now present some examples of stellar convection simulations. An eigenvalue solver much like the one detailed in Section 3.2.2 has been used to find values of the critical Rayleigh number ( $Ra_c$ ) for given stratification ( $N_\rho$ ) and rotation rate ( $Ta$ ). These values can then be used to inform choices of the input Rayleigh number ( $Ra$ ) to achieve a desired supercriticality ( $Ra/Ra_c$ ).

### 4.1 Model Setup

#### 4.1.1 Domain Geometry

In this chapter we will explore convection in a Cartesian box on the surface of a rotating sphere (see 4.1). This is known as a tilted f-plane. Our coordinate system is such that the horizontal coordinates,  $x$  and  $y$ , correspond to the longitudinal and latitudinal directions respectively. The vertical coordinate,  $z$ , then corresponds to the radial direction. The domain is bounded by two impermeable and stress-free boundaries located at  $z = 0$  and  $z = d$ . The rotation vector,  $\Omega$ , is identically perpendicular to the longitudinal coordinate,  $x$ , and so  $\Omega_x = 0$ . This means the rotation vector takes the form

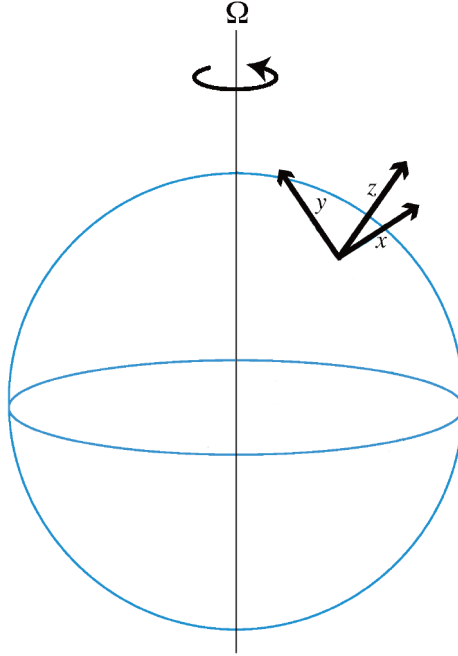


**Figure 4.1:** A schematic view of the location of our cartesian layer on a rotating sphere.

$\Omega = (0, \Omega_y, \Omega_z) = (0, \Omega \cos \phi, \Omega \sin \phi)$ , where  $\Omega$  is the magnitude of the rotation vector and  $\phi$  is the latitude. The resulting Coriolis term then takes the form,

$$2\Omega \times \mathbf{u} = 2\Omega \begin{pmatrix} w \cos \phi - v \sin \phi \\ u \sin \phi \\ -u \cos \phi \end{pmatrix}, \quad (4.1)$$

where  $u$ ,  $v$ , and  $w$ , are the  $x$ ,  $y$ , and  $z$ , components of the fluid velocity,  $\mathbf{u}$  respectively.

### 4.1.2 2.5D approximation

Consider first a two-dimensional system. As we are studying convective motions we require our vertical coordinate,  $z$ , and so we have a choice of which horizontal direction to model and which to exclude. If we adopted an  $x$ - $z$  plane then our rotation vector would be pointing out of the plane of our domain. This would result in any Taylor-Proudman-like features being suppressed (see discussion in Chapter 2 on Taylor-Proudman theorem). Therefore if we wish to study the effects of rotation in a two-dimensional system it would be better to model the  $y$ - $z$  plain and exclude our  $x$ -coordinate. This isn't as straightfor-

ward as one might expect however. Consider for a moment the y- and z-components of the Coriolis term,  $\vec{f}$  in the momentum equation (equation 5.11),

$$\begin{aligned} f_y &= u \sin \phi \\ f_z &= -u \cos \phi \end{aligned} \quad (4.2)$$

If we exclude the x-coordinate, then  $u = 0$  and so  $f_y = f_z = 0$ . Despite selecting our domain such that we include rotational effects, the lack of any zonal velocity means by definition we have no Coriolis effect. To counter this, we assume "2.5D" geometry in that we take our x-coordinate to be essentially one grid-point in depth. Our domain is now of the shape  $Nx, Ny, Nz = (1, Ny, Nz)$ , allowing for three-dimensional vectors but assuming our x-axis to be axisymmetric. That is,

$$\begin{aligned} \mathbf{u} &= u \hat{\mathbf{x}} + v \hat{\mathbf{y}} + w \hat{\mathbf{z}} \\ \partial_x &= 0. \end{aligned} \quad (4.3)$$

Consider now the x-component of the momentum equation 3.50 with the addition of the rotational Coriolis term  $2\Omega \times \mathbf{u}$  on the left-hand side expanded fully, that is,

$$\begin{aligned} \frac{\partial u}{\partial t} + u \frac{\partial u}{\partial x} + v \frac{\partial u}{\partial y} + w \frac{\partial u}{\partial z} + 2\Omega(w \cos \phi - v \sin \phi) &= \frac{-1}{\bar{\rho}} \frac{\partial P}{\partial x} \\ + \nu \left[ \frac{4}{3} \frac{\partial^2 u}{\partial x^2} + \frac{\partial^2 u}{\partial y^2} + \frac{\partial^2 u}{\partial z^2} + \frac{1}{3} \frac{\partial^2 v}{\partial x \partial y} + \frac{1}{3} \frac{\partial^2 w}{\partial x \partial z} + \frac{1}{\bar{\rho}} \frac{\partial \bar{\rho}}{\partial z} \left( \frac{\partial u}{\partial z} + \frac{\partial w}{\partial x} \right) \right]. \end{aligned} \quad (4.4)$$

We then simply neglect any  $\partial_x$  terms, giving us a much simpler

$$\frac{\partial u}{\partial t} + v \frac{\partial u}{\partial y} + w \frac{\partial u}{\partial z} + 2\Omega(w \cos \phi - v \sin \phi) = \nu \left[ \frac{\partial^2 u}{\partial y^2} + \frac{\partial^2 u}{\partial z^2} + \frac{1}{\bar{\rho}} \frac{\partial \bar{\rho}}{\partial z} \frac{\partial u}{\partial z} \right]. \quad (4.5)$$

This then allows the x-component of the velocity to evolve with time, and therefore yields non-zero values for our Coriolis force in the y- and z-directions.

#### 4.1.2.1 Equation set

Building on the work outlined in Chapters 2 & 3, and specifically leading on from section 3.2.3 we can go on to define our main set of governing equations. In short, the model setup largely follows that of Currie and Browning (2017) with the addition of the Coriolis term and the corresponding 2.5D geometry. We take a polytropic ideal gas reference state such that,

$$\begin{aligned} \bar{T} &= T_0(1 - \beta z), \\ \bar{\rho} &= \rho_0(1 - \beta z)^m, \\ \bar{p} &= R\rho_0T_0(1 - \beta z)^{m+1}, \end{aligned} \quad (4.6)$$

where  $m$  the polytropic index and  $R$  is the ideal gas constant. The inverse temperature scale height  $\beta$  is a measure of the stratification and is given by  $\beta = \frac{g}{c_p,0T_0}$ , where  $g$  is the acceleration due to gravity and  $c_p$  is the specific heat capacity. From here onwards however, we will almost exclusively refer to the number of density scale heights across our layer,  $N_\rho$ , when quantifying the degree of stratification within our domain.  $N_\rho$  is defined as,

$$N_\rho = -m \ln(1 - \beta d) \quad (4.7)$$

We use the anelastic equation set under the Lantz-Braginsky-Roberts (LBR) approximation (Lantz 1992, Braginsky and Roberts (1995)) and as a result diffuse entropy instead of

temperature (Lecoanet et al. 2014). This approximation is valid when fluid flows are sufficiently subsonic and the reference state is nearly adiabatic. Both conditions are satisfied in the interiors of typical stellar convection zones. Additionally, we fix the polytropic index as  $m = 1.5$ , such that the ratio of specific heat capacities is equal to  $5/3$ , appropriate for adiabatic processes within a monatomic gas. We also consider only the hydrodynamical problem, such that the electric current,  $j$ , is zero, and so we have no Lorentz contribution to our momentum equations and all of our dissipation is purely viscous.

Our equation set therefore takes the form,

$$\begin{aligned} \frac{\partial \mathbf{u}}{\partial t} + (\mathbf{u} \cdot \nabla) \mathbf{u} + 2\boldsymbol{\Omega} \times \mathbf{u} &= -\nabla \tilde{p} + \frac{g_s}{c_p} \hat{\mathbf{e}}_z \\ &+ \nu \left[ \frac{1}{\bar{\rho}} \frac{\partial}{\partial x_j} \left( \bar{\rho} \left( \frac{\partial u_i}{\partial x_j} + \frac{\partial u_j}{\partial x_i} \right) \right) - \frac{2}{3\bar{\rho}} \frac{\partial}{\partial x_i} \left( \bar{\rho} \frac{\partial u_j}{\partial x_j} \right) \right], \end{aligned} \quad (4.8)$$

$$\nabla \cdot (\rho \mathbf{u}) = 0, \quad (4.9)$$

$$\bar{\rho} \bar{T} \left( \frac{\partial s}{\partial t} + (\mathbf{u} \cdot \nabla) s \right) = \nabla \cdot (\kappa \bar{\rho} \bar{T} \nabla s) + \tau_{ij} \frac{\partial u_i}{\partial x_j}, \quad (4.10)$$

where

$$\tau_{ij} = \nu \bar{\rho} \left( \frac{\partial u_i}{\partial x_j} + \frac{\partial u_j}{\partial x_i} - \frac{2}{3} \delta_{ij} \nabla \cdot \mathbf{u} \right), \quad (4.11)$$

is the viscous stress tensor. Note again that when we are considering two-dimensional cases we still evolve a three-dimensional velocity field and simply consider  $\partial_x = 0$ . We fully non-dimensionalise our system by the viscous timescale,  $\tau_v = d^2/\nu$ , and the domain depth,  $d$ , and define the following non-dimensional parameters

$$\text{Pr} = \frac{\nu}{\kappa}, \quad \text{Ta} = \frac{4\Omega^2 d^4}{\nu^2}, \quad \text{Ra} = \frac{gd^4 F}{\nu \kappa^2 \rho_0 c_{p,0} T_0}, \quad \theta = \frac{gd}{c_{p,0} T_0}, \quad (4.12)$$

where  $\text{Pr}$  is our Prandtl number,  $\text{Ta}$  is our Taylor number,  $\text{Ra}$  is our flux-based Rayleigh number (Duarte et al. 2016), and  $\theta$  is a non-dimensionalised version of the our thermal scale height  $\beta$ . More detailed coverage of these non-dimensional parameters can be seen in Section 2.2. This allows us to fully define our parameter space by our polytropic index,  $m$ , and equations (4.7), and (4.12). Applying our non-dimensionalisation to equations (4.8), (4.9), and (4.10), our governing equations become

$$\begin{aligned} \frac{\partial \hat{\mathbf{u}}}{\partial \hat{t}} + (\hat{\mathbf{u}} \cdot \hat{\nabla}) \hat{\mathbf{u}} &= -\hat{\nabla} \hat{p} + \frac{\text{Ra}}{\text{Pr}} \hat{s} \hat{\mathbf{e}}_z \\ &+ \left[ \frac{1}{\hat{\rho}} \frac{\partial}{\partial \hat{x}_j} \left( \hat{\rho} \left( \frac{\partial \hat{u}_i}{\partial \hat{x}_j} + \frac{\partial \hat{u}_j}{\partial \hat{x}_i} \right) \right) - \frac{2}{3\hat{\rho}} \frac{\partial}{\partial \hat{x}_i} \left( \hat{\rho} \frac{\partial \hat{u}_j}{\partial \hat{x}_j} \right) \right], \end{aligned} \quad (4.13)$$

$$\hat{\nabla} \cdot (\hat{\rho} \hat{\mathbf{u}}) = 0, \quad (4.14)$$

$$\text{Pr} \hat{\rho} \hat{T} \left( \frac{\partial \hat{s}}{\partial \hat{t}} + (\hat{\mathbf{u}} \cdot \hat{\nabla}) \hat{s} \right) = \hat{\nabla} \cdot (\hat{\rho} \hat{T} \hat{\nabla} \hat{s}) + \frac{\text{Pr}^2 \theta}{\text{Ra}} \hat{\tau}_{ij} \frac{\partial \hat{u}}{\partial \hat{x}_j}, \quad (4.15)$$

Our lower boundary condition is taken to be fixed flux, where we state that the flux given at the bottom boundary ( $z = \hat{z} = 0$ ) is purely conductive and therefore,

$$F|_{z=0} = -\kappa \rho_0 T_0 \frac{\partial s}{\partial z} \Big|_{z=0}, \quad (4.16)$$

which when non-dimensionalised becomes,

$$\begin{aligned} F|_{\hat{z}=0} &= -\kappa\rho_0 T_0 \frac{1}{d} \left( \frac{\partial}{\partial \hat{z}} \left[ \frac{Fd}{\kappa\rho_0 T_0} \hat{s} \right] \right) \Big|_{\hat{z}=0} \\ F|_{\hat{z}=0} &= -\kappa\rho_0 T_0 \frac{1}{d} \frac{d}{\kappa\rho_0 T_0} F|_{\hat{z}=0} \frac{\partial \hat{s}}{\partial \hat{z}} \Big|_{\hat{z}=0} \end{aligned} \quad (4.17)$$

and so,

$$\frac{\partial \hat{s}}{\partial \hat{z}} \Big|_{\hat{z}=0} = -1, \quad (4.18)$$

We take the upper boundary ( $z = d$ , and therefore  $\hat{z} = 1$ ) to be fixed entropy, and set this equal to zero.

$$\hat{s}|_{\hat{z}=1} = 0, \quad (4.19)$$

Additionally we assume these boundaries to be impermeable,

$$\hat{w}|_{\hat{z}=0,1} = 0 \quad (4.20)$$

and stress free,

$$\begin{aligned} \frac{\partial \hat{u}}{\partial \hat{z}} \Big|_{\hat{z}=0,1} &= 0 \\ \frac{\partial \hat{v}}{\partial \hat{z}} \Big|_{\hat{z}=0,1} &= 0 \end{aligned} \quad (4.21)$$

Note that for the rest of this chapter we will simply drop the hat notation (^) and assume all variables to non-dimensionalised, unless otherwise specified.

Using the methods outlined in section 3.2, the equations (4.13), (4.14), and (4.15)

can then be solved using Dedalus (Burns et al. 2020). A full expansion of the equations in a Dedalus compatible format can be viewed in Appendix A.

## 4.2 Fluxes

One way to examine the heat transport is to examine how the luminosity  $L$  varies with height. An expression for  $L$  at some given depth  $z = z'$  can be obtained by integrating either the internal energy equation (3.47) or the total energy equation (3.46) over the volume enclosed between the bottom boundary and  $z = z'$ . As we are supplying the system with a total luminosity  $L$  at our bottom boundary, the subsequent integrals of these equations are equal to  $L$ . Starting with the internal energy, integration results in,

$$L = \int_{V_{z'}} \nabla \cdot (\bar{\rho} \bar{T} s \mathbf{u}) dV + \int_{V_{z'}} -\nabla \cdot (\kappa \bar{\rho} \bar{T} \nabla s) dV + \int_{V_{z'}} -s \bar{\rho} (\mathbf{u} \cdot \nabla) \bar{T} dV + \int_{V_{z'}} -\tau_{ij} \frac{\partial u_i}{\partial x_j} dV. \quad (4.22)$$

The divergence theorem can then be applied to the first two integrals, transforming them from volume to surface integrals,

$$L = \int_{S_{z'}} \bar{\rho} \bar{T} s w dS + \int_{S_{z'}} -\kappa \bar{\rho} \bar{T} \frac{\partial s}{\partial z} dS + \int_{V_{z'}} -s \bar{\rho} (\mathbf{u} \cdot \nabla) \bar{T} dV + \int_{V_{z'}} -\tau_{ij} \frac{\partial u_i}{\partial x_j} dV, \quad (4.23)$$

where the four terms represent the convective ( $L_{conv}$ ), conductive ( $L_{cond}$ ), buoyancy ( $L_{buoy}$ ), and dissipative ( $L_{diss}$ ) luminosities respectively. That is,

$$L_{conv} = \int_{S_z'} \bar{\rho} \bar{T} s w dS, \quad (4.24)$$

$$L_{cond} = \int_{S_z'} -\kappa \bar{\rho} \bar{T} \frac{\partial s}{\partial z} dS, \quad (4.25)$$

$$L_{buoy} = \int_{V_z'} -s \bar{\rho} (\mathbf{u} \cdot \nabla) \bar{T} dV, \quad (4.26)$$

$$L_{diss} = \int_{V_z'} -\tau_{ij} \frac{\partial u_i}{\partial x_j} dV. \quad (4.27)$$

Note that  $\bar{T} = 1 - \theta z$ , therefore  $\frac{\partial \bar{T}}{\partial x} = 0$  and so,

$$(\mathbf{u} \cdot \nabla) \bar{T} = u \frac{\partial \bar{T}}{\partial x} + w \frac{\partial \bar{T}}{\partial z} = w \frac{\partial \bar{T}}{\partial z}, \quad (4.28)$$

thus we can express  $L_{buoy}$  as follows,

$$L_{buoy} = \int_{V_z'} -s \bar{\rho} w \frac{\partial \bar{T}}{\partial z} dV. \quad (4.29)$$

Now to calculate these luminosities using the outputs from our simulations, we need to non-dimensionalise the expressions in (4.23),

$$L_{conv} = \rho_0 T_0 \frac{Fd}{\kappa \rho_0 T_0} \frac{v}{d} d^2 \hat{L}_{conv} = Fd^2 \frac{v}{\kappa} \hat{L}_{conv}, \quad (4.30)$$

$$L_{cond} = \kappa \rho_0 T_0 \frac{1}{d} \frac{Fd}{\kappa \rho_0 T_0} \frac{1}{\kappa} d^2 \hat{L}_{conv} = Fd^2 \hat{L}_{cond}, \quad (4.31)$$

$$L_{buoy} = \frac{Fd}{\kappa \rho_0 T_0} \rho_0 \frac{v}{d} \frac{T_0}{d} d^3 \hat{L}_{buoy} = Fd^2 \frac{v}{\kappa} \hat{L}_{buoy}, \quad (4.32)$$

$$L_{diss} = \frac{\rho_0 v^2}{d^2} \frac{v}{d^2} d^3 \hat{L}_{diss} = \frac{\rho_0 v^3}{d} \hat{L}_{diss}, \quad (4.33)$$

where,

$$\hat{L}_{conv} = \int_{S_z'} \hat{\bar{\rho}} \hat{T} \hat{s} \hat{w} d\hat{S}, \quad (4.34)$$

$$\hat{L}_{cond} = \int_{S_z'} -\hat{\bar{\rho}} \hat{T} \frac{\partial \hat{s}}{\partial \hat{z}} d\hat{S}, \quad (4.35)$$

$$\hat{L}_{buoy} = \int_{V_z'} -\hat{s} \hat{\bar{\rho}} \hat{w} \frac{\partial \hat{T}}{\partial \hat{z}} d\hat{V}, \quad (4.36)$$

$$\hat{L}_{diss} = \int_{V_z'} -\hat{\tau}_{ij} \frac{\partial \hat{u}_i}{\partial \hat{x}_j} d\hat{V}, \quad (4.37)$$

and additionally note that we can non-dimensionalise the total luminosity  $L$  by  $L = Fd^2 \hat{L}$ . Dividing through by  $Fd^2$ , dropping the hat notation, and assuming all variables are now their non-dimensional versions,

$$L = \frac{\nu}{\kappa} L_{conv} + L_{cond} + \frac{\nu}{\kappa} L_{buoy} + \frac{\rho_0 \nu^3}{Fd^3} L_{diss}, \quad (4.38)$$

or rather,

$$L = Pr L_{conv} + L_{cond} + Pr L_{buoy} + \frac{Pr^2 \theta}{Ra} L_{diss}. \quad (4.39)$$

Alternatively, if we consider the total energy equation (3.46), we can obtain a different (but equivalent) flux decomposition.

$$L = \int_{S_z'} \bar{\rho} c_p w T' dS + \int_{S_z'} -\kappa \bar{\rho} \bar{T} \frac{\partial s}{\partial z} dS + \int_{S_z'} \frac{1}{2} \bar{\rho} |\mathbf{u}^2| w dS + \int_{S_z'} -(\tau_{ij} u_i) \cdot \hat{\mathbf{e}}_z dS \quad (4.40)$$

where the four terms represent the enthalpy ( $L_e$ ), conductive ( $L_{cond}$ ), kinetic energy ( $L_{KE}$ ), and viscous ( $L_{visc}$ ) luminosities.  $T'$  is defined as,

$$T' = \frac{1}{c_p} (\bar{T}s + \tilde{P}). \quad (4.41)$$

This allows us to express  $L_e$  as follows,

$$L_e = \int_{S_{z'}} \bar{\rho} \bar{T} s w dS + \int_{S_{z'}} \bar{\rho} w \tilde{P} dS, \quad (4.42)$$

(4.43)

where the first integral is our previously encountered  $L_{conv}$ , and the second integral is the pressure dilatation,  $L_p$ , (see Viallet et al. 2013). The new luminosities are therefore,

$$L_p = \int_{S_{z'}} \bar{\rho} w \tilde{P} dS, \quad (4.44)$$

$$L_{KE} = \int_{S_{z'}} \frac{1}{2} \bar{\rho} |\mathbf{u}^2| w dS, \quad (4.45)$$

$$L_{visc} = \int_{S_{z'}} -(\tau_{ij} u_i) \cdot \hat{\mathbf{e}}_z dS, \quad (4.46)$$

which after applying a similar non-dimensionalisation as before can be written as,

$$L_p = \rho_0 \frac{v}{d} \frac{\nu^2}{d^2} d^2 \hat{L}_p = \frac{\rho_0 \nu^3}{d} \hat{L}_p, \quad (4.47)$$

$$L_{KE} = \rho_0 \frac{\nu^2}{d^2} \frac{v}{d} d^2 \hat{L}_{KE} = \frac{\rho_0 \nu^3}{d} \hat{L}_{KE}, \quad (4.48)$$

$$L_{visc} = \frac{\rho_0 \nu^2}{d^2} \frac{v}{d} d^2 \hat{L}_{visc} = \frac{\rho_0 \nu^3}{d} \hat{L}_{visc}, \quad (4.49)$$

where the non-dimensional luminosities are defined as,

$$\hat{L}_p = \int_{S_z'} \hat{\rho} \hat{w} \hat{P} d\hat{S}, \quad (4.50)$$

$$\hat{L}_{KE} = \int_{S_z'} \frac{1}{2} \hat{\rho} |\hat{\mathbf{u}}|^2 \hat{w} d\hat{S}, \quad (4.51)$$

$$\hat{L}_{visc} = \int_{S_z'} -(\hat{\tau}_{ij} \hat{u}_i) \cdot \hat{\mathbf{e}}_z d\hat{S}. \quad (4.52)$$

Dividing out the factor of  $Fd^2$  from  $L = Fd^2 \hat{L}$  and once again dropping our hat notation and assuming all variables to be non-dimensional, we have,

$$L = \frac{\nu}{\kappa} L_{conv} + \frac{\rho_0 \nu^3}{Fd^3} L_p + L_{cond} + \frac{\rho_0 \nu^3}{Fd^3} L_{KE} + \frac{\rho_0 \nu^3}{Fd^3} L_{visc}, \quad (4.53)$$

$$L = Pr L_{conv} + \frac{Pr^2 \theta}{Ra} L_p + L_{cond} + \frac{Pr^2 \theta}{Ra} L_{KE} + \frac{Pr^2 \theta}{Ra} L_{visc}. \quad (4.54)$$

### 4.3 An aside on timescales

An important question to ask is, what is a relevant timescale for particular features to evolve? The governing equations outlined in Section 4.1 have been non-dimensionalised by our viscous timescale. That is,

$$\tau_\nu = \frac{d^2}{\nu}, \quad (4.55)$$

where  $d$  is the fluid depth and  $\nu$  is the viscous diffusivity as before. This is the unit of time. An example of a quantity that evolves on this timescale in non-rotating cases is the dissipative flux,  $L_{diss}$ , given by equation (4.27). As seen in Figure 4.2 the vertical profile of  $L_{diss}$  converges to an equilibrium at simulation times of  $t \simeq \tau_\nu$ .

Another relevant timescale is instead the thermal timescale, defined as,

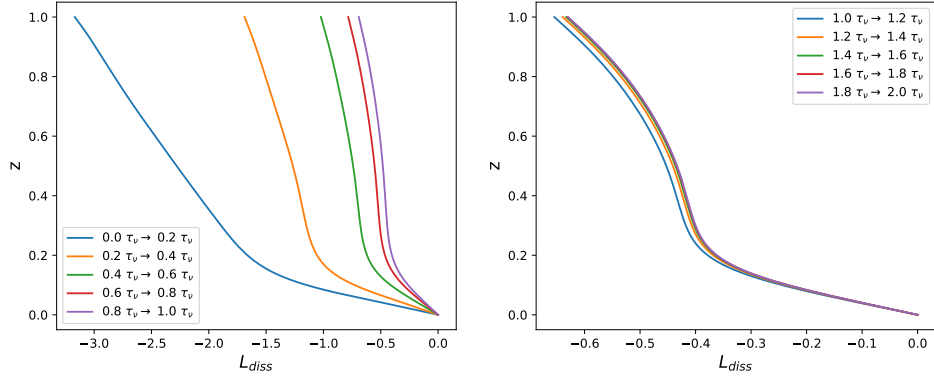


**Figure 4.2:** Vertical profiles of  $L_{diss}$  taken from a typical non-rotating convective simulation, with  $\text{Ra} = 1\text{e}5$ ,  $\text{Pr} = 1$ ,  $\text{Ta} = 0$ ,  $N_p = 1$ . Each is averaged over  $0.2 \tau_v$  at a range of points during the simulation. The plot is split across two panels for ease of x-axis scaling.

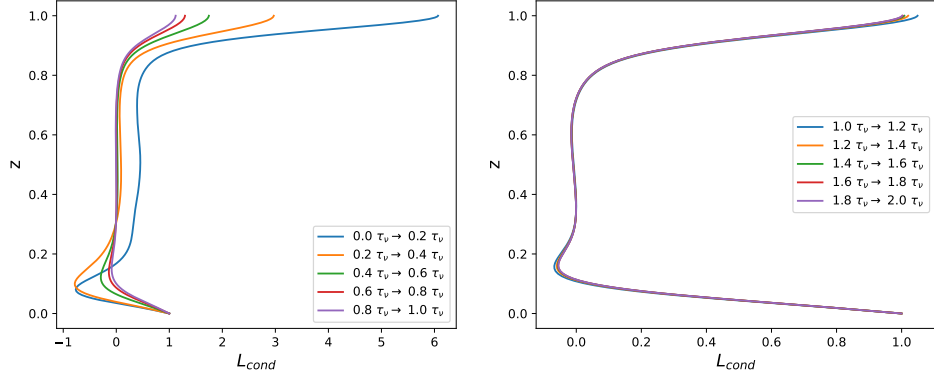


**Figure 4.3:** Vertical profiles of  $L_{cond}$  taken from a typical non-rotating convective simulation.  $\text{Ra} = 1\text{e}5$ ,  $\text{Pr} = 1$ ,  $\text{Ta} = 0$ ,  $N_p = 1$ . Each is averaged over  $0.2 \tau_\kappa$  at a range of points during the simulation. The plot is split across two panels for ease of x-axis scaling.

$$\tau_\kappa = \frac{d^2}{\kappa}. \quad (4.56)$$

where  $\kappa$  is our thermal diffusivity. As introduced in Section 2.2.3 the ratio of these two timescales is given by the Prandtl number  $\text{Pr}$ , which for the majority of this work fixed at unity, however Section 4.5.1 will demonstrate how varying this parameter can result in certain features and quantities of the flow evolving on different timescales. A quantity that typically evolves on the thermal timescale is the conductive flux,  $L_{cond}$ , given by equation (4.25). This can be seen in Figure 4.3 where the vertical profiles of  $L_{cond}$  converge at simulation times of  $t \simeq \tau_\kappa$ .

Another relevant timescale in this work is the convective turnover time, which physically

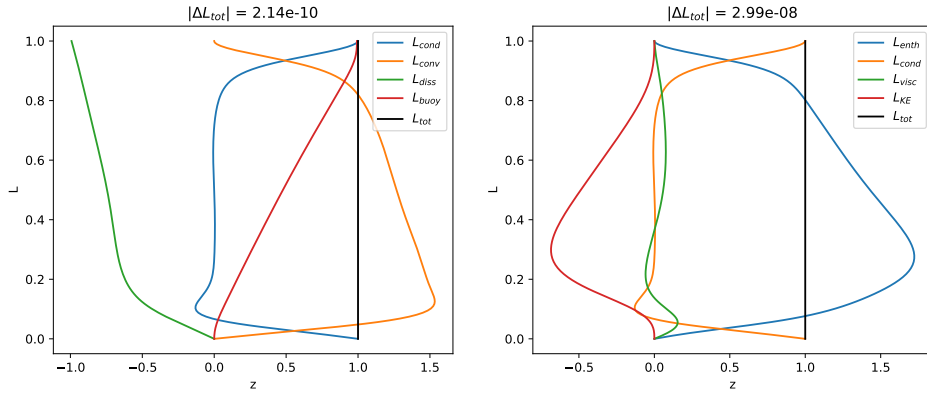


**Figure 4.4:** An example plot of a equilibrated flux plot is shown for non-rotating convection with,  $\text{Ra}/\text{Ra}_c = 10^3$ ,  $N_p = 1.4$ , and  $\text{Pr} = 1$ .

is defined as the time it takes for parcel of convecting fluid to rise from across our domain.

Explicitly, this is,

$$\tau_{conv} = \frac{d}{U}, \quad (4.57)$$

where  $U$  is a typical velocity scale. Recalling the Reynolds number,  $\text{Re}$ , from the previous discussion in Section 2.2.7, specifically equation (2.39), the convective turnover time,  $\tau_{conv}$ , can expressed in terms of the viscous timescale  $\tau_\nu$ . That is,

$$\tau_{conv} = \frac{d}{U} = \frac{\nu}{dU} \frac{d^2}{\nu} = \frac{\tau_\nu}{\text{Re}}. \quad (4.58)$$

This states that for a more turbulent flow, and therefore higher  $\text{Re}$ , the convective turnover time is significantly smaller than the our viscous timescale.

## 4.4 Flux balance

As the systems dynamical and thermal structures evolve on different timescales, we must define an appropriate point at which a simulation can be classified as sufficiently evolved. For the calculations presented in Chapters 4 and 5, this point is typically taken as being when the simulation has achieved flux balance. That is, when averaged over a sufficiently large time period both equation (4.23) and equation (4.40) equal unity. As demonstrated

in the previous section the required length of time varies based upon the parameter space, especially with the Prandtl number. Qualitatively flux balance is achieved when the black line representing  $L_{tot}$  is vertically straight at unity. Quantitatively, a measure that can be used is  $|\Delta L_{tot}| = |L_{tot} - 1|_m$ , where the subscript  $m$  indicates the maximum value in the vertical domain and so  $|\Delta L_{tot}|$  represents the largest deviation that occurs anywhere in the simulated domain of  $L_{tot}$  from 1. Values of  $|\Delta L_{tot}| \leq 10^{-2}$  are taken to be sufficiently equilibrated. This is shown schematically in Figure 4.4. It is worth noting that due to having two equations for our total flux, (4.23) and (4.40), we have two ways of calculating  $|\Delta L_{tot}|$ . As they are composed of different fluxes which themselves may evolve on different timescales, they can result in different values of  $|\Delta L_{tot}|$  however the constraint for flux balance is set on both formulations.

## 4.5 Convective structure

As shown in Section 4.1 the system is fully described by the collection of non-dimensional parameters, Ra, Pr,  $N_p$ , and Ta, and the polytropic index,  $m$ . The rest of this chapter will be dedicated towards exploring this parameter space and discussing the various effects these parameters have on convection. In particular we will focus on the Rayleigh number, Ra, the Taylor number, Ta, and the degree of stratification,  $N_p$ . The polytropic index will be held at  $m = 1.5$ , and with the exception of Section 4.5.1 the Prandtl number, Pr, will be fixed at unity.

Once a simulation has achieved sufficient equilibrium the dynamical structure of the convection can be clearly seen (see Figure 4.5). The first panel shows the total entropy of the fluid whereas the second and third panels show the horizontal and vertical velocities respectively. The fluid has formed into a singular convective cell (common for 2D geometry, see Hepworth 2014 for one example) where the velocity fields show typical convective structures in the form of rising hot flows and descending cold flows with connecting horizontal motions at the top and bottom boundaries.

As seen in Section 2.2.7, the Reynolds number, Re, is a measure of the turbulent nature of the flow. It quantifies the relative strength of the inertial and viscous forces.

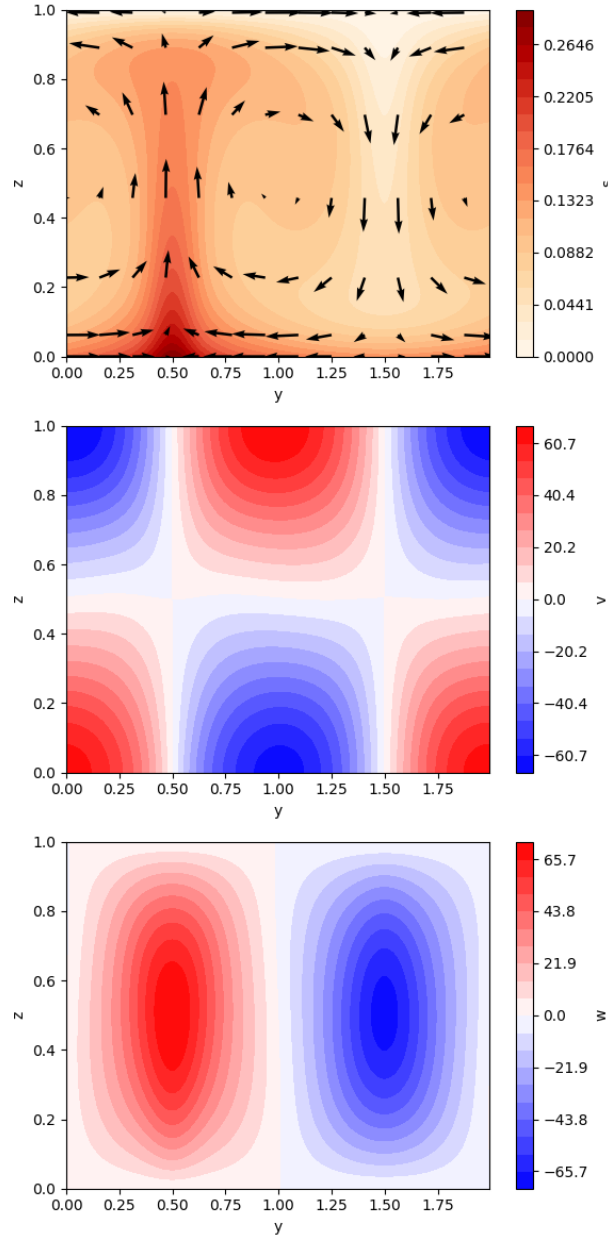


**Figure 4.5:** A snapshot of the convective structure for a non-rotating, unstratified fluid with  $\text{Ra}/\text{Ra}_c = 10^2$ ,  $N_p = 0$ , and  $\text{Pr} = 1$ . The first panel shows the total entropy structure of the fluid domain with the direction of the fluid motion indicated with streamline arrows. The second and third panels show the individual horizontal and vertical components of the velocity fields respectively. As the horizontal boundaries are periodic, the plots have been horizontally re-scaled so that the main features of the convection are centralised.

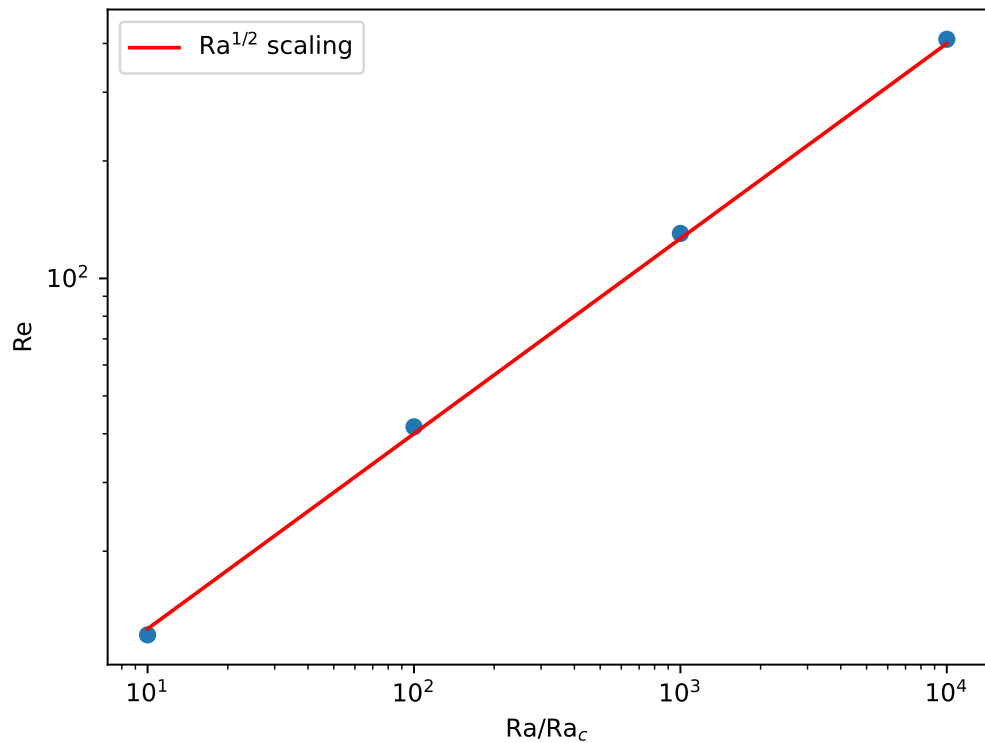


**Figure 4.6:** Values of mean Reynolds number for a range of non-rotating ( $\text{Ta} = 0$ ), unstratified ( $N_\rho = 0$ ), convective simulations at  $\text{Pr} = 1$  and a range of  $\text{Ra}/\text{Ra}_c$ . Increasing the supercriticality shows a clear trend in increasing the resulting Reynolds number, that is, the flow becomes less laminar and more turbulent in nature.

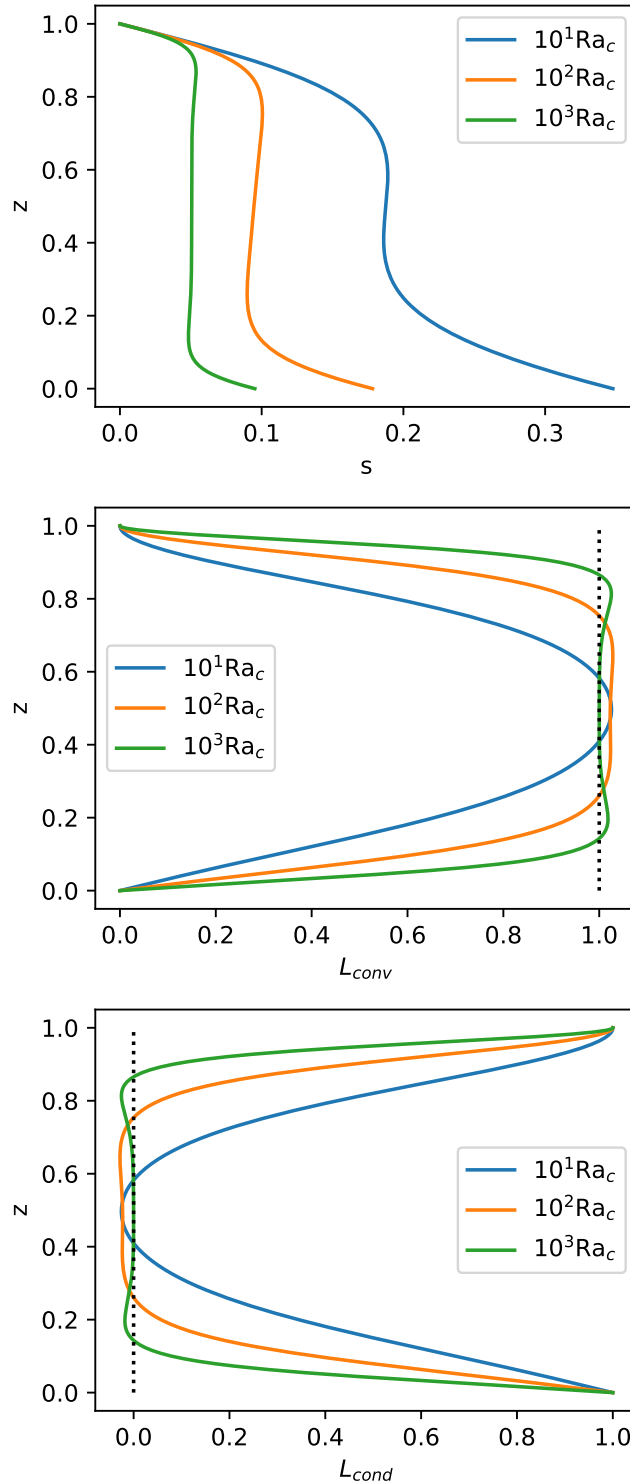


**Figure 4.7:** Vertical profiles of the horizontally averaged total entropy (top), the convective flux (middle), and conductive flux (bottom), in non-rotating ( $\text{Ta} = 0$ ), unstratified ( $N_\rho = 0$ ,) convective simulations at  $\text{Pr} = 1$  and a range of supercriticality. The convective and conductive flux profiles have been overplotted (black dotted) with the bulk values expected from sufficiently stratified convection (1 and 0 respectively).

Generally low values of  $\text{Re}$  correspond to slow moving, viscous motions whereas larger  $\text{Re}$  tends towards more turbulent and faster fluid motions. It follows then, that for increasing  $\text{Ra}/\text{Ra}_c$  (that is, increasing the buoyancy forcing provided to the system relative to the dissipative effects present and scaled by a measure of its convective stability,  $\text{Ra}_c$ ), the value of  $\text{Re}$  would also increase. This is seen clearly in Figure 4.6. The  $\text{Re}-\text{Ra}$  scaling observed in Figure 4.6 is in good agreement with the scaling  $\text{Re} \sim \text{Ra}^{1/2}$  arising from the so-called "VAC" (viscous-Archimedean-Coriolis) balance (see discussions in Hepworth 2014, Gastine et al. 2016, for examples).

It is worth noting that in unstratified cases where  $N_\rho$  and therefore  $\theta$  are zero, the flux equations (4.39) and (4.54) reduce to,

$$L_{tot} = \text{Pr}L_{conv} + L_{cond}. \quad (4.59)$$

Therefore, once the system is sufficiently equilibrated the flux balance is entirely between the conductive and convective heat fluxes. The effect of increasingly turbulent convection can be seen in Figure 4.7. As the fluid becomes more thoroughly mixed through more efficient convection the fluid bulk becomes more and more isentropic. This can be seen in the horizontally averaged total entropy profiles shown in the first panel of Figure 4.7. Additionally, this increase in convective efficiency results in more of the energy transport being performed provided by convective motions rather than conductive effects. This change can be seen in the second and third panels. It can also be seen from equation (4.59) that this balance is dependent on the Prandtl number.

### 4.5.1 Varying Prandtl number

Recall that the Prandtl number,  $\text{Pr}$ , is the ratio of viscous to thermal diffusivities, that is,

$$\text{Pr} = \frac{\nu}{\kappa}. \quad (4.60)$$

It has long been established in prior literature that  $\text{Ra}_c$  is independent of  $\text{Pr}$  (Chandrasekhar

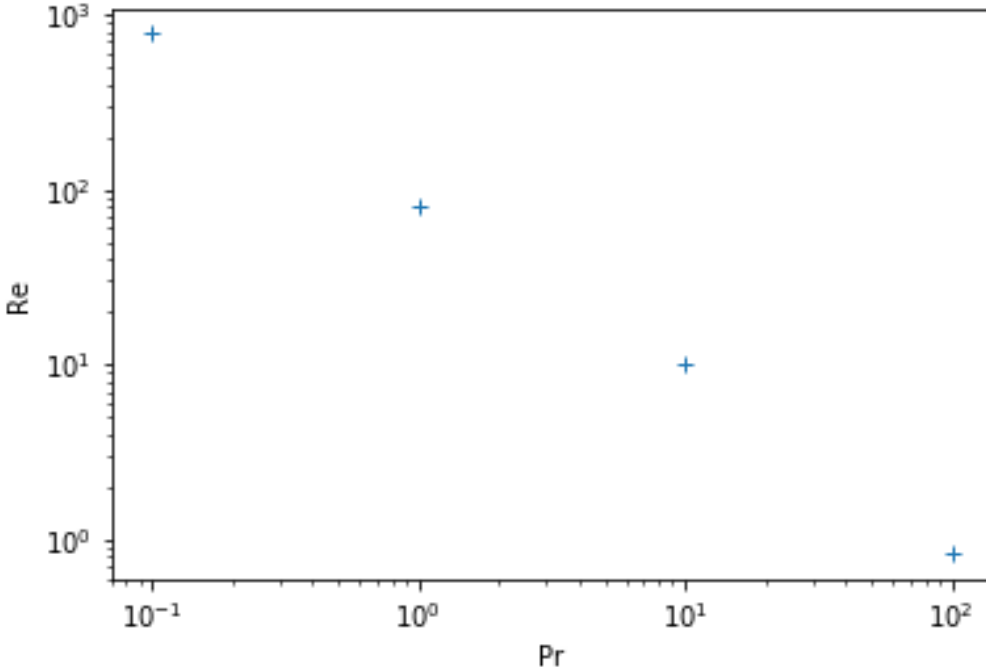


**Figure 4.8:** Values of mean Reynolds number for a range of non-rotating convective simulations with  $\text{Ra} = 1\text{e}5$ ,  $N_p = 1$ ,  $\text{Ta} = 0$ , for a range of  $\text{Pr}$ . Increasing Prandtl number shows a clear trend away from turbulent flows and towards more laminar convection.

1961). This means that for a given stratification ( $N_p$ ) or rotation rate (Ta), the supercriticality of the flow remains unchanged. Increasing Pr for a fixed supercriticality results in a larger viscous diffusivity relative to thermal diffusivity and can be viewed as essentially increasing the viscosity of our fluid and resulting in more laminar flows (note that in the infinite Pr limit, the inertial term is identically zero). This is quantified in our Reynolds number and can be seen in Figure 4.8.

One way to view these relationships is that by increasing the supercriticality the result is to increase the typical velocity scale,  $u$ , whereas increasing Pr has the effect of increasing  $v$ . Their relationships with Re then follow from equation (2.39) and can be seen in Figures 4.6 & 4.8. Much like how increasing the supercriticality results in more efficient convection and a shift in the flux balance towards convective heat transport, increasing Pr results in a more viscous, and laminar fluid flow that swings the balance back towards stronger conductive energy transport. This can be seen more quantitatively by rearranging (4.59) at  $L_{tot} = 1$ ,

$$L_{conv} = \frac{1 - L_{cond}}{\text{Pr}}, \quad (4.61)$$

where  $L_{conv} \propto \text{Pr}^{-1}$ .

### 4.5.2 Stratification

This section will discuss the effects of introducing density stratification to the fluid. As discussed in Section 4.1, the degree of stratification is given by the number of density scale heights across the fluid layer,  $N_\rho$ . This is given by the equation (4.7). Another quantity used to measure this same degree of stratification and that is commonly used in this work is  $\theta$ , a non-dimensional thermal scale height which is directly related to  $N_\rho$  by the equation  $N_\rho = -m \ln(1 - \theta)$ . Importantly, the system reduces to an unstratified one at  $N_\rho = \theta = 0$ .

One thing to immediately note is that by the inclusion of stratification, a number of additional energy transport terms are now present in the overall flux balance equations (4.39) and (4.54). In the internal energy flux decomposition, (4.39), there is now a buoyancy term,  $L_{buoy}$  representing the work done against the stratification, and a dissipative term  $L_{diss}$ , that represents the portion of the overall viscous forces that act to deform and heat a fluid parcel. In the unstratified case, there is no background stratification to work against,  $\theta = 0$  and so  $\bar{T} = 1$ , and it follows from equation (4.26) that,

$$L_{buoy} = \text{Pr} \int_{V_z'} -s \bar{\rho} w \frac{\partial \bar{T}}{\partial z} dV = \text{Pr} \int_{V_z'} -s \bar{\rho} w \frac{\partial(1)}{\partial z} dV = \text{Pr} \int_{V_z'} -s \bar{\rho} w(0) dV = 0. \quad (4.62)$$

Additionally  $L_{diss}$  contains a factor of  $\theta$  and so is identically zero. For stratified cases where  $\theta \neq 0$ ,  $L_{buoy}$  and  $L_{diss}$  must cancel when averaged over the entire domain. To see this, take the internal energy equation (3.47), assume a steady state, and integrate over the volume  $V$ . This yields,

$$\int_V (\mathbf{u} \cdot \nabla) P dV + \Phi = 0, \quad (4.63)$$

where,

$$\Phi = \int_V \tau_{ij} \frac{\partial u_i}{\partial x_j} + \frac{j^2}{\sigma} dV, \quad (4.64)$$

is the total dissipative heating. Note for the cases in this chapter the electric current,  $j$  is taken to be zero and only hydro-cases are considered. Then using the first law of thermodynamics,

$$Tds = de - \frac{P}{\rho^2} d\rho, \quad (4.65)$$

and mass continuity in a steady state,

$$\nabla \cdot (\rho \mathbf{u}) = 0, \quad (4.66)$$

we can rewrite equation (4.63) as,

$$\int_V \rho s(\mathbf{u} \cdot \nabla) T dV + \int_V \tau_{ij} \frac{\partial u_i}{\partial x_j} dV = 0. \quad (4.67)$$

These two integrals are equivalent to  $L_{buoy}$  and  $L_{diss}$  evaluated at  $z' = d$ , that is, equations (4.26) and (4.27) respectively. While these two energy transport terms must cancel globally, they do not necessarily cancel at individual fluid layers, and so can affect the balance between  $L_{conv}$  and  $L_{cond}$  that is present in unstratified convection.

In the total energy flux decomposition (4.54) there are three additional integrals to consider in the regime of  $\theta > 0$ . These are the kinetic energy flux  $L_{KE}$ , the viscous flux  $L_{visc}$ , and a "pressure flux"  $L_p$  which itself is the difference between the enthalpy flux  $L_e$  and  $L_{conv}$ . Note that  $L_{visc}$  differs from  $L_{diss}$  in that  $L_{diss}$  represents the total work done by all surface forces whereas  $L_{visc}$  is only the portion of this that acts to deform the fluid. Deconstructed in this way, there is an equivalency between the "other" fluxes that are present in the overall energy balance from both the internal energy and total energy

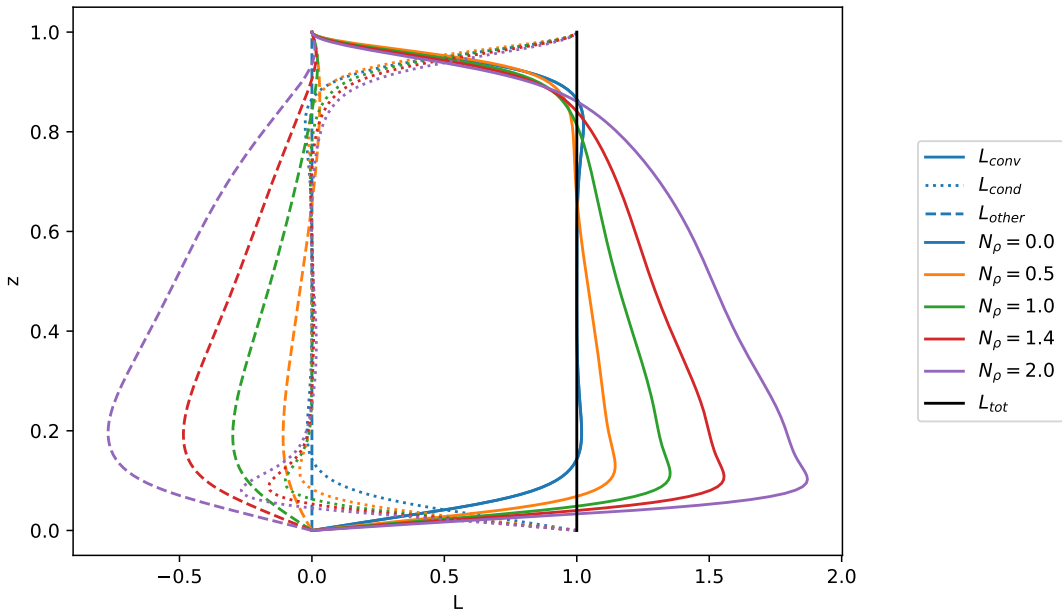


**Figure 4.9:** A comparison plot of the flux balance for four different non-rotating convective simulations with  $\text{Ra}/\text{Ra}_c = 1.78 \times 10^3$ ,  $\text{Pr} = 1$ , and values of  $N_\rho = 0.5, 1.0, 1.4$ , and  $2.0$ . The solid colour, dotted, and dashed lines represent the convective, conductive, and "other" energy transport terms where  $L_{\text{other}}$  is given by  $L_{\text{other}} = L_{\text{diss}} + L_{\text{buoy}} = L_p + L_{\text{KE}} + L_{\text{visc}}$  and encapsulates the additional transport terms present due to the influence of stratification. The solid black line represents the overall sum of all energy transport terms,  $L_{\text{tot}}$ .

decomposition's, in that,

$$L_{\text{buoy}} + L_{\text{diss}} = L_p + L_{\text{KE}} + L_{\text{visc}}. \quad (4.68)$$

As can be seen in Figure 4.9 as the stratification of the system increases (increasing  $N_\rho$ ) the energy transport shifts away from the balance between  $L_{\text{cond}}$  and  $L_{\text{conv}}$  that is present in the unstratified cases and due to the increasingly larger influence of  $L_{\text{other}}$  results in primarily changing the profile of the convective flux. The conductive flux profile also varies however this is mainly concentrated in the boundary layers and  $L_{\text{cond}}$  remains approximately zero throughout the bulk of the fluid.

The horizontally averaged entropy structure of the fluid is similarly affected by the introduction of stratification as can be seen in Figure 4.10. As  $L_{\text{cond}} \propto \frac{\partial s}{\partial z}$  the general structure is largely unchanged much like  $L_{\text{cond}}$ . The profile in the bulk appears largely unchanged, remaining mostly isentropic throughout the layer, however there are some important features to note. Firstly, increasing  $N_\rho$  appears to lead to "less efficient" trans-

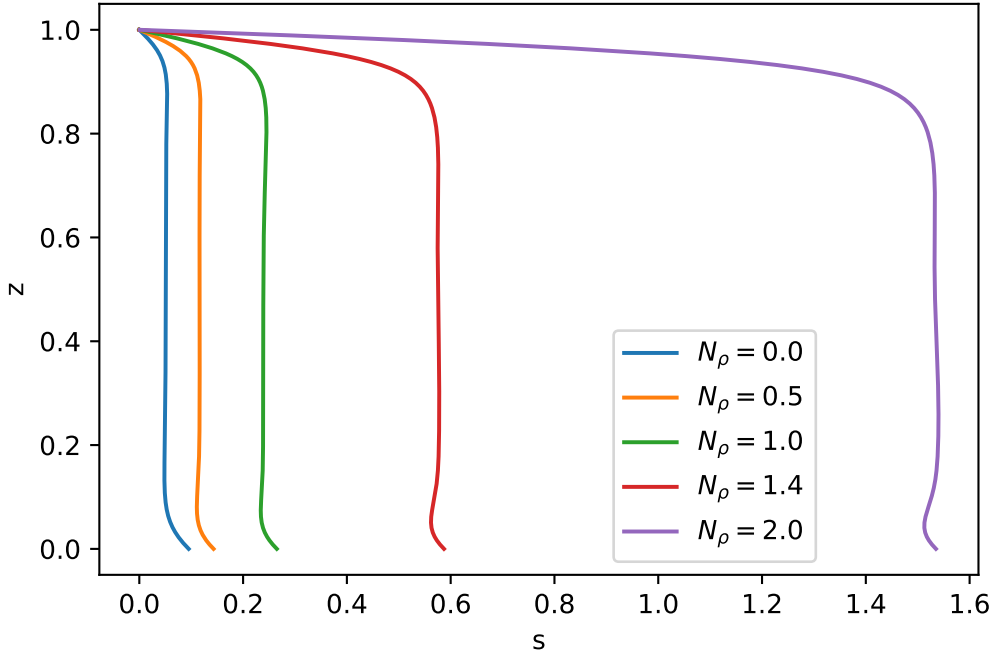


**Figure 4.10:** A comparison plot of the horizontally averaged entropy profiles for four different non-rotating convective simulations with  $\text{Ra}/\text{Ra}_c = 1.78 \times 10^3$ ,  $\text{Pr} = 1$ , and values of  $N_\rho = 0.5, 1.0, 1.4$ , and  $2.0$ .

port, that is, a somewhat larger  $\Delta s$  across the layer, the majority of which is confined to the upper boundary layer, which itself has also grown in size. Near the bottom boundary layer however a sub-adiabatic layer has formed the extent of which appears to depend upon the stratification. This feature has previously been seen in a variety of settings (Korre et al. 2019, Käpylä et al. 2019).

Another feature of introducing stratification is the change to the shape of the convection itself. There is a resulting broadening of the upwelling plumes of hot fluid, which due to the stratification expands into the surrounding less dense medium. Similarly, the cold downward directed plumes contract as they descend. For increasingly stratified systems this results in broad upflows which dominate the horizontal extent of the domain, and returning narrow downflows. Additionally there is a similar change in the height at which the horizontal motions experience a sign change (approximately corresponding to the “midplane” of a convective cell). That is, the horizontal motions in the upper portion of the domain have broadened vertically (they extend across more of the vertical domain) and those in the deeper portion have narrowed. These changes can be seen in Fig-

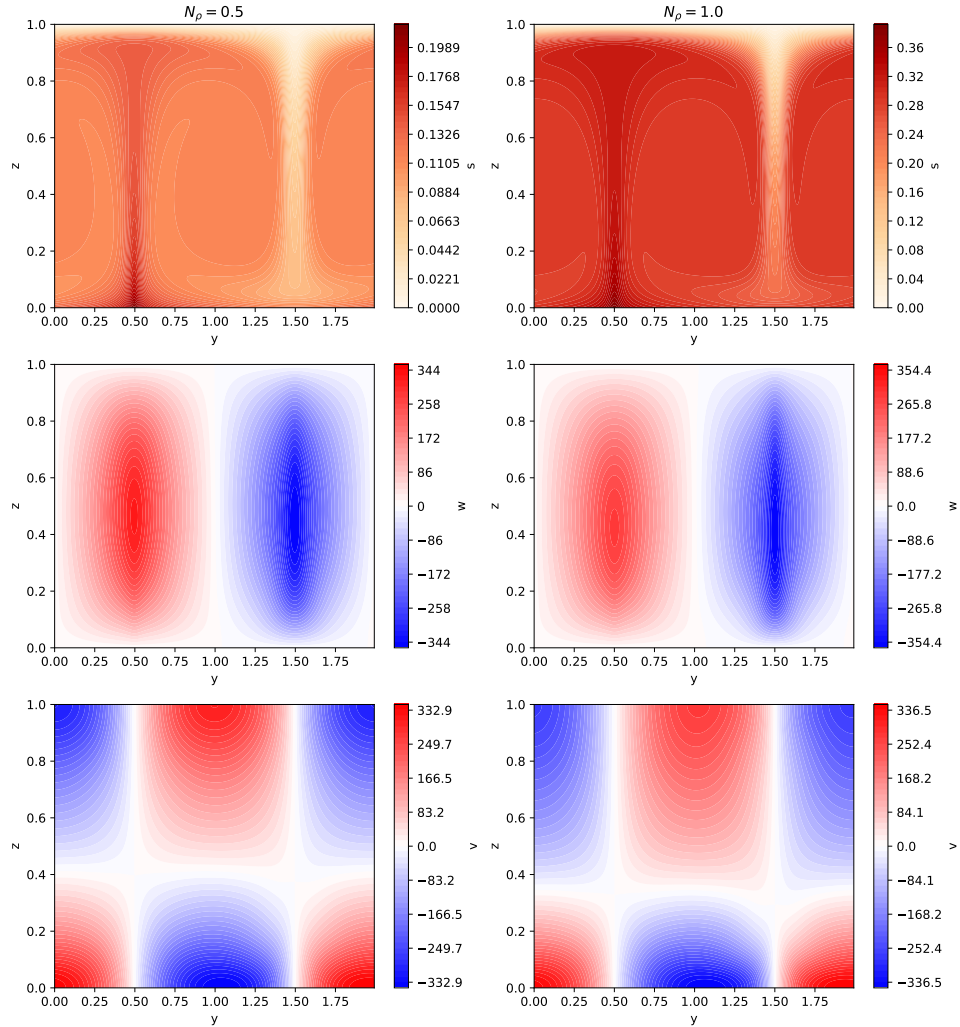


**Figure 4.11:** A comparison of the full fields of the total entropy, vertical component of the velocity, and horizontal component of the velocity (top, middle, and bottom rows respectively) for non-rotating convective simulations with  $\text{Ra}/\text{Ra}_c = 1.78 \times 10^3$ ,  $\text{Pr} = 1$ , and values of  $N_\rho = 0.5$  (left column) and  $1.0$  (right column).

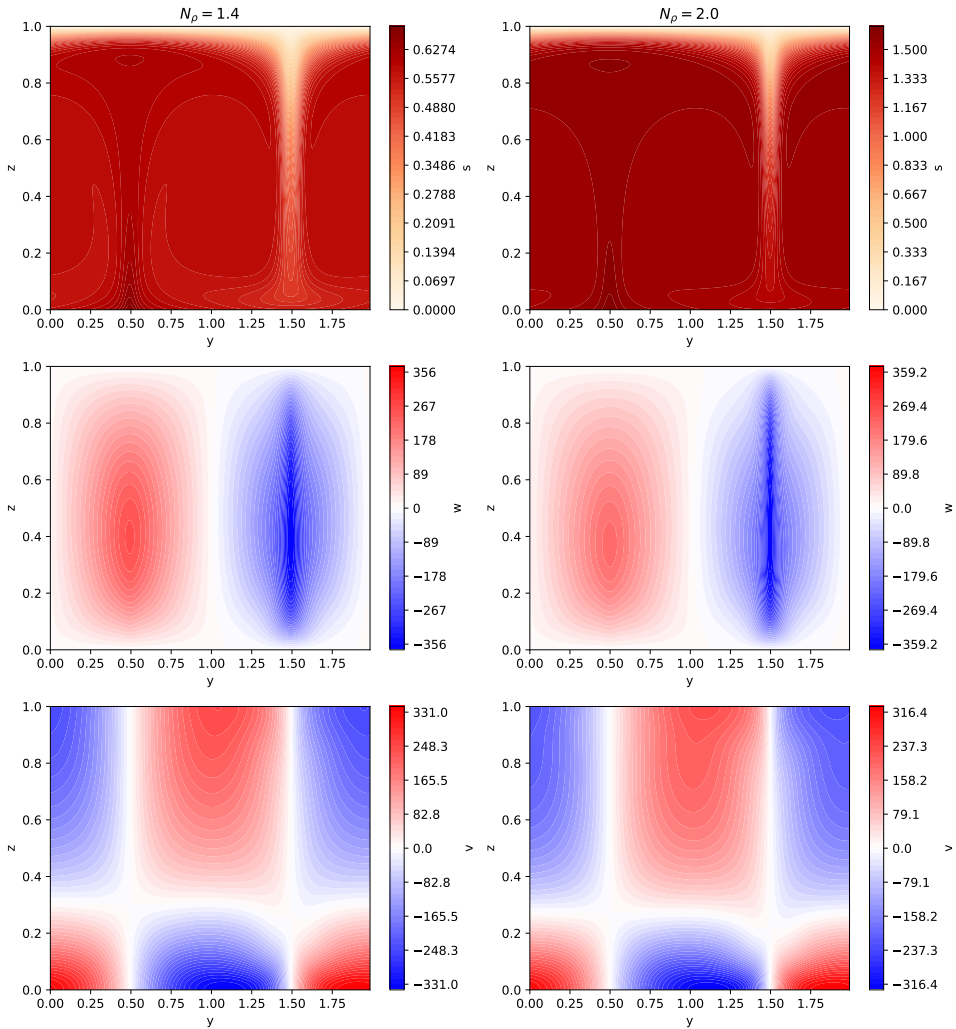


**Figure 4.12:** A comparison of the full fields of the total entropy, vertical component of the velocity, and horizontal component of the velocity (top, middle, and bottom rows respectively) for non-rotating convective simulations with  $\text{Ra}/\text{Ra}_c = 1.78 \times 10^3$ ,  $\text{Pr} = 1$ , and values of  $N_\rho = 1.4$  (left column) and  $2.0$  (right column).

ures 4.11 and 4.12 where the entropy field is shown along with the vertical and horizontal components of velocity for a range of increasing values of  $N_p$ .

Along with the shape of these flows changing, so too have the strength of these flows. The top panel of Figure 4.13 shows relative difference between the velocities of the upwelling and downwelling fluids whereas the bottom panel shows a similar difference for the horizontal motions. The broadening and narrowing of these convective motions can also be seen in Figure 4.13.

### 4.5.3 Varying Taylor number

The rotation rate can be varied by changing the Taylor number,  $Ta$ , which as shown in 2.2.5 is defined as,

$$Ta = \frac{4\Omega^2 d^4}{\nu^2}. \quad (4.69)$$

Recall from Section 2.2.5, the Taylor number  $Ta$  is analogous to the Ekman number,  $Ek$ , another commonly used dimensionless quantity for characterising the strength of rotational forces to viscous effects. This relation is given by  $Ek = Ta^{-1/2}$ . Another important relation of  $Ta$  is its effect on the critical Rayleigh number,  $Ra_c$ . It follows from linear theory (see Chandrasekhar 1961 for more details) that  $Ra_c \propto Ta^{2/3}$ . This result was used to verify the validity of the solutions from the linear stability code that produced the  $Ra_c$  values. As can be seen in Figure 4.14, there is a clear  $Ra_c \propto Ta^{2/3}$  relation.

As discussed in Chapter 2 for significantly high values of  $Ta$  the fluid flow becomes rotationally constrained and forms Taylor-Proudmann-like features. These are where the convective cells become tilted and align themselves with the rotational axis, instead of with the direction of gravity. To understand whether a given system is rotationally constrained we turn to the Rossby number (see 2.2.6). The Rossby number characterises the importance of rotation in a fluid by measuring the ratio of inertial forces to Coriolis ones, more explicitly,

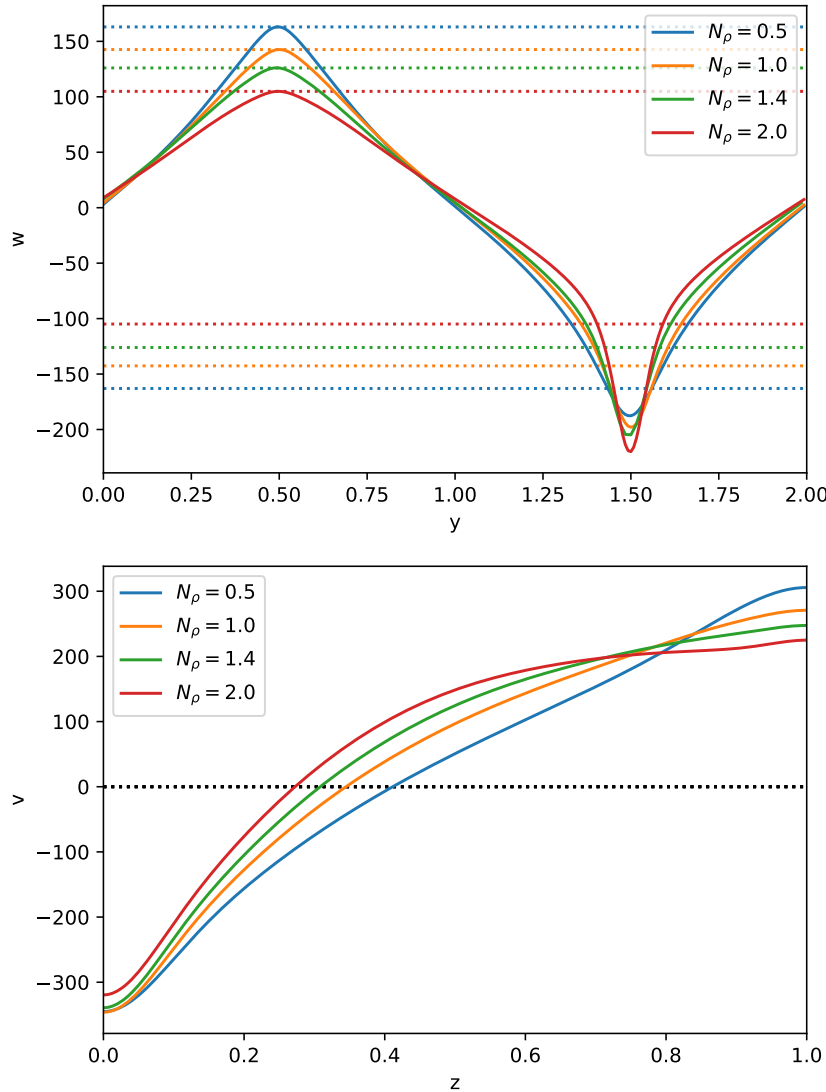


**Figure 4.13:** A two panel plot showing different velocity profiles for four different non-rotating convective simulations with  $\text{Ra}/\text{Ra}_c = 1.78 \times 10^3$ ,  $\text{Pr} = 1$ , and values of  $N_\rho = 0.5, 1.0, 1.4$ , and  $2.0$ . The first panel shows the column averaged vertical component of the velocity fields. The solid lines represent the actual values of  $w$  whereas the dashed lines represent the peak value and its negative mirror for the purpose of highlighting the asymmetry in the peak velocity values of the upflows and downflows. The second panel shows a slice of the horizontal component of the velocity,  $v$ , taken at the middle of a convective cell ( $y = 1$ ) with the dashed black line representing zero horizontal motion.

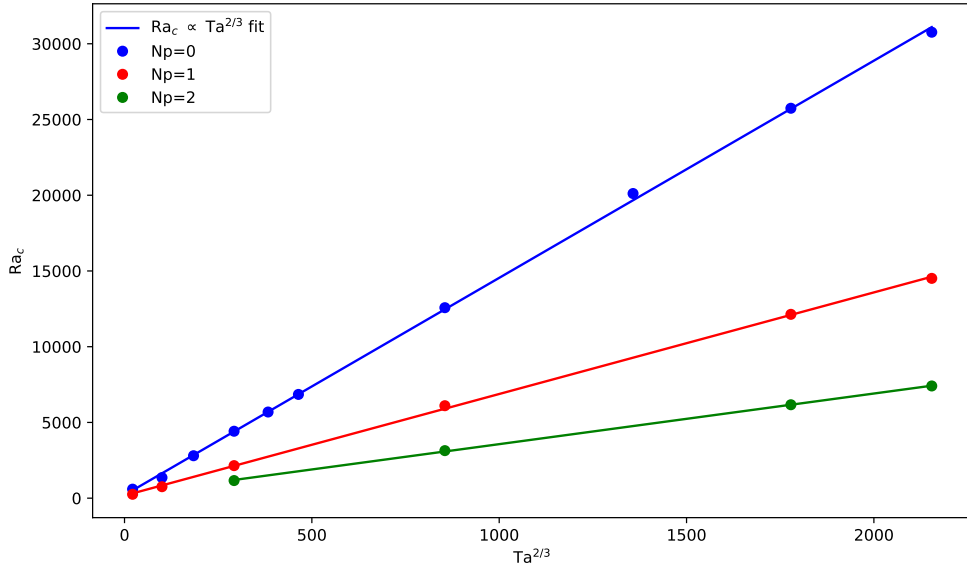


**Figure 4.14:** Results of the EVP outputs of  $\text{Ra}_c$  for increasing  $\text{Ta}$  at  $N_\rho = 0, 1, 2$  in blue, red, and green respectively. The circles are the exact outputs from the EVP with the lines representing linear regression fits with corresponding Pearson correlation coefficients of 0.9998, 0.9998, and 0.9999 for  $N_\rho = 0, 1, 2$  respectively.

$$\text{Ro} = \frac{(\mathbf{u} \cdot \nabla) \mathbf{u}}{|2\boldsymbol{\Omega} \times \mathbf{u}|}. \quad (4.70)$$

However, for the model setup described in Section 4.1 this is an output of a simulation, and so cannot be used to inform the initial parameter choice of the simulation if a specific degree of rotational influence and supercriticality is desired. The Taylor number is unsuitable here as it itself interacts with the critical Rayleigh number (as seen in Figure 4.14) and in turn varies the supercriticality. A commonly used proxy for characterising the degree of rotational influence is instead the convective Rossby number,  $\text{Ro}_c$  (Gilman 1977). This is given by,

$$\text{Ro}_c = \sqrt{\frac{\text{Ra}}{\text{PrTa}}}. \quad (4.71)$$

As will be explored in the subsequent section, the degree of rotational constraint has a significant impact on not only the resulting structure of convection, but the distribution of dissipation throughout the convective layer, which in turn appears to influence the overall

heat transport.

## 4.6 Chapter summary

This chapter presented a suite of convection simulations produced using the non-linear, anelastic, and rotating convective code introduced in Chapter 3. It began with the introduction of the the 2.5D geometry required for incorporating rotation in a 2D domain, before going on to detailing some of the typical outputs of the flow used to quantify the energy transport and flow regime. We discussed how these properties vary with the inclusion of stratification, setting the scene for the inclusion of rotation in Chapter 5. Particular features of note that are highlighted here are the breaking of vertical symmetry as a result of the system's stratification, and the stabilisation of the system by rotation (higher rotation rate resulting in a higher  $\text{Ra}_c$ ).

## Chapter 5

# Viscous Dissipation and Dynamics in Rotating, Stratified Convection

Chapter 1 introduced some of the astrophysical flows that are present within stars and planets, and highlighted some of the currently outstanding puzzles that remain in these fields. Chapter 2 then proceeded to outline some of the theoretical background relevant to the study of these flows. This was built upon in Chapter 3 where some numerical approaches to studying these fluids were presented, and then Chapter 4 used these preceding methods to establish a numerical code for studying stratified convection in a rotating Cartesian box, as well as presenting some typical results. With this groundwork established, this Chapter will now look at the magnitude and effects of viscous dissipation in highly stratified convection using a range of 2D simulations on rotating planes at various latitudes.

### 5.1 Introduction

The convection that occurs within the interiors of every main-sequence star and planet must, in a steady state, be maintained against viscous and Ohmic dissipation. In a steady state, the dynamics and the dissipation are therefore intrinsically linked, and constraints on one yield constraints on the other.

Many authors have explored this link. For example, the widely-employed theory of Rayleigh-Benard convection developed by Grossmann and Lohse (2000) and discussed in Section 2.3, relies on the exact relationship between viscous dissipation and heat transport. In their model the heat transport depends crucially on whether the viscous and thermal dissipation occurs primarily in the bulk of the convective domain or in the boundary layers that form at its top and base. Jones et al. (2022) have recently explored an extension of this theory to the density-stratified case, with the spatial distribution of the dissipation again playing a vital role. In the stellar context, Anders et al. (2022) have shown that the magnitude of the dissipation within a convection zone strongly influences the amount of convective overshooting that occurs into adjacent stable layers. The form and magnitude of the dissipation is likewise crucial in a variety of efforts to go “beyond mixing length theory” (Canuto et al. 1996, Meakin and Arnett 2010, Viallet et al. 2013, Arnett et al. 2015, Kupka et al. 2022). In the Sun, where the form and magnitude of convective flows in the deep convection zone are currently the subject of much debate (see Vasil et al. 2021), the total dissipation may provide important constraints on the flows (Ginet 1994). More broadly, Ohmic dissipation in particular is thought to limit the depth of zonal winds in Jupiter (Liu et al. 2008, Kaspi et al. 2020) and Saturn (Galanti et al. 2019), may constrain magnetism in the interiors of low-mass stars (Browning et al. 2016), and could influence the radii of hot Jupiters (Batygin and Stevenson 2010).

Astrophysical codes such as 1D stellar evolution models often neglect this dissipation (Chabrier and Baraffe 1997) however it is not clear that its contribution is in fact negligible. In this Chapter we investigate this issue within one of the simplest possible systems that captures convection, rotation, and stratification, by conducting a series of hydrodynamic simulations of stratified (anelastic) convection in a rotating Cartesian domain, situated at a fixed latitude. These simulations are “2.5D” in which we assume axisymmetry in the third spatial dimension, and many elements that are important in real stars (including, crucially, magnetic fields) are absent here. This setup is advantageous however in that it allows us to sample parameter regimes that would be computationally difficult or impossible to probe in equivalent detail in a full 3D spherical geometry.

In particular, we are able to assess how the dissipation scales with luminosity, rota-

tion rate, and stratification in the astrophysically-interesting limit where the diffusivities are very small (i.e., when the convective supercriticality is very high). In what follows, we show that in this limit the dissipation rate (integrated over the convection zone) becomes independent of the rotation rate or the diffusivities, and depends only on the luminosity and the stratification. However, the spatial distribution of this dissipation, (and as a result, many other aspects of the dynamics) do depend on rotation as detailed below.

### 5.1.1 Prior work - Energetics of dissipation

In the interior of a star, the microphysical diffusion of momentum, heat, or magnetic fields is typically very small compared to inertia, buoyancy, or magnetic induction. That is, the Reynolds, Rayleigh, and magnetic Reynolds numbers are usually very large (e.g., Kulsrud 2005, Brun and Browning 2017). This need not imply, however, that viscous and Ohmic dissipation are negligible. Indeed, in a steady state the total rate of dissipation must balance the rate of energy injection (typically on large scales), as realised for example in the famed Kolmogorov model of the turbulent cascade (Frisch 1995); in this picture, what changes as the viscosity is reduced is the *scale* on which energy is dissipated, not its magnitude.

Although such dissipation is not explicitly included in classical mixing length theory (Gough and Weiss 1976), many authors have discussed its effects and implications for stellar convection (Arnett et al. 2009, Canuto et al. 1996). On energetic grounds, we might generally expect the total dissipation to be of order the luminosity  $L$  in a region where convection dominates the heat transport. For example, in the Kolmogorov theory the viscous dissipation rate (per unit volume per unit time) is  $\epsilon_u \sim \rho u^3/l$ , with  $l$  a damping length and  $u$  a velocity scale, so that the total dissipation within a volume  $d^3$  is  $\sim d^3 \rho u^3/l \sim d^2 \rho u^3$  if the dissipation length  $l$  is of order the largest possible eddies in the system (i.e., the depth of the layer) (see, Arnett et al. 2015). Likewise the convective flux is, either by MLT or on dimensional grounds,  $F \sim \rho u^3$ , so  $L \sim d^2 F \sim d^2 \rho u^3$  as well. Of course this is only an order of magnitude estimate, but it demonstrates that the total (viscous plus Ohmic) dissipation might plausibly be a) independent of the actual value of the diffusivities and b) of order the stellar luminosity.

When strong background temperature and density variations are also present, as they are for example in the envelope convection zones of Sun-like stars (or the convection zones of some gaseous planets), estimating the dissipation becomes more complex. Previous work however has shown that the total dissipative heating rate when integrated over the convecting volume is not bounded by the luminosity  $L$ , but by  $Ld/H_T$ , with  $d$  the depth of the layer and  $H_T$  a suitably defined temperature scale height. This means that for larger stratifications in which  $d \gg H_T$ , the dissipative heating can exceed the luminosity being supplied to the layer (Hewitt et al. 1975). This is thermodynamically permitted because the energy dissipated does not escape from the system; it goes back into the internal energy of the layer and may in turn drive flow elsewhere. By comparison, under the conditions usually assumed in deriving the Boussinesq approximation,  $d$  is restricted to be much smaller than  $H_T$ ; so in this limit the dissipative heating remains small compared to the luminosity.

The result of Hewitt et al. (1975) is only an upper bound, but in certain circumstances convection can approach a version of this bound. Hewitt et al. (1975) demonstrated that for the specific case of a Boussinesq liquid without magnetism, the integrated dissipation approached a value of order the bound at high enough Rayleigh numbers,  $\text{Ra}$  (measuring the ratio of buoyancy driving to viscous and thermal dissipation, see Section 2.2.2). Jarvis and McKenzie (1980) expanded on this by investigating the case of compressible convection in the infinite Prandtl number,  $\text{Pr}$ , (defined as the ratio of viscous to thermal diffusivities,  $\nu/\kappa$ , see Section 2.2.3) regime, appropriate for convection within the Earth's mantle where  $\text{Pr} \approx 10^{22}$ . They performed a suite of numerical simulations (presented here in Figure 5.1) that provided further confirmation that the total viscous heating is bounded by  $\frac{d}{H_T}L$ , and provided the first example of a published simulation in which the total dissipation exceeded  $L$  (labelled D1). Much later, Currie and Browning 2017 extended these results to a gas at finite  $\text{Pr}$ , as appropriate for convection in stellar interiors. In a series of 2D hydrodynamic simulations without rotation, they found many more numerical examples in which the total viscous heating exceeded  $L$ , but remained below the upper bound of Hewitt et al. (1975). They also provided a tighter bound obeyed by the total dissipative heating in their calculations, specifically (defining  $E \equiv \Phi/L$ , with  $\Phi$  the total viscous heating and  $L$  the luminosity)

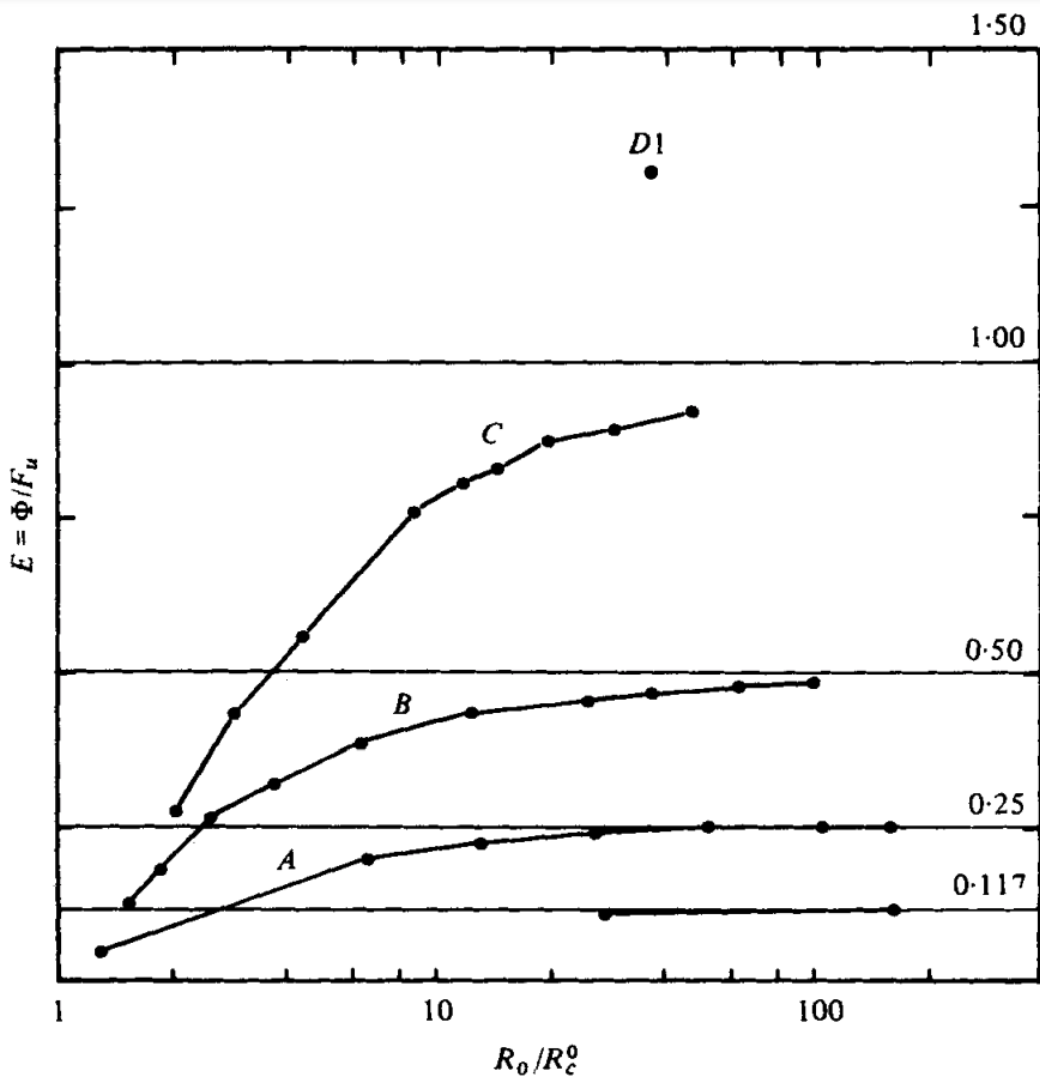


**Figure 5.1:** Plot taken from Jarvis and McKenzie (1980), Figure 15. This shows the values of viscous dissipation normalised by the flux passing through the layer as a function of supercriticality for infinite Prandtl number. The solid black lines represents the thermodynamical upper limit provided by Hewitt et al. 1975. The simulation D1 is of particular note due to having a value of  $E = \frac{\Phi}{L} > 1$ .

$$E = \frac{d}{\hat{H}_T}, \quad (5.1)$$

where

$$\hat{H}_T = \frac{H_{T,0} H_{T,u}}{H_{T,z^*}}, \quad (5.2)$$

is a modified thermal scale height involving the scale height at the top and bottom boundaries, and some vertical height  $z^*$ , defined such that half of the fluid mass lies above and below  $z^*$ . They showed that for sufficiently high supercriticalites, that is, once most of the energy passing through the fluid layer was transported by convection, the value of  $E$  appeared to approach equation 5.1 asymptotically. A significant aim of this study is to investigate how the inclusion of rotational effects changes this proposed upper limit.

Finally, we note that not *all* convective systems appear to approach these upper bounds, even when convection is extremely vigorous. Recently Albuissière et al. (2022), studying 2D convection with an unusual equation of state in which entropy is solely dependent on density found significantly lower levels of dissipation in most cases, even at asymptotically high Ra. They attributed the difference in part to the different boundary conditions adopted in their work, and in particular showed that for their equation of state, very high levels of dissipation (approaching the bound in equation 5.1) were only realised in cases with rigid walls as were employed in Currie and Browning (2017), and not in those with periodic boundary conditions. Clarifying whether this result also holds for a more astrophysically-relevant equation of state (namely an ideal gas) is another goal of our work.

While the magnitude of the dissipation is important, it has been shown extensively that the location of the dissipation is also of crucial importance. As discussed in Section 2.3, in Boussinesq convection Grossmann and Lohse (2000) present various scaling regimes in the Ra – Pr parameter space that are defined based primarily on whether the dissipation is dominantly produced in the bulk, or in the boundary layers. These scaling relations provide information on how parameters such as the the Nusselt number, Nu, or Reynolds

number,  $\text{Re}$  varying inside the  $\text{Ra} - \text{Pr}$  parameter space. That is, simply knowing where the dissipation is occurring within the domain can provide significant information on the overall dynamics of the flow such as the efficiency or turbulent nature of the convection. Another facet of this work therefore is to explore the spatial distribution of the dissipation and its effects on the resulting dynamics and heat transport.

### 5.1.2 Bounds and constraints on dissipative heating

To place our discussion on a firmer footing, and to highlight some of the aims of our work, we briefly describe the thermodynamic constraints on the dissipation here. More complete discussions can be found in Hewitt et al. (1975), Backus (1975), Currie and Browning (2017), Alboussière and Ricard (2013), and Alboussière et al. (2022).

Consider a volume  $V$  of convecting fluid with an associated magnetic field  $\mathbf{B}$ , enclosed by some surface  $S$ . Assume this surface is impenetrable and either stress-free or no-slip, so that the normal component of the fluid velocity  $\mathbf{u}$ , and either all components of  $\mathbf{u}$  or the tangential stress vanish on  $S$ . The local rate of change of *total* energy can be expressed by

$$\begin{aligned} \frac{\partial}{\partial t} \left( \rho e + \frac{1}{2} \rho u^2 + \frac{B^2}{2\mu_0} - \rho \Psi \right) &= -\nabla \cdot \left( \rho \left( e + \frac{1}{2} u^2 - \Psi \right) \mathbf{u} \right. \\ &\quad \left. + \frac{(\mathbf{E} \times \mathbf{B})}{\mu_0} + P \mathbf{u} - \tau \cdot \mathbf{u} - k \nabla T \right) + H, \end{aligned} \quad (5.3)$$

with  $e$  the fluid's internal energy,  $\rho$  its density,  $\Psi$  the gravitational potential satisfying  $\mathbf{g} = \nabla \Psi$ ,  $P$  the pressure,  $\tau_{ij}$  the contribution to the total stress tensor from irreversible processes,  $k$  the thermal conductivity,  $T$  the temperature,  $H$  the rate of internal heat generation (e.g., by nuclear fusion or radioactive decay), and  $\frac{\mathbf{E} \times \mathbf{B}}{\mu_0}$  the Poynting flux (involving the electric field  $\mathbf{E}$  and  $\mu_0$  the permeability of free space). Physically, the rate of total energy change at a point is given by the sum of the net inward flux of energy (the divergence terms in eqn. (5.3)) and the rate of internal heat generation.

The most obvious global constraint is that the total energy be conserved, but this

turns out not to yield much insight into the magnitude of the dissipative heating. Integrating (5.3) over  $V$  gives

$$\int_S k \frac{\partial T}{\partial x_i} dS_i + \int_V H dV = 0, \quad (5.4)$$

assuming both a steady state and that the electric current,  $\mathbf{j}$ , vanishes everywhere outside  $V$ . Equation (5.4) implies that the net flux out of  $V$  is equal to the total rate of internal heating. But dissipative terms do not appear in this equation; viscous and ohmic heating do not contribute to the overall heat flux.

To constrain the magnitude and form of the total dissipation, we turn instead to the internal equation, which can be written as:

$$\rho \left( \frac{\partial e}{\partial t} + (\mathbf{u} \cdot \nabla) e \right) = \nabla \cdot (k \nabla T) - P(\nabla \cdot \mathbf{u}) + \tau_{ij} \frac{\partial u_i}{\partial x_j} + \frac{j^2}{\sigma} + H. \quad (5.5)$$

where  $\sigma$  is the electrical conductivity and  $j$  is the electric current. Integrating over the fluid volume  $V$ , assuming a steady state, and recalling that our boundaries are impermeable, it can be shown that

$$\int_V (\mathbf{u} \cdot \nabla) P dV + \Phi = 0, \quad (5.6)$$

where the total dissipative heating rate,  $\Phi$ , is defined as

$$\Phi = \int_V \tau_{ij} \frac{\partial u_i}{\partial x_j} + \frac{j^2}{\sigma} dV. \quad (5.7)$$

The first and second terms inside the integral represent the contributions due to viscous and Ohmic effects. This equation implies that the total dissipative heating, integrated over the volume, is exactly balanced by the work done against the background stratification. In Hewitt et al. (1975) the entropy diffusion equation is used along with thermodynamic constraints to derive an upper limit on the total amount of dissipative heating that can

occur in a convective layer. For classical Rayleigh-Bénard convection in a plane layer this is given by

$$E \equiv \frac{\Phi}{L} < \frac{T_l - T_u}{T_u}, \quad (5.8)$$

where the subscripts  $u$  and  $l$  denote the upper and lower boundary values of the labeled variable respectively.  $E$  is therefore the total dissipative heating rate normalised by the luminosity passing through the convective layer. As discussed in the previous section, the work performed by both Jarvis and McKenzie (1980) and Currie and Browning (2017) numerically show that under high stratification the total dissipative heating can exceed the total flux passing through the layer, that is,  $E > 1$ . Additionally the extension to the stratified regime by Currie and Browning (2017) provided a tighter bound in the form of equation 5.1. It is not clear then, that heating due to viscous dissipation can be ignored.

### 5.1.3 Convective penetration

Throughout the bulk of the convective regions in stars and planets, the heat transport is dominated by convection, however the behaviour at the boundaries is still not entirely understood and remains an active area of research.

The convective overshooting that occurs at these boundaries can have significant effects on a star's evolution. One example of this is through chemical mixing. In post main sequence evolution, namely on the red giant and asymptotic giant branches, the observed surface abundances can be altered via the dredging up of material from nuclear burning regions and transported up through the fully mixed layers regions by overshooting surface convection (Salaris and Cassisi 2005). It is clear therefore that stellar models need to include some form of representation of the convective penetration to be effectively compared to any chemical abundances inferred from spectroscopic observations. This chemical mixing can also alter the overall evolution of the star by extending its lifetime (Salaris and Cassisi 2017).

Convective overshooting may additionally influence the establishment of the over-

all magnetic field and differential rotation profiles. A study by Beaudoin et al. (2018) shows that the inclusion of a stably-stratified layer underlying the convective zone in a set of global numerical simulations allows for the development of a latitudinal temperature gradient beneath the convective region as a result of penetrative convection, and leads to a subsequent breaking of Taylor-Proudman constraints. This constraint has previously been broken by the use of such latitudinal temperature gradients in the form of boundary conditions (Miesch et al. 2006); however the inclusion of a stably-stratified region into which the convection can then penetrate allowed this gradient to naturally develop as a result of overshooting. Korre et al. 2021 turns to overshooting as a mechanism for the confinement of large scale magnetic fields to the underlying radiative zone in the Sun. In the presence of less turbulent convection the initially seeded large scale field decreases in strength as a result of diffusion, whereas in the highly turbulent region, the effects of turbulent pumping leads to a confinement of the magnetic field beneath the overshooting region. These results are of particular interest for understanding the development of the uniform rotational profile of the Sun's radiative zone, for which a confined poloidal field is a proposed requirement (Gough and McIntyre 1998).

The reason for highlighting the above points is to stress the importance that the phenomenon of convective overshooting has on the overall evolution and dynamics of stars. The question remains however, what influences the strength and presence of penetrative convection? Anders et al. (2022) frame the formation of these overshooting or "penetrative" zones by the balance, or lack thereof, between the globally averaged buoyancy work and dissipation (see Anders et al. (2022) equation 9, as well as the discussion around equation 4.67 in the previous section). They present the following equation,

$$\int_{CZ} \bar{\mathcal{B}} dz = \int_{CZ} \bar{\Phi} dz + \int_{PZ} \bar{\Phi} dz - \int_{PZ} \bar{\mathcal{B}} dz, \quad (5.9)$$

where  $z$  is the radial coordinate,  $\bar{\mathcal{B}}$  and  $\bar{\Phi}$  are the horizontally averaged buoyancy energy generation and viscous dissipation, and the subscripts  $CZ$  and  $PZ$  denote the unstable convective region, and the stably stratified penetrative region respectively. They then define the ratio,

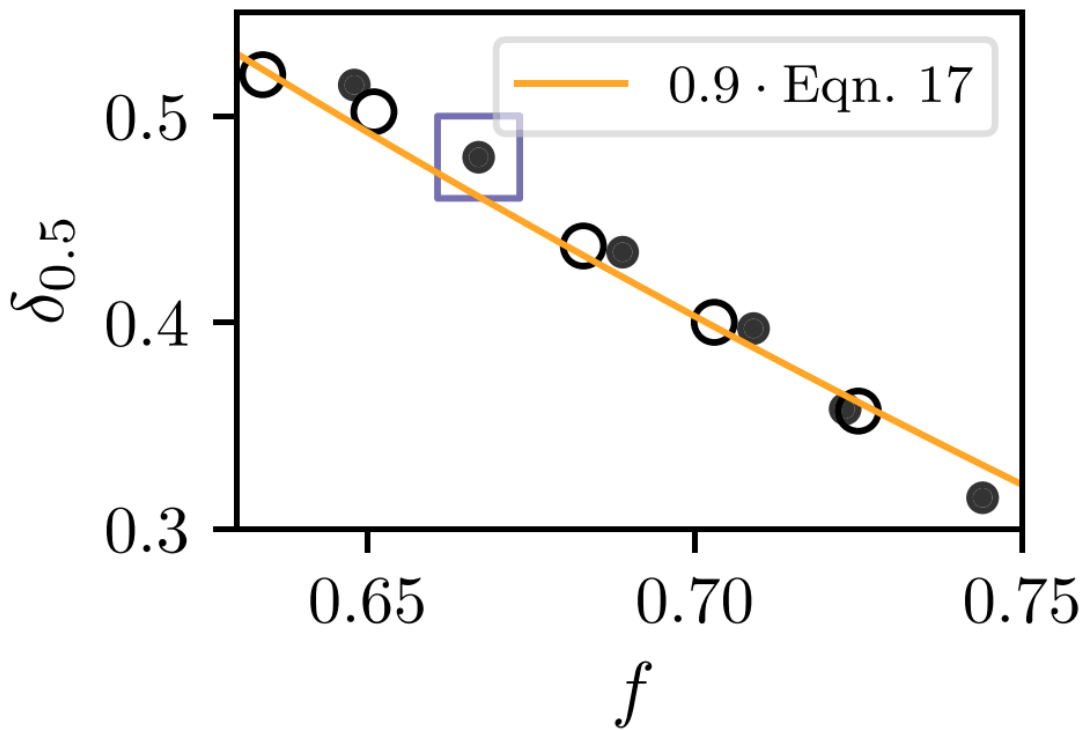


**Figure 5.2:** Plot taken from Anders et al. (2022) showing how the depth of the penetrative region, or rather, specifically the 50% departure point  $\delta_{0.5}$  varies with increasing values of  $f$ , the fraction of the buoyancy work that is being dissipated within the convective region.

$$f = \frac{\int_{CZ} \bar{\Phi} dz}{\int_{CZ} \bar{\mathcal{B}} dz}, \quad (5.10)$$

as the fraction of buoyancy work generated in the convective layer that is then being dissipated there. The case where this fraction,  $f$ , is equal to unity is equivalent to the case where there is no convective overshooting and therefore the dissipation completely balances the buoyancy work. They proceed to measure the depth of penetrating fluid by so-called departure points,  $\delta$ , which is the fractional value of how far the realised temperature gradient has evolved away from the adiabatic one. As can be seen in Figure 5.2 the depth of the penetrative zone has a clear dependence on the amount of viscous dissipation present. This also makes physical sense. For a given fluid parcel that has generated some amount of buoyant energy within a convectively unstable layer, increasing  $f$  corresponds to more of that energy being dissipated. As a result, such a parcel would have less momentum remaining to penetrate into a stably stratified region, and therefore would result in thinner penetrative regions. Quantifying the magnitude of the viscous dissipation, and

alongside it the amount of buoyancy energy generation present in a convective layer, is therefore an important feature in quantifying the convective penetration that occurs in stars.

## 5.2 Model Setup

The model setup used here is as described in Section 4.1 and a more detailed description can be seen there, however this section will provide a brief overview of the key elements.

### 5.2.1 Domain Geometry

The domain consists of a layer of fluid contained between two impermeable, stress-free boundaries at  $z = 0$  and  $z = d$ . To investigate the effects of rotation on such a convective layer a tilted f-plane is considered where the coordinate system is such that the horizontal coordinates,  $x$  and  $y$ , correspond to longitudinal and latitudinal directions respectively, and the vertical coordinate,  $z$ , corresponds to the radial axis. As a result the rotation vector takes the form  $\Omega = (0, \Omega_y, \Omega_z) = (0, \Omega \cos \phi, \Omega \sin \phi)$ , and the resulting Coriolis term is,

$$2\Omega \times \mathbf{u} = 2\Omega \begin{pmatrix} w \cos \phi - v \sin \phi \\ u \sin \phi \\ -u \cos \phi \end{pmatrix} \quad (5.11)$$

where  $u$ ,  $v$ , and  $w$ , are the  $x$ ,  $y$ , and  $z$ , components of the fluid velocity,  $\mathbf{u}$ ,  $\Omega$  is the magnitude of the rotation vector, and  $\phi$  is the latitude.

To sample the broadest possible parameter space with finite computational resources simulations are performed in largely 2D geometries. For two-dimensional geometries there is a choice available for which horizontal coordinate to model, and which to suppress. A more detailed discussion of this can be seen in Section 4.1.2; in summary, choosing a x-z plane results in a rotational vector tilted out of the domain and thus suppressing any rotational features, whereas choosing a y-z plane results in our Coriolis terms being identically zero in the momentum equation. In our the simulations a "2.5D" geometry is adopted, where the x, y, and z-components of the fluid velocity are solved for, but all

variables are taken to be constant in the x-direction. That is,  $\partial_x = 0$ .

### 5.2.2 Governing equations

The fully non-dimensionalised equation set takes the form

$$\begin{aligned} \frac{\partial \mathbf{u}}{\partial t} + (\mathbf{u} \cdot \nabla) \mathbf{u} + 2\boldsymbol{\Omega} \times \mathbf{u} &= -\nabla \tilde{p} + \frac{g_s}{c_p} \hat{\mathbf{e}}_z \\ &+ \nu \left[ \frac{1}{\bar{\rho}} \frac{\partial}{\partial x_j} \left( \bar{\rho} \left( \frac{\partial u_i}{\partial x_j} + \frac{\partial u_j}{\partial x_i} \right) \right) - \frac{2}{3\bar{\rho}} \frac{\partial}{\partial x_i} \left( \bar{\rho} \frac{\partial u_j}{\partial x_j} \right) \right], \end{aligned} \quad (5.12)$$

$$\nabla \cdot (\hat{\rho} \mathbf{u}) = 0, \quad (5.13)$$

$$\bar{\rho} \bar{T} \left( \frac{\partial s}{\partial t} + (\mathbf{u} \cdot \nabla) s \right) = \nabla \cdot (\kappa \bar{\rho} \bar{T} \nabla s) + \tau_{ij} \frac{\partial u_i}{\partial x_j}, \quad (5.14)$$

where

$$\tau_{ij} = \nu \bar{\rho} \left( \frac{\partial u_i}{\partial x_j} + \frac{\partial u_j}{\partial x_i} - \frac{2}{3} \delta_{ij} \nabla \cdot \mathbf{u} \right), \quad (5.15)$$

is the viscous stress tensor, and the relevant non-dimensional parameters are

$$\text{Pr} = \frac{\nu}{\kappa}, \quad \text{Ta} = \frac{4\Omega^2 d^4}{\nu^2}, \quad \text{Ra} = \frac{gd^4 F}{\nu \kappa^2 \rho_0 c_{p,0} T_0}, \quad \theta = \frac{gd}{c_{p,0} T_0}. \quad (5.16)$$

These equations are then solved using the psuedo-spectral code Dedalus (Burns et al. 2020) with mixed boundary conditions such that the flux is fixed at the bottom of the domain and entropy is fixed at the top. Only the hydrodynamical case is considered ( $j = 0$ ) and therefore the total dissipative heating rate,  $\Phi$ , is composed purely of viscous effects and given by,

$$E = \frac{\Phi}{L_u} = \frac{\text{Pr}^2 \theta}{\text{Ra}} \int_V \hat{\tau}_{ij} \frac{\partial \hat{u}_i}{\partial \hat{x}_j} d\hat{V}. \quad (5.17)$$

### 5.3 Overview of resulting dynamics

The convective flows in this system are influenced by rotation, by stratification, and by the amount of energy passing through the system. A series of simulations have been conducted that sample a wide variety of possible states within this multi-dimensional parameter space. In all of these cases we fix the polytropic index,  $m$  to be equal to 1.5, and the Prandtl number,  $\text{Pr}$ , to 1. Unless otherwise specified, the aspect ratio of the box is taken to be 2, and the resolution ranges from 256 horizontal gridpoints by 128 vertical gridpoints, to 1024 by 512 for the more turbulent cases. We quantify the degree of stratification by  $N_p$ , and consider cases ranging from the nearly-Boussinesq limit ( $N_p = 0.2$ , with a density contrast from top to bottom of  $8.2 \times 10^{-1}$ ) up to strong stratifications with  $N_p = 5$  (density contrast  $6.7 \times 10^{-3}$ ). The energy passing through the system is quantified by the Rayleigh number  $\text{Ra}$ , specifically for this work (and for that presented in Currie and Browning (2017)), a flux based Rayleigh number  $\text{Ra}_F$  will be used, as defined in Section 2. The simulations shown sample both highly viscous, laminar flows that are near convective onset with  $\text{Ra}_F$  values close to the critical Rayleigh number  $\text{Ra}_c$ , as well as much more turbulent states that have  $\text{Ra}_F \sim 10^6 \text{Ra}_c$ . The rotation rate in the simulations is quantified by the Taylor number (as defined above) which varies from non-rotating cases between  $\text{Ta} = 0$  and  $\text{Ta} = 10^{11}$  with both polar and tilted boxes being considered (latitudes  $45^\circ$  and  $90^\circ$ ). It can be assumed that the latitude is taken to be  $90^\circ$  (e.g. vertically aligned rotation vector) unless otherwise specified. It is worth noting that the Ekman number is also commonly used to measure the importance of rotation in fluid dynamics and has a direct relationship with  $\text{Ta} = 0$  given by  $\text{Ek} = \text{Ta}^{-1/2}$ . The rotational parameter space explored in Ekman number is between  $\text{Ek} = 3.16 \times 10^{-1}$  and  $\text{Ek} = 3.16 \times 10^{-6}$ . One of the drawbacks of using  $\text{Ta}$  or  $\text{Ek}$  to measure the degree of rotational influence on a system can be seen by the relationship between  $\text{Ta}$  and  $\text{Ra}_c$ , previously discussed in Chapter 4, and shown in Figure 4.14. In short, increasing rotation rate stabilises the system against convection, increasing the value of  $\text{Ra}_c$ , that is  $\text{Ra}_c \propto \text{Ta}^{2/3}$ , and therefore inhibiting convection. In practice it is

more useful to assess the influence of rotation relative to some property of the realised convection, as a way of gauging whether Coriolis forces play any dynamical role. One such measure is the fluid Rossby number  $\text{Ro} = |\nabla \times \mathbf{u}|/\Omega$ , which quantifies the local vorticity relative to rotation; rapidly rotating cases thus have  $\text{Ro} \ll 1$  (see section 2.2.6). Another way to quantify the degree of rotational influence in relation to the buoyancy forcing is through the convective Rossby number,  $\text{Ro}_c$ , which again is discussed in more detail in Chapter 4. The convective Rossby number is a function only of the non-dimensional input parameters  $\text{Ra}$ ,  $\text{Pr}$ , and  $\text{Ta}$ . A discussion of the various Rossby numbers can be seen in Anders et al. (2019). The parameter space explored includes rapidly rotating systems that are heavily influenced by rotational forces ( $\text{Ro}_c \sim 0.03$ ) as well as those of which have little to no rotational influence and for all intents and purposes can be considered non-rotating ( $\text{Ro}_c \sim \infty$ ). It is however of note that due to the nature of a stratified system, the interpretation of these numbers is complicated. As shown in section 4.5.2, the introduction of stratification can lead to large variations in convective velocities throughout the domain and to strong asymmetries between upflows and downflows. As a result the rotational influence may vary throughout the domain and spatial differences and subtleties are often lost when using global descriptive quantities such as the convective Rossby number.

Many different types of flow are possible within this parameter space. For illustrative purposes, a few of these different examples can be seen in Figure 5.3, which shows from left to right the entropy, and the vertical and horizontal velocity components of the fluid for four different 2D cases. The top two rows show non-rotating cases at  $\text{Ra} = 10^4 \text{Ra}_c$  at a low and moderate density stratification ( $N_\rho = 0.2$  and  $1.4$  respectively) demonstrating the symmetry breaking that occurs between the upflows and downflows. The bottom two rows show rotating cases at a moderate stratification of  $N_\rho = 1.4$ , with the third and forth rows showing two cases at different degrees of rotational influence,  $\text{Ro}_c = 1.25$  and  $\text{Ro}_c = 0.29$  respectively in an even more rapidly rotating, strongly stratified regime (bottom panels).

In the non-rotating, stratified cases shown in the upper half of Fig. 5.3, the convection tends to be steady except at very high  $\text{Ra}$  (as discussed in CB17; examples of the higher- $\text{Ra}$  regime can be seen in Rogers et al. 2003 among others); typically it consists of a

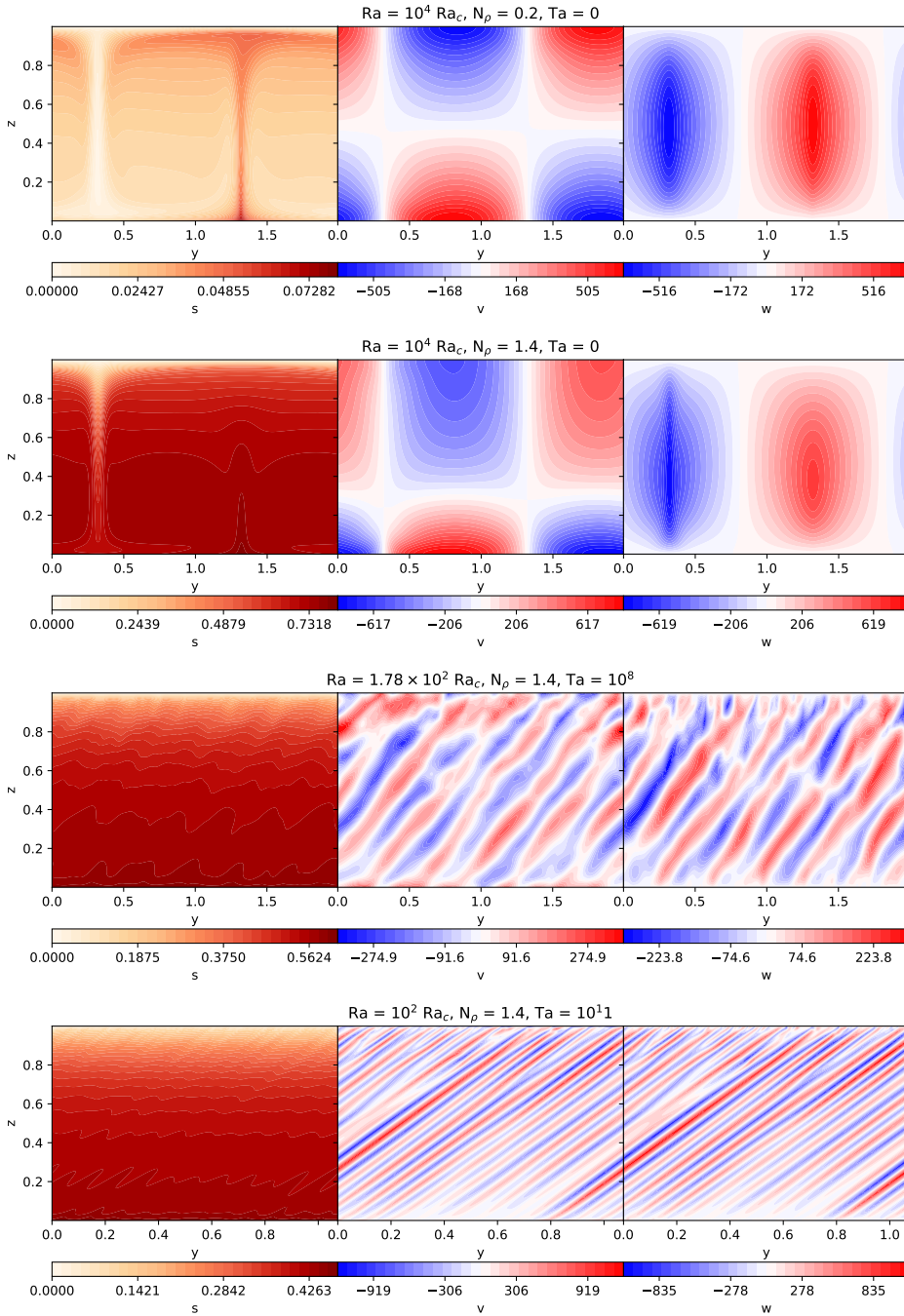


**Figure 5.3:** Example dynamics of four cases sampling different parameter regimes. Shown are entropy  $s$ , vertical velocity  $w$ , and horizontal velocity  $v$  for four different cases. The top two rows are for non-rotating cases at  $\text{Ra} = 10^4 \text{Ra}_c$  showing both lightly and heavily stratified regimes with  $N_\rho = 0.2$  and  $1.4$  respectively. The bottom two rows show rotating cases at two different degrees of rotational influence where  $N_\rho = 1.4$ ,  $\text{Ta} = 10^8$ ,  $\text{Ra} = 1.78 * 10^8 \text{Ra}_c$  and  $N_\rho = 1.4$ ,  $\text{Ta} = 10^{11}$ ,  $\text{Ra} = 100 \text{Ra}_c$ . Note the bottom case has a different aspect ratio of 1.075.

small number of convective cells as shown here. When rotation is present however, as is shown in the bottom half of the figure, the convective patterns tend to align with the axis of rotation in accordance with the Taylor-Proudman theorem (Taylor 1923). The Boussinesq ( $N_\rho = 0$ ) limit possesses an exact symmetry between upward and downward motions, so in weakly stratified cases the flow consists of upflow-downflow pairs that align with the local rotation axis (which here is tilted at 45 degrees with respect to the vertical). However, when stratification is strong, the downflows (which contract as they descend) tend to be stronger and narrower than upflows (which expand as they ascend). The variance in the velocities and spatial scales of these ascending and descending flows results in different degrees of rotational constraint (see equation 2.37). At high Ra and high Ta, as sampled in the bottom panels, the flow is structured on much smaller horizontal scales (see discussions in, e.g., Currie and Tobias (2020)) but still aligns with the local rotation vector.

## 5.4 The magnitude and spatial distribution of viscous dissipation

### 5.4.1 The maximum value of viscous dissipation at high Ra

As discussed in Section 5.1.2, prior theory has shown that there exists a thermodynamic upper bound on the volume-integrated viscous dissipation dependent only on the luminosity  $L$  and the thermal scale height (that itself depends only on the layer depth and the stratification of the system). This upper bound can exceed unity for sufficiently stratified systems (see, Hewitt et al. (1975), Backus (1975), Jarvis and McKenzie (1980)). Prior 2D simulations of the non-rotating convection in an ideal gas demonstrated that the dissipation actually approached a similar bound (equation 5.1) when the convection was sufficiently vigorous (i.e., at high enough  $Ra$ ). On the other hand, recent 2D simulations with a different equation of state (Alboussière and Ricard 2013) found significantly lower levels of dissipation in most cases, and attributed the difference in part to the different boundary conditions adopted; in their simulations, high levels of dissipation (that is, approaching the bound presented in equation 5.1) were realised only in cases with rigid horizontal boundary conditions such as those present in Currie and Browning (2017) rather than periodic boundary conditions.

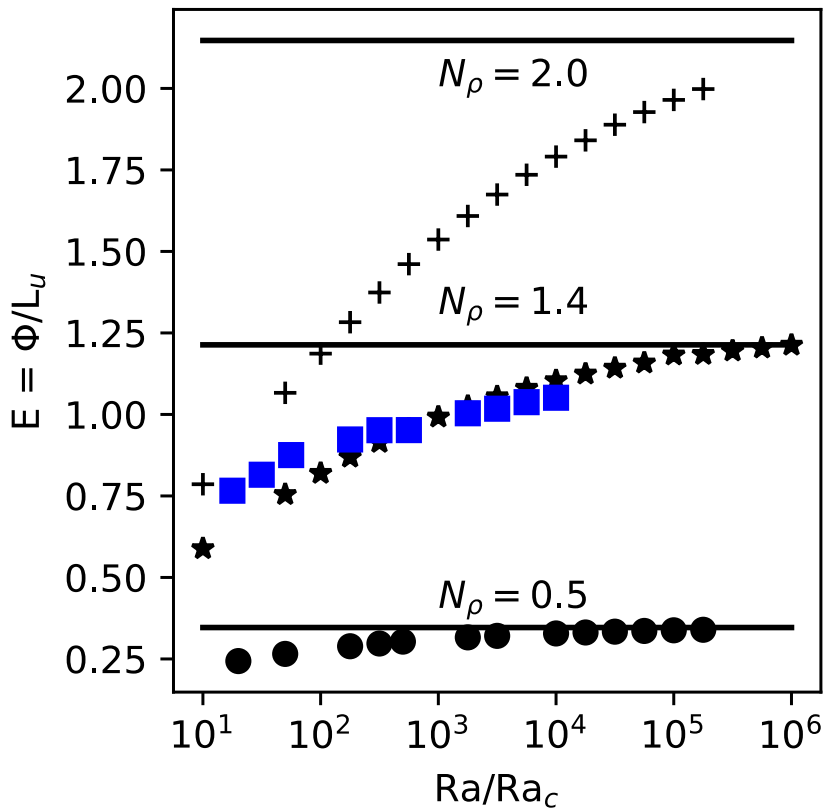


**Figure 5.4:** Calculated values for  $E$  at a range of stratifications and supercriticalities for some non-rotating (black) and rotating cases (blue). Values of  $N_\rho = 0.5$  (circles), 1.4 (stars and squares), and 2.0 (pluses) are used. The horizontal black lines represent the value of equation 5.1 for a given value of  $N_\rho$ . It is of note that due to the effect of rotation on the critical Rayleigh number, the rotating cases have considerably larger values of  $Ra$  for a given stratification.

This work examines whether the high levels of dissipation found in Currie and Browning (2017) are realised in the rotating case. We find that they are, and that the rotating simulations appear to approach the same dissipative upper bound as the non-rotating ones. Additionally, the models here were conducted with different boundary conditions (here periodic, impermeable in Currie and Browning 2017) and demonstrate that these results are, at least for an ideal gas equation of state, not directly dependent on rigid boundaries. We also present simulations with a different aspect ratio. The horizontal extent of our domain is double that of the layer depth, whereas in Currie and Browning (2017) they are taken to be equal. We show therefore that while the apparent upper bound in equation 5.1 depends on the depth of the fluid layer, it appears to be independent of the corresponding horizontal extent.

We calculate the magnitude of dissipative heating that occurs in our simulations over a range of  $N_p$ , Ra, and Ta. Figure 5.4 shows  $E$  for a selection of cases at different Ra and Ta, shown here for three different stratifications as a function of  $Ra/Ra_c$ . At high enough supercriticalities, both the rotating and non-rotating cases appear to approach the same limiting value, equation (5.1), which is dependent on the layer depth and stratification but independent of Ra (and likewise also independent of viscosity or diffusivity).

It is clear from Figure 5.4 that this upper bound on dissipative heating is approached only for sufficiently high  $Ra/Ra_c$ , and that the value of  $Ra/Ra_c$  needed to reach the upper bound is higher for larger  $N_p$ . An alternate view of this bound can be seen in Figure 5.5. Note that the larger  $N_p$  cases have not yet reached the asymptotic upper limit as they have not been performed at a high enough supercriticality.

A complementary view but instead focused on the influence of rotation is provided by Figure 5.6, which shows  $E$  for a selection of cases at fixed supercriticality (here  $Ra = 10^2 Ra_c$ ) and two different  $N_p$  but varying  $Ta$  (i.e., with varying rotational influence relative to viscous effects). In the regime probed here, it is clear that in the limit of very vigorous convection (high enough supercriticality), the presence of rotation does not directly alter the volume-integrated magnitude of viscous dissipation despite an evident change in dynamical structure. As can be seen in Figure 5.7 which shows two  $N_p = 1$  cases at  $Ta = 10^5$  and  $10^9$  ( $Ro_c = 3.81$  and  $0.703$  respectively), the influence of rotation dramatically alters the flows.

It is useful here to be reminded of the influence that rotation has on the onset of convection. As previously shown both in this work and in many other prior studies, rotation stabilises a system against the onset of convection, that is,  $Ra_c \propto Ta^{\frac{2}{3}}$  (Chandrasekhar 1961). Therefore cases with fixed supercriticality often have considerable difference in their values for Ra. For example, cases with  $Ta = 10^{11}$  will require values of Ra that are  $10^7$  times larger than those needed in their non-rotating counterparts in order to achieve the same  $Ra/Ra_c$ . As shown in both Figures 5.3 & 5.7, even lightly rotationally constrained cases demonstrate considerably more complex flow fields consisting of vigorous and time-dependent flows. In the rotating regime these operate on multiple spatial scales and are aligned to the rotation axis of the system. Non-rotationally influenced cases however con-

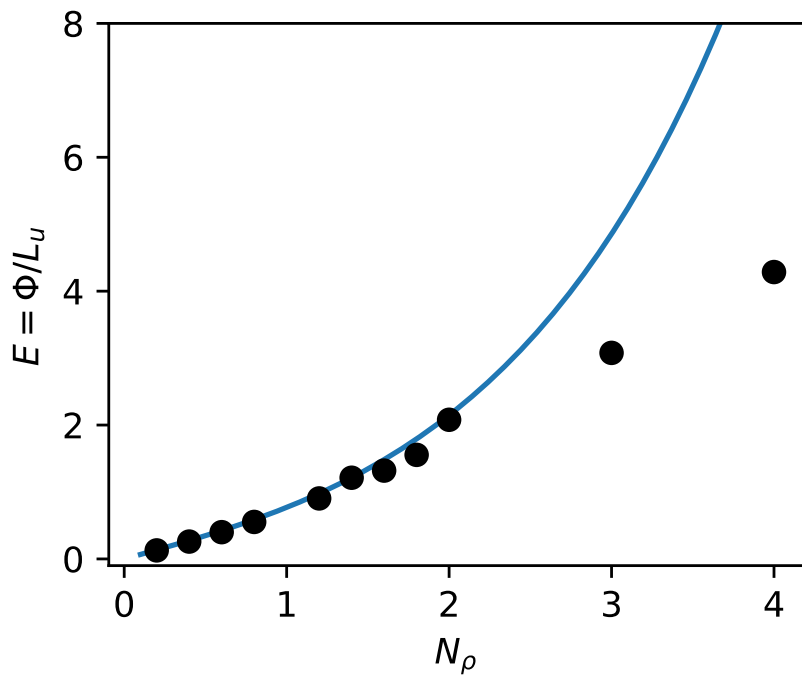


**Figure 5.5:** The maximum value of  $E$  achieved for a given  $N_\rho$ . The blue line represents the upper bound limit presented in equation 5.1. The values of  $E$  for  $N_\rho = 3$  and  $4$  appear much lower than the asymptotic limit having not yet been performed at the required supercriticality.

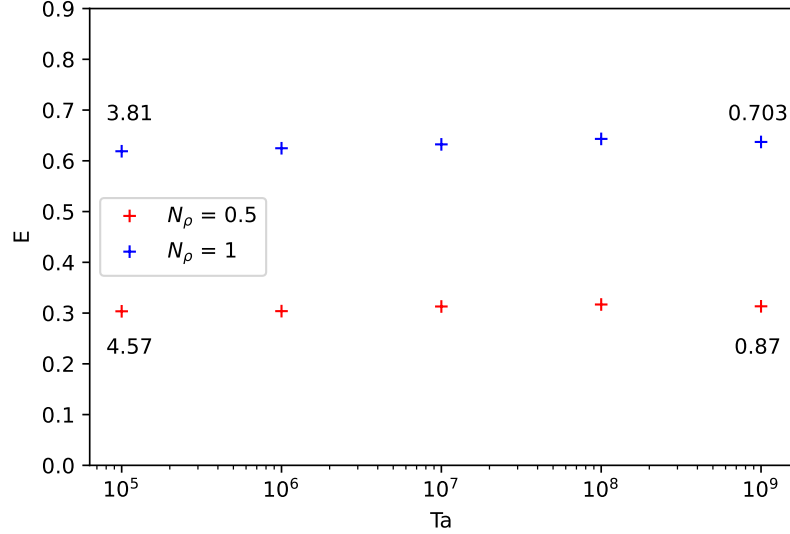


**Figure 5.6:** The values of  $E$  for a range of rotation rates. All cases have a fixed supercriticality of  $Ra/Ra_c = 10^2$ , and are shown at two different stratifications of  $N_\rho = 0.5$  and 1. The black labels at the highest and lowest values of  $Ta$  for each stratification show the value of the convective Rossby number  $Ro_c$ .

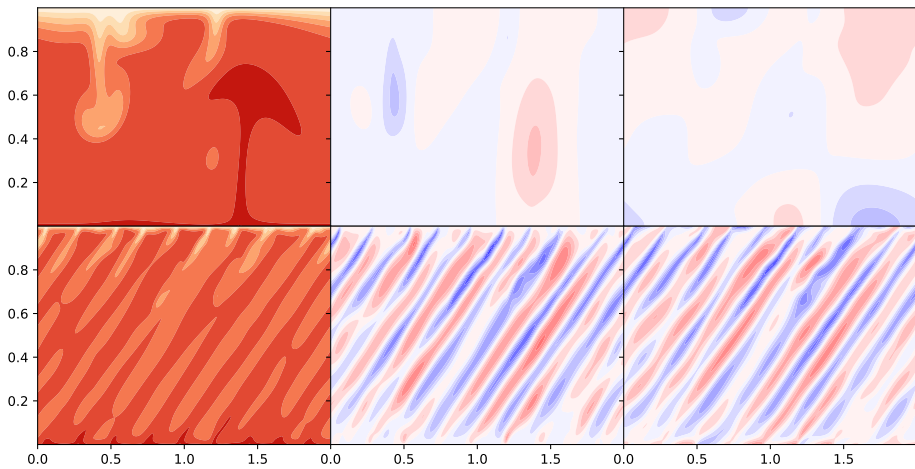


**Figure 5.7:** Comparison snapshots demonstrating the different dynamical flows present in two simulations of  $Ra = 10^2 Ra_c$ ,  $N_\rho = 1$ , at  $Ta = 10^5$ ,  $Ro_c = 3.81$  (top row) and at  $Ta = 10^9$ ,  $Ro_c = 0.703$ . From left to right the plots show the total entropy of the fluid, and the vertical and horizontal velocities.

sistently produce singular, large scale, steady convective cells. It is therefore interesting that despite such drastically different dynamical regimes that the viscous dissipation appears to asymptote towards the same limit.

The following sections show that while the amount of dissipative heating remains the same, the spatial distribution of the dissipation varies as a result of the changing dynamics due to the increase in fluid shearing that occurs in the rotationally constrained cases.

#### 5.4.2 The spatial distribution of dissipation

In the previous section, we established that in both rotating and non-rotating cases, the total viscous dissipation at first increases with increased buoyancy driving (higher  $Ra$ ) and then plateaus at a fixed value (5.1) that depends on the layer height and stratification but is independent of the rotation rate or diffusivities. Here, we establish how this arises. We present the spatial distribution of the dissipation within in the simulations, and show by examination of a so called "dissipation half-height" (that is, the height by which half of the total dissipation has already occurred) that the cases at high  $Ra$  which approach the CB17 upper bound correspond to situations in which much of the dissipation occurs close to the bottom of the domain and there is negligible entropy generation by conduction in the bulk.

A first, qualitative look at the locations where dissipation occurs is provided by Figure 5.8. The left-hand side shows the natural log of the dissipative heating  $\tau_{i,j} \frac{\partial u_i}{\partial x_j}$  alongside snapshots of the vertical velocity for four cases sampling different parameter regimes. The topmost case is non-rotating (with  $Ra = 10^6 Ra_c$ ); the others are all rotating ( $Ta = 10^8$ ) but are situated at different latitudes (at the pole in second row, and at 45 degrees in the bottom two rows) and sample different levels of turbulent driving ( $Ra = 10^3 Ra_c$  in second and third rows,  $Ra = 10^4 Ra_c$  in bottom row) and as such probe different degrees of rotational constraint.

Some immediate observations can be made. Firstly in the bulk of the convection zone it is clear that areas in which the viscous dissipation is particularly strong are often

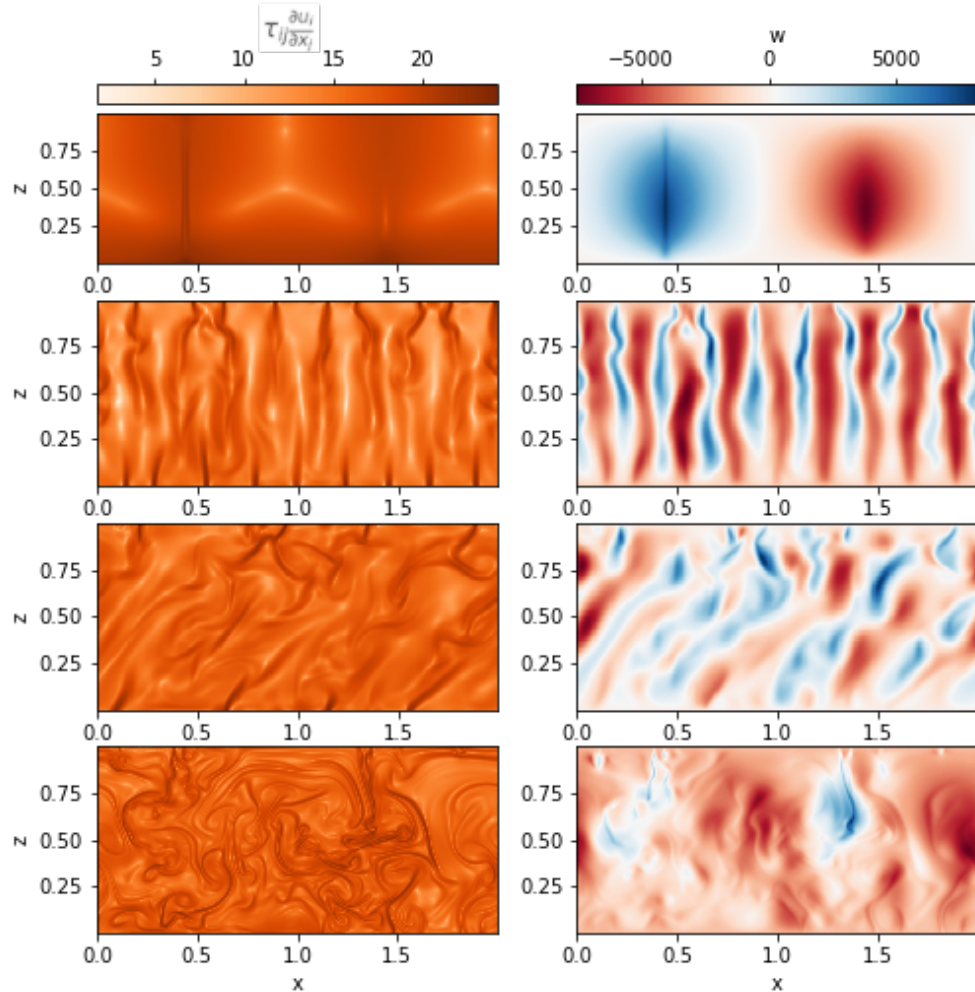


**Figure 5.8:** Local dissipative heating and vertical velocities in a sample of cases. Left panels show  $Q_{diss}$ , right panels  $w$ . Top row shows a non-rotating case at  $Ra = 10^6 Ra_c$ ; the other rows all consider cases at  $Ta = 10^8$ , at varying supercriticalities ( $Ra = 1.78 \times 10^2 Ra_c$  in the middle two rows;  $Ra = 10^4 Ra_c$  in the bottom row) and latitudes (at the pole in the first rotating example; at 45 degrees in the bottom two).

closely correlated to the boundaries between the upflows and downflows. For example, in the non-rotating case (top row of Figure 5.8) when the convection consists of a large single cell, the strongest bulk dissipation is found along the edges of the single upflow. This is also the case in the more complex dynamics that are shown in the rotationally constrained cases. In the rotationally constrained cases, specifically the middle two rows where the convective flow has aligned itself with the axis of rotation, there is once again a correlation between the edges of the fluid flow and the regions of high dissipative heating. As previously mentioned this is as expected. The stress tensor on which  $Q_{diss}$  depends is largest in regions where the flow changes strength over a short distance, that is in regions of high shear flows. The bottom case shown in Figure 5.8 has much more irregularly distributed dissipation throughout its bulk, however this dissipation still tracks closely with so called velocity "fronts" (in particular this case strongly follows the horizontal flow features, although these are not plotted here.)

Additionally Figure 5.8 shows that there is a significant amount of dissipative heating occurring near the boundaries. Once again this tracks with the notion that the dissipative heating is largest where the velocity changes quickly. Vertical flows that are impinging on the boundaries are deflected horizontally and as such would correspond to high levels of dissipation. This can be seen clearly in the non-rotating case. The middle two rows show comparable dissipation in both the bulk and the boundaries, whereas the complex flow structure in the bottom row appears to result in a bulk-dominated dissipation regime. It seems that there is an overall shift from boundary to bulk dissipation with increasing rotational influence.

To examine the distribution between bulk and boundary dissipation more quantitatively we can turn to the horizontally-averaged quantities in Figure 5.9, that is,  $L_{diss}(z) = \int_0^z Q_{diss} dz$  and  $L_{buoy}(z) = \int_0^z Q_{buoy} dz$  as introduced in Chapter 4.  $L_{diss}$  is the total dissipative heating that has occurred between the bottom boundary and the height it is evaluated at. Therefore at  $z = d$ , the result is simply the volume integrated dissipation,  $E$ . For the case where the heating is uniformly distributed throughout the domain (that is,  $Q_{diss} = constant$ ) then  $L_{diss}$  would simply be a linear function with height.  $L_{buoy}$  is the integrated buoyancy work, again, up to the height at which it has been evaluated. These

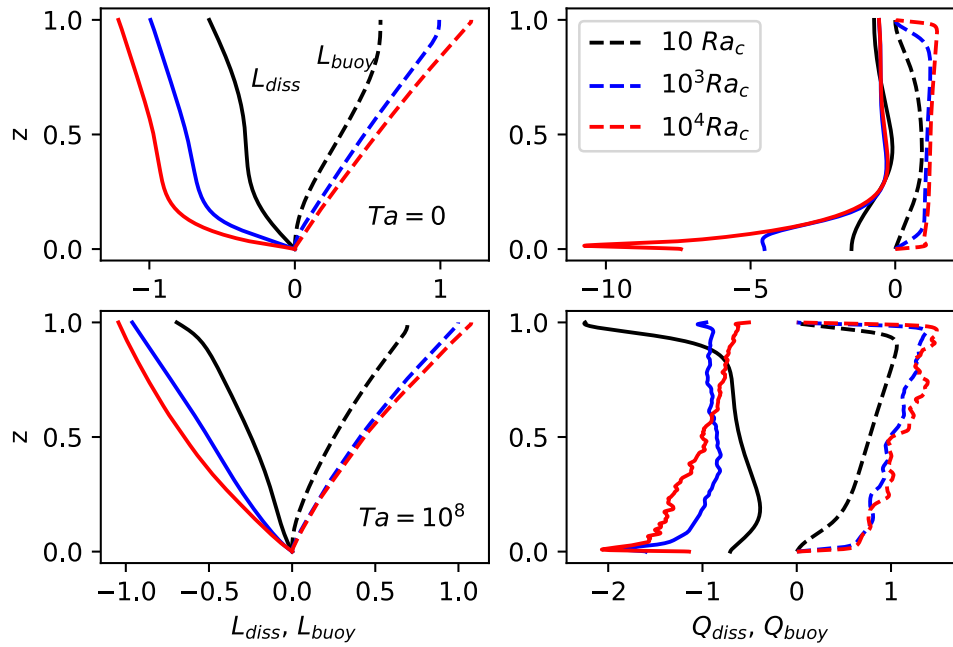


**Figure 5.9:** Dissipative heating integrated from 0 to  $z$ ,  $L_{diss}(z)$ , and integrated buoyancy work  $L_{buoy}$  for a sample of non-rotating cases (top panel) and rotating ones. Solid lines represent  $L_{diss}$  and  $Q_{diss}$  in the left and right columns respectively, whereas dashed lines represent  $L_{buoy}$  and  $Q_{buoy}$ . The non-rotating cases sample a range of  $Ra$ ; the rotating cases are those shown in the previous figure. As can be seen in the rotationally constrained cases in the bottom right panel, the more dynamically complex flow structure requires significantly longer time averages to smooth out.

two quantities must cancel globally, that is when evaluated at the top of the domain, however they are not required to do so locally (see Figure 4. of Currie and Browning 2017). The left-hand panels of Figure 5.9 show these two quantities as a function of height for a non-rotating (top) and rotating (bottom) case at a range of supercriticalities. The right-hand side shows the horizontally integrated values of  $Q_{diss}$  and  $Q_{buoy}$ . The rotating cases are at  $Ta = 10^8$ .

For the non-rotating cases we can see that  $L_{buoy}$  increases approximately linearly with depth up to  $E$ . The more supercritical the convection is the more pronounced this effect appears to be, however even in the laminar case of  $Ra = 10Ra_c$  the trend is still largely linear. This is not the case with  $L_{diss}$ . As was observed in Figure 5.8, the majority of the dissipation occurs at the bottom boundary, and after approximately  $z = 0.25$  the profile is approximately linear up to the value of  $E$ . This effect is considerably more pronounced in the horizontally-averaged profiles of  $Q_{diss}$  and  $Q_{buoy}$  shown on the right-hand side.  $Q_{diss}$  has a particularly sharp peak near the bottom boundary before leveling back out, whereas  $Q_{buoy}$  is approximately linear throughout the whole interior. The rotational cases are largely similar in their profiles of  $L_{buoy}$  and have also have an approximately linear profile. The behaviour of  $L_{diss}$  however appears much more linear, again mirroring the observations made in the discussion of Figure 5.8 in that the dissipation is much more uniformly distributed throughout the fluid bulk and not necessarily concentrated at the boundaries.

As discussed previously these differences are reflective of the dynamical structure of the rotating and non-rotating systems. We can use simple scaling arguments to reinforce this as well. Looking at  $Q_{diss}$  we have,

$$|Q_{diss}| = \tau_{ij} \frac{\partial u_i}{\partial x_j}, \quad (5.18)$$

where both  $\tau_{ij}$  and  $\frac{\partial u_i}{\partial x_j}$  scale like  $U/\delta$ , and  $U$  and  $\delta$  are characteristic velocity and length scales for the flow. That is,

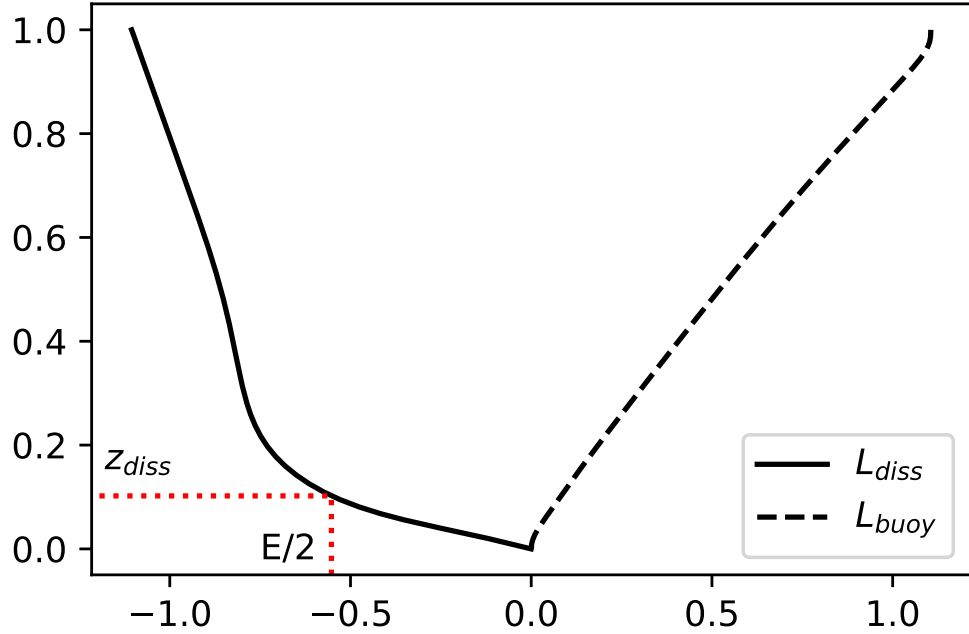


**Figure 5.10:** Vertical profiles of  $L_{diss}$  and  $L_{buoy}$  for a non-rotating stratified case with  $N_\rho = 1.4$ , and  $\text{Ra} = 10^4 \text{Ra}_c$ .

$$|Q_{diss}| \sim \left(\frac{U}{\delta}\right)^2. \quad (5.19)$$

In the non-rotating case, there is a single large-convective cell of order the box size, that is  $\delta \sim d$  whereas in the rotationally constrained cases we have much narrower convective cells and therefore  $\delta$  is some fractional value of  $d$ . It follows therefore that we would expect values of  $Q_{diss}$  in the bulk of the fluid to be larger in the rotationally constrained cases. Notably, as can be seen in the bottom panels of Figure 5.3, the more rotationally constrained a system is, the finer the convection motions are, and so the smaller  $\delta$  we have.

Another way to evaluate the distribution of the dissipation is by looking at a newly defined  $z_{diss}$ , termed the dissipation half height. The dissipation half height is defined as the point at which the absolute value of  $L_{diss}$  is equal to half of its maximum value,  $E$ . That is,

$$|L_{diss}(z_{diss})| = \int_0^{z_{diss}} Q_{diss} dz = \frac{E}{2}. \quad (5.20)$$

In the case of  $Q_{diss} = const.$  and the resulting  $L_{diss}$  profile being a linear function of  $z$  from 0 to  $E$ , then  $z_{diss}$  would simply be 0.5. Similarly if the dissipation is skewed towards the bottom boundary (as from our previous analysis we would expect in the non-rotating cases) then the value for  $z_{diss}$  would be  $< 0.5$ . This can be seen schematically in 5.10 which shows some vertical profiles of  $L_{diss}$  and  $L_{buoy}$  for a stratified case, with the point at which  $L_{diss}$  is equal to half of  $E$  labelled. Figure 5.11, which shows values for  $z_{diss}$  at a for a range of both non-rotating and rotating cases at a number of different stratifications, demonstrates this further.

Both the rotating and non-rotating cases display a decrease in the value of  $z_{diss}$  with increasing supercriticality, implying more of the dissipation occurs deeper in the domain, closer to the bottom boundary. This tracks with the ideas of heavily forced convection resulting in the interior heat transport being almost entirely driven by convective flows and essentially negligible dissipation contributions. For sufficiently turbulent convection the value of  $z_{diss}$  tapers out to a nearly constant value. This is in contrast to the thermal boundary layer which gets continually narrower for increasing values of  $Ra$  as discussed below.

Much like with our initial qualitative analysis of the full  $Q_{diss}$  distribution in Figure 5.8, and the subsequent analysis of the horizontally averaged  $L_{diss}$  and  $Q_{diss}$  vertical profiles, the values of  $z_{diss}$  in the rotational cases suggest a much more even distribution of dissipation throughout the convective layer. The rotational cases also appear to show a downwards trend with increasing supercriticality, however this is influenced by our adoption of a fixed  $Ta$  with increasing supercriticality. As previously discussed this results in an increasing Rossby number,  $Ro$ , that is, a decrease in the rotational influence on the dynamics of the fluid at higher  $Ra$ . For cases with fixed supercriticality but increasing  $Ta$ , that is, increasing rotational influence we see a clear trend in shifting towards more bulk dissipation (as previously discussed). This is seen in Figure 5.12 where we see a clear trend in increasing  $z_{diss}$  with increasing  $Ta$ . The  $N_p = 1.4$  cases with  $Ta < 10^4$  that lie at

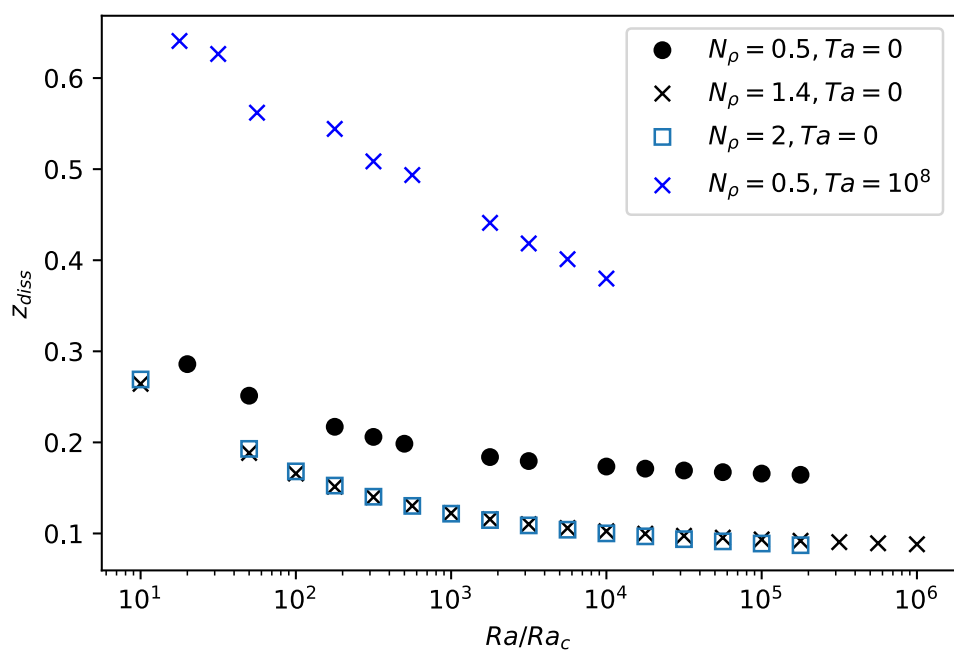


**Figure 5.11:** Values of  $z_{diss}$  for a range of non-rotating and rotating simulations at a range of stratifications,  $N_\rho$ .

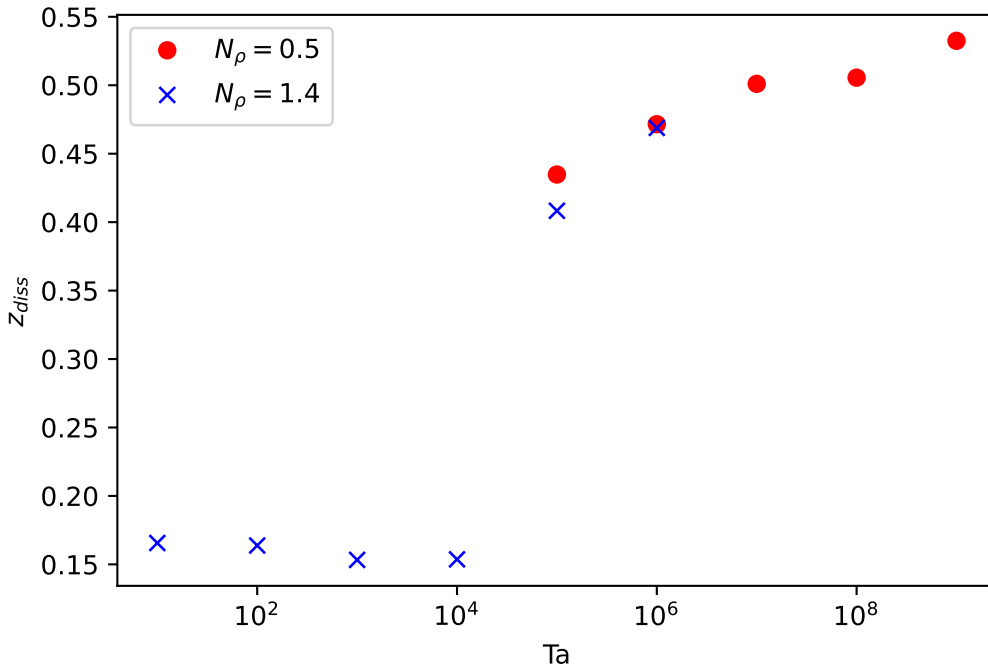


**Figure 5.12:** Values of  $z_{diss}$  for a range of simulations at fixed supercriticality,  $\text{Ra} = 10^2 \text{Ra}_c$  for stratifications of  $N_\rho = 0.5$  (red circles) and 1.4 (blue crosses) and a range of  $Ta$ .

low  $z_{diss}$  are in the non-rotationally constrained regime of  $Ro >> 1$  and as such appear as the non-rotating cases do with values of  $z_{diss}$  representing negligible bulk dissipation and significant dissipation near the lower boundary layer.

## 5.5 Links between dynamics, heat transport, and dissipation

In a steady state, dissipation and dynamics are linked, and so insight into one yields constraints on the other. In this section we will show how systematic variations in the governing parameters of this problem (namely  $\text{Ra}_F$ ,  $Ta$ , and  $N_\rho$ ) lead to changes in the energy transport and in the flow fields, and we explore how these are related to changes in the magnitude and spatial distribution of the dissipation. Our discussion here is also intended to help place our work in context with a large body of previous research on heat transport in both non-rotating and rotating convection.

As discussed in Section 2.3, one of the main purposes of a convective theory in the context of stellar astrophysics is to provide estimates of the entropy gradient that is required to carry a given luminosity outwards (e.g. Gough and Weiss 1976). For example,

in standard stellar evolution theory, the radius of a star depends on its specific entropy, and how this varies with depth (see discussions in Ireland and Browning 2018 for example). There is also substantial astrophysical interest in properties of the flow itself, such as its magnitude at each depth, as these in turn will affect mixing, the transport of heat and angular momentum, and the generation of magnetic fields. Hence, we focus our discussions here on the heat transport, on the related question of how entropy varies with height in our simulations, and on the magnitude of the flows themselves. We conclude this section by demonstrating that a quantity of particular interest, the kinetic energy flux, can be estimated given knowledge of the dissipative heating.

### 5.5.1 Energy balances and transport

Section 4.2 introduced two complimentary decompositions for quantifying the heat transport within a given convective simulation by considering integrals of the total energy (3.46) and internal energy (3.47) equations over the convective volume. For completeness they are reiterated here. Integrating the total energy equation over the volume, and applying the divergence theorem produces

$$L = FA = \underbrace{\int_{S_{z'}} \bar{\rho} c_p w T' dS}_{L_e = AF_e} + \underbrace{\int_{S_{z'}} -\kappa \bar{\rho} \bar{T} \frac{\partial s}{\partial z} dS}_{L_{cond} = AF_{cond}} + \underbrace{\int_{S_{z'}} \frac{1}{2} \bar{\rho} |u|^2 |w| dS}_{L_{KE} = AF_{KE}} + \underbrace{\int_{S_{z'}} -(\tau_{ij} u_i) \cdot \mathbf{e}_z dS}_{L_{visc} = AF_{visc}}, \quad (5.21)$$

in which we define the enthalpy flux ( $F_e$ ), the conductive flux ( $F_{cond}$ ) the kinetic energy flux ( $F_{KE}$ ), and the viscous flux ( $F_{visc}$ ). Similarly, instead integrating over the internal energy equation yields,

$$L = FA = \underbrace{\int_{S_{z'}} \bar{\rho} \bar{T} s w dS}_{L_{conv} = AF_{conv}} + \underbrace{\int_{S_{z'}} -\kappa \bar{\rho} \bar{T} \frac{\partial s}{\partial z} dS}_{L_{cond} = AF_{cond}} + \underbrace{\int_{V_{z'}} -s \bar{\rho} (\mathbf{u} \cdot \nabla) \bar{T} dV}_{L_{buoy} = V Q_{buoy}} + \underbrace{\int_{V_{z'}} -\tau_{ij} \frac{\partial u_i}{\partial x_j} dV}_{L_{diss} = V Q_{diss}}, \quad (5.22)$$

defining the convective flux ( $F_{conv}$ ). Recall from Section 5.4.2 that the total dissipative heat-

ing ( $Q_{diss}$ ) and the work done against the background stratification ( $Q_{buoy}$ ) must exactly balance when integrated over the entire convective volume, but do not have to balance at each depth. If they do not, those regions will begin to experience a net heating or cooling. In a steady state the flux of energy out of each layer must adjust to compensate via transport terms that would otherwise be absent. In practice this means that the fluxes of enthalpy and of kinetic energy are different in highly stratified, dissipative convection than in unstratified cases. Our goal here is to quantify these differences, and to show that consideration of the dissipation can yield insight into the spatial form and magnitude of the various transport terms (or vice versa).

Figure 5.13 presents these various transport terms defined by equation 5.21 in the left-hand column, and equation 5.22 in the right-hand column for a range of stratifications, supercriticalities, and non-rotating and rotating cases. With an imposed flux at the bottom boundary and in the absence of any internal heating terms, the sum of the various transport terms must equal the total luminosity  $L$  and remain constant throughout the layer (regardless of which flux decomposition we consider). This is used as an indicator for when our simulations have achieved thermal equilibrium and can be seen as the solid blue line in Figure 5.13. All cases have been averaged over at least 0.1 viscous timescale ( $\tau_v$ ), and the calculations themselves have been evolved over an average of several  $\tau_v$  (corresponding to hundreds or thousands of convective overturning times) to reach a steady state. The rotating cases that have been presented in this chapter required considerably more time to achieve a steady state (typically  $> 10\tau_v$ ).

We note first that as the Rayleigh number increases, the conductive transport becomes increasingly confined to narrow thermal boundary layers at the top and bottom of the domain as seen between the top two rows. In the top row (the non-rotating, weakly stratified,  $Ra_F = 50Ra_c$  case) these conductive layers extend over about the bottom and top twenty percent of the domain whereas at higher  $Ra_F$  (as sampled in the panels in the second row) they are much narrower. Convective transport (encapsulated mainly by either  $L_e$  in the total energy decomposition, or by  $L_c$  in the internal energy decomposition) always dominates in the bulk whereas the corresponding conductive transport (encapsulated by  $L_{cond}$ ) is approximately zero. At high  $Ra_F$ , near the bottom of the domain there are also

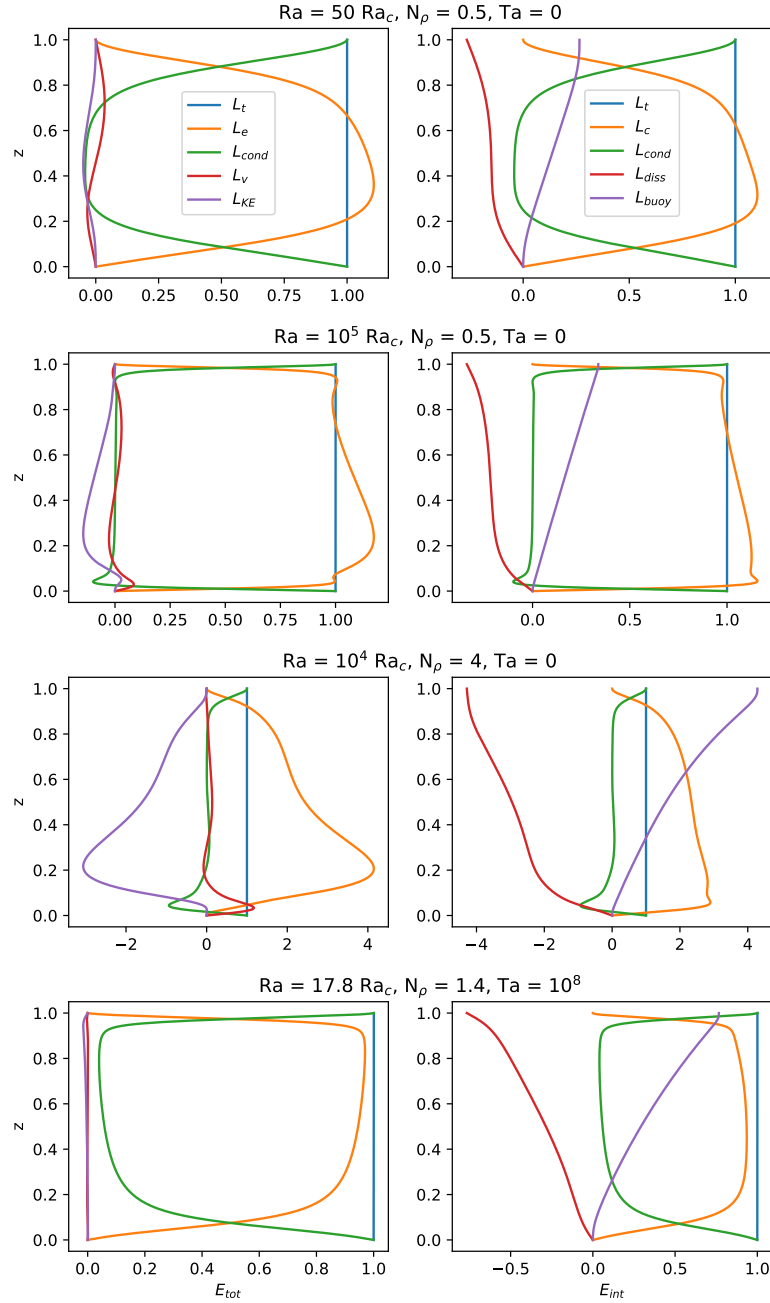


**Figure 5.13:** Fluxes of energy provided by different transport terms in the total energy equation (left panels) and internal energy equation (right panels), for example 2D cases at varying  $\text{Ra}$ ,  $N_\rho$ , and  $\text{Ta}$ .

substantial contributions to the transport from viscous effects ( $L_{visc}$ ), and the conductive transport becomes inward-directed there. This arises because of the development of small regions of stable stratification, discussed more below.

The effects of stratification are also evident. In non-rotating cases at sufficiently high  $Ra_F$ , the enthalpy flux exceeds the total flux in magnitude and this excess is compensated largely by a negative (inward-directed) kinetic energy flux. This behaviour is visible for example in the third row, where  $L_e$  reaches more than four times the total luminosity ( $L_t = 1$ ). Broadly similar transport, and in particular the presence of a large inward-directed kinetic energy flux, has been observed in simulations of stratified convection for decades (see, Hurlburt et al. 1984 in 2D; Stein and Nordlund 1989; Featherstone and Hindman 2016 for examples). Dynamically, the inward-directed KE flux arises because downflowing plumes contract in the background density stratification; they are faster and narrower than upflows, and occupy a smaller filling factor. This asymmetry, which does not exist in Boussinesq convection, is a key feature of the stratified cases considered here.

By contrast, in the rotating cases (bottom row) the kinetic energy flux remains small even at high  $Ra_F$ . The enthalpy flux is approximately equal to the total luminosity, and the conductive transport small outside the boundary layers. At this particular  $Ra_F$ , the boundary layers are still relatively large, and there is evident asymmetry between the top and bottom boundary layers. This asymmetry will be discussed further in Section 5.5.4. For comparison, despite the widely different supercriticalities, the non-rotating case shown in the second row has a comparable  $Ra_F$  to the rotating case on the bottom row ( $3.99 \times 10^7$  compared to the rotating case of  $1.57 \times 10^7$ ) due to the stabilising effect of rotation on convection.

The connection between this transport and the viscous dissipation is made clearer by comparison to the right-hand column of Figure 5.13, which considers the internal energy decomposition for the same cases. As discussed in Section 5.4.2 above, in all cases the buoyancy work is fairly evenly distributed throughout the domain, that is, outside of the bottom boundary layer  $L_{buoy}$  rises linearly towards the top domain. This implies that  $Q_{buoy}$  (the local rate of buoyancy working) is constant with depth. In the non-rotating cases, the dissipative heating  $Q_{diss}$  is much less uniform and much of the dissipation is

occurring near the bottom boundary. Rotating cases, by contrast have much more uniform dissipative heating, with  $L_{diss}$  also linear (that is,  $Q_{diss}$  is constant) outside the boundary layers. At the upper boundary, both  $L_{buoy}$  and  $L_{diss}$  must approach  $\pm E$ , respectively as globally these must balance, and they do so in both the rotating and non-rotating cases. What is different in the rotating and non-rotating cases however is the spatial distribution of  $L_{diss}$ . These results are in agreement with those presented in Section 5.4.2 (see discussion of  $z_{diss}$ ). In the non-rotating cases the convective luminosity is often larger than  $L_{tot}$  (considerably so in the high stratification case) in accordance with the fact that  $L_{diss}$  is consistently greater in magnitude than  $L_{buoy}$  throughout the convective zone. In these cases much of the dissipative heating occurs at the bottom of the layer and so the local difference between these two heating terms is made up for by an increase in the convective luminosity. In the rotating cases, where there is approximate local balance (as well as exact global balance) between the dissipative heating and the “cooling” by buoyancy work, the convective luminosity is closer to unity. In both cases the conductive transport is again small in the bulk of the convection zone, but carries all the flux at the top and bottom boundaries. Note that perfect knowledge of  $L_{buoy}$  would allow prediction of the spatial form and magnitude of  $L_{conv}$ : specifically, it can be shown that  $L_{conv}/T = (1/\theta)dL_{buoy}/dz$ . We consider links between the “transport” and “heating/cooling” terms more carefully in section 5.5 below.

### 5.5.2 Entropy profiles and Nusselt number scalings

In the previous section, we saw that the energy transport in our simulations, specifically the relative contributions of conduction and convection, varied in response to changes in the key controlling parameters  $N_p$ ,  $Ra_F$ , and  $Ta$ . Here we explore how these variations arise, and in particular how they are linked to the entropy gradients established by the convection.

Before analysing these in detail, it is helpful to consider what entropy profiles we expect for the slightly unusual setup described here; for a more thorough review, see Goluskin (2015). In our work entropy is fixed (to zero) at the upper boundary whereas at the lower boundary its gradient is fixed. Recall also that we have employed the LBR approx-

imation, in which the conductive transport is proportional to entropy gradients (rather than temperature gradients). Together, these imply that in the *absence* of convection, we would expect a linear specific entropy profile, extending from  $s = 0$  at the top to some value  $s_{cond}$  at the bottom, with a total entropy variation across the domain  $\Delta s_{cond} = s_{cond}$ . For the models considered here,  $\Delta s_{cond}$  can be determined analytically,

$$\Delta s_{cond} = \frac{F}{\kappa \bar{\rho}_0 \bar{T}_0} \frac{1}{\beta m} [(1 - \beta d)^{-m} - 1], \quad (5.23)$$

where all symbols are as defined above.

Convection transports the heat more efficiently than the static conduction state, and so a smaller total  $\Delta s$  is required to carry the same imposed  $F$ . We have imposed impenetrable top and bottom boundary conditions, so within some distance of the boundary we expect little convective transport and all the flux to be carried by conduction resulting in a relatively steep entropy gradient in this region. By contrast, we expect a smaller entropy gradient in the bulk. As the convection becomes increasingly efficient (as we expect it should do as the diffusivities are made lower, or  $Ra_F$  made higher) the value of  $s$  at the bottom boundary should thus become closer to its (fixed) value at the top boundary. Similarly, the value of  $s$  in the middle of the convection zone should tend towards the top boundary value (here  $s = 0$ ) at high  $Ra$ . In short, we expect efficient and turbulent convection to develop isentropic entropy profiles.

In Figure 5.14 we examine the realised entropy profiles in our simulations and compare them to our expectations outlined above. The top panel shows non-rotating cases at  $N_p = 1.4$  at varying supercriticalities, the middle panel shows non-rotating cases at fixed supercriticality ( $10^4 Ra_c$ ) but varying  $N_p$ , and the bottom panel shows rotating cases at fixed  $Ta = 10^8$  but varying  $Ra_F$ . Note that as discussed above, due to the stabilising effects of rotation  $Ra_c$  is considerably higher in the rotating cases than the non-rotating ones. For example, at  $Ta = 10^8$ ,  $Ra_c \approx 6.7 \times 10^5$ , whereas in the non-rotating cases at the same stratification  $Ra_c \approx 227$ . A useful comparison here is that the rotating case of  $Ra_F = 17.8Ra_c$  shown in the bottom panel has  $Ra_F$  comparable to that of the non-rotating  $10^4 Ra_c$  case in the top panel.

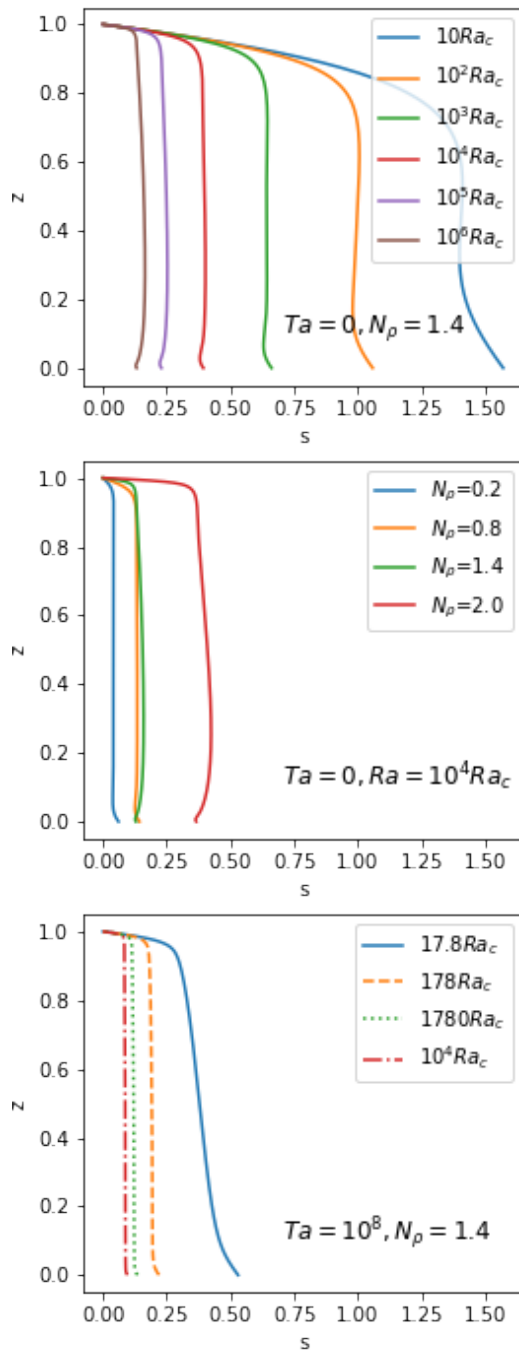


**Figure 5.14:** Specific entropy,  $s$ , as a function of depth in a variety of non-rotating and rotating cases at a range of stratifications, and  $Ra_F$ . The top panel shows non-rotating cases with  $N_\rho = 1.4$  at a range of supercriticalities, the middle panel shows non-rotating cases at fixed supercriticality but varying  $N_\rho$ , and the bottom panel shows rotating cases with  $Ta = 10^8$  and  $N_\rho = 1.4$  at varying supercriticality.

In the non-rotating cases (top) it is clear that increasing  $Ra$  implies a smaller total  $\Delta s$  across the domain, with both the bottom boundary value of  $s$  and the value at mid-layer approaching  $s = 0$  (the value fixed at the top of the domain). This is in keeping with our expectation that lower-diffusivity, more efficient convection should transport the same flux with greater ease resulting in a smaller entropy contrast across the convective layer. At high enough  $Ra_F$  the interior is nearly isentropic, but there are boundary layers at top and bottom. One striking feature is that these are clearly asymmetric, with the top thermal boundary layer substantially thicker than the bottom one. Another noticeable feature is that at some sufficiently high  $Ra_F$ , the interior is actually on average slightly subadiabatic (that is, has a positive slope and would imply local stability to convection). The latter feature has been seen in a variety of settings (Korre et al. (2019), Käpylä et al. (2019)). We discuss the asymmetry of the boundary layers in more detail below (see Section 5.5.4), but note that it was anticipated theoretically (Jones et al. 2022).

At fixed supercriticality (middle panel), increasing  $N_\rho$  appears to lead to "less efficient" transport, that is, a somewhat larger  $\Delta s$  across the layer, and interior profiles that are less isentropic. The extent of the aforementioned subadiabatic regions appears to depend on the stratification as well. At the  $Ra_F$  shown here these regions are essentially absent in the nearly-Boussinesq calculations ( $N_\rho = 0.2$ ) but are clearly present in the more stratified cases.

In the rotating cases sampled in the bottom panel, the cases at very high  $Ra$  are not dynamically influenced by rotation ( $Ro_c > 1$ ) and as a result their entropy profiles resemble those of the non-rotating cases at high  $Ra_F$ . Like those cases, they possess narrow thermal boundary layers and nearly isentropic interiors. When rotation plays a significant role, however, the entropy profile is quite different. Comparing the rotating simulation at  $Ra_F = 17.8Ra_c$  (blue line in the bottom panel) to the  $10^4Ra_c$  non-rotating case (red line in the top panel), which has a comparable  $Ra_F$ , we see that the rotating case requires a larger  $\Delta s$ , that is, the presence of rotation has made the convection less efficient. The interior entropy profile is, for this and other cases in which rotation is dynamically important, no longer nearly isentropic and there is a pronounced negative slope implying superadiabaticity at all depths within the bulk.

To analyse the trends detailed above more quantitatively we turn now to an average measure of the heat transport over the domain (rather than to its spatial variation). In studies of Rayleigh-Benard convection, it is customary to encapsulate this via the Nusselt number  $\text{Nu}$ , a dimensionless measure of the heat transport relative to that provided by conduction (see Section 2.2.2). Additionally, this will help us frame the results observed here in the context of prior studies of convective theory as discussed in Section 2.3. There is no universally-accepted definition of  $\text{Nu}$  that makes sense for all boundary conditions, stratifications, and with/without rotation, but it is sensible to define it such that the value is large for efficient convection, and unity for fully conductive transport. For the mixed fixed-flux, fixed-entropy boundary conditions used here, we therefore to adopt

$$\text{Nu} = \frac{\Delta s_{\text{cond}}}{\Delta s}, \quad (5.24)$$

as our definition of  $\text{Nu}$ . This is a global measure of the efficiency of the convective flow and the resulting entropy contrast that is established, normalised to the  $\Delta s_{\text{cond}}$  that would be required to carry the imposed flux in the absence of any convection. Efficient convection should result in a small  $\Delta s$  across the layer and therefore a higher  $\text{Nu}$ . It is of note that the normalisation is irrelevant when comparing cases that vary  $\text{Ra}_F$  for a fixed  $N_p$  (as  $\Delta s_{\text{cond}}$  depends only on the stratification), but is necessary for comparing simulations of different  $N_p$ . This definition of the Nusselt number is analogous to that used for Boussinesq convection by Kazemi et al. (2022).

The resulting measures of  $\text{Nu}$  are plotted for a sample of cases with varying  $\text{Ra}_F$ ,  $N_p$ , and  $\text{Ta}$  in Figure 5.15. We have also overplotted several scaling relations that have been previously proposed in the literature (again, see Section 2.3 for a review of those relevant to this discussion). As  $\text{Ra}_c$  varies so much across the simulations sampled here we have chosen here not to normalise each case by  $\text{Ra}_c$ . In general, each "track" of simulations shown begins with  $\text{Ra}_F$  of order ten times critical at the given  $N_p$  and  $\text{Ta}$ . Note that  $\text{Ra}$  and  $\text{Ra}_F$  are related by equation (2.26), that is  $\text{Ra}_F = \text{Ra}\text{Nu}$ , and extensive use of this relation will be used throughout this section when comparing to prior literature.

First, consider the non-rotating, weakly-stratified cases at  $N_p = 0.5$ . These are well-

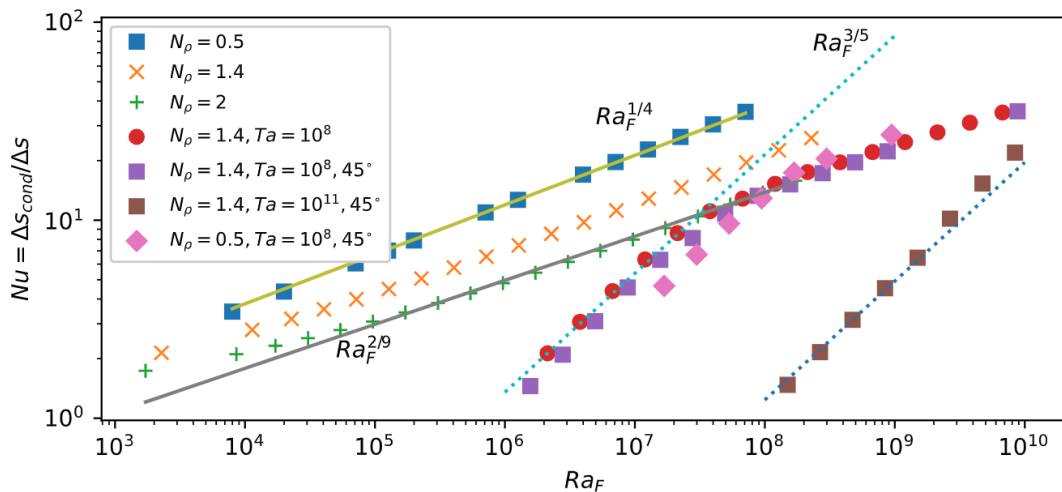


**Figure 5.15:** Calculated values of the Nusselt number,  $\text{Nu}$ , as a function of  $\text{Ra}_F$  for a wide sample of both non-rotating and rotating calculations at a range of different  $N_\rho$  and latitudes.

matched by the power law  $\text{Nu} \propto \text{Ra}_F^{1/4}$ , equivalent to the classic  $\text{Nu} \propto \text{Ra}^{1/3}$  scaling proposed by Malkus (1954b). This scaling is expected if transport within the bulk is entirely by convection, transport within narrow thermal boundary layers is by conduction, and the width of the boundary layers is set by the requirement that they be marginally stable against convection. The scaling at other  $N_\rho$  appears to be slightly different. For comparison, we have overplotted  $\text{Nu} \propto \text{Ra}_F^{2/9}$ , which is equivalent to the  $\text{Nu} \propto \text{Ra}^{2/7}$  scaling that has often been reported in non-rotating experiments and simulations (see discussions in Grossmann and Lohse (2000), Shraiman and Siggia (1990) for example). None of our calculations are consistent with the so-called "ultimate regime" scaling  $\text{Nu} \propto (\text{Ra}\text{Pr})^{1/2}$ , which has been conjectured to apply at very high  $\text{Ra}$ , and forms the basis for astrophysical mixing length theory.

The rotating cases exhibit different scalings. Figure 5.15 shows a series of rotating cases at fixed  $\text{Ta} = 10^8$  (situated at both the pole, and  $45^\circ$ ) and a smaller number of cases at  $\text{Ta} = 10^{11}$ . A transition in scaling relations is observed as the simulations increase in  $\text{Ra}_F$  due to the relative decrease in the dynamical influence of rotation, that is, as they move from a regime in which  $\text{Ro}_c < 1$  to one where  $\text{Ro}_c > 1$ . Those cases with  $\text{Ro}_c < 1$  – are therefore considered to be rotationally constrained – show good agreement with the much steeper rotational scaling of  $\text{Nu} \propto \text{Ra}_F^{3/5}$ . As the level of turbulent driving increases and the rotational cases transition towards a regime in which the influence of rotation on

the dynamics becomes negligible, the cases begin to follow the non-rotating 2/7ths power law scaling. This behaviour is exhibited in both tracks of the  $Ta = 10^8$  cases, however we do not have enough points at  $Ta = 10^{11}$  to draw reliable conclusions there.

This behaviour is consistent with a wide array of prior results in different settings such as 3D simulations in both local and global geometries, Boussinesq calculations in 2D and 3D, and lab experiments, but to our knowledge has not previously been demonstrated for the setup described here (namely 2D anelastic convection with rotation and an imposed flux). The general trends described here, including the transition from a steep "rotating"  $Nu(Ra)$  relation to a shallower "non-rotating" one, have been the subject of considerable recent interest (King et al. (2012), Aurnou et al. (2020)). Interestingly, the results from our rotating cases are in accord with the expectations of rotating mixing-length theory (Currie and Tobias 2020, Barker et al. 2014, Stevenson 1979). The same scaling law also arises in the classical "CIA balance," which supposes a dynamical balance between Coriolis, inertial, and buoyancy ("Archimedan") terms in the momentum equation (Aurnou et al. 2020, Vasil et al. 2021) and in asymptotic theories of convection at low Rossby number (Julien et al. 2012). Unlike the non-rotating scalings exhibited here, this relation is diffusion-free, indicating that in the rapidly-rotating limit the diffusive boundary layers are playing a less significant role in the heat transport. In dimensional terms, this scaling implies that the entropy gradient in the bulk of the convection zone should become steeper when rotation is more rapid, scaling as  $ds/dz \propto \Omega^{4/5}$ , with  $\Omega$  the angular velocity, in this limit. The finite negative slope of the entropy profiles at mid-layer in our low-Rossby cases that we observe (Figure 5.14, bottom panel,  $Ra_F = 17.8Ra_c$ ) is therefore consistent with this limit.

### 5.5.3 Flow amplitudes

Another quantity of keen astrophysical interest is the amplitude of convective motions, as these proceed to influence the mixing, the transport of angular momentum, and the generation of magnetic fields within astrophysical objects. Here we briefly analyse the amplitude of motions encapsulated by the Reynolds number,  $Re$  (see Section 2.2.7) in our simulations as the key parameters are varied. Figure 5.16 shows the non-dimensional velocity (the Reynolds number) as a function of both the supercriticality  $Ra_F/Ra_c$  (top)

and  $\text{Ra}_F$  alone (bottom). We sample a variety of  $N_\rho$  and include both non-rotating cases and rotating ones at  $Ta = 10^8$ . We have overplotted the scaling  $\text{Re} \propto \text{Ra}_F^{1/2}$  to help guide our discussion.

All the non-rotating data appear to be well-matched by the illustrated  $\text{Re} \propto \text{Ra}_F^{1/2}$  scaling. The rotating data also appear to lie close to this, but exhibit a slightly steeper dependence on  $\text{Ra}_F$  in some parameter regimes (namely when  $\text{Ra}_F$  is still low enough that the Rossby number is small). The data at  $N_\rho = 1.4$  and  $N_\rho = 2$  lie essentially on top of one another in this plot, suggesting that the modest differences in stratification between these two cases have little effect on the volume-integrated flow speeds. The calculations at an even weaker stratification ( $N_\rho = 0.5$ ) appear somewhat offset from these in the bottom panel – at fixed  $\text{Ra}_F$ , the weakly-stratified cases have a higher Reynolds number – but this difference disappears if plotted in terms of the supercriticality of the convection (top panel) where the data for all three non-rotating stratifications are indistinguishable from one another. At any fixed  $\text{Ra}_F$ , it is also clear (from the bottom panel) that the rotating cases have weaker flows (lower  $\text{Re}$ ).

A few other aspects of these scalings are notable. One is that our simulations have evidently not attained a "diffusion-free" limit for the flow velocities. Such a limit would correspond (since  $\text{Re} = ul/\nu$  and at  $Pr = 1$ ,  $\text{Ra} \propto \Delta S/\nu^2$ ) to  $\text{Re} \propto \text{Ra}^{1/2}$ , not  $\text{Ra}_F^{1/2}$ . Thus dissipation within the domain is continuing to influence the flow even at the highest  $\text{Ra}_F$  probed here. Similar scalings have been reported in a variety of non-rotating Boussinesq calculations in both 2D and 3D (see discussions in Hepworth (2014), Gastine et al. (2016)), and arises for example if the so-called "VAC balance" (involving the viscous, Coriolis, and buoyancy forces) holds.

It is also striking that the rotating and non-rotating cases here exhibit similar trends, despite their heat transport being quite different as shown in the previous section. In either "rotating mixing length theory" (as described in Currie and Tobias (2020), Barker et al. (2014), Stevenson (1979)) or equivalently in CIA balance (Aurnou et al. (2020), Vasil et al. (2021), Gastine et al. (2016)), typical velocities in the rapid-rotation limit are expected to scale as  $u \propto \text{Ra}_F^{2/5}$ , which is slightly less steep than shown here. If anything, our rotating calculations exhibit a somewhat steeper scaling than the non-rotating ones. Prior calcula-

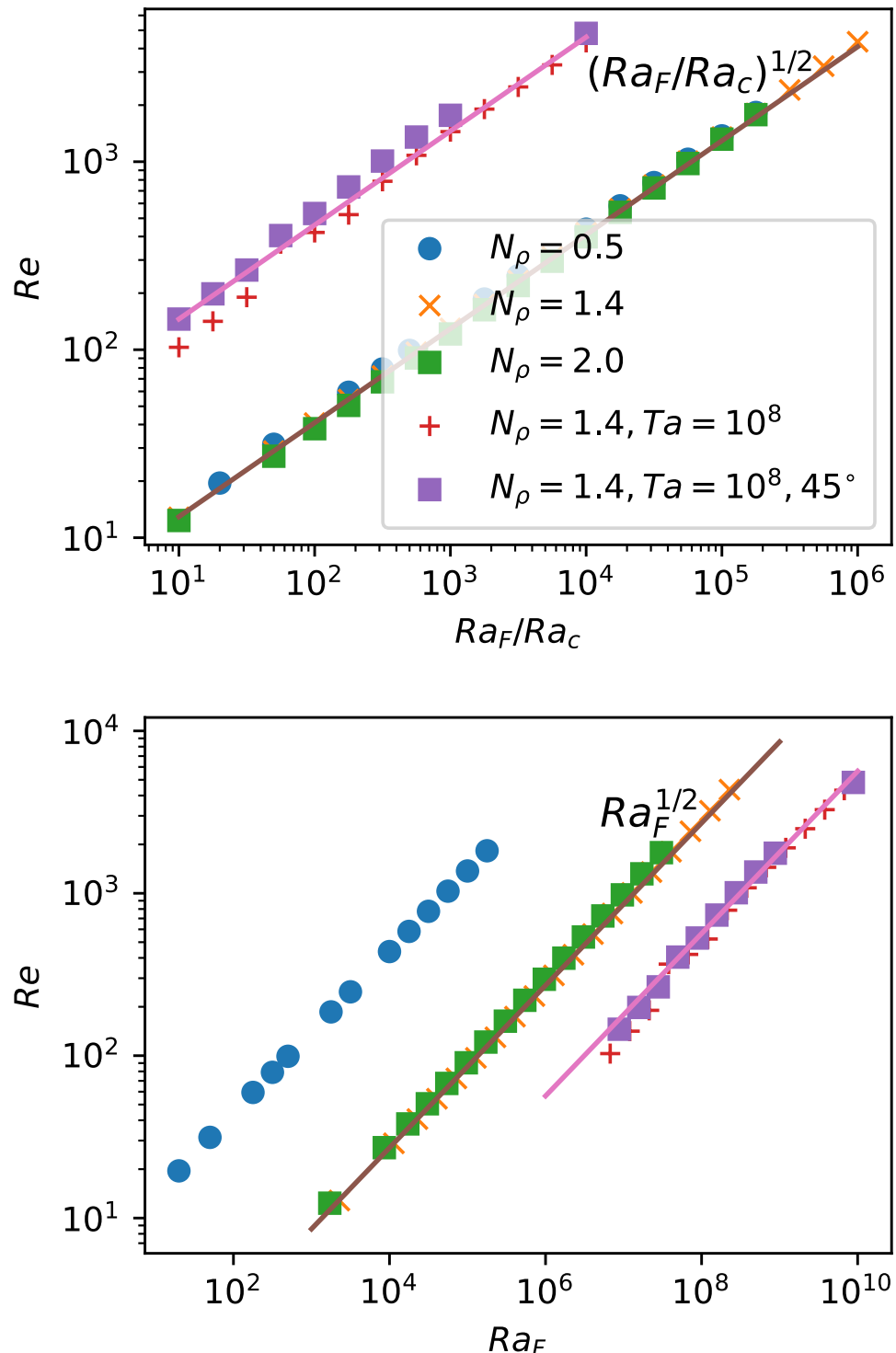


**Figure 5.16:** Values of the non-dimensionalised velocity (the Reynolds number,  $Re$ ) as a function of  $Ra_F$  for a wide sample of both non-rotating and rotating calculations at a range of different  $N_\rho$  and latitudes. The top panel is plotted against  $Ra_F/Ra_c$  whereas the bottom panel is plotted against  $Ra_F$ .

tions in 3D (e.g., Gillet and Jones (2006), Schmitz and Tilgner (2009)) and in 2D (Hepworth (2014)) have likewise noted this discrepancy, and suggested various reasons why it occurs. Broadly, the discrepancy is linked to the continuing role of viscous and thermal boundary layers in both our rotating and non-rotating calculations. This motivates our discussion of these layers in section 5.5.4 below.

#### 5.5.4 Boundary layers and the link to dissipation

The trends explored above arise partly from the varying influence of viscous and thermal boundary layers in our simulations. In this section, we briefly explore how the widths (or rather, depths) and other properties of these boundary layers vary as the supercriticality of the convection, the density stratification, and the rotational influence are changed. We also discuss the manner in which the boundary layers, heat transport, flow amplitudes, and dissipation are linked, and then demonstrate explicitly that knowledge of some of these aspects constrains the others.

Many different definitions of the boundary layers have been employed in the literature on Boussinesq convection, but our inclusion of rotation, our use of a fixed-flux thermal boundary condition at the bottom boundary, and our adoption of stress-free velocity boundary conditions together implies that some of these definitions are not relevant (see discussion in Long et al. (2020)). We choose here to adopt the simple method suggested by Long et al. (2020), that is, by defining the width of these layers (near the top and bottom of the domain) to be the points at which the advective and conductive contributions to the heat transport are equal. As discussed in Section 5.5.1, inside the boundary layer conduction dominates the heat transport whereas in the bulk convection dominates. Long et al. (2020) demonstrate that this method gives sensible results in a variety of Boussinesq settings (with and without rotation), though to our knowledge it has not been previously employed to study anelastic convection simulations.

At the top and bottom boundaries conduction must carry all the energy (because in our simulations the vertical convective velocity goes to zero there). The value of the entropy gradient  $\partial S / \partial z$  at the bottom boundary is therefore determined by the energy flux entering the domain. At the top boundary, the entropy is fixed (rather than its gradient),

but in a steady state the simulation must still develop a sufficiently large entropy gradient to carry the same energy flux out the top boundary. As we have assumed that conduction diffuses entropy, we must have

$$F_{tot} = F = \kappa \bar{\rho} \bar{T} \nabla S \quad (5.25)$$

at both the top and bottom boundaries. Because we are considering stratified convection, the top and bottom densities can be very different (as discussed recently in both Sections 5.5.1 and 5.5.2), so we expect the entropy gradients  $\nabla S$  that develop will in general be different at the two boundaries.

We now suppose that within the conductive boundary layers  $\partial S / \partial z$  is approximately uniform, and equal to

$$\frac{\partial S}{\partial z} \approx \frac{\Delta S_{bl}}{\delta_{bl}} \approx \frac{F}{\kappa \bar{\rho} \bar{T}} \quad (5.26)$$

where  $\Delta S_{bl}$  is the entropy jump across the boundary layer and  $\delta_{bl}$  is its depth, and where we have assumed conduction carries *all* the flux within the boundary layer (as opposed to just the majority of the flux, which must be true given our definition of the boundary layer).

In the top panel of Figure 5.17 we compare the resulting predictions for  $\Delta S_{bl} / \delta_{bl}$  to measurements in example simulations. We show the ratio of  $\Delta S_{bl} / \delta_{bl}$  in the top boundary layer to that in the bottom (the latter is order unity for our setup at all  $Ra_F$ , by design). The agreement between the measured values and the estimated value is good at high  $Ra_F$  for all stratifications shown, in both rotating and non-rotating cases. At low  $Ra_F$  the agreement is less exact. With increasing  $N_\rho$  the boundary layers become increasingly asymmetric, so that for example in cases with  $N_\rho = 2$ ,  $\Delta S / \delta$  is more than twenty five times larger in the top boundary layer than in the bottom. This, again, is a consequence of the much smaller densities and temperatures at the top of these stratified domains, which then require a much larger entropy gradient to carry the imposed flux out the top boundary.

A corollary to the above is that at all  $Ra$  studied, we must have  $\Delta S_{bl} \propto \delta_{bl}$  across

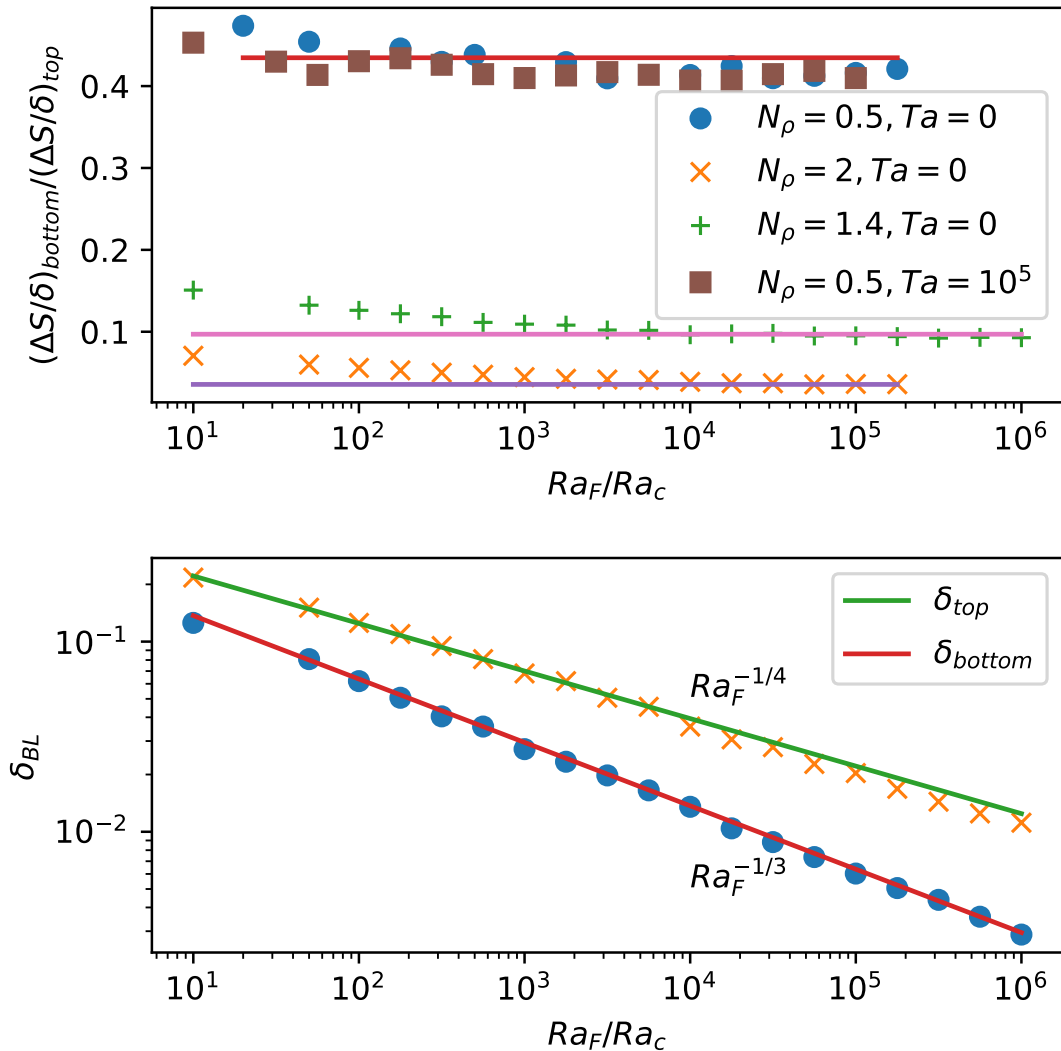


**Figure 5.17:** Properties of top and bottom boundary layers at varying  $Ra_F$ ,  $N_\rho$ , and  $Ta$  shown as a function of supercriticality. The top panel shows the predicted values of the ratio top and bottom boundary layer entropy gradients, compared to those calculated from convective simulations. The bottom panel shows how the depth of the top and bottom boundary layers  $\delta_{BL}$ , overplotted with  $Ra_F^{1/4}$  and  $Ra_F^{1/3}$  scalings.

both boundary layers. That is, although the boundary layers grow thinner at high  $Ra$ ,  $\Delta S$  across the boundary layer must drop in the same way.

In the bottom panel of Figure 5.17 we show how the top and bottom boundary layer depths vary with  $Ra_F$  for example cases at  $N_p = 1.4$ . As expected, the boundary layers grow thinner at higher  $Ra_F$ . However, interestingly the top and bottom boundary layers appear to follow slightly different trends. We have overplotted two scaling relations which we have found to fit the data well, specifically  $\delta \propto Ra_F^{-1/4}$  for the top boundary layer, as well as  $Ra_F^{-1/3}$ , which matches the bottom boundary layer well. This asymmetry in the scaling behaviour of the two boundary layers has not to our knowledge previously been predicted. In principle, it could be a consequence of our different boundary conditions on the two surfaces (fixed entropy at the top, fixed  $\partial S/\partial z$  at the bottom), though we note that prior work such as that presented in Long et al. (2020) has not, in the Boussinesq case, observed different scaling behaviour in the boundary layers for mixed boundary calculations. It is also possible that this behaviour arises from the different flows that prevail in the top and bottom of the domain, and which influence the boundary layer depth. In Boussinesq convection this "wind of turbulence" plays a significant role (Grossmann and Lohse (2000)), and the anelastic equivalent need not be the same at the top and bottom of the domain because the symmetry that exists about midplane, which is present in unstratified convection, is absent in the stratified regime.

These findings are consistent with, and aid in understanding, our findings for the dynamics and heat transport (such as the  $Nu(Ra_F)$  scalings) in previous sections. In the non-rotating cases at high  $Ra_F$  the interior is nearly isentropic, so nearly the entire  $\Delta S$  across the whole domain occurs in the top and bottom boundary layers. As a result their depth determines the overall Nusselt number for the entire domain. These boundary layers act to form a "thermal bottleneck" that inhibits the transport and the top boundary layer is (in our stratified calculations) probably the more restrictive of these because it is thicker. We expect that in these calculations the Nusselt number should scale approximately as the total depth of the domain,  $d$ , divided by the depth of this layer,  $\delta_{bl}$ , e.g.  $d/\delta_{bl}$ . This implies that  $Nu$  should scale as  $Ra_F^{1/4}$ . This is broadly in agreement with many of our findings in Section 5.5.2 above. However, as the total behaviour is likely to be a

combination of what is occurring in the bulk and in both boundary layers, so it is perhaps not surprising that the Nu(Ra<sub>F</sub>) scaling deviates slightly from this in some regimes.

It is clear then, that the rotating cases must exhibit different heat-transport scalings. Prior discussions in 5.4.2 on the value of  $z_{diss}$  showed that simulations of rotationally constrained convection have more of their dissipation occurring in the bulk. This has been demonstrated in prior Boussinesq calculations in both 2D and 3D (Gastine et al. (2016)), but not for the setup investigated here. It arises, fundamentally, because the dissipation and the work done against the background stratification must balance; this balance gives rise to the exact relationship in Boussinesq convection between the Nu(Ra) relationship and the viscous dissipation (Shraiman and Siggia 2000), and to a more complex analogue of this in the anelastic case (as shown recently by Jones et al. 2022). Changes in where the dissipation occurs, which themselves arise because the convective velocities and lengthscales change in the presence of rotation (as discussed above), thus also give rise to changes in the heat transport (as quantified by the Nu(Ra) relation).

In particular we find that cases that fall on the rotating scaling relation systematically have larger  $z_{diss}$  than those which follow the non-rotating heat transport scaling. In our simulations the threshold between these two regimes (the high  $z_{diss}$ , rotating cases, and the low  $z_{diss}$ , non-rotating cases) occurs around  $z_{diss} \sim 0.5$ . It is striking that knowledge of  $z_{diss}$  alone appears sufficient to determine whether our simulation will follow the rotating or non-rotating scaling law.

### 5.5.5 Predicting the kinetic energy flux from the viscous dissipation

The transport revealed here differs in some important ways from that envisioned in mixing length theory (MLT), and some of these differences are connected to where the viscous dissipation occurs. In this section we consider, in particular, the kinetic energy flux, which is not present in classical MLT but is a robust feature of stratified convection in stellar environments. Generally we (like many authors in a variety of settings, in both 2D and 3D) find that the enthalpy flux exceeds the total luminosity by a considerable amount, and is compensated for by the inward-directed (negative) KE flux. However, prior work has not clearly established what sets the amplitude of these fluxes. Might it be possible, for

example, for a star like the Sun to have a thousand solar luminosities moving outwards in the enthalpy flux, and 999 moving inwards via the KE flux? In this section we show that knowledge of the viscous dissipation can answer this question, and more generally provide constraints on the magnitude and spatial form of the kinetic energy flux.

Following Currie and Browning (2017), we define  $F_{other} = \int_0^{z'} (Q_{buoy} + Q_{diss}) dz$ , so that if conduction is negligible (as it is in the bulk of our simulations) the total flux  $F \approx F_{conv} + F_{other}$ . Physically,  $F_{other}$  gives the local difference between heating (by dissipation) and cooling (by work against the stratification). Once again, these quantities must balance when integrated over the entire domain, but they do not have to balance at each  $z$ . Equivalently,  $F_{other} = F_p + F_{KE} + F_{visc}$ , where  $F_p = \frac{1}{A} \int_{S_z} w p dS$  is the difference between the enthalpy flux  $F_e$  and the convective flux  $F_{conv}$  (sometimes called the “pressure dilatation” flux, e.g. Viallet et al. (2013)). Hence  $F_{other}$  is equivalent to the steady-state transport associated with processes other than the convective flux as defined above. Outside of the boundary layers, we find that  $F_{KE}$  is always larger in magnitude than  $F_p$  or  $F_{visc}$ , so that in the bulk  $F_{other} \approx F_{KE}$ .

If the local heating and work terms *do* balance at each depth, then  $F_{other}$  is zero. This in turn implies negligible kinetic energy flux. This is approximately the state attained in many of our rotating cases as discussed in Section 5.5.1 where both  $L_{diss}$  and  $L_{buoy}$  are linear in  $z$ , and of similar magnitude, such that  $F_{other} \ll F_{tot}$ .

In our non-rotating 2D cases, by contrast, the concentration of much of the dissipative heating near the bottom boundary implies a substantial mismatch between heating and cooling throughout much of the bulk, so  $F_{other}$  is no longer negligible. This in turn requires that there be a substantial kinetic energy flux. Physically, if viscous dissipation is preferentially occurring in part of the convection zone, that area will tend to heat up, and in a steady state, fluxes must develop that carry the excess heat away from this region.

We can use these ideas to place simple bounds on the magnitude and spatial form of the kinetic energy flux. Consider the extreme case in which *none* of the viscous dissipation occurs in the bulk (i.e., it is all in a comparatively narrow bottom boundary layer). At some depth just *above* this boundary layer, then, nearly all the integrated viscous heating

will have occurred, but very little of the integrated work (which is distributed over the whole domain) will have. In the notation employed here,  $L_{buoy}$  will be close to zero, while  $L_{diss}$  will be nearly equal to its value at the top of the domain. The latter is bounded by  $E = d/\tilde{H}_T$ , as discussed in Section 5.4.1, so we have  $L_{other} \approx E$ . Hence, if the “other” transport is dominated by the KE flux (rather than  $L_p$  or  $L_{visc}$ ) we expect the maximum value of  $L_{KE}$  to be bounded by the value of  $E$  at each stratification.

We examine this prediction in Figure 5.18, which shows (top panel) the maximum value of the kinetic energy flux in a series of calculations at varying  $N_\rho$  but fixed supercriticality  $Ra_F = 10^4 Ra_c$ , along with the limiting value of  $E$  predicted by equation 5.1 and the actual value of  $E$  attained in the simulation. For cases at  $N_\rho$  of two or less, the measured  $E$  values adhere closely to the limiting value (indicated by the black line); at the highest  $N_\rho$ , the measured values are lower than the theory, which (as discussed above) we think occurs because even higher  $Ra_F$  would be required to reach the “dissipative asymptote.” The KE flux closely tracks the measured value of  $E$  at each stratification (lying slightly below it), in keeping with the simple model described above.

These results suggest that at high enough Ra the maximum amplitude of the kinetic energy flux may be reasonably well-estimated simply by calculating  $E = d/\tilde{H}_T$  (equation (5.1)). We suggest that non-rotating (or very weakly rotating) systems may approach this limit. However (as noted in Section 5.5.1) in the rotating cases the dissipative heating appears to almost completely balance the buoyancy work at each height, leading to significantly smaller kinetic energy fluxes. Predicting the spatial *form* of the kinetic energy flux is more difficult, and we have not found a reliable way to do so at all  $N_\rho$  and Ra considered here.

## 5.6 Chapter summary

We have presented the first systematic investigation of viscous dissipation in a rotating, stratified plane layer of convection, studied here within the anelastic approximation for an ideal gas. We have shown that the dissipative heating in rotating and non-rotating cases appears to approach a similar upper bound when the convection is vigorous enough

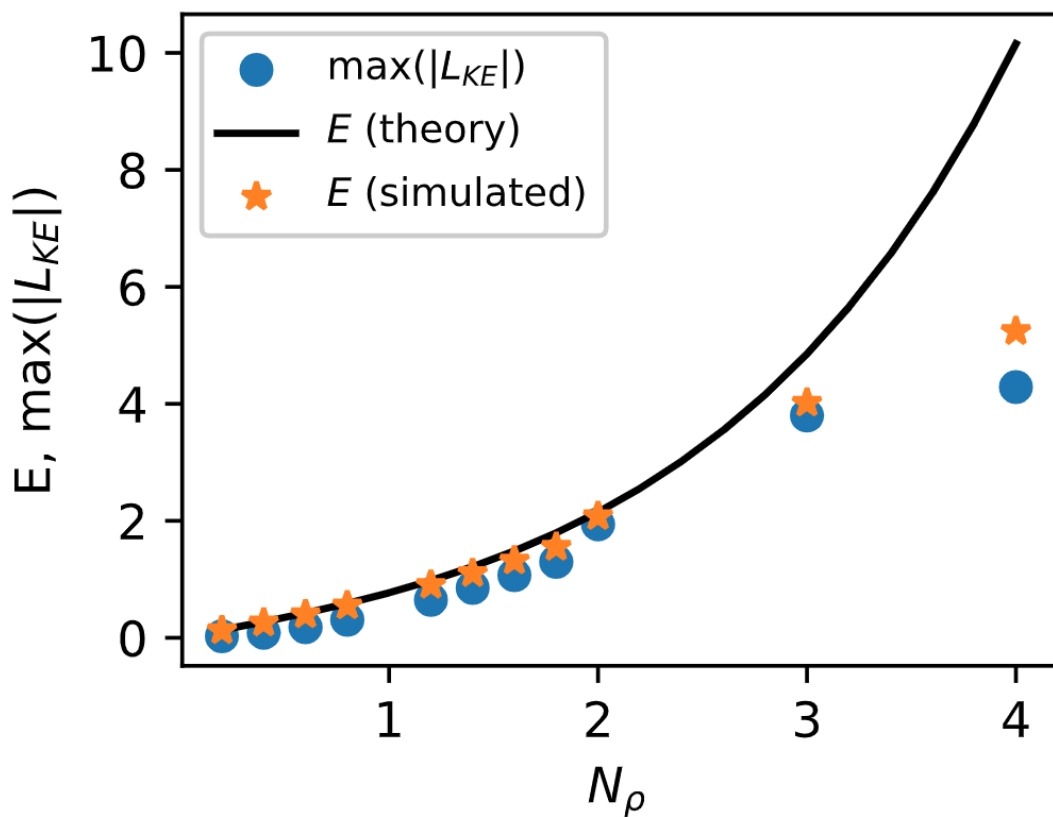


**Figure 5.18:** A plot of KE flux magnitudes for varying  $N_\rho$  at asymptotically high  $Ra_F$ , compared to simulations at finite  $Ra_F$ .

(i.e., at high enough supercriticalities  $\text{Ra}/\text{Ra}_c$ ) as seen in Currie and Browning (2017) for the non-rotating case with different boundary conditions and box size. However, as in prior Boussinesq calculations, the spatial *distribution* of the dissipation does vary with rotation rate, and this has a number of important consequences for the dynamics and heat transport. We have investigated these in some detail, and recapitulate some of our main findings below, before commenting on their possible astrophysical implications.

First, we recall that the upper bound on the volume-integrated dissipative heating, as approached in our cases, scales with the vertical depth of the layer divided by a version of the local scale height. This means that in deep, stratified layers the total dissipation can exceed the luminosity passing through the layer, a result not possible in Boussinesq systems. This upper bound does not depend directly on the diffusivities or on rotation rate.

We have shown that in rotating cases the viscous dissipation is much more uniformly distributed throughout the layer than in corresponding non-rotating cases. In the non-rotating simulations, much of the dissipation occurs near the bottom of the computational domain, so that although there is a global balance between dissipation and work done against the background stratification, these quantities do not balance at each depth. We defined a new quantity  $z_{diss}$ , the height at which half the total viscous dissipation has occurred, which encapsulates the spatial distribution of the dissipation in a simple way, and used it to characterise our simulations in different regimes.

We have noted that the heat transport properties of the rotating and non-rotating cases are different. We have shown in particular that the heat transport scalings ( $\text{Nu}(\text{Ra})$ ) in our rotating cases appear to be consistent with theoretical diffusion-free predictions arising from either "rotating mixing length theory" (Stevenson 1979; Barker et al. 2014; Currie et al. 2020) or, equivalently, from a conjectured balance between Coriolis, inertial, and buoyancy forces (Aurnou et al. 2020; Gastine et al. 2016; Vasil et al. 2021). Prior work has shown this in other settings (mainly Boussinesq), but not for the specific system studied here (namely, a 2.5D anelastic gas with an imposed heat flux and stress-free boundaries). We have also explored how the entropy profiles and flow speeds in our simulations vary with stratification, rotation rate, and convective supercriticality.

We have shown that these changes in heat transport are linked to where in the domain the dissipation occurs. This is similar to the case in Boussinesq convection, where prior work (such as Grossmann and Lohse (2000)) has established that the Nu(Ra) heat transport relation varies depending on whether the dissipation is "bulk" or "boundary" dominated, and broadly in line with very recent theoretical predictions for the anelastic case (Jones et al. 2022). Here, the situation is more complex because of the background stratification, but the same basic trends appear to hold. In particular, we find that cases which follow the "rotating" heat transport relation are those for which  $z_{diss}$  is especially high (namely  $z_{diss} > 0.5$ ), indicating that more than half the dissipation occurs in the upper convection zone.

We also established that for the setup examined here, the thermal boundary layers in our simulations are asymmetric as a result of the stratification (the top one being considerably larger than the bottom) and that the thicknesses of the top and bottom boundary layers scale differently with Ra. To our knowledge, this has not previously been demonstrated. In the non-rotating cases, knowledge of the boundary layer width suffices to determine the overall heat transport scaling, as there is little dissipation and a negligible entropy gradient within the bulk of the convection zone.

Finally, we have explored the link between dissipation and the kinetic energy flux. We developed a simple model of the kinetic energy flux in our non-rotating cases based on the idea that dissipation approaches the upper bound at high enough Ra, and that much of the dissipation occurs near the lower boundary. This model provided a reasonably accurate prediction of the maximum (negative) kinetic energy flux attained in our simulations for each stratification at high enough Ra.

There are many limitations and caveats to our work. Perhaps the most severe of these is that almost all of our simulations were conducted within a "2.5D" approximation (Section 5.2.1), assuming axisymmetry in one dimension. It may well be that the dissipative properties in the full 3D problem are very different. Additionally we have neglected magnetism meaning all the dissipation here is viscous. In real stars most of the dissipation is likely to be Ohmic (Brandenburg 2014). At a more basic level, we have not explored how variations in the equation of state, or in other properties like the fluid Prandtl num-

ber, affect our results; there is evidence that very different results can be obtained for other equations of state (Alboussière et al. 2022).

Nonetheless it is interesting to speculate about what implications our findings might have, if similar results are obtained in real stars.

One conclusion is that rotating stars should likely exhibit less convective overshooting into adjacent stably-stratified regions. From the perspective adopted here, this is because the buoyancy work at each depth is more nearly balanced *locally* (rather than just globally) by dissipation. Equivalently, the rotating cases have more dissipation per unit volume in the bulk (all else being equal). For a fixed stratification, this will imply (following the discussion in Anders et al. 2022) that convective motions in rotating cases will have less momentum "left over" as they reach the boundary of the convectively-unstable region, and so they will penetrate less deeply into the adjacent layers.

Similarly, we expect a smaller kinetic energy flux in rotating stars and planets than in non-rotating ones. The dynamical consequences of this are not yet clear – the kinetic energy flux is not even present in standard 1D models of the convection, though it is of similar magnitude to the enthalpy flux – but we intend to explore this issue in the future.

We have also noted that heat transport in our most highly stratified, non-rotating cases is less efficient, that is, has a lower Nusselt number at any fixed Ra than in weakly-stratified cases. In the context of stellar astrophysics, this might be observable in the form of a different effective "mixing length" being required to match data for stars with different stratifications. We hope to examine these predictions in future work.

## Chapter 6

# Influence of the interior convective heat flux on planetary atmospheres

The previous chapters of this thesis have been focused on the study of convection in idealised fluids, and by necessity in parameter regimes that are often very distant from those more representative of a real star. This chapter will take a step closer towards the study of more physically realised fluids, that is, the study of their atmospheres of young hot Jupiters and brown dwarfs. In particular it will focus on the relatively unexplored and somewhat nonphysical bottom boundary conditions commonly used in numerical studies of these objects. The work presented in this chapter is still very much ongoing, and as such the results presented here are to be viewed as preliminary.

### 6.1 Basic simulations of hot Jupiters and brown dwarfs

Due to the large distances between the Earth and these hot Jupiter exoplanets, observational constraints on the atmospheric circulation and dynamics are almost impossible to obtain with some exceptions (Louden and Wheatley 2015) (see discussion in Section 1.1.2). Instead, we turn to numerical simulations such as those performed using the Unified Model, or UM (see Section 3.3), to study the development of their dynamics. In particular, the focus is on developing the nonphysical treatment of the radiative-convective boundaries that lie at the bottom of these planetary atmospheres. It is reasonable to believe that

in a real hot Jupiter this boundary is not a impermeable layer with a constant heat flux across it but a dynamical region enables exchange between the convective interior and the overlying atmosphere.

### 6.1.1 An introduction to radius inflation in hot Jupiters

The anomalously inflated radii of highly irradiated, tidally locked gas giant planets (known as hot Jupiters) has been a long standing problem in the field of exoplanet studies since the discovery of HD 209458 b (Brown et al. 2001).

Several mechanisms have been proposed in an attempt to explain the inflation of these exoplanet's radii (see Baraffe et al. 2010; Baraffe et al. 2014; Fortney and Nettelmann 2010 for reviews) however as of now there does not appear to be a satisfactory resolution to the problem. One promising mechanism is through some additional energy dissipation in the planet's interior leading to a warmer internal adiabat and thus inflating their radii. Lubow et al. (1997) showed that tidal synchronisation of these hot Jupiters could give rise to a large heat flux however this mechanism is constrained to the planet's early evolution and so would quickly become negligible as the timescales on which this mechanism operate are considerably shorter than the ages of these hot Jupiter planets. In a similar vein Bodenheimer et al. (2001) argued that this internal heating could result from tidal circularisation of the orbits eccentricity, however again, this is a transient process would last  $\sim 10^8$  years and so unless the planet had a massive companion capable of exciting the eccentricity then this heating source is inappropriate for. These two potential sources of this "missing energy" are therefore not convincing.

Showman and Guillot 2002 demonstrated that if a small fraction ( $\sim 1\%$ ) of the incident stellar flux is transformed into kinetic energy in the planetary atmosphere and carried down to the interior where it is then subsequently dissipated as thermal energy then the observed radius of HD 209458 b could be reproduced. Growing observational evidence of a correlation between inflated radii and incident stellar flux (Demory and Seager 2011; Laughlin et al. 2011; Weiss et al. 2013 for example) further supports the proposal that this missing energy source is in fact the high levels of irradiance that these planets receive. Additionally, more recent numerical work presents the vertical advection of po-

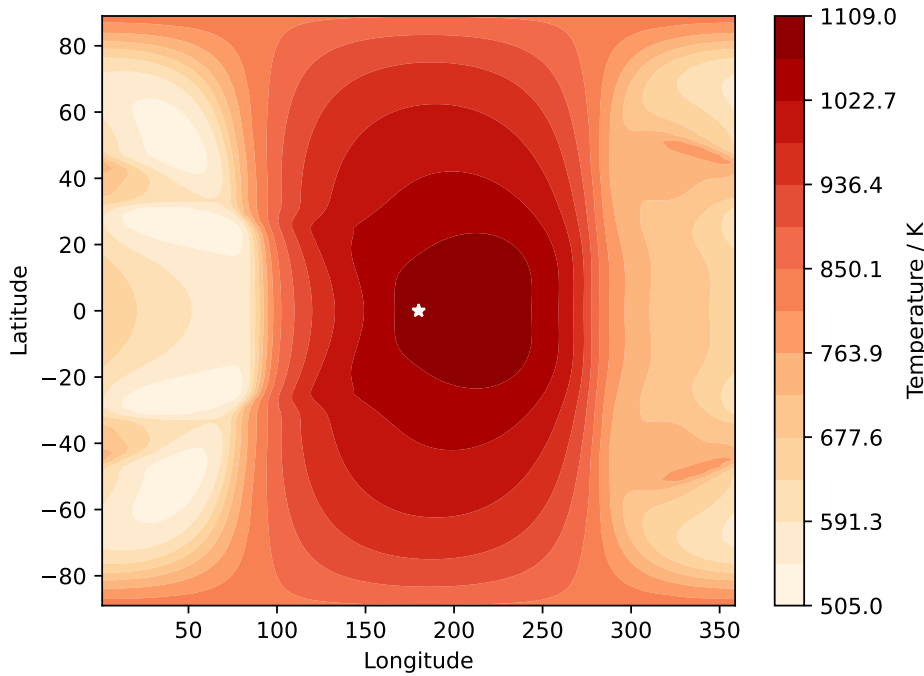


**Figure 6.1:** A latitude-longitude global map of the temperature at the top of the atmosphere for an evolved HD 209458 b atmosphere at  $t = 1150$  days. The white star marker indicates the position of the sub-stellar point.

tential temperature as a robust mechanism for the transport of this additional heating to the internal adiabat (Tremblin et al. 2017; Sainsbury-Martinez et al. 2019; Sainsbury-Martinez et al. 2021). These motions are formed as a result of the large scale circulations established by the non-uniform surface heating.

### 6.1.2 A typical numerical simulation of a hot Jupiter atmosphere

The simulations presented in this thesis are performed using The Unified Model (UM) developed by the UK Met Office and introduced in more detail in Section 3.3. It is a 3D general circulation model (GCM) that was originally developed for simulating the weather and climate of the Earth and has since been adapted to study of atmospheric flows present on exoplanets. It solves the fully compressible, non-hydrostatic equations of motion detailed in Section 3.3.1 in a spherical shell (see Figure 3.5).

This chapter will focus on numerical simulations of HD 209458 b, a commonly studied hot Jupiter. A list of the key parameters used in this model can be seen in Table 6.1.

Parameter	Value
Radius, $R_p$	$9 \times 10^7$ m
Mass, $M_p$	$1.31 \times 10^{27}$ kg
Specific heat capacity, $c_p$	$1.3 \times 10^4$ J kg $^{-1}$ K $^{-1}$
Specific gas constant, $\bar{R}$	3556.8 J kg $^{-1}$ K $^{-1}$
Intrinsic temperature, $T_{int}$	100 K or 500 K
Rotation rate, $\Omega$	$2.06 \times 10^{-5}$ s $^{-1}$
Lower boundary pressure, $P_{bottom}$	200 bar or 10 bar
Upper boundary height	$9.0 \times 10^6$ m
Horizontal resolution	144 (longitude), 90 (latitude)
Vertical resolution	66
Dynamical timestep	30 s
Radiative timestep	150 s

**Table 6.1:** Table of key parameters for simulations of HD 209458b. These are largely similar to those seen in Amundsen et al. 2016 with differences in the bottom boundary pressure,  $T_{int}$ , and the vertical extent of the atmosphere as explained in this chapter.

Due to their short period orbits, hot Jupiters are tidally locked resulting in permanent day and night sides. This uneven heating develops large longitudinal and latitudinal temperature gradients which establish the large scale circulation patterns so commonly seen in studies of these objects. These features can be seen in Figure 6.1 which shows a global temperature map from a typical simulation of HD 209458 b's atmosphere. There is a clear temperature gradient between the day side and night side of the planet is present, with terminators at longitude values of  $90^\circ$  and  $270^\circ$ . Additionally, there is a temperature hot spot near the sub-stellar point as would be expected for a tidally locked planet. Interestingly however, this is offset not insignificantly from the longitudinal position of the true sub-stellar point ( $180^\circ$ ).

The reason for this can be seen in Figure 6.2. As previously mentioned the large scale temperature differential established as a result of the uneven surface irradiation establishes large scale circulation patterns. In particular, these large scale equatorial jets as seen in Figure 6.2 are characteristic of these hot Jupiter simulations, and they act to offset the hot spot from the sub-stellar point due to the horizontal advection of temperature. Similar flows and structures such as the off-set hotspot and large scale zonal flows can be seen in simpler dynamical systems such as the shallow water treatment presented in Showman and Polvani 2011, see Figure 6.3. This feature of hot Jupiter atmospheres was first predicted by Showman and Guillot (2002) and then observed by Knutson et al. (2009).

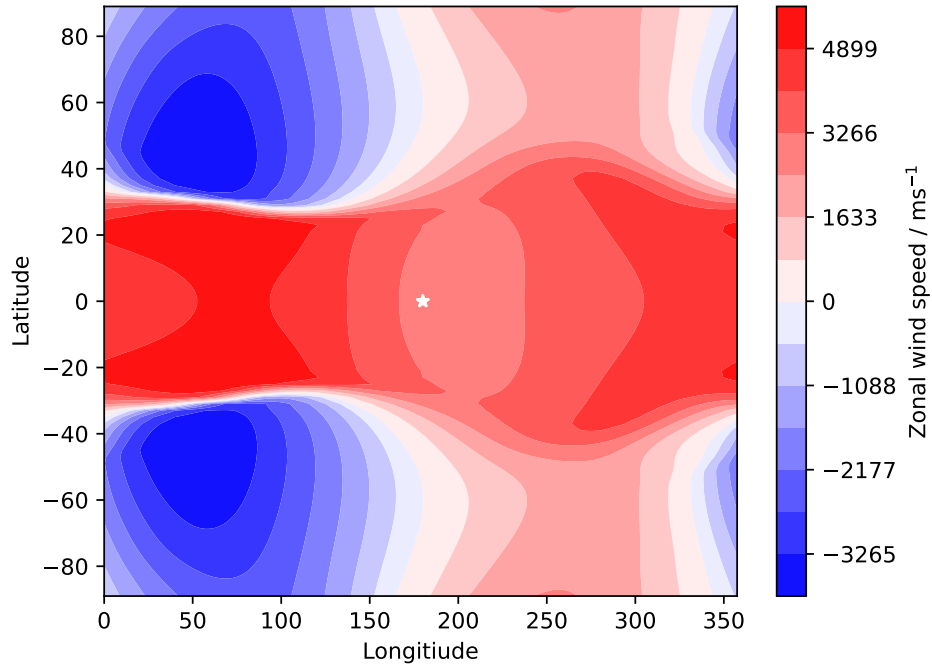


**Figure 6.2:** A latitude-longitude global map of the zonal wind at the top of the atmosphere for an evolved HD 209458 b atmosphere at  $t = 1150\text{days}$ . The white star marker indicates the position of the sub-stellar point.

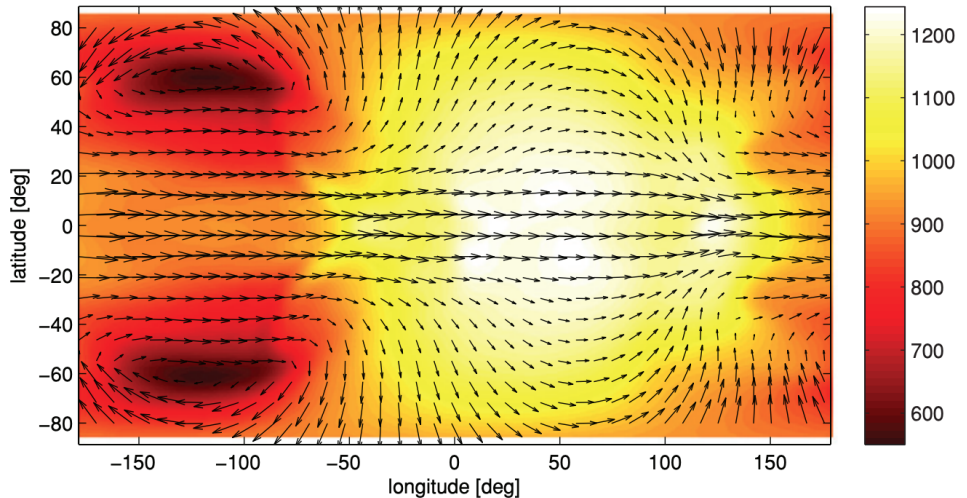


**Figure 6.3:** Figure taken from Showman and Polvani 2011, Figure 12. A latitude-longitude global map of the temperature (colour scale, K) and wind speed (arrows) at 30 mbar pressure of the shallow-water solar-metallicity model of HD 189733b.

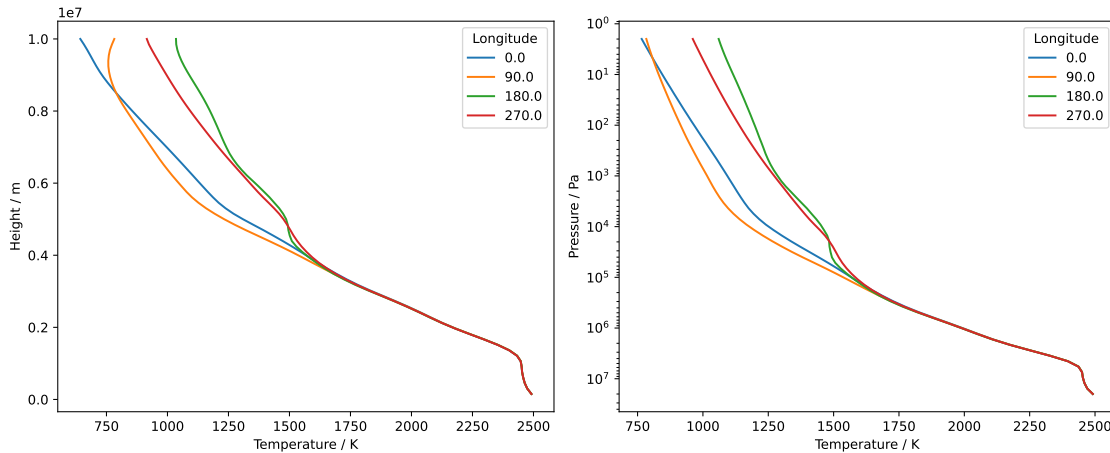


**Figure 6.4:** Vertical profiles of the latitudinally averaged temperature plotted against atmospheric height (first panel) or pressure (second panel) at 4 different longitudes corresponding to the sub-stellar point (green), the anti-sub-stellar point (blue), and the two terminators (yellow and red)

As for the vertical features of these objects, Figure 6.4 presents the latitudinally averaged vertical temperature profiles at the sub-stellar point, the two terminators, and the anti-sub-stellar point. The temperature gradient persists in the upper portion of the atmosphere as the optical depth is still sufficiently small, such that the uneven surface irradiation is able to penetrate down and heat the atmosphere. At increasing depths however the temperature becomes invariant in longitude and the temperature profiles connect to the interior adiabat. The influence of the dominant equatorial jet can be seen on the temperature values at the top of the atmosphere of the two terminators. In the absence of circulation it would be expected that the temperature of these two terminators (yellow and red lines in Figure 6.4) would be equal at the top of the atmosphere. Instead, advection as a result of the equatorial jet brings hot, day-side fluid across the  $270^\circ$  terminator, and cold, night-side fluid across the  $90^\circ$  terminator providing a temperature difference.

The vertical structure of the large eastward equatorial jet, and the relatively weaker counter-rotating westward jets at the mid-latitudes can be seen in the top panel of Figure 6.5. These extend almost the full extent of the atmosphere with stronger counter rotating jets in the deep mid-latitudes. The bottom panel shows the meridional (poleward) circulation, which shows flow away from the equator and towards the mid-latitudes. These circulation patterns are driven by angular momentum transport from the poles and from the deep interior, and are typical features of hot Jupiter atmospheres. One of the primary questions being asked in the following section is how these circulation patterns change

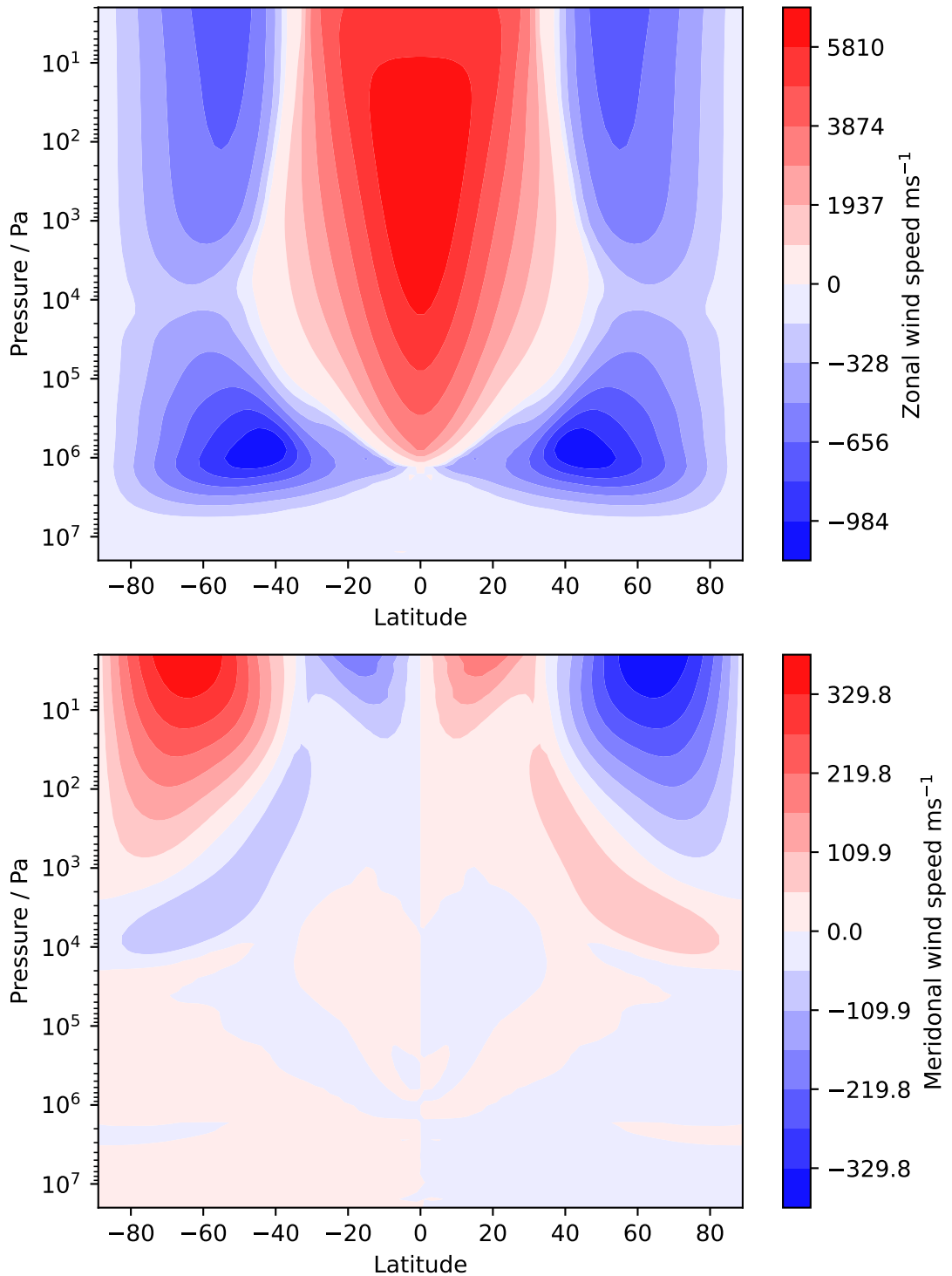


**Figure 6.5:** Zonal (top panel) and meridional (bottom panel) wind profiles averaged in longitude, and plotted as a function of latitude and atmospheric height (first panel) or pressure (second panel). The simulation is of an evolved HD 209458 b atmosphere at  $t = 1150\text{days}$ .

with variation to the internal heating.

## 6.2 Varying the magnitude of the internal heat flux

### 6.2.1 Motivation

While the UM provides us with a way to simulate the atmosphere of these exoplanets one thing it does not explicitly include is the planet's interior convection and the corresponding heat fluxes that are associated with such convective motions. In fact, this is an element of current atmospheric GCMs which is significantly under represented in the literature. As described in Section 3.3.2, this radiative-convective boundary (RCB) is often parameterised in some way at the bottom of the domain by the inclusion of some boundary condition. In the case of the UM, this convective heat flux is parameterised by an upwards heat flux at the bottom boundary of the form  $\sigma T_{int}^4$  where typically  $T_{int} = 100\text{K}$  (Amundsen et al. 2016). This value for  $T_{int}$  is largely inspired by "Jupiter-like" values however observations of the inflated radii of hot Jupiters implies a hotter interior and thus it is reasonable to assume that  $T_{int}$  may in fact be considerably higher.

Similarly, the pressure at which the RCB occurs at is also largely unknown and has historically been taken as "Jupiter-like" of 1 kbar. At such depths however the exact choice is somewhat inconsequential on the resulting evolved atmospheric flow. The timescales on which the deep domain evolve are much slower than the upper atmosphere, and typically are not sufficiently resolved in most simulations (see the bottom of the vertical temperature profiles of our 200 bar simulations in Figure 6.4). However, it follows that the inflated radii suggests hotter and more luminous interiors (higher  $T_{int}$ ), and so implies a shallower radiative-convective boundaries than the historical 1kbar. These "truncated" atmospheres have appeared in some previous literature (Komacek and Youdin (2017) as one example) however have not been extensively studied. Thorngren et al. (2019) derive an equilibrium relation between  $T_{eq}$ , a simple function of the planets irradiance, and the internal heat flux  $T_{int}$ . They suppose that if the mechanism responsible for inflating these hot Jupiters is in fact a result of depositing surplus heat into the interior, then eventually they will achieve some thermal equilibrium where  $E_{in} = E_{out}$  on some timescale potentially as short as tens of megayears (Thorngren and Fortney 2018). Upon reaching equilibrium, the intrinsic

temperature is given by,

$$4\pi R^2 \sigma T_{int}^4 = \pi R^2 F \epsilon(F), \quad (6.1)$$

$$T_{int} = \left( \frac{F \epsilon(F)}{4\sigma} \right)^{\frac{1}{4}} T_{eq}, \quad (6.2)$$

where  $R$  is the radius of the planet,  $\sigma$  is the Stefan-Boltzmann constant,  $F$  is the incident flux on the planet, and  $\epsilon$  is the fraction of flux that heats the interior.  $\epsilon$  itself is a function of the incident flux and by matching model planets with an observed hot Jupiter population in, they infer,

$$T_{int} \approx 0.39 T_{eq} \exp \left( -\frac{(\log(F) - 0.14)^2}{1.095} \right) \quad (6.3)$$

where  $T_{eq}$  is the equilibrium temperature, that is, the temperature a planet would be if it was in radiative equilibrium for a given incident flux. Values of  $T_{int}$  as calculated from equation (6.2) are shown in Figure 6.6. Additionally, Thorngren et al. (2019) go on to present calculated values for the RCB pressure as a function of  $T_{eq}$  as can be seen in Figure 6.6. For HD 209458 b -like values of  $T_{eq}$  and surface gravity, this suggests RCB pressures as shallow as 1-2 bar. In fact, no hot Jupiter with a surface gravity less than  $25\text{ms}^{-2}$  with at least solar-like metallicity should be expected to have an RCB as low as 1 kbar.

### 6.2.2 Numerical simulations

As detailed in the previous section, it is physically possible that these highly irradiated and inflated hot Jupiter exoplanets have much hotter and much shallower radiative-convective boundaries than those that have been previously studied. This section will present some preliminary results on the effects of increasing intrinsic heat flux on the overlying atmosphere, specifically in the case of a truncated atmosphere (RCB pressures  $\sim 10\text{bar}$ ) where the "deep" atmosphere evolves on sufficiently quick time scales that its influence on the overlaying dynamics can be sufficiently resolved.

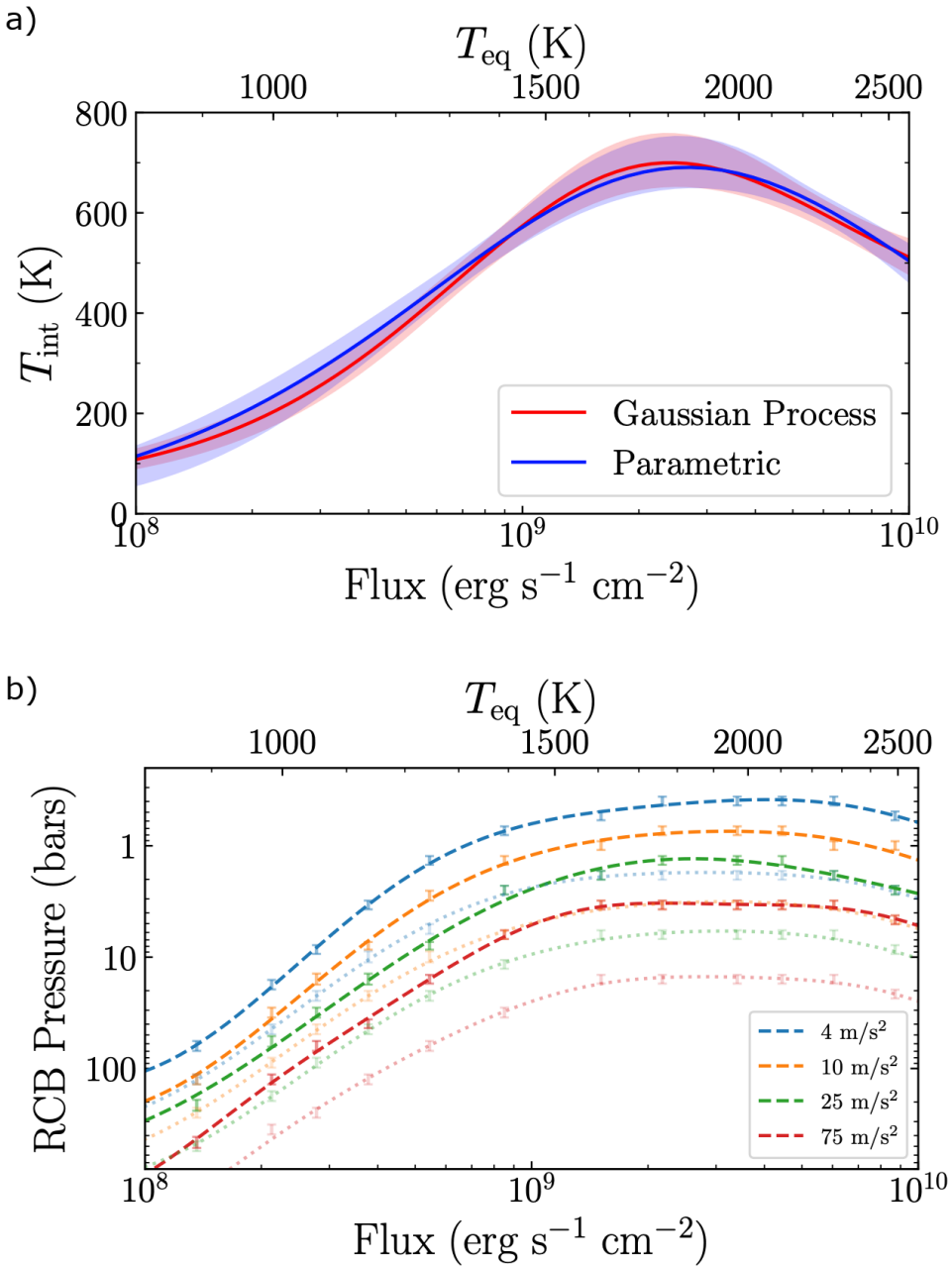


**Figure 6.6:** Figure adapted from Thorngren et al. 2019, Figure 1 & 4. The top panel (a) shows intrinsic temperatures calculated from equation (6.2) using two different heating models Thorngren and Fortney 2019. For the "HD 209458 b"-like planet being studied within this chapter, such a relation yields  $T_{int}$  values in excess of 500K. The bottom panel (b) shows radiative-convective boundary pressures as a function of  $T_{eq}$  for a range of surface gravities. HD 209458 b has a surface gravity of  $9.4 \text{ ms}^{-2}$

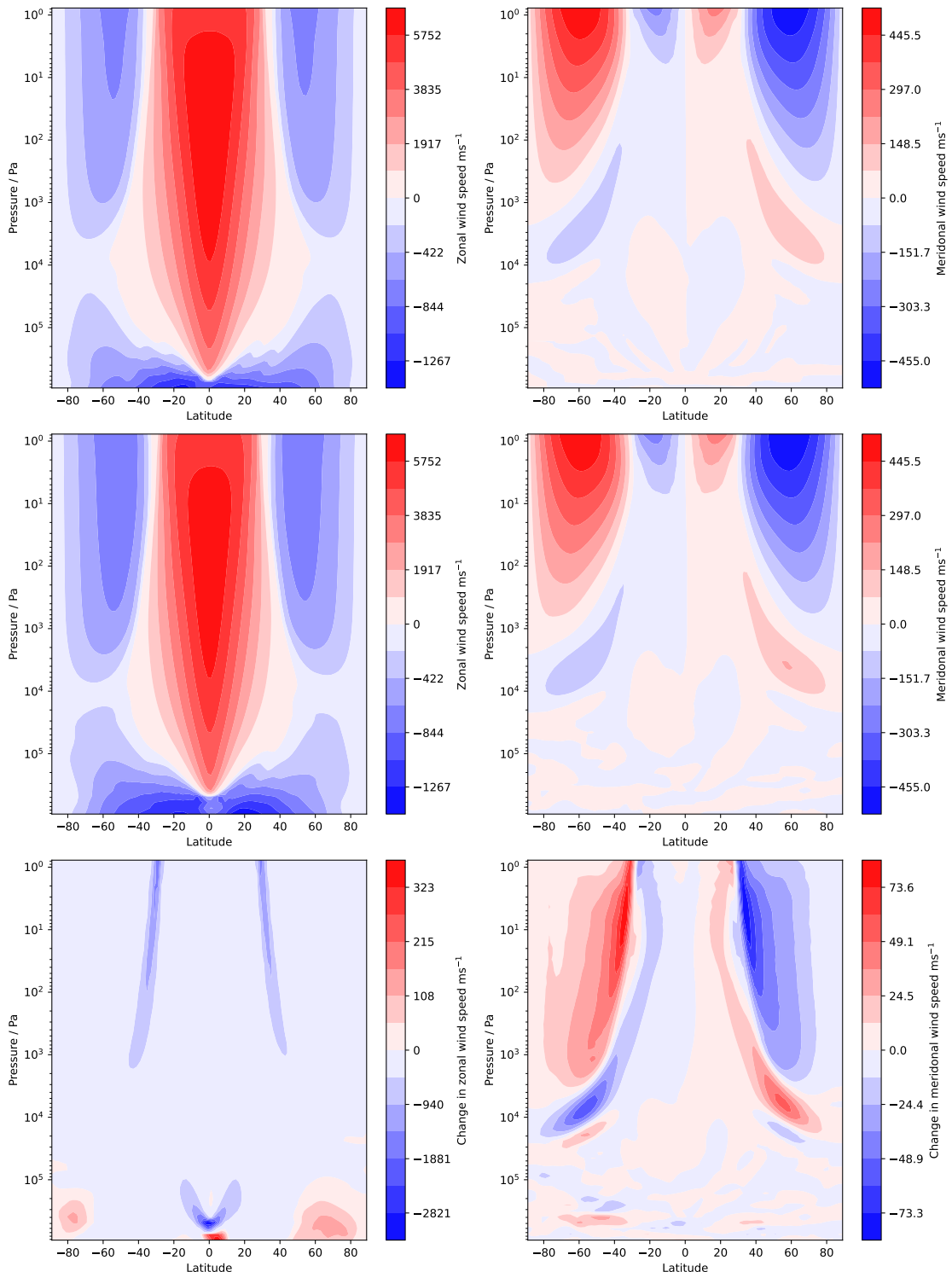


**Figure 6.7:** Longitudinally averaged zonal (left) and meridonal (right) flow profiles for a  $T_{int} = 100\text{K}$  (top) and  $T_{int} = 500\text{K}$  (middle) case. The bottom row shows the difference between these two cases  $((u, v)_{T=500\text{K}} - (u, v)_{T=100\text{K}})$ .

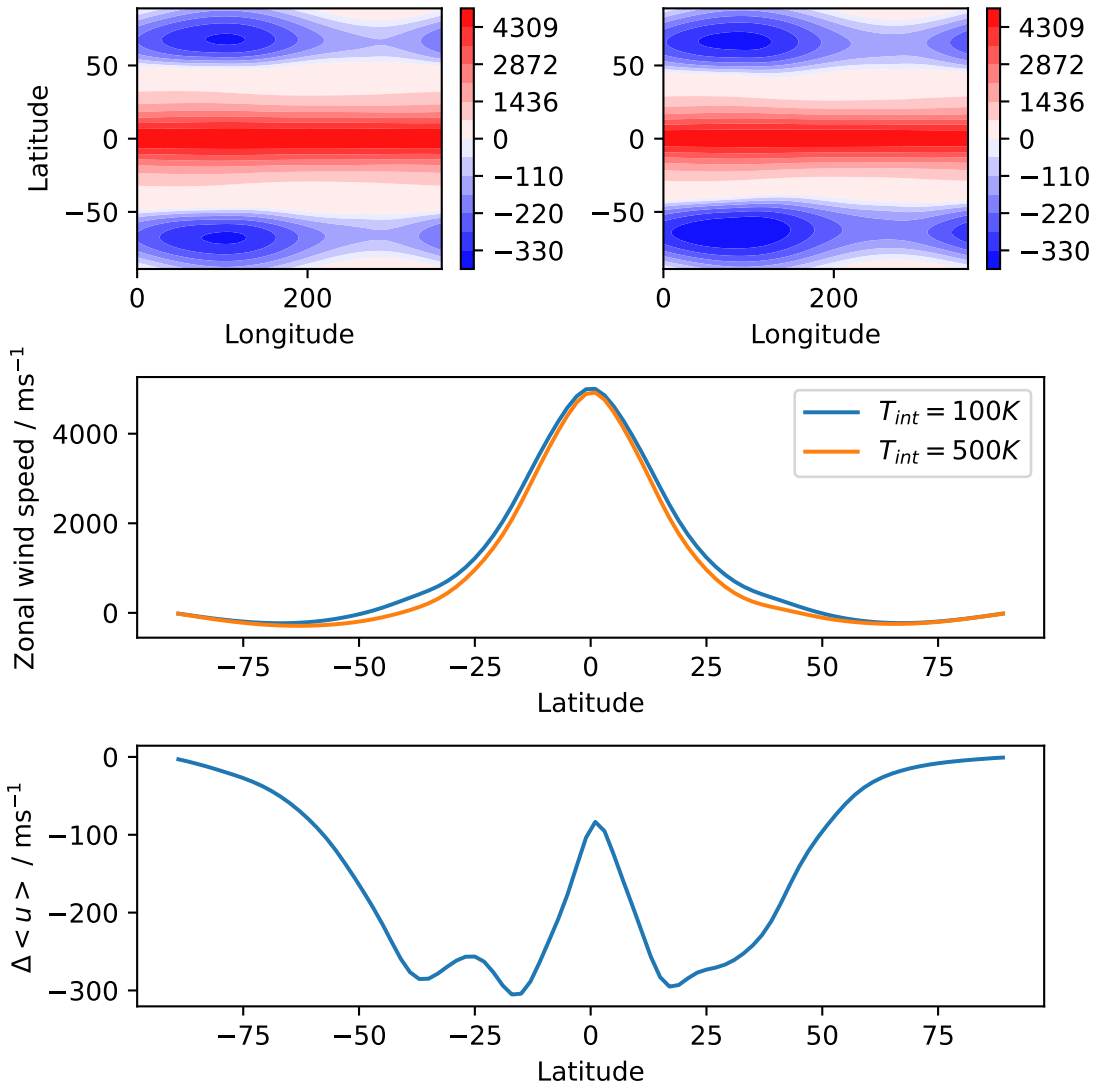


**Figure 6.8:** The top two panels show zonal wind profiles for both the  $T_{int} = 100K$  (left) and  $T_{int} = 500K$  (right) cases as a function of longitude and latitude. These are accompanied by longitudinally averaged zonal profiles for both cases (middle) and the difference between them (bottom). These profiles are for a horizontal slice at  $p = 3.68 \times 10^4$  Pa which encapsulates both the eastward equatorial jet and the westward mid-latitude jets at a moderate atmospheric depth.

Zonal and meridional wind profiles for two simulations one with  $T_{int} = 100\text{K}$  (top row), and one with  $T_{int} = 500\text{K}$  (middle row) can be seen in Figure 6.7. The left hand column shows the zonal wind, and the right hand column shows the meridional winds, with the bottom row showing the differences between the "hot" and "cold" cases,  $((u, v)_{T=500\text{K}} - (u, v)_{T=100\text{K}})$ . Focusing first on the left hand column with the zonal flows, in some regions the circulation is considerably slower by almost 50% of the global zonal wind speed. Additionally, the variations are also not only isolated to the bottom of the domain where the change in internal heat flux would be expected to make an immediate effect. At the top of the atmosphere the flanks of the large scale zonal jet in the mid-latitudes appear to be similarly slowed. What is perhaps clearer in the horizontal slice shown in Figure 6.8 at a pressure depth of  $3.68 \times 10^4\text{Pa}$ , is that this increase in convective interior heat flux has acted to decrease eastward zonal flows at all latitudes. Comparing this to the full zonal flow profiles of both the cases in Figure 6.7, the higher interior heat flux acts to generally weaken and narrow the eastward jet at the equator, however it acts to enhance the pre-existing westward flowing jets at the mid-latitudes. One potential question of interest here is whether higher but still physically realistic values of  $T_{int}$  can be significant enough that its influence on the deep zonal flows is able to shut-down or flip the direction of the jet itself?

### 6.3 Latitudinal dependence of the internal heat flux

As previously discussed the additional heat flux being supplied to our atmospheric layer at its bottom boundary due to the assumed effects of convection is given by the parameter  $Q$ , defined as,

$$Q = \sigma T_{int}^4, \quad (6.4)$$

where  $T_{int}$  is a constant intrinsic temperature. Much like the "Jupiter-like" values of  $T_{int}$  and RCB pressure, the lack of spatial variation in this interior heat flux is an oversimplification. It implies the strength of the convection occurring within the interior is constant at all latitudes and it is well known that spherical shell rotating convection varies signif-

icantly between the polar regions (in which rotationally aligned Taylor-columns become aligned with the radial axis) and the low latitudes (Busse and Cuong 1977; Gastine and Aurnou 2023 and others). Furthermore, it is also clear from simulations of deep convection that in some regimes even very small latitudinal variations in temperature or heat flux can result in significant changes in the resulting flows (Miesch et al. 2008).

This latitude dependence can be introduced to the parameterised internal heat flux in two ways:

- Case A: Allow  $Q$  to decrease with distance from the equator,

$$Q = \sigma [T_{int} (1 - \alpha[1 - \cos(\phi)])]^4. \quad (6.5)$$

- Case B: Allow  $Q$  to increase with distance from the equator,

$$Q = \sigma [T_{int} (1 - \alpha \cos(\phi))]^4. \quad (6.6)$$

where  $\alpha$  is a scaling factor for the extent at which  $T_{int}$  varies with latitude. The profiles of this sort of boundary condition parameterisation can be see in Figure 6.9 which shows the profiles of the effective  $T_{int}$  (such that the heat flux is of the form  $Q = \sigma T_{int}^4$ ) for the spatially invariant case, and the latitude dependent cases A and B.

Preliminary simulations have been performed for case A, equation (6.5), at initial values of  $T_{int} = 100\text{K}$ ,  $\alpha = 0.2$  and can be seen in Figure 6.10. These initial results show some significant variations in the flow speeds at high pressure ( $\sim 10\%$ ) with more minor (but not negligible) variations at lower pressures. Motivated by Thorngren et al. 2019 and the preliminary results discussed Section 6.2, future work will involve further investigating this latitude-dependant forcing at higher initial values of  $T_{int}$ , as well as increasing the strength of the latitudinal variation by changing  $\alpha$ .

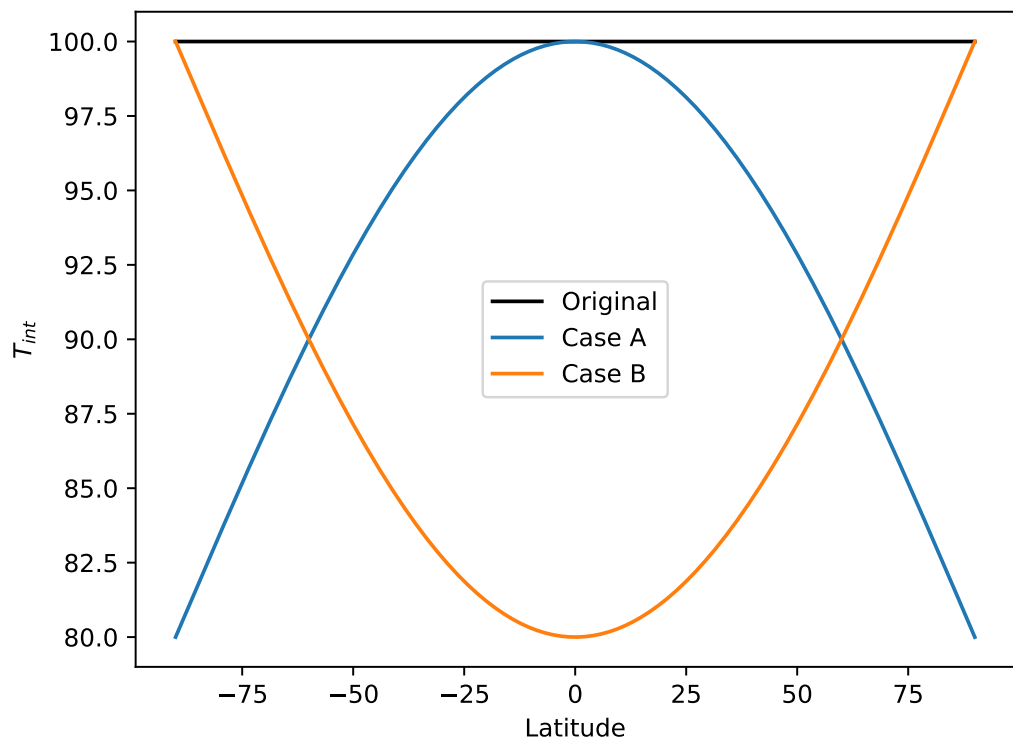


**Figure 6.9:** Latitudinal profiles of the bottom boundary intrinsic heat flux  $T_{int}$  for the original spatially invariant case, and the two latitude dependent cases.

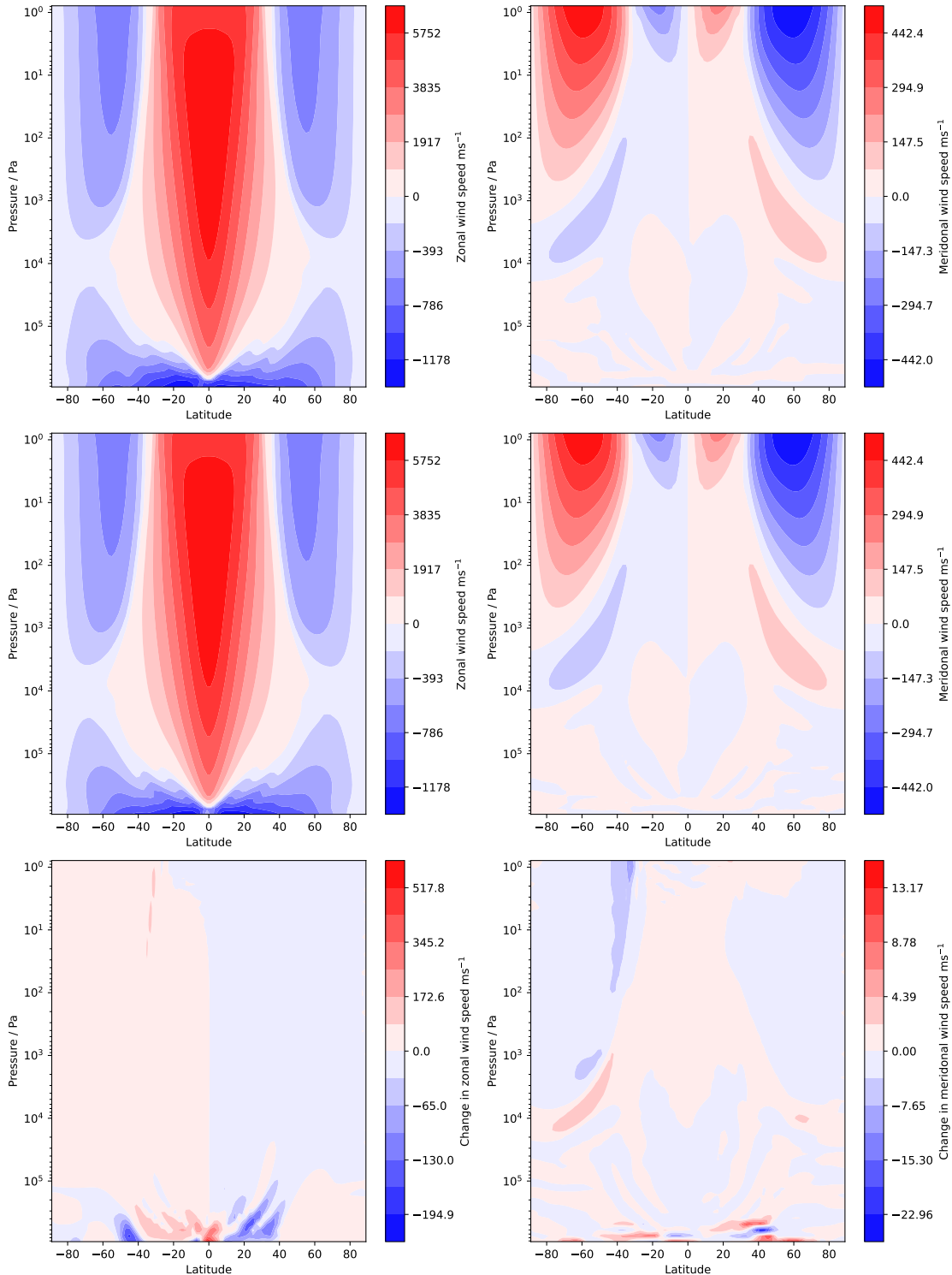


**Figure 6.10:** Longitudinally averaged zonal (left) and meridonal (right) flow profiles for a constant surface temperature forcing with  $T_{int} = 100\text{K}$  (top) and variable forcing as given by equation 6.5, with  $T_{int} = 100\text{K}$ ,  $\alpha = 0.2$  (middle). The bottom row shows the difference between these two cases (constant flux minus variable flux).

## 6.4 Chapter summary

The preliminary results contained within this chapter seem to suggest that for larger values of intrinsic heat fluxes appropriate for highly irradiated hot Jupiters, the deep zonal jet structure and overall circulation of the atmosphere can be significantly altered. A general westward acceleration has been observed in simulations of  $T_{int}$  values up to 500K, resulting in both a deceleration and narrowing of eastward equatorial jet with a corresponding increase in strength of the westward mid-latitude jets. It is possible that for sufficiently high intrinsic heat fluxes, the eastward zonal jet (a ubiquitous feature of prior numerical simulations) could break down, or even reverse direction.

Initial simulations exploring the spatial variation of this intrinsic heat flux in the form of a simple latitude dependence yielded minimal change in the wind structure, however these initial cases were restricted to "Jupiter-like" values for  $T_{int}$  and further study with more appropriate, "hot", interiors may present more of an influence. Lastly, prior work has been performed using a more physically realised "plume-like" boundary condition, more representative of convective overshooting (Zhang and Showman 2014). Incorporating a similar plume-like boundary condition to the UM would be a logical next step in developing more physically motivated convective parameterisations.

## Chapter 7

# Conclusions and discussion of future work

### 7.1 Conclusion

This thesis has concerned itself largely with the study of convection and fluid flows within astrophysical systems. The effects of stratification and rotation have been studied using 2.5D numerical simulations of anelastic, rotating convection on tilted f-planes, with particular interest in their influence on the dissipation and overall heat transport that occurs within such a system. In particular, we provided the first systematic study of dissipation, in rotating, stratified convection in a plane layer. Preliminary work on the effects of more physically motivated interior convective heat flux parameterisations on highly irradiated and tidally-locked gas giant planets (hot Jupiters) in full 3D general circulation models has also been presented.

Chapter 1 provided a broad overview of the types of fluid flow that are prevalent in stars and planets, looking at convection both on the stellar surface, and in the deep interiors of stars and planets, as well as giving an overview of the typical flow structures that are observed in the atmospheres of hot Jupiters. The chapter continues on to detail some of the outstanding puzzles that exist in such systems, like the anomalously inflated radii of aforementioned hot Jupiters, and the so called "convective conundrum" in which helio-

seismic measurements of the Sun suggest convective velocity amplitudes that are much smaller than those predicted by global convective models. Chapter 2 goes on to supply the mathematical rigour that underpins the study of such fluid dynamical systems, providing the background for the governing equations that are subsequently used to study such a system numerically. It then defines various non-dimensional parameters that are of significant use in quantifying the relative strengths of different dynamical processes, and that are used at length in subsequent chapters of the thesis. Lastly the chapter finishes by providing a brief summary of current state of convective theory, specifically detailing the various scaling laws that these parameters appear to follow in a variety of fluid regimes and parameter spaces. Chapter 3 then provides an overview of the numerical methods involved, beginning with an initial derivation of a linear Boussinesq convection code, introducing the various numerical steps involved, and detailing more explicitly the point of convective onset in a numerical context. The chapter then continues on to introduce the computational framework Dedalus (Burns et al. 2020), and outlines the method involved for developing a code for solving a full initial value problem (as is done for the convective code used in Chapters 4 and 5) as well as for an eigenvalue problem (as is done for calculating the relevant values of  $\text{Ra}_c$ ). Lastly this chapter outlines some of the core numerical methods involved in the UK Met Office’s Unified Model (UM) (Mayne et al. 2014b), as well as the governing equations that it solves. This is the primary code used within Chapter 6.

These first three chapters have provided the scientific motivation, the relevant underlying mathematics of fluid dynamics, and established the numerical methods that will be utilised throughout the rest of the thesis. Chapter 4 makes use of these and presents a suite of convection simulations produced using the non-linear, anelastic, and rotating convective code detailed in the previous chapter. It begins by introducing the 2.5D geometry required for rotation in 2D, before detailing some of the typical outputs of the flow used to quantify the energy transport and flow regime, and discussing how these vary in the anelastic and compressible regime. Particular features of interest that are highlighted here are the breaking of vertical symmetry as a result of the system’s stratification, and the stabilisation of the system by rotation.

In Chapter 5, which forms the bulk of this thesis, we present the first systematic

study of heat transport and dissipation in stratified, rotating convection. Beginning with an introductory discussion on the study of dissipation in convection, in particular highlighting its absence in many astrophysical codes, and its potential links to the development of convective overshooting.

The chapter then proceeds to present the full set of governing equations for the rotating, anelastic convection model with stress-free boundaries, based on that used in Currie and Browning 2017, and provides the first systematic numerical study of viscous dissipation and convection in a Cartesian layer, in the highly stratified, rotating regime, and mixed fixed entropy and fixed flux boundary conditions. A wide range of parameter regimes were probed, the number of density scale heights across the domain,  $N_\rho$ , varying from the near Boussinesq limit of  $N_\rho = 0.2$  (with a corresponding density contrast from top to bottom of  $8.2 \times 10^{-1}$ ) to significantly strong stratifications with  $N_\rho = 5$  (density contrast  $6.7 \times 10^{-3}$ ). The buoyancy driving of the convection was quantified by a flux-based Rayleigh number,  $\text{Ra}_F$ , with simulations sampling both the highly viscous and laminar flows near convective onset where  $\text{Ra}_F$  is close  $\text{Ra}_c$ , and more turbulent states up to  $\text{Ra}_F \sim 10^6 \text{Ra}_c$ . Similarly a range of rotational rates were sampled from non-rotating cases up to Taylor numbers in the range  $\text{Ta} = 10$  to  $\text{Ta} = 10^{11}$ , ensuring the parameter space includes a wide range of flows including those heavily influenced by rotational forces with  $\text{Ro}_c$  as low as 0.03 (as seen in Figure 5.3).

Of particular interest was how the magnitude of the viscous dissipation varied under the influence of rotation. Figures 5.4 and 5.5 show the values of  $E$  for a range of cases. The non-rotating cases show strong agreement with the asymptotic behaviour of  $E$  with increasing supercriticality as presented in Currie and Browning (2017). It is also of note that the cases presented here differ to that in Currie and Browning (2017) in that the horizontal extent of the fluid layer is taken to be twice that of the fluid depth. In the case of Currie and Browning (2017) these are taken to be equal. Additionally, their horizontal boundary conditions are taken to be impermeable, whereas the cases presented within this thesis are taken to be periodic. It therefore appears that these high levels of dissipative heating, and their asymptotic behaviour towards the modified upper bound of equation (5.1) are not a feature of the rigid horizontal boundaries. Furthermore, these results appear in contrast

to those of Alboussière et al. (2022) who, while using a different equation of state, argue the limit approached by Currie and Browning (2017) only occurs for systems with rigid boundaries.

Interestingly the rotational cases also appear to follow the same behaviour. The invariance of  $E$  along the axis of increasing rotational influence can be seen in Figure 5.6 where for fixed supercriticalities and stratifications, the value of  $E$  remains constant as the flow becomes increasingly rotationally constrained. This result is somewhat surprising due to the very different dynamical structures that exist between the rotating and non-rotating cases. The non-rotating cases typically organise themselves into one large convective cell with small spatial variations in the velocity field outside of the boundary layers and the convective channels. Rotationally constrained convection on the other hand attempts to align vertical motions to the direction of the rotational axis and results in much narrower convective channels. This results in more rapid variations in the velocity field over much smaller spatial scales. Figure 5.7 shows the difference in flow structure between the most and least rotationally constrained  $N_p$  cases in Figure 5.6. It is shown in the subsequent section (specifically Section 5.4.2, Figure 5.8) that the spatial distribution of the viscous dissipation is directly correlated with areas of high shear flow. This is expected behaviour as the viscous stress tensor  $\tau_{ij}$  is largest in regions of high fluid shear. More specifically, the dissipation in the rotational regime is much more focused in the bulk of the fluid, as opposed to the boundary dominated dissipation seen in the non-rotational cases. In short, the total amount of dissipative heating that occurs is constrained by the asymptotic limit given by Currie and Browning 2017, however its spatial distribution differs between the rotationally, and non-rotationally constrained cases.

Continuing this analysis of the bulk vs. boundary dissipation, a similar trend can be seen in the horizontally averaged profiles of the dissipative heating,  $L_{diss}$ , in which a shift towards a more linear profile with height is observed for increasingly rotationally constrained flow. Additionally a new quantity we term the "dissipation half-height",  $z_{diss}$ , is then defined which represents the height at which half of the total volume-averaged dissipation has occurred, that is,  $|L_{diss}(z_{diss})| = E/2$ . As expected based on previous discussions, increasing rotational constraint results in an increase in  $z_{diss}$  (see Figures 5.11

and 5.12).

Comparisons are drawn between the calculated values of the Nusselt number,  $\text{Nu}$ , a dimensionless measure of the efficiency of heat transport by convection, and the trends presented in prior literature on convective theory. For non-rotating, weakly stratified, cases, the Nusselt number matches the classical  $\text{Nu} \sim \text{Ra}^{1/3}$  power law presented by Malkus 1954b. This scaling is expected for regimes in which the bulk and boundary heat transport is dominated by convection and conduction respectively. Additionally it is expected that the boundary layers themselves be marginally stable against convection. Other non-rotating cases at more significant  $N_p$  present reasonable agreement with the frequently observed  $\text{Nu} \sim \text{Ra}^{2/7}$  scaling discussed at the end of Chapter 2. For the rotating cases a transition in scaling relations is observed as the simulations transition from a  $\text{Ro}_c < 1$  regime to a  $\text{Ro}_c > 1$  one. Those that have  $\text{Ro}_c < 1$  and therefore are considered to be rotationally constrained show good agreement with the rotation scaling of  $\text{Nu} \sim \text{Ra}^{3/2}$ . As the level of turbulent driving increases and the rotational cases transition towards a regime in which the influence of rotation on the dynamics becomes negligible, the cases begin to follow the non-rotating 2/7ths power law scaling. This transitional behaviour is broadly consistent with prior results across a range of both 2D and 3D simulations, in both local and global geometries, as well as with those regimes accessible in lab experiments. Prior to this work however, they have not been verified for the setup detailed here – including crucially the presence of stratification, rotation, and imposed heat flux. That is, 2D anelastic, rotating, convection. The general trends observed here are in good agreement with a wide variety of recent literature, such as the transition from a steep  $\text{Nu}(\text{Ra})$  scaling to a non-rotating one (Aurnou et al. 2020), and agree with the expected scalings from rotating mixing-length theory (Currie et al. 2020 and references therein). In particular, we find that cases which follow the "rotating" heat transport relation are those for which  $z_{diss}$  is especially high (namely  $z_{diss} > 0.5$ ), indicating that more than half the dissipation occurs in the upper convection zone. It is striking that knowledge of  $z_{diss}$  alone appears sufficient to determine whether our simulation will follow the rotating or non-rotating scaling law. The presence of density stratification does introduce new effects – including a strong asymmetry between the top and bottom boundary layers not present in earlier Boussinesq work – which may be important in some contexts. The work shown here is

therefore an important building block in working towards constructing a complete theory of stratified, rotating convection.

The thermal boundary layers in our simulations are asymmetric as a result of the stratification (the top one being considerably larger than the bottom) and that the thicknesses of the top and bottom boundary layers scale differently with Ra. To our knowledge, this has not previously been demonstrated. In the non-rotating cases, knowledge of the boundary layer width suffices to determine the overall heat transport scaling, as there is little dissipation and a negligible entropy gradient within the bulk of the convection zone. Finally, we have explored the link between dissipation and the kinetic energy flux. We developed a simple model of the kinetic energy flux in our non-rotating cases based on the idea that dissipation approaches the upper bound at high enough Ra, and that much of the dissipation occurs near the lower boundary. This model provided a reasonably accurate prediction of the maximum (negative) kinetic energy flux attained in our simulations for each stratification at high enough Ra.

The work presented in Chapter 6 moves away from the direct study of interior convection and instead attempts to better constrain the influence of such motions on the overlying atmospheres in the context of highly irradiated and tidally locked planets, known as hot Jupiters. Specifically it focuses on adapting the parameterisation of the interior convective heat flux typically applied at the bottom boundary of these numerical simulations which historically has been set to "Jupiter-like" parameters and then largely remained untouched. The presence of many hot Jupiters with inflated radii seem to suggest warmer internal adiabats and therefore some missing mechanism for this additional energy dissipation within the planetary interior. Given the growing observational evidence of a correlation between incident stellar flux and inflated radii an obvious candidate for this so called "missing energy" is the host star itself. Additionally, there is growing numerical evidence that suggests the vertical advection of potential temperature forms a robust mechanism for transport of this surface heating to the interior adiabat. As argued by Thorngren et al. 2019, if it is the case that the mechanism responsible for inflating these hot Jupiters is in fact this additional heating of the internal adiabat as a result of the incident stellar flux, then eventually they will achieve some form of equilibrium. Following

this logic they derive a relationship between the effective temperature  $T_{eff}$  and the intrinsic temperature  $T_{int}$ , and find much higher values of  $T_{int}$  than the typical "Jupiter-like" values commonly used in exoplanet literature. Additionally, they also find considerably shallower radiative-convective boundaries than the canonical 1 kbar commonly used for these objects.

This chapter goes on to present global numerical simulations using the UK Met Office's Unified Model (UM) of a typical hot Jupiter atmosphere (specifically that of HD 209458 b) before using the arguments of Thorngren et al. 2019 as motivation to present preliminary results for atmospheres with shallower radiative convective boundaries, and hotter interiors. The results shown here seem to suggest a relatively significant reduction in eastward zonal flows across the entire domain, resulting in a general deceleration and narrowing of the deep eastward equatorial jet, and an enhancing of the counter-rotating westward mid-latitude jets. However, such results are only preliminary and caution is advised before any conclusive observations can be drawn. Lastly the convective parameterisation is allowed to vary as a function of latitude, motivated by the well known latitudinal variation in the strength of convection as seen in rotating spherical shell convection. Initial results show minimal conclusive variations in the large scale circulation as a result of this latitudinal dependence, however as of yet only cold, "Jupiter-like" interiors have been explored in the latitude-dependent case and further study with more appropriate "hot" interiors may present more significant variations.

## 7.2 Future Work

As discussed above, the bulk of the work contained within this thesis has concerned itself with the study of convection in astrophysical fluids, with a large focus on the heat transport and dissipation that occurs within such flows, working towards developing a more complete convective theory in regimes that are likely to be realised in stars and planets. While significant progress has been made towards previously understudied regimes, there are many physical processes that have still been omitted and will undoubtedly have significant roles to play in understanding these real objects.

### 7.2.1 Magnetohydrodynamics

While the work in Chapter 5 concerned itself primarily with the influence and amount of viscous dissipation that can occur within a given fluid layer, at no point is the presence of magnetic fields expressly forbidden. When considering the equation for the total dissipative heating,

$$\Phi = \int_V \tau_{ij} \frac{\partial u_i}{\partial x_j} + \frac{j^2}{\sigma} dV, \quad (7.1)$$

the integral consists of both a viscous component,  $\tau_{ij} \frac{\partial u_i}{\partial x_j}$ , and an Ohmic component,  $\frac{j^2}{\sigma}$ . In fact, Hewitt et al. 1975 even considered the case of convectively driven hydromagnetic spherical dynamo of radius  $a$  in which  $\Phi$  was dominated by ohmic effects, that is

$$\Phi = \int_V \frac{j^2}{\sigma} dV, \quad (7.2)$$

and showed theoretically that

$$E = \frac{\Phi}{L} = \frac{a}{H_T}, \quad (7.3)$$

an expression similar in form to the upper bound derived for the viscous only case, equation 5.1. The question remains then how such limits would be affected by the inclusion of magnetic fields in the anelastic magnetohydrodynamical regime, and whether the additional mechanism by which energy can be dissipated would affect the observed asymptotic limit seen in both Currie and Browning 2017 and the cases presented in Chapter 5. Preliminary work has already been done on producing an anelastic, magnetoconvection code and some initial results can be seen in Figure 7.1.

This initial case was only performed at a moderate value of  $Q = 10$  (the Chandrasekhar number, see section 2.2.8) and  $Pm = 1$  (the magnetic Prandtl number, see section 2.2.3) however even at such slight magnetic field strengths some features can be observed. There are two additional heat transport terms that appear in both the internal and total

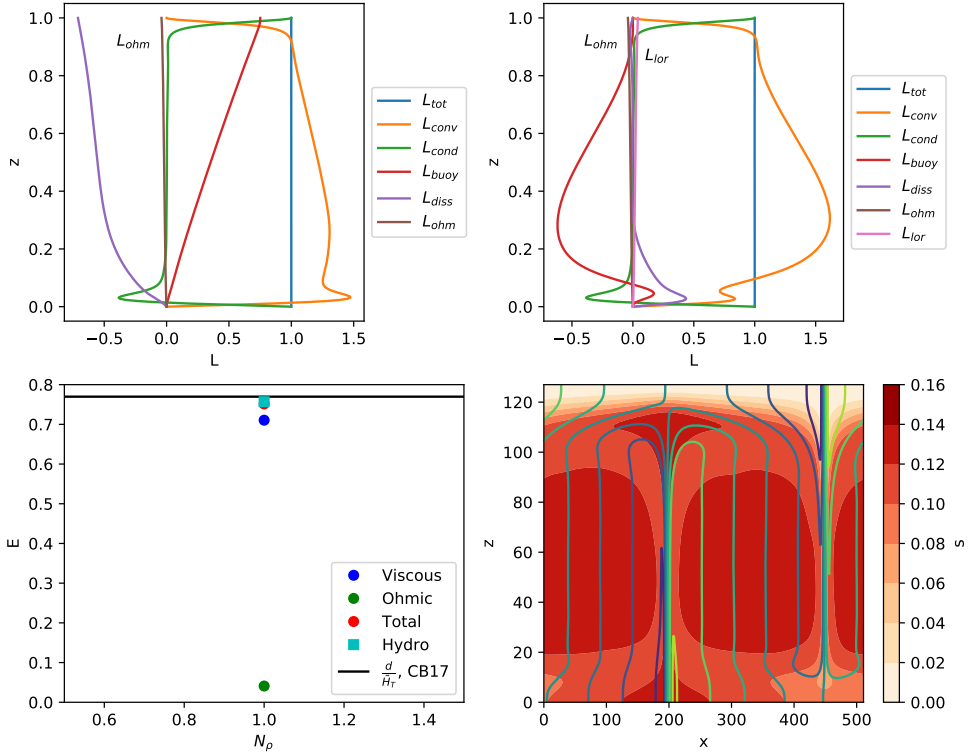


**Figure 7.1:** Four different plots showing outputs from a preliminary MHD convective simulation at  $\text{Ra}_F = 3.8 \times 10^7$ ,  $N_\rho = 1$ ,  $Q = 10$ , and  $\text{Pr} = \text{Pm} = 1$ . A vertical background magnetic field of strength  $B_0$  exists, with both the top and bottom boundary conditions such that the field is purely vertical at boundaries. The top two panels show the two flux decompositions previously discussed, showing the additional magnetic terms  $L_{ohm}$  and  $L_{lor}$  given by equations (7.4) and (7.5) respectively. The bottom left panel shows the value of  $E$ , as well as the ohmic and viscous components, for both a magnetic and non-magnetic case of comparable  $\text{Ra}_F$ . The bottom right panel shows the time-averaged entropy structure over which lines of constant magnetic potential (magnetic field lines) are plotted.

energy flux decompositions given by,

$$L_{ohm} = \int_V -\frac{j^2}{\sigma} dV = \int_V -\frac{\eta}{\mu_0} (\nabla \times \mathbf{B}) \cdot (\nabla \times \mathbf{B}) dV, \quad (7.4)$$

and

$$L_{lor} = \int_V \frac{1}{\mu_0} (\mathbf{u} \times \mathbf{B}) \cdot (\nabla \times \mathbf{B}) dV, \quad (7.5)$$

which emerge from the Ohmic dissipation and the Poynting flux force terms in the internal and total energy equations. These heat transport terms are small in the case shown in Figure 7.1, however they both scale directly with  $Q$  and so are expected to be significant in the presence of stronger magnetic fields. Additionally, approximately 10% of the total dissipation  $E$  is ohmic in nature and the total value of  $E$  is comparable to that of the non-magnetic case at comparable  $\text{Ra}_F$ . With only a single magnetic case to compare no conclusive statements can be presented, however it is interesting that the total dissipative heating rate  $E$  still falls beneath the asymptotic limit presented by Currie and Browning 2017. A more thorough exploration of magnetic cases at a range of  $Q$  and  $N_p$  would be the logical next step in exploring these limits.

### 7.2.2 3D geometry

As was discussed in Chapter 5, accessing the desired parameter regimes can be numerically difficult. The combination of the fact that increasing the rotation rate stabilises the system against convection, and the nature of the asymptotic behaviour of the dissipation requiring high levels of supercriticality, means that the large values of  $\text{Ra}_F$  that are required to probe the desired parameter regime of  $\text{Ro} \ll 1$  and  $\text{Ra}_F \gg \text{Ra}_c$  quickly become computationally expensive. As a result, the 2.5D geometry detailed in Section 5.2.1 was adopted to allow for the more computationally expensive regimes to be probed in a more numerically cost-effective manner.

The convective zones within the interiors of real stars and planets are however,

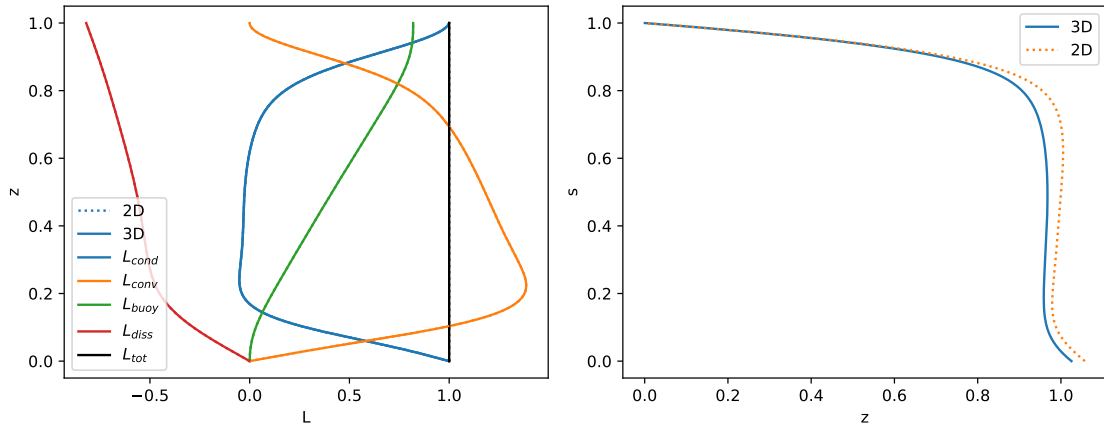


**Figure 7.2:** Comparison between the internal energy flux decomposition (left) and the horizontally averaged vertical entropy profiles (right) of two non-rotating, stratified, simulations within the same parameter regime of  $\text{Ra}_F = 100\text{Ra}_c$  and  $N_\rho = 1/4$ . Differences in the overall flux balances are negligible, with the largest deviation in  $L_{tot}$  between the 2D and 3D cases being  $\sim 0.05\%$  and the overall entropy contrast across the domain varying by 3.04%.

clearly not 2D, and so initial work has begun on the exploration of a small sample of fully 3D convective simulations as an attempt to verify these results in a more physically realistic scenario. Vertical heat transport profiles and a horizontally averaged entropy profile for a non-rotating 3D case of  $N_\rho = 1.4$  and  $\text{Ra} = 10^2\text{Ra}_c$  can be seen in Figure 7.2.

They appear to show reasonable agreement with the 2D case, with near identical flux profiles and an overall vertical entropy contrast of within  $\sim 3.04\%$ . Calculated values for the Nusselt number,  $\text{Nu}$ , for the 3D case were  $\text{Nu} = 3.27$  compared to  $\text{Nu} = 3.17$ , an agreement of within  $\sim 3.06\%$ . This puts the 3D simulation neatly on the  $\text{Nu} \sim \text{Ra}_F^{2/9}$  scaling track for the  $N_\rho = 1.4$  cases in Figure 5.15 (orange crosses). Work has begun on rotating 3D simulations however these are still ongoing and have not yet been sufficiently evolved to be presented here.

### 7.2.3 Development of the bottom boundary in hot Jupiter simulations

The work presented in Chapter 6 focuses largely on the development of more realistic bottom boundary conditions for the application to numerical simulations of hot Jupiter exoplanets. A proposed mechanism for the inflated radius observed in these objects is a heating of the interior, likely as a result of the advection of potential temperature down from the surface and into the deeper layers, developing a hotter interior adiabat and therefore a larger overall radius. In such a scenario the convective heat flux supplied across the

radiative-convective boundary, and the pressure at which this boundary occurs are likely to differ from the canonical cold and deep "Jupiter-like" values that are currently used in numerical studies of these atmospheres.

As previously discussed, the introduction of a more realistic "hot" interior, at a shallower radiative-convective boundary pressure appears to have a significant effect on the resulting zonal jet structure that is typical for hot Jupiter atmospheres. Specifically, the eastward equatorial jet appears to experience a considerable deceleration and narrowing as a result of an increased interior flux, along with an acceleration of the counter-rotating westward jets at the mid latitudes. This therefore begs the question: could the deep zonal jet be sufficiently disrupted to break down entirely, or even reverse direction, given a large enough interior heat flux? An extension of this work will be performed to cover a wider range of intrinsic heat flux values and radiative-convective boundary pressures. The discussion contained within Thorngren et al. 2019 suggest boundaries as shallow as 1 bar and interior heat flux values as high as 700K. It is also feasible that for younger, newly formed hot Jupiters or brown dwarfs, the interior heat flux could be even larger.

Additionally, the spatial variation of the interior convective flux is not currently encapsulated in current parameterisations of this supplied interior heat flux. Chapter 6 introduces a basic latitude dependent heat flux in an attempt to capture this behaviour however initial simulations with a cold "Jupiter-like" interior show little change in the resulting dynamics. Application of such a spatially varying boundary condition to the proposed, hotter and shallower bottom boundaries could prove more influential, and so another avenue currently being explored is extending this latitudinal dependence to a wide range of interior heat fluxes and with different rates for latitudinal drop off. This would be the first step towards incorporating even more physically realistic convective parameterisations, and the intention is develop this further by incorporating a "plume-like" boundary condition like that proposed in Zhang and Showman 2014. This would allow for a boundary in which the interior heat flux is not only a constant value that varies spatially, but a more stochastic representation of convective overshooting that varies both spatially and temporally.

Caution must be had however in raising the radiative-convective boundary too high

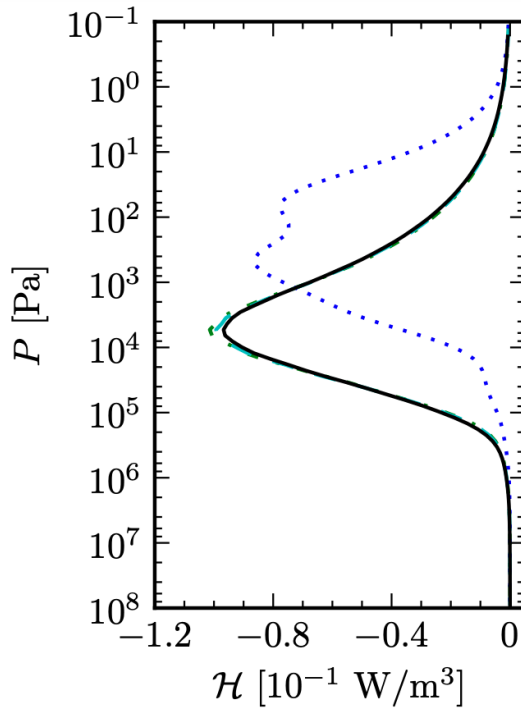


**Figure 7.3:** Figure adapted from Amundsen et al. 2014, Figure 4. Heating rates as a function of atmospheric pressure obtained from the radiation scheme used within the UM (green and cyan) compared to the 1D radiative-convective equilibrium code ATMO (black). The dotted blue line shows heating rates from using band-averaged mean absorption coefficients. The flaws of using these mean absorption coefficients is discussed in more depth in Section 4.4 of Amundsen et al. (2014).

without further consideration of the effects on the resulting flow. Amundsen et al. 2014 present an accuracy study of the radiation schemes used in hot Jupiter GCMs, and a figure of particular note is their Figure 4 (shown here in Figure 7.3). This figure presents the heating rates as a result of radiation as a function of depth. In Chapter 6 the radiative-convective boundary has been raised to pressures of 10bar, or  $10^6\text{Pa}$ , and even at this height, it can be seen in Figure 7.3 a small amount of the heating as a result of stellar irradiance is being ignored. Moving this boundary up further to as low as 1 bar, or  $10^5\text{Pa}$ , will result in significant amounts of this heating being excluded. This heating is largely responsible for the formation of the large scale advective motions that form. A trade off exists therefore between fully encapsulating the heating from stellar irradiance and therefore the driving of these motions correctly from above, and accurately parameterising the interior convection correctly by placing the boundary at the appropriate depth and correctly influencing these motions from below. It is unclear as of yet which of these is most appropriate, and stresses the importance of the next significant step in studying the influence of the convective interior on its overlying atmosphere: The need for the development

of numerical simulations of an overlying radiative atmosphere coupled fully to a resolved convective interior. In such a way, both a realistic radiative convective boundary could be obtained, without ignoring a significant portion of the radiative heating.

In conclusion, although our work has yielded new insights into both the dynamics of convection in deep, stratified interiors, and the flow in planetary atmospheres, much remains to be done. We hope in particular to extend our work to more realistic parameter regimes (including magnetism) and, ultimately to explore the coupling between these two regions.

**THE  
APPENDICES**

## Appendix A

### Dedalus input equations - 3d

#### Anelastic (rotating)

##### A.1 Non-dimensionalisation

Consider first the case of no magnetic influence. Our governing equations are as follows:

$$\frac{\partial \mathbf{u}}{\partial t} + (\mathbf{u} \cdot \nabla) \mathbf{u} + 2\Omega \times \mathbf{u} = -\nabla \tilde{p} + \frac{gs}{c_p} \hat{\mathbf{e}}_z + \nu \left[ \frac{1}{\bar{\rho}} \frac{\partial}{\partial x_j} \left( \bar{\rho} \left( \frac{\partial u_i}{\partial x_j} + \frac{\partial u_j}{\partial x_i} \right) \right) - \frac{2}{3\bar{\rho}} \frac{\partial}{\partial x_i} \left( \bar{\rho} \frac{\partial u_j}{\partial x_j} \right) \right] \quad (\text{A.1})$$

$$\nabla \cdot (\bar{\rho} \mathbf{u}) = 0 \quad (\text{A.2})$$

$$\bar{\rho} \bar{T} \left( \frac{\partial s}{\partial t} + (\mathbf{u} \cdot \nabla) s \right) = \nabla \cdot (\kappa \bar{\rho} \bar{T} \nabla s) + \tau_{ij} \frac{\partial u_i}{\partial x_j} + H \quad (\text{A.3})$$

where  $\mathbf{u}$  is the fluid velocity,  $\Omega$  is our angular velocity,  $\tilde{p} = \frac{p}{\bar{\rho}}$  is the modified pressure,  $g$  is the acceleration due to gravity,  $s$  is the specific entropy,  $c_p$  is the specific heat capacity at constant pressure,  $\nu$  is the kinematic viscosity, and  $\kappa$  is the thermal diffusivity. We additionally consider the case of no internal heat generation and so  $H = 0$  and

instead we impose a flux ( $F$ ) on our bottom boundary. Note that we have applied the LBR approximation so that we are diffusing entropy as opposed to temperature. We assume a constant  $\nu$  and  $\kappa$ . Additionally,

$$\tau_{ij} = \nu \bar{\rho} \left( \frac{\partial u_i}{\partial x_j} + \frac{\partial u_j}{\partial x_i} - \frac{2}{3} \delta_{ij} \nabla \cdot \mathbf{u} \right) \quad (\text{A.4})$$

is the viscous stress tensor.

We non-dimensionalise our system by the viscous timescale, that is,

$$\frac{\partial}{\partial t} = \frac{\nu}{d^2} \frac{\partial}{\partial \hat{t}} \quad \nabla = \frac{1}{d} \hat{\nabla} \quad \mathbf{u} = \frac{\nu}{d} \hat{\mathbf{u}} \quad \tilde{p} = \frac{\nu^2}{d^2} \hat{p} \quad s = \frac{Fd}{\kappa \rho_0 T_0} \hat{s} \quad \boldsymbol{\Omega} = \Omega \hat{\boldsymbol{\Omega}} \quad (\text{A.5})$$

where terms denoted by a  $\hat{\cdot}$  symbol represent non-dimensional variables, and noting that  $\tau_{ij} = \frac{\rho_0 \nu^2}{d^2} \hat{\tau}_{ij}$ . Additionally, we need to introduce four non-dimensional numbers. The flux-based Rayleigh number,  $Ra$ , describing the turbulent nature of the flow, the Prandtl number,  $Pr$ , the ratio of the viscous and thermal diffusivities,  $\theta$ , a non-dimensional measure of stratification equivalent to the inverse temperature scale height, and the Taylor number,  $Ta$ , the ratio of the centrifugal to viscous forces.

$$Ra = \frac{g F d^4}{\nu \kappa^2 c_p \rho_0 T_0}, \quad Pr = \frac{\nu}{\kappa}, \quad \theta = \frac{g d}{c_p T_0}, \quad Ta = \frac{4 \Omega^2 d^4}{\nu^2} \quad (\text{A.6})$$

Starting with the momentum equation, (A.1),

$$\frac{\nu^2}{d^3} \left( \frac{\partial \hat{\mathbf{u}}}{\partial \hat{t}} + (\hat{\mathbf{u}} \cdot \hat{\nabla}) \hat{\mathbf{u}} \right) + \frac{2 \Omega \nu}{d} \hat{\boldsymbol{\Omega}} \times \hat{\mathbf{u}} = - \frac{\nu^2}{d^3} \hat{\nabla} \hat{p} + \frac{Fd}{\kappa \rho_0 T_0} \frac{g}{c_p} \hat{s} \hat{\mathbf{e}}_z + \frac{\nu^2}{d^3} \left[ \frac{1}{\hat{\rho}} \frac{\partial}{\partial \hat{x}_j} \left( \hat{\rho} \left( \frac{\partial \hat{u}_i}{\partial \hat{x}_j} + \frac{\partial \hat{u}_j}{\partial \hat{x}_i} \right) \right) - \frac{2}{3 \hat{\rho}} \frac{\partial}{\partial \hat{x}_i} \left( \hat{\rho} \frac{\partial \hat{u}_j}{\partial \hat{x}_j} \right) \right] \quad (\text{A.7})$$

rearranging yields,

$$\frac{\partial \hat{u}}{\partial \hat{t}} + (\hat{u} \cdot \hat{\nabla}) \hat{u} + \frac{2\Omega d^2}{\nu} \hat{\Omega} \times \hat{u} = -\hat{\nabla} \hat{p} + \frac{gFd^4}{\nu^2 \kappa c_p \rho_0 T_0} \hat{s} \hat{e}_z + \left[ \frac{1}{\hat{\rho}} \frac{\partial}{\partial \hat{x}_j} \left( \hat{\rho} \left( \frac{\partial \hat{u}_i}{\partial \hat{x}_j} + \frac{\partial \hat{u}_j}{\partial \hat{x}_i} \right) \right) - \frac{2}{3\hat{\rho}} \frac{\partial}{\partial \hat{x}_i} \left( \hat{\rho} \frac{\partial \hat{u}_j}{\partial \hat{x}_j} \right) \right] \quad (\text{A.8})$$

and then finally, notice that

$$\frac{Ra}{Pr} = \frac{gFd^4}{\nu^2 \kappa c_p \rho_0 T_0} \quad \text{and} \quad Ta^{\frac{1}{2}} = \frac{2\Omega d^2}{\nu} \quad (\text{A.9})$$

Substituting this in, we have our non-dimensional momentum equation,

$$\frac{\partial \hat{u}}{\partial \hat{t}} + (\hat{u} \cdot \hat{\nabla}) \hat{u} + Ta^{\frac{1}{2}} \hat{\Omega} \times \hat{u} = -\hat{\nabla} \hat{p} + \frac{Ra}{Pr} \hat{s} \hat{e}_z + \left[ \frac{1}{\hat{\rho}} \frac{\partial}{\partial \hat{x}_j} \left( \hat{\rho} \left( \frac{\partial \hat{u}_i}{\partial \hat{x}_j} + \frac{\partial \hat{u}_j}{\partial \hat{x}_i} \right) \right) - \frac{2}{3\hat{\rho}} \frac{\partial}{\partial \hat{x}_i} \left( \hat{\rho} \frac{\partial \hat{u}_j}{\partial \hat{x}_j} \right) \right] \quad (\text{A.10})$$

Next, consider the entropy diffusion equation, (A.3),

$$\frac{F\nu}{\kappa d} \hat{\rho} \hat{T} \left( \frac{\partial \hat{s}}{\partial \hat{t}} + (\hat{u} \cdot \hat{\nabla}) \hat{s} \right) = \frac{F}{d} \hat{\nabla} \cdot (\hat{\rho} \hat{T} \hat{\nabla} \hat{s}) + \frac{\rho_0 \nu^3}{d^4} \hat{\tau}_{ij} \frac{\partial \hat{u}_i}{\partial \hat{x}_j} \quad (\text{A.11})$$

rearranging yields,

$$\frac{\nu}{\kappa} \hat{\rho} \hat{T} \left( \frac{\partial \hat{s}}{\partial \hat{t}} + (\hat{u} \cdot \hat{\nabla}) \hat{s} \right) = \hat{\nabla} \cdot (\hat{\rho} \hat{T} \hat{\nabla} \hat{s}) + \frac{\rho_0 \nu^3}{Fd^3} \hat{\tau}_{ij} \frac{\partial \hat{u}_i}{\partial \hat{x}_j} \quad (\text{A.12})$$

and finally, notice that,

$$\frac{Pr^2 \theta}{Ra} = \frac{\nu^2}{\kappa^2} \frac{gd}{c_p T_0} \frac{\nu \kappa^2 c_p \rho_0 T_0}{g F d^4} = \frac{\rho_0 \nu^3}{Fd^3} \quad (\text{A.13})$$

Substituting this in, we have our non-dimensional entropy diffusion equation,

$$Pr\hat{\rho}\hat{T}\left(\frac{\partial\hat{s}}{\partial\hat{t}} + (\hat{u}\cdot\hat{\nabla})\hat{s}\right) = \hat{\nabla}\cdot\left(\hat{\rho}\hat{T}\hat{\nabla}\hat{s}\right) + \frac{Pr^2\theta}{Ra}\hat{\tau}_{ij}\frac{\partial\hat{u}_i}{\partial\hat{x}_j} \quad (\text{A.14})$$

Lastly, we have our continuity equation, (A.2),

$$\frac{\rho_0\nu}{d^2}\hat{\nabla}\cdot(\hat{\rho}\hat{u}) = 0 \quad (\text{A.15})$$

$$\hat{\nabla}\cdot(\hat{\rho}\hat{u}) = 0 \quad (\text{A.16})$$

We can also consider the non-dimensional forms of our reference state variables,  $\bar{\rho} = \rho_0\hat{\rho}$  and  $\bar{T} = T_0\hat{T}$  where  $\hat{\rho} = (1 - \theta\hat{z})^m$  and  $\hat{T} = 1 - \theta\hat{z}$ . Using these relations, we can analytically expand our continuity equation,

$$\frac{\partial}{\partial\hat{x}}(\hat{\rho}\hat{u}) + \frac{\partial}{\partial\hat{y}}(\hat{\rho}\hat{u}) + \frac{\partial}{\partial\hat{z}}(\hat{\rho}\hat{w}) = 0 \quad (\text{A.17})$$

$$\hat{\rho}\left(\frac{\partial\hat{u}}{\partial\hat{x}} + \frac{\partial\hat{v}}{\partial\hat{y}} + \frac{\partial\hat{w}}{\partial\hat{z}}\right) + \frac{\partial\hat{\rho}}{\partial\hat{z}}\hat{w} = 0 \quad (\text{A.18})$$

$$\left(\frac{\partial\hat{u}}{\partial\hat{x}} + \frac{\partial\hat{v}}{\partial\hat{y}} + \frac{\partial\hat{w}}{\partial\hat{z}}\right) + \frac{1}{\hat{\rho}}\frac{\partial\hat{\rho}}{\partial\hat{z}}\hat{w} = 0 \quad (\text{A.19})$$

note that,

$$\frac{\partial\hat{\rho}}{\partial\hat{z}} = -\theta m(1 - \theta\hat{z})^{m-1} \quad (\text{A.20})$$

$$\frac{1}{\hat{\rho}}\frac{\partial\hat{\rho}}{\partial\hat{z}} = -\frac{\theta m}{(1 - \theta\hat{z})} \quad (\text{A.21})$$

and so,

$$\left(\frac{\partial\hat{u}}{\partial\hat{x}} + \frac{\partial\hat{v}}{\partial\hat{y}} + \frac{\partial\hat{w}}{\partial\hat{z}}\right) - \frac{\theta m}{(1 - \theta\hat{z})}\hat{w} = 0 \quad (\text{A.22})$$

giving us the final form of the continuity equation used in the anelastic code,

$$(1 - \theta\hat{z}) \left( \frac{\partial \hat{u}}{\partial \hat{x}} + \frac{\partial \hat{v}}{\partial \hat{y}} + \frac{\partial \hat{w}}{\partial \hat{z}} \right) - \theta m \hat{w} = 0 \quad (\text{A.23})$$

Note that in the Boussinesq case,  $N_\rho = 0$  and then  $\theta = 1 - \exp(-\frac{0}{1.5}) = 0$ , so equation A.23 reduces to the recognisable form,

$$\left( \frac{\partial \hat{u}}{\partial \hat{x}} + \frac{\partial \hat{v}}{\partial \hat{y}} + \frac{\partial \hat{w}}{\partial \hat{z}} \right) = \hat{\nabla} \cdot \hat{\mathbf{u}} = 0 \quad (\text{A.24})$$

## A.2 Equation Expansion

To summarise, if we simply assume all variables to now be non-dimensional and drop the hat (^) notation, we have the following governing equations,

$$\begin{aligned} \bar{\rho} \left( \frac{\partial \mathbf{u}}{\partial t} + (\mathbf{u} \cdot \nabla) \mathbf{u} \right) &= -\bar{\rho} \nabla \tilde{p} + \frac{Ra}{Pr} \bar{\rho} s \hat{\mathbf{e}}_z - Ta^{\frac{1}{2}} \bar{\rho} \boldsymbol{\Omega} \times \mathbf{u} \\ &+ \left[ \frac{\partial}{\partial x_j} \left( \bar{\rho} \left( \frac{\partial u_i}{\partial x_j} + \frac{\partial u_j}{\partial x_i} \right) \right) - \frac{2}{3} \frac{\partial}{\partial x_i} \left( \bar{\rho} \frac{\partial u_j}{\partial x_j} \right) \right] \end{aligned} \quad (\text{A.25})$$

$$Pr \bar{\rho} \bar{T} \left( \frac{\partial s}{\partial t} + (\mathbf{u} \cdot \nabla) s \right) = \nabla \cdot (\bar{\rho} \bar{T} \nabla s) + \frac{Pr^2 \theta}{Ra} \tau_{ij} \frac{\partial u_i}{\partial x_j} \quad (\text{A.26})$$

$$(1 - \theta z) \left( \frac{\partial u}{\partial x} + \frac{\partial w}{\partial z} \right) - \theta m w = 0 \quad (\text{A.27})$$

Note we multiplied through by a factor of  $\bar{\rho}$  in (A.25) and moved the Coriolis term to the right hand side.

For our equations to be recognised by Dedalus's symbolic equation entry, we need to fully expand each of our terms. Equation (A.59) is already in this expanded form, however some rearrangement and expansions is required still for the momentum and

entropy diffusion equations. Starting with the momentum equation, where we have three equations for each of the components of momentum.

$$\begin{aligned} \bar{\rho} \left( \frac{\partial u}{\partial t} + u \frac{\partial u}{\partial x} + v \frac{\partial u}{\partial y} + w \frac{\partial u}{\partial z} \right) &= -\bar{\rho} \frac{\partial}{\partial x} \left( \frac{p}{\bar{\rho}} \right) - T a^{\frac{1}{2}} \bar{\rho} (w \cos \phi - v \sin \phi) \\ &\quad + \left[ \frac{\partial}{\partial x_j} \left( \bar{\rho} \left( \frac{\partial u_i}{\partial x_j} + \frac{\partial u_j}{\partial x_i} \right) \right) - \frac{2}{3} \frac{\partial}{\partial x_i} \left( \bar{\rho} \frac{\partial u_j}{\partial x_j} \right) \right] \cdot \hat{e}_x \end{aligned} \quad (\text{A.28})$$

$$\begin{aligned} \bar{\rho} \left( \frac{\partial v}{\partial t} + u \frac{\partial v}{\partial x} + v \frac{\partial v}{\partial y} + w \frac{\partial v}{\partial z} \right) &= -\bar{\rho} \frac{\partial}{\partial y} \left( \frac{p}{\bar{\rho}} \right) - T a^{\frac{1}{2}} \bar{\rho} u \sin \phi \\ &\quad + \left[ \frac{\partial}{\partial x_j} \left( \bar{\rho} \left( \frac{\partial u_i}{\partial x_j} + \frac{\partial u_j}{\partial x_i} \right) \right) - \frac{2}{3} \frac{\partial}{\partial x_i} \left( \bar{\rho} \frac{\partial u_j}{\partial x_j} \right) \right] \cdot \hat{e}_y \end{aligned} \quad (\text{A.29})$$

$$\begin{aligned} \bar{\rho} \left( \frac{\partial w}{\partial t} + u \frac{\partial w}{\partial x} + v \frac{\partial w}{\partial y} + w \frac{\partial w}{\partial z} \right) &= -\bar{\rho} \frac{\partial}{\partial z} \left( \frac{p}{\bar{\rho}} \right) + \frac{Ra}{Pr} \bar{\rho} s + T a^{\frac{1}{2}} \bar{\rho} u \cos \phi \\ &\quad + \left[ \frac{\partial}{\partial x_j} \left( \bar{\rho} \left( \frac{\partial u_i}{\partial x_j} + \frac{\partial u_j}{\partial x_i} \right) \right) - \frac{2}{3} \frac{\partial}{\partial x_i} \left( \bar{\rho} \frac{\partial u_j}{\partial x_j} \right) \right] \cdot \hat{e}_z \end{aligned} \quad (\text{A.30})$$

Let us first expand the pressure gradient terms, where we have already substituted in our reduced pressure,  $\tilde{p} = \frac{p}{\bar{\rho}}$ . Now,  $\bar{\rho} = (1 - \theta z)^m$ , therefore,  $\frac{\partial}{\partial x, y} \left( \frac{1}{\bar{\rho}} \right) = 0$

$$\bar{\rho} \frac{\partial}{\partial x} \left( \frac{p}{\bar{\rho}} \right) = \bar{\rho} \left( \frac{1}{\bar{\rho}} \frac{\partial p}{\partial x} + p \frac{\partial}{\partial x} \left( \frac{1}{\bar{\rho}} \right) \right) = \frac{\partial p}{\partial x} \quad (\text{A.31})$$

similarly

$$\bar{\rho} \frac{\partial}{\partial y} \left( \frac{p}{\bar{\rho}} \right) = \bar{\rho} \left( \frac{1}{\bar{\rho}} \frac{\partial p}{\partial y} + p \frac{\partial}{\partial y} \left( \frac{1}{\bar{\rho}} \right) \right) = \frac{\partial p}{\partial y} \quad (\text{A.32})$$

however  $\frac{\partial}{\partial z} \left( \frac{1}{\bar{\rho}} \right) \neq 0$

$$\frac{\partial}{\partial z} \left( \frac{1}{\bar{\rho}} \right) = \frac{\partial}{\partial z} ((1 - \theta z)^{-m}) = m\theta(1 - \theta z)^{-m-1} = \frac{m\theta}{\bar{\rho}\bar{T}} \quad (\text{A.33})$$

and so,

$$\bar{\rho} \frac{\partial}{\partial z} \left( \frac{p}{\bar{\rho}} \right) = \bar{\rho} \left( \frac{1}{\bar{\rho}} \frac{\partial p}{\partial z} + p \frac{m\theta}{\bar{\rho}\bar{T}} \right) = \frac{\partial p}{\partial z} + \frac{m\theta}{\bar{T}} p \quad (\text{A.34})$$

If we substitute in (A.31), (A.32), and (A.34), and multiply our equation for the z-component of momentum through by a factor of  $\bar{T}$ , we obtain,

$$\begin{aligned} \bar{\rho} \left( \frac{\partial u}{\partial t} + u \frac{\partial u}{\partial x} + v \frac{\partial u}{\partial y} + w \frac{\partial u}{\partial z} \right) &= -\frac{\partial p}{\partial x} - T a^{\frac{1}{2}} \bar{\rho} (w \cos \phi - v \sin \phi) \\ &\quad + \left[ \frac{\partial}{\partial x_j} \left( \bar{\rho} \left( \frac{\partial u_i}{\partial x_j} + \frac{\partial u_j}{\partial x_i} \right) \right) - \frac{2}{3} \frac{\partial}{\partial x_i} \left( \bar{\rho} \frac{\partial u_j}{\partial x_j} \right) \right] \cdot \hat{e}_x \end{aligned} \quad (\text{A.35})$$

$$\begin{aligned} \bar{\rho} \left( \frac{\partial v}{\partial t} + u \frac{\partial v}{\partial x} + v \frac{\partial v}{\partial y} + w \frac{\partial v}{\partial z} \right) &= -\frac{\partial p}{\partial y} - T a^{\frac{1}{2}} \bar{\rho} u \sin \phi \\ &\quad + \left[ \frac{\partial}{\partial x_j} \left( \bar{\rho} \left( \frac{\partial u_i}{\partial x_j} + \frac{\partial u_j}{\partial x_i} \right) \right) - \frac{2}{3} \frac{\partial}{\partial x_i} \left( \bar{\rho} \frac{\partial u_j}{\partial x_j} \right) \right] \cdot \hat{e}_y \end{aligned} \quad (\text{A.36})$$

$$\begin{aligned} \bar{\rho} \bar{T} \left( \frac{\partial w}{\partial t} + u \frac{\partial w}{\partial x} + v \frac{\partial w}{\partial y} + w \frac{\partial w}{\partial z} \right) &= -\bar{T} \frac{\partial p}{\partial z} - m\theta p + \frac{Ra}{Pr} \bar{\rho} \bar{T} s + T a^{\frac{1}{2}} \bar{\rho} u \cos \phi \\ &\quad + \bar{T} \left[ \frac{\partial}{\partial x_j} \left( \bar{\rho} \left( \frac{\partial u_i}{\partial x_j} + \frac{\partial u_j}{\partial x_i} \right) \right) - \frac{2}{3} \frac{\partial}{\partial x_i} \left( \bar{\rho} \frac{\partial u_j}{\partial x_j} \right) \right] \cdot \hat{e}_z \end{aligned} \quad (\text{A.37})$$

Finally, we need to expand the viscous term,

$$\frac{\partial}{\partial x_j} \left( \bar{\rho} \left( \frac{\partial u_i}{\partial x_j} + \frac{\partial u_j}{\partial x_i} \right) \right) - \frac{2}{3} \frac{\partial}{\partial x_i} \left( \bar{\rho} \frac{\partial u_j}{\partial x_j} \right) \quad (\text{A.38})$$

For the x-component,  $i = 1$ , sum over the repeated index  $j$ ,

$$\begin{aligned} \frac{\partial}{\partial x_j} \left( \bar{\rho} \left( \frac{\partial u}{\partial x_j} + \frac{\partial u_j}{\partial x} \right) \right) - \frac{2}{3} \frac{\partial}{\partial x} \left( \bar{\rho} \frac{\partial u_j}{\partial x_j} \right) &= \frac{\partial}{\partial x} \left( \bar{\rho} \left( \frac{\partial u}{\partial x} + \frac{\partial u}{\partial x} \right) \right) - \frac{2}{3} \frac{\partial}{\partial x} \left( \bar{\rho} \frac{\partial u}{\partial x} \right) \\ &\quad + \frac{\partial}{\partial y} \left( \bar{\rho} \left( \frac{\partial u}{\partial y} + \frac{\partial v}{\partial x} \right) \right) - \frac{2}{3} \frac{\partial}{\partial x} \left( \bar{\rho} \frac{\partial v}{\partial y} \right) \\ &\quad + \frac{\partial}{\partial z} \left( \bar{\rho} \left( \frac{\partial u}{\partial z} + \frac{\partial w}{\partial x} \right) \right) - \frac{2}{3} \frac{\partial}{\partial x} \left( \bar{\rho} \frac{\partial w}{\partial z} \right) \end{aligned} \quad (\text{A.39})$$

which after some tidying,

$$\begin{aligned} \frac{\partial}{\partial x_j} \left( \bar{\rho} \left( \frac{\partial u}{\partial x_j} + \frac{\partial u_j}{\partial x} \right) \right) - \frac{2}{3} \frac{\partial}{\partial x} \left( \bar{\rho} \frac{\partial u_j}{\partial x_j} \right) &= \bar{\rho} \left( \frac{4}{3} \frac{\partial^2 u}{\partial x^2} + \frac{\partial^2 u}{\partial y^2} + \frac{\partial^2 u}{\partial z^2} + \frac{1}{3} \frac{\partial^2 v}{\partial x \partial y} + \frac{1}{3} \frac{\partial^2 w}{\partial x \partial z} \right) \\ &\quad + \frac{\partial \bar{\rho}}{\partial z} \left( \frac{\partial u}{\partial z} + \frac{\partial w}{\partial x} \right) \end{aligned} \quad (\text{A.40})$$

For the y-component,  $i = 2$ , sum over the repeated index  $j$ ,

$$\begin{aligned} \frac{\partial}{\partial x_j} \left( \bar{\rho} \left( \frac{\partial v}{\partial x_j} + \frac{\partial u_j}{\partial y} \right) \right) - \frac{2}{3} \frac{\partial}{\partial y} \left( \bar{\rho} \frac{\partial u_j}{\partial x_j} \right) &= \frac{\partial}{\partial x} \left( \bar{\rho} \left( \frac{\partial v}{\partial x} + \frac{\partial u}{\partial y} \right) \right) - \frac{2}{3} \frac{\partial}{\partial y} \left( \bar{\rho} \frac{\partial u}{\partial x} \right) \\ &\quad + \frac{\partial}{\partial y} \left( \bar{\rho} \left( \frac{\partial v}{\partial y} + \frac{\partial v}{\partial y} \right) \right) - \frac{2}{3} \frac{\partial}{\partial y} \left( \bar{\rho} \frac{\partial v}{\partial y} \right) \\ &\quad + \frac{\partial}{\partial z} \left( \bar{\rho} \left( \frac{\partial v}{\partial z} + \frac{\partial w}{\partial y} \right) \right) - \frac{2}{3} \frac{\partial}{\partial y} \left( \bar{\rho} \frac{\partial w}{\partial z} \right) \end{aligned} \quad (\text{A.41})$$

which after some tidying,

$$\begin{aligned} \frac{\partial}{\partial x_j} \left( \bar{\rho} \left( \frac{\partial u}{\partial x_j} + \frac{\partial u_j}{\partial x} \right) \right) - \frac{2}{3} \frac{\partial}{\partial x} \left( \bar{\rho} \frac{\partial u_j}{\partial x_j} \right) &= \bar{\rho} \left( \frac{\partial^2 v}{\partial x^2} + \frac{4}{3} \frac{\partial^2 v}{\partial y^2} + \frac{\partial^2 v}{\partial z^2} + \frac{1}{3} \frac{\partial^2 u}{\partial x \partial y} + \frac{1}{3} \frac{\partial^2 w}{\partial y \partial z} \right) \\ &\quad + \frac{\partial \bar{\rho}}{\partial z} \left( \frac{\partial v}{\partial z} + \frac{\partial w}{\partial y} \right) \end{aligned} \quad (\text{A.42})$$

For the z-component,  $i = 3$ , sum over the repeated index  $j$ ,

$$\begin{aligned} \frac{\partial}{\partial x_j} \left( \bar{\rho} \left( \frac{\partial w}{\partial x_j} + \frac{\partial u_j}{\partial z} \right) \right) - \frac{2}{3} \frac{\partial}{\partial z} \left( \bar{\rho} \frac{\partial u_j}{\partial x_j} \right) &= \frac{\partial}{\partial x} \left( \bar{\rho} \left( \frac{\partial w}{\partial x} + \frac{\partial u}{\partial z} \right) \right) - \frac{2}{3} \frac{\partial}{\partial z} \left( \bar{\rho} \frac{\partial u}{\partial x} \right) \\ &\quad + \frac{\partial}{\partial y} \left( \bar{\rho} \left( \frac{\partial w}{\partial y} + \frac{\partial v}{\partial z} \right) \right) - \frac{2}{3} \frac{\partial}{\partial z} \left( \bar{\rho} \frac{\partial v}{\partial y} \right) \\ &\quad + \frac{\partial}{\partial z} \left( \bar{\rho} \left( \frac{\partial w}{\partial z} + \frac{\partial w}{\partial z} \right) \right) - \frac{2}{3} \frac{\partial}{\partial z} \left( \bar{\rho} \frac{\partial w}{\partial z} \right) \end{aligned} \quad (\text{A.43})$$

which again, after some tidying becomes,

$$\begin{aligned} \frac{\partial}{\partial x_j} \left( \bar{\rho} \left( \frac{\partial w}{\partial x_j} + \frac{\partial u_j}{\partial z} \right) \right) - \frac{2}{3} \frac{\partial}{\partial z} \left( \bar{\rho} \frac{\partial u_j}{\partial x_j} \right) &= \bar{\rho} \left( \frac{\partial^2 w}{\partial x^2} + \frac{\partial^2 w}{\partial y^2} + \frac{4}{3} \frac{\partial^2 w}{\partial z^2} + \frac{1}{3} \frac{\partial^2 u}{\partial x \partial z} + \frac{1}{3} \frac{\partial^2 v}{\partial y \partial z} \right) \\ &\quad + \frac{2}{3} \frac{\partial \bar{\rho}}{\partial z} \left( 2 \frac{\partial w}{\partial z} - \frac{\partial u}{\partial x} - \frac{\partial v}{\partial y} \right) \end{aligned} \quad (\text{A.44})$$

We can compute  $\frac{\partial \bar{\rho}}{\partial z}$  analytically, and note the fact that if we multiple this by a factor of  $\bar{T} = 1 - \theta z$  as we have done in our z-momentum equation we can simplify as follows,

$$\bar{T} \frac{\partial \bar{\rho}}{\partial z} = (1 - \theta z) m \theta (1 - \theta z)^{m-1} = -m \theta \bar{\rho} \quad (\text{A.45})$$

substituting (A.45) into (A.44),

$$\begin{aligned} \frac{\partial}{\partial x_j} \left( \bar{\rho} \left( \frac{\partial w}{\partial x_j} + \frac{\partial u_j}{\partial z} \right) \right) - \frac{2}{3} \frac{\partial}{\partial z} \left( \bar{\rho} \frac{\partial u_j}{\partial x_j} \right) &= \bar{\rho} \left( \frac{\partial^2 w}{\partial x^2} + \frac{\partial^2 w}{\partial y^2} + \frac{4}{3} \frac{\partial^2 w}{\partial z^2} + \frac{1}{3} \frac{\partial^2 u}{\partial x \partial z} + \frac{1}{3} \frac{\partial^2 v}{\partial y \partial z} \right) \\ &\quad - \frac{2}{3} \frac{m \theta \bar{\rho}}{\bar{T}} \left( 2 \frac{\partial w}{\partial z} - \frac{\partial u}{\partial x} - \frac{\partial v}{\partial y} \right) \end{aligned} \quad (\text{A.46})$$

Substituting these into our momentum equations, we obtain our fully expanded momentum equations,

$$\begin{aligned} \bar{\rho} \left( \frac{\partial u}{\partial t} + u \frac{\partial u}{\partial x} + v \frac{\partial u}{\partial y} + w \frac{\partial u}{\partial z} \right) = & - \frac{\partial p}{\partial x} - T a^{\frac{1}{2}} \bar{\rho} (w \cos \phi - v \sin \phi) \\ & + \bar{\rho} \left( \frac{4}{3} \frac{\partial^2 u}{\partial x^2} + \frac{\partial^2 u}{\partial y^2} + \frac{\partial^2 u}{\partial z^2} + \frac{1}{3} \frac{\partial^2 v}{\partial x \partial y} + \frac{1}{3} \frac{\partial^2 w}{\partial x \partial z} \right) \\ & + \frac{\partial \bar{\rho}}{\partial z} \left( \frac{\partial u}{\partial z} + \frac{\partial w}{\partial x} \right) \end{aligned} \quad (\text{A.47})$$

$$\begin{aligned} \bar{\rho} \left( \frac{\partial v}{\partial t} + u \frac{\partial v}{\partial x} + v \frac{\partial v}{\partial y} + w \frac{\partial v}{\partial z} \right) = & - \frac{\partial p}{\partial y} - T a^{\frac{1}{2}} \bar{\rho} u \sin \phi \\ & + \bar{\rho} \left( \frac{\partial^2 v}{\partial x^2} + \frac{4}{3} \frac{\partial^2 v}{\partial y^2} + \frac{\partial^2 v}{\partial z^2} + \frac{1}{3} \frac{\partial^2 u}{\partial x \partial y} + \frac{1}{3} \frac{\partial^2 w}{\partial y \partial z} \right) \\ & + \frac{\partial \bar{\rho}}{\partial z} \left( \frac{\partial v}{\partial z} + \frac{\partial w}{\partial y} \right) \end{aligned} \quad (\text{A.48})$$

$$\begin{aligned} \bar{\rho} \bar{T} \left( \frac{\partial w}{\partial t} + u \frac{\partial w}{\partial x} + v \frac{\partial w}{\partial y} + w \frac{\partial w}{\partial z} \right) = & - \bar{T} \frac{\partial p}{\partial z} - m \theta p + \frac{Ra}{Pr} \bar{\rho} \bar{T} s + T a^{\frac{1}{2}} \bar{\rho} \bar{T} u \cos \phi \\ & + \bar{\rho} \bar{T} \left( \frac{\partial^2 w}{\partial x^2} + \frac{\partial^2 w}{\partial y^2} + \frac{4}{3} \frac{\partial^2 w}{\partial z^2} + \frac{1}{3} \frac{\partial^2 u}{\partial x \partial z} + \frac{1}{3} \frac{\partial^2 v}{\partial y \partial z} \right) \\ & - \frac{2}{3} m \theta \bar{\rho} \left( 2 \frac{\partial w}{\partial z} - \frac{\partial u}{\partial x} - \frac{\partial v}{\partial y} \right) \end{aligned} \quad (\text{A.49})$$

Next we have our entropy diffusion equation. Starting with our divergence term,

$$\nabla \cdot (\bar{\rho} \bar{T} \nabla s) = \frac{\partial}{\partial x} \left( \bar{\rho} \bar{T} \frac{\partial s}{\partial x} \right) + \frac{\partial}{\partial z} \left( \bar{\rho} \bar{T} \frac{\partial s}{\partial z} \right) = \bar{\rho} \bar{T} \left( \frac{\partial^2 s}{\partial x^2} + \frac{\partial^2 s}{\partial z^2} \right) + \frac{\partial s}{\partial z} \frac{\partial}{\partial z} (\bar{\rho} \bar{T}) \quad (\text{A.50})$$

however,

$$\frac{\partial}{\partial z} (\bar{\rho} \bar{T}) = \frac{\partial}{\partial z} \left( (1 - \theta z)^{m+1} \right) = (m+1)(1 - \theta z)^m = (m+1)\bar{\rho} \quad (\text{A.51})$$

and so,

$$\nabla \cdot (\bar{\rho} \bar{T} \nabla s) = \bar{\rho} \bar{T} \left( \frac{\partial^2 s}{\partial x^2} + \frac{\partial^2 s}{\partial z^2} \right) + (m+1) \bar{\rho} \frac{\partial s}{\partial z} \quad (\text{A.52})$$

which when substituted in yields,

$$Pr \bar{\rho} \bar{T} \left( \frac{\partial s}{\partial t} + u \frac{\partial s}{\partial x} + w \frac{\partial s}{\partial z} \right) = \bar{\rho} \bar{T} \left( \frac{\partial^2 s}{\partial x^2} + \frac{\partial^2 s}{\partial z^2} \right) + \bar{\rho} (m+1) \frac{\partial s}{\partial z} + \frac{Pr^2 \theta}{Ra} \hat{\tau}_{ij} \frac{\partial u_i}{\partial x_j} \quad (\text{A.53})$$

Lastly we need to expand our viscous term using (A.4). Both i and j are repeated index's in this term and so we sum over both,

$$\hat{\tau}_{ij} \frac{\partial u_i}{\partial x_j} = \bar{\rho} \left( \frac{\partial u_i}{\partial x_j} + \frac{\partial u_j}{\partial x_i} - \frac{2}{3} \delta_{ij} \nabla \cdot \mathbf{u} \right) \frac{\partial u_i}{\partial x_j} \quad (\text{A.54})$$

$$\begin{aligned} \hat{\tau}_{ij} \frac{\partial u_i}{\partial x_j} &= \bar{\rho} \left( 2 \frac{\partial u}{\partial x} - \frac{2}{3} \nabla \cdot \mathbf{u} \right) \frac{\partial u}{\partial x} \\ &\quad + \bar{\rho} \left( \frac{\partial u}{\partial z} + \frac{\partial w}{\partial x} \right) \frac{\partial u}{\partial z} \\ &\quad + \bar{\rho} \left( \frac{\partial w}{\partial x} + \frac{\partial u}{\partial z} \right) \frac{\partial w}{\partial x} \\ &\quad + \bar{\rho} \left( 2 \frac{\partial w}{\partial z} - \frac{2}{3} \nabla \cdot \mathbf{u} \right) \frac{\partial w}{\partial z} \end{aligned} \quad (\text{A.55})$$

$$\hat{\tau}_{ij} \frac{\partial u_i}{\partial x_j} = 2 \bar{\rho} \left[ \left( \frac{\partial u}{\partial x} \right)^2 + \left( \frac{\partial w}{\partial z} \right)^2 + \frac{\partial u}{\partial z} \frac{\partial w}{\partial x} + \frac{1}{2} \left( \left( \frac{\partial u}{\partial z} \right)^2 + \left( \frac{\partial w}{\partial x} \right)^2 \right) - \frac{1}{3} \left( \frac{\partial u}{\partial x} + \frac{\partial w}{\partial z} \right)^2 \right] \quad (\text{A.56})$$

Which gives us our final, fully expanded diffusion equation, noting that we have divided out the common factor of  $\bar{\rho}$ ,

$$\begin{aligned}
Pr\bar{T} \left( \frac{\partial s}{\partial t} + u \frac{\partial s}{\partial x} + w \frac{\partial s}{\partial z} \right) &= \bar{T} \left( \frac{\partial^2 s}{\partial x^2} + \frac{\partial^2 s}{\partial z^2} \right) + (m+1) \frac{\partial s}{\partial z} \\
&+ 2 \frac{Pr^2 \theta}{Ra} \left[ \left( \frac{\partial u}{\partial x} \right)^2 + \left( \frac{\partial w}{\partial z} \right)^2 + \frac{\partial u}{\partial z} \frac{\partial w}{\partial x} + \frac{1}{2} \left( \left( \frac{\partial u}{\partial z} \right)^2 + \left( \frac{\partial w}{\partial x} \right)^2 \right) - \frac{1}{3} \left( \frac{\partial u}{\partial x} + \frac{\partial w}{\partial z} \right)^2 \right]
\end{aligned} \tag{A.57}$$

### A.3 2.5D approximation

Now that we have our fully 3D governing equations expanded out in a dedalus-readable format (equations A.59, A.47, A.48, A.49, and A.57) reducing them to 2.5D is relatively straightforward. As seen in Section 4.1.2 we need to make a choice regarding which dimension to make axisymmetric, and given the nature of the system we are trying to solve the x-dimension is chosen. To reduce the above equations to 2.5D, we now simply neglect all variations in the x-direction, that is,

$$\partial_x = 0 \tag{A.58}$$

and therefore we are left with,

$$(1 - \theta z) \left( \frac{\partial w}{\partial z} \right) - \theta m w = 0 \tag{A.59}$$

$$\begin{aligned}
\bar{\rho} \left( \frac{\partial u}{\partial t} + v \frac{\partial u}{\partial y} + w \frac{\partial u}{\partial z} \right) &= - T a^{\frac{1}{2}} \bar{\rho} (w \cos \phi - v \sin \phi) \\
&+ \bar{\rho} \left( \frac{\partial^2 u}{\partial y^2} + \frac{\partial^2 u}{\partial z^2} \right) \\
&+ \frac{\partial \bar{\rho}}{\partial z} \left( \frac{\partial u}{\partial z} \right)
\end{aligned} \tag{A.60}$$

$$\begin{aligned} \bar{\rho} \left( \frac{\partial v}{\partial t} + v \frac{\partial v}{\partial y} + w \frac{\partial v}{\partial z} \right) = & - \frac{\partial p}{\partial y} - T a^{\frac{1}{2}} \bar{\rho} u \sin \phi \\ & + \bar{\rho} \left( \frac{4}{3} \frac{\partial^2 v}{\partial y^2} + \frac{\partial^2 v}{\partial z^2} + \frac{1}{3} \frac{\partial^2 w}{\partial y \partial z} \right) \\ & + \frac{\partial \bar{\rho}}{\partial z} \left( \frac{\partial v}{\partial z} + \frac{\partial w}{\partial y} \right) \end{aligned} \quad (\text{A.61})$$

$$\begin{aligned} \bar{\rho} \bar{T} \left( \frac{\partial w}{\partial t} + v \frac{\partial w}{\partial y} + w \frac{\partial w}{\partial z} \right) = & - \bar{T} \frac{\partial p}{\partial z} - m \theta p + \frac{Ra}{Pr} \bar{\rho} \bar{T} s + T a^{\frac{1}{2}} \bar{\rho} \bar{T} u \cos \phi \\ & + \bar{\rho} \bar{T} \left( \frac{\partial^2 w}{\partial y^2} + \frac{4}{3} \frac{\partial^2 w}{\partial z^2} + \frac{1}{3} \frac{\partial^2 v}{\partial y \partial z} \right) \\ & - \frac{2}{3} m \theta \bar{\rho} \left( 2 \frac{\partial w}{\partial z} - \frac{\partial v}{\partial y} \right) \end{aligned} \quad (\text{A.62})$$

$$\begin{aligned} Pr \bar{T} \left( \frac{\partial s}{\partial t} + w \frac{\partial s}{\partial z} \right) = & \bar{T} \left( \frac{\partial^2 s}{\partial z^2} \right) + (m+1) \frac{\partial s}{\partial z} \\ & + 2 \frac{Pr^2 \theta}{Ra} \left[ + \left( \frac{\partial w}{\partial z} \right)^2 + \frac{1}{2} \left( \left( \frac{\partial u}{\partial z} \right)^2 \right) - \frac{1}{3} \left( \frac{\partial w}{\partial z} \right)^2 \right] \end{aligned} \quad (\text{A.63})$$



# Bibliography

- Alboussière, Thierry, Jezabel Curbelo, Fabien Dubuffet, Stéphane Labrosse, and Yanick Ricard. 2022. ‘A playground for compressible natural convection with a nearly uniform density.’ *Journal of Fluid Mechanics* 940 (June): A9.
- Alboussière, Thierry, and Yanick Ricard. 2013. ‘Reflections on dissipation associated with thermal convection.’ *Journal of Fluid Mechanics* 725:R1.
- Amundsen, David S., Isabelle Baraffe, Pascal Tremblin, et al. 2014. ‘Accuracy tests of radiation schemes used in hot Jupiter global circulation models.’ *Astronomy & Astrophysics* 564 (April): A59.
- Amundsen, David S., Nathan J. Mayne, Isabelle Baraffe, et al. 2016. ‘The UK Met Office global circulation model with a sophisticated radiation scheme applied to the hot Jupiter HD 209458b.’ *Astronomy & Astrophysics* 595 (October): A36.
- Anders, Evan H., Adam S. Jermyn, Daniel Lecoanet, and Benjamin P. Brown. 2022. ‘Stellar Convective Penetration: Parameterized Theory and Dynamical Simulations.’ *The Astrophysical Journal* 926, no. 2 (February): 169.
- Anders, Evan H., Cathryn M. Manduca, Benjamin P. Brown, Jeffrey S. Oishi, and Geoffrey M. Vasil. 2019. ‘Predicting the Rossby Number in Convective Experiments.’ *The Astrophysical Journal* 872, no. 2 (February): 138.
- Arnett, David, Casey Meakin, and Patrick A. Young. 2009. ‘Turbulent Convection in Stellar Interiors. II. The Velocity Field.’ *The Astrophysical Journal* 690, no. 2 (January): 1715–1729.

- Arnett, W. David, Casey Meakin, Maxime Viallet, et al. 2015. ‘Beyond Mixing-length Theory: A Step Toward 321D.’ *The Astrophysical Journal* 809, no. 1 (August): 30.
- Ascher, Uri M., Steven J. Ruuth, and Raymond J. Spiteri. 1997. ‘Implicit-explicit Runge-Kutta methods for time-dependent partial differential equations.’ Special Issue on Time Integration, *Applied Numerical Mathematics* 25 (2): 151–167.
- Aurnou, Jonathan M., Susanne Horn, and Keith Julien. 2020. ‘Connections between nonrotating, slowly rotating, and rapidly rotating turbulent convection transport scalings.’ *Physical Review Research* 2, no. 4 (October): 043115.
- Backus, George E. 1975. ‘Gross Thermodynamics of Heat Engines in Deep Interior of Earth.’ *Proceedings of the National Academy of Science* 72, no. 4 (April): 1555–1558.
- Baraffe, I., G. Chabrier, and T. Barman. 2008. ‘Structure and evolution of super-Earth to super-Jupiter exoplanets. I. Heavy element enrichment in the interior.’ *Astronomy & Astrophysics* 482, no. 1 (April): 315–332.
- . 2010. ‘The physical properties of extra-solar planets.’ *Reports on Progress in Physics* 73, no. 1 (January): 016901.
- Baraffe, I., G. Chabrier, J. Fortney, and C. Sotin. 2014. ‘Planetary Internal Structures.’ In *Protostars and Planets VI*, edited by Henrik Beuther, Ralf S. Klessen, Cornelis P. Dullemond, and Thomas Henning, 763–786. January.
- Baraffe, I., J. Pratt, D. G. Vlaykov, et al. 2021. ‘Two-dimensional simulations of solar-like models with artificially enhanced luminosity. I. Impact on convective penetration.’ *Astronomy & Astrophysics* 654 (October): A126.
- Barker, Adrian J., Adam M. Dempsey, and Yoram Lithwick. 2014. ‘Theory and Simulations of Rotating Convection.’ *The Astrophysical Journal* 791, no. 1 (August): 13.
- Batygin, Konstantin, and David J. Stevenson. 2010. ‘Inflating Hot Jupiters with Ohmic Dissipation.’ *The Astrophysical Journal Letters* 714, no. 2 (May): L238–L243.
- Beaudoin, Patrice, Antoine Strugarek, and Paul Charbonneau. 2018. ‘Differential Rotation in Solar-like Convective Envelopes: Influence of Overshoot and Magnetism.’ *The Astrophysical Journal* 859, no. 1 (May): 61.

- Beebe, Reta. 1996. 'Jupiter, the giant planet / Smithsonian Institution Press, 1994; 2nd ed. 1996.' *Earth Moon and Planets* 73 (January): 107.
- Bodenheimer, Peter, D. N. C. Lin, and R. A. Mardling. 2001. 'On the Tidal Inflation of Short-Period Extrasolar Planets.' *The Astrophysical Journal* 548, no. 1 (February): 466–472.
- Bodin, Bastien, and Daniel Cordier. 2022. 'Numerical simulations of cryolava flows at the surface of Titan.' In *European Planetary Science Congress*, EPSC2022–419. September.
- Boutle, Ian A., Nathan J. Mayne, Benjamin Drummond, et al. 2017. 'Exploring the climate of Proxima B with the Met Office Unified Model.' *Astronomy & Astrophysics* 601 (May): A120.
- Braginsky, Stanislav I., and Paul H. Roberts. 1995. 'Equations governing convection in earth's core and the geodynamo.' *Geophysical and Astrophysical Fluid Dynamics* 79, no. 1 (January): 1–97.
- Brandenburg, Axel. 2014. 'Magnetic Prandtl Number Dependence of the Kinetic-to-magnetic Dissipation Ratio.' *The Astrophysical Journal* 791, no. 1 (August): 12.
- Brown, Timothy M., David Charbonneau, Ronald L. Gilliland, Robert W. Noyes, and Adam Burrows. 2001. 'Hubble Space Telescope Time-Series Photometry of the Transiting Planet of HD 209458.' *The Astrophysical Journal* 552, no. 2 (May): 699–709.
- Browning, Matthew K., Mark S. Miesch, Allan Sacha Brun, and Juri Toomre. 2006. 'Dynamo Action in the Solar Convection Zone and Tachocline: Pumping and Organization of Toroidal Fields.' *The Astrophysical Journal Letters* 648, no. 2 (September): L157–L160.
- Browning, Matthew K., Maria A. Weber, Gilles Chabrier, and Angela P. Massey. 2016. 'Theoretical Limits on Magnetic Field Strengths in Low-mass Stars.' *The Astrophysical Journal* 818, no. 2 (February): 189.
- Brun, Allan Sacha, and Matthew K. Browning. 2017. 'Magnetism, dynamo action and the solar-stellar connection.' *Living Reviews in Solar Physics* 14, no. 1 (September): 4.

- Brun, Allan Sacha, and Juri Toomre. 2002. ‘Turbulent Convection under the Influence of Rotation: Sustaining a Strong Differential Rotation.’ *The Astrophysical Journal* 570, no. 2 (May): 865–885.
- Burns, Keaton J., Geoffrey M. Vasil, Jeffrey S. Oishi, Daniel Lecoanet, and Benjamin P. Brown. 2020. ‘Dedalus: A flexible framework for numerical simulations with spectral methods.’ *Physical Review Research* 2, no. 2 (April): 023068.
- Busse, F. H., and P. G. Cuong. 1977. ‘Convection in rapidly rotating spherical fluid shells.’ *Geophysical and Astrophysical Fluid Dynamics* 8, no. 1 (January): 17–41.
- Canuto, V. M., I. Goldman, and I. Mazzitelli. 1996. ‘Stellar Turbulent Convection: A Self-consistent Model.’ *The Astrophysical Journal* 473 (December): 550.
- Castaing, Bernard, Gemunu Gunaratne, François Heslot, et al. 1989. ‘Scaling of hard thermal turbulence in Rayleigh-Bénard convection.’ *Journal of Fluid Mechanics* 204:1–30.
- Chabrier, Gilles, and Isabelle Baraffe. 1997. ‘Structure and evolution of low-mass stars.’ *Astronomy & Astrophysics* 327 (November): 1039–1053.
- Chandrasekhar, Subrahmanyam. 1961. *Hydrodynamic and hydromagnetic stability*.
- Cioni, S., S. Ciliberto, and J. Sommeria. 1997. ‘Strongly turbulent Rayleigh Bénard convection in mercury: comparison with results at moderate Prandtl number.’ *Journal of Fluid Mechanics* 335, no. 1 (March): 111–140.
- Crass, Jonathan, B. Scott Gaudi, Stephanie Leifer, et al. 2021. ‘Extreme Precision Radial Velocity Working Group Final Report.’ *arXiv e-prints* (July): arXiv:2107.14291.
- Currie, Laura K., Adrian J. Barker, Yoram Lithwick, and Matthew K. Browning. 2020. ‘Convection with misaligned gravity and rotation: simulations and rotating mixing length theory.’ *Monthly Notices of the Royal Astronomical Society* 493, no. 4 (April): 5233–5256.
- Currie, Laura K., and Matthew K. Browning. 2017. ‘The Magnitude of Viscous Dissipation in Strongly Stratified Two-dimensional Convection.’ *The Astrophysical Journal Letters* 845, no. 2 (August): L17.
- Currie, Laura K., and Steven M. Tobias. 2020. ‘Generation of shear flows and vortices in rotating anelastic convection.’ *Physical Review Fluids* 5, no. 7 (July): 073501.

- Davis, A.H. 1922. 'LXXIX. Natural convective cooling in fluids.' *The London, Edinburgh, and Dublin Philosophical Magazine and Journal of Science* 44 (263): 920–940.
- de Beurs, Zoe. L., Andrew Vanderburg, Christopher J. Shallue, et al. 2022. 'Identifying Exoplanets with Deep Learning. IV. Removing Stellar Activity Signals from Radial Velocity Measurements Using Neural Networks.' *The Astronomical Journal* 164, no. 2 (August): 49.
- Demory, Brice-Olivier, and Sara Seager. 2011. 'Lack of Inflated Radii for Kepler Giant Planet Candidates Receiving Modest Stellar Irradiation.' *The Astrophysical Journal Supplement* 197, no. 1 (November): 12.
- Doering, Charles R. 2020. 'Turning up the heat in turbulent thermal convection.' *Proceedings of the National Academy of Science* 117, no. 18 (May): 9671–9673.
- Dravins, D., L. Lindegren, and A. Nordlund. 1981. 'Solar granulation - Influence of convection on spectral line asymmetries and wavelength shifts.' *Astronomy & Astrophysics* 96, nos. 1-2 (March): 345–364.
- Drummond, B., N. J. Mayne, I. Baraffe, et al. 2018. 'The effect of metallicity on the atmospheres of exoplanets with fully coupled 3D hydrodynamics, equilibrium chemistry, and radiative transfer.' *Astronomy & Astrophysics* 612 (May): A105.
- Drummond, Benjamin, Eric Hébrard, Nathan J. Mayne, et al. 2020. 'Implications of three-dimensional chemical transport in hot Jupiter atmospheres: Results from a consistently coupled chemistry-radiation-hydrodynamics model.' *Astronomy & Astrophysics* 636 (April): A68.
- Duarte, Lúcia D. V., Johannes Wicht, Matthew K. Browning, and Thomas Gastine. 2016. 'Helicity inversion in spherical convection as a means for equatorward dynamo wave propagation.' *Monthly Notices of the Royal Astronomical Society* 456, no. 2 (February): 1708–1722.
- Eager-Nash, Jake K., Nathan J. Mayne, Arwen E. Nicholson, et al. 2023. '3D climate simulations of the Archean find that methane has a strong cooling effect at high concentrations.' *arXiv e-prints* (February): arXiv:2302.12518.

- Featherstone, N. A., and B. Hindman. 2016. 'The Spectral Signature of Rotating, Stratified Convection.' In *AGU Fall Meeting Abstracts*, vol. 2016, GP12A–10. December.
- Featherstone, Nicholas A., and Mark S. Miesch. 2015. 'Meridional circulation in solar and stellar convection zones.' *The Astrophysical Journal* 804, no. 1 (May): 67.
- Fortney, Jonathan J., and Nadine Nettelmann. 2010. 'The Interior Structure, Composition, and Evolution of Giant Planets.' *Space Sci. Rev.* 152, nos. 1-4 (May): 423–447.
- Frisch, Uriel. 1995. *Turbulence. The legacy of A.N. Kolmogorov*.
- Galanti, E., Y. Kaspi, Y. Miguel, et al. 2019. 'Saturn's Deep Atmospheric Flows Revealed by the Cassini Grand Finale Gravity Measurements.' *Geophysical Research Letters* 46, no. 2 (January): 616–624.
- Gao, Peter, Daniel P. Thorngren, Elspeth K. H. Lee, et al. 2020. 'Aerosol composition of hot giant exoplanets dominated by silicates and hydrocarbon hazes.' *Nature Astronomy* 4 (May): 951–956.
- Gastine, T., R. K. Yadav, J. Morin, A. Reiners, and J. Wicht. 2013. 'From solar-like to antisolar differential rotation in cool stars.' *Monthly Notices of the Royal Astronomical Society* 438, no. 1 (December): L76–L80.
- Gastine, Thomas, and Jonathan M. Aurnou. 2023. 'Latitudinal regionalization of rotating spherical shell convection.' *Journal of Fluid Mechanics* 954 (January): R1.
- Gastine, Thomas, Johannes Wicht, and Julien Aubert. 2016. 'Scaling regimes in spherical shell rotating convection.' *Journal of Fluid Mechanics* 808 (December): 690–732.
- Gillet, N., and C. A. Jones. 2006. 'The quasi-geostrophic model for rapidly rotating spherical convection outside the tangent cylinder.' *Journal of Fluid Mechanics* 554 (May): 343–369.
- Gilman, P. A. 1977. 'Nonlinear Dynamics of Boussinesq Convection in a Deep Rotating Spherical Shell. I.' *Geophysical and Astrophysical Fluid Dynamics* 8 (January): 93–135.
- Ginet, Gregory P. 1994. 'Downflow Plumes and Entropy Balance in Deep Convection Zones.' *The Astrophysical Journal* 429 (July): 899.

- Girichidis, Philipp, Stella S. R. Offner, Alexei G. Krtsuk, et al. 2020. 'Physical Processes in Star Formation.' *Space Science Reviews* 216, no. 4 (June): 68.
- Glatzmaier, Gary A. 2013. *Introduction to Modelling Convection in Planets and Stars*.
- Goluskin, David. 2015. 'Internally heated convection and Rayleigh-Bénard convection.' *arXiv e-prints* (June): arXiv:1506.01656.
- Gough, D. O. 1969. 'The Anelastic Approximation for Thermal Convection.' *Journal of Atmospheric Sciences* 26, no. 3 (May): 448–456.
- Gough, D. O., and M. E. McIntyre. 1998. 'Inevitability of a magnetic field in the Sun's radiative interior.' *Nature* 394, no. 6695 (August): 755–757.
- Gough, D. O., and N. O. Weiss. 1976. 'The calibration of stellar convection theories.' *Monthly Notices of the Royal Astronomical Society* 176 (September): 589–607.
- Gough, Douglas, and Juri Toomre. 1991. 'Seismic observations of the solar interior.' *Annual Review of Astronomy and Astrophysics* 29 (January): 627–684.
- Greer, Benjamin J., Bradley W. Hindman, Nicholas A. Featherstone, and Juri Toomre. 2015. 'Helioseismic imaging of fast convective flows throughout the near-surface shear layer.' *The Astrophysical Journal Letters* 803, no. 2 (April): L17.
- Grossmann, Siegfried, and Detlef Lohse. 2000. 'Scaling in thermal convection: a unifying theory.' *Journal of Fluid Mechanics* 407, no. 1 (March): 27–56.
- Hammond, Mark, and Neil T. Lewis. 2021. 'The rotational and divergent components of atmospheric circulation on tidally locked planets.' *Proceedings of the National Academy of Science* 118, no. 13 (March): e2022705118.
- Hanasoge, Shravan M., Thomas L. Duvall, and Katepalli R. Sreenivasan. 2012. 'Anomalously weak solar convection.' *Proceedings of the National Academy of Sciences* 109 (30): 11928–11932.
- Haywood, R. D., T. W. Milbourne, S. H. Saar, et al. 2022. 'Unsigned Magnetic Flux as a Proxy for Radial-velocity Variations in Sun-like Stars.' *The Astrophysical Journal* 935, no. 1 (August): 6.

- Hepworth, Benjamin James. 2014. 'Nonlinear two-dimensional Rayleigh-Bénard convection.' PhD diss., University of Leeds, March.
- Heslot, F., B. Castaing, and A. Libchaber. 1987. 'Transitions to turbulence in helium gas.' *Physical Review A* 36, no. 12 (January): 5870–5873.
- Hewitt, J. M., D. P. McKenzie, and N. O. Weiss. 1975. 'Dissipative heating in convective flows.' *Journal of Fluid Mechanics* 68 (April): 721–738.
- Hurlburt, N. E., J. Toomre, and J. M. Massaguer. 1984. 'Two-dimensional compressible convection extending over multiple scale heights.' *The Astrophysical Journal* 282 (July): 557–573.
- Ireland, Lewis G., and Matthew K. Browning. 2018. 'The Radius and Entropy of a Magnetized, Rotating, Fully Convective Star: Analysis with Depth-dependent Mixing Length Theories.' *The Astrophysical Journal* 856, no. 2 (April): 132.
- Iserles, Arieh. 1996. *A first course in the numerical analysis of differential equations*.
- Jarvis, G. T., and D. P. McKenzie. 1980. 'Convection in a compressible fluid with infinite Prandtl number.' *Journal of Fluid Mechanics* 96 (January): 515–583.
- Jones, C. A., P. Boronski, A. S. Brun, et al. 2011. 'Anelastic convection-driven dynamo benchmarks.' *Icarus* 216, no. 1 (November): 120–135.
- Jones, Chris A., Krzysztof A. Mizerski, and Mouloud Kessar. 2022. 'Fully developed anelastic convection with no-slip boundaries.' *Journal of Fluid Mechanics* 930 (January): A13.
- Julien, Keith, Edgar Knobloch, Antonio M. Rubio, and Geoffrey M. Vasil. 2012. 'Heat Transport in Low-Rossby-Number Rayleigh-Bénard Convection.' *Physical Review Letters* 109, no. 25 (December): 254503.
- Käpylä, P. J., M. Viviani, M. J. Käpylä, A. Brandenburg, and F. Spada. 2019. 'Effects of a subadiabatic layer on convection and dynamos in spherical wedge simulations.' *Geophysical and Astrophysical Fluid Dynamics* 113, nos. 1-2 (March): 149–183.
- Karak, B. B., P. J. Käpylä, M. J. Käpylä, et al. 2015. 'Magnetically controlled stellar differential rotation near the transition from solar to anti-solar profiles.' *Astronomy & Astrophysics* 576 (April): A26.

- Kaspi, Y., E. Galanti, W. B. Hubbard, et al. 2018. 'Jupiter's atmospheric jet streams extend thousands of kilometres deep.' *Nature* 555, no. 7695 (March): 223–226.
- Kaspi, Yohai, Eli Galanti, Adam P. Showman, et al. 2020. 'Comparison of the Deep Atmospheric Dynamics of Jupiter and Saturn in Light of the Juno and Cassini Gravity Measurements.' *Space Sci. Rev.* 216, no. 5 (June): 84.
- Kazemi, Sina, Rodolfo Ostilla-Mónico, and David Goluskin. 2022. 'Transition between Boundary-Limited Scaling and Mixing-Length Scaling of Turbulent Transport in Internally Heated Convection.' *Physical Review Letters* 129, no. 2 (July): 024501.
- King, Andrew, and Ken Pounds. 2015. 'Powerful Outflows and Feedback from Active Galactic Nuclei.' *Annual Review of Astronomy and Astrophysics* 53 (1): 115–154.
- King, E. M., S. Stellmach, and J. M. Aurnou. 2012. 'Heat transfer by rapidly rotating Rayleigh–Bénard convection.' *Journal of Fluid Mechanics* 691:568–582.
- Kippenhahn, Rudolf, Alfred Weigert, and Achim Weiss. 2013. *Stellar Structure and Evolution*.
- Knutson, Heather A., David Charbonneau, Nicolas B. Cowan, et al. 2009. 'Multiwave-length Constraints on the Day-Night Circulation Patterns of HD 189733b.' *The Astrophysical Journal* 690, no. 1 (January): 822–836.
- Komacek, Thaddeus D., Peter Gao, Daniel P. Thorngren, Erin M. May, and Xianyu Tan. 2022. 'The Effect of Interior Heat Flux on the Atmospheric Circulation of Hot and Ultra-hot Jupiters.' *The Astrophysical Journal Letters* 941, no. 2 (December): L40.
- Komacek, Thaddeus D., and Andrew N. Youdin. 2017. 'Structure and Evolution of Internally Heated Hot Jupiters.' *The Astrophysical Journal* 844, no. 2 (August): 94.
- Korre, L., NH Brummell, P. Garaud, and C. Guervilly. 2021. 'On the dynamical interaction between overshooting convection and an underlying dipole magnetic field - I. The non-dynamo regime.' *Monthly Notices of the Royal Astronomical Society* 503, no. 1 (May): 362–375.

- Korre, L., P. Garaud, and N. H. Brummell. 2019. ‘Convective overshooting and penetration in a Boussinesq spherical shell.’ *Monthly Notices of the Royal Astronomical Society* 484, no. 1 (March): 1220–1237.
- Kovalevsky, Dmitry V., Igor L. Bashmachnikov, and Genrikh V. Alekseev. 2020. ‘Formation and decay of a deep convective chimney.’ *Ocean Modelling* 148:101583.
- Kraichnan, Robert H. 1962. ‘Turbulent Thermal Convection at Arbitrary Prandtl Number.’ *Physics of Fluids* 5:1374–1389.
- Kulsrud, Russell M. 2005. *Plasma Physics for Astrophysics*.
- Kundu, Pijush K. 1990. *Fluid Mechanics: First Edition*.
- Kupka, F., F. Ahlborn, and A. Weiss. 2022. ‘Stellar evolution models with overshooting based on 3-equation non-local theories. I. Physical basis and the computation of the dissipation rate.’ *Astronomy & Astrophysics* 667 (November): A96.
- Lantz, Steven Richard. 1992. ‘Dynamical Behavior of Magnetic Fields in a Stratified, Convecting Fluid Layer.’ PhD diss., Cornell University, New York, January.
- Laughlin, Gregory, Matteo Crismani, and Fred C. Adams. 2011. ‘On the Anomalous Radii of the Transiting Extrasolar Planets.’ *The Astrophysical Journal Letters* 729, no. 1 (March): L7.
- Lecoanet, Daniel, Benjamin P. Brown, Ellen G. Zweibel, et al. 2014. ‘Conduction in Low Mach Number Flows. I. Linear and Weakly Nonlinear Regimes.’ *The Astrophysical Journal* 797, no. 2 (December): 94.
- Liebing, F., S. V. Jeffers, A. Reiners, and M. Zechmeister. 2021. ‘Convective blueshift strengths of 810 F to M solar-type stars.’ *Astronomy & Astrophysics* 654 (October): A168.
- Lines, S., N. J. Mayne, J. Manners, et al. 2019. ‘Overcast on Osiris: 3D radiative-hydrodynamical simulations of a cloudy hot Jupiter using the parametrized, phase-equilibrium cloud formation code EDDYSED.’ *Monthly Notices of the Royal Astronomical Society* 488, no. 1 (September): 1332–1355.
- Liu, Junjun, Peter M. Goldreich, and David J. Stevenson. 2008. ‘Constraints on deep-seated zonal winds inside Jupiter and Saturn.’ *Icarus* 196, no. 2 (August): 653–664.

- Long, Robert S., Jon E. Mound, Christopher J. Davies, and Steven M. Tobias. 2020. 'Thermal boundary layer structure in convection with and without rotation.' *Physical Review Fluids* 5 (11): 113502.
- Louden, Tom, and Peter J. Wheatley. 2015. 'Spatially Resolved Eastward Winds and Rotation of HD 189733b.' *The Astrophysical Journal Letters* 814, no. 2 (December): L24.
- Lubow, S. H., C. A. Tout, and M. Livio. 1997. 'Resonant Tides in Close Orbiting Planets.' *The Astrophysical Journal* 484, no. 2 (July): 866–870.
- Malkus, W. V. R. 1954a. 'Discrete Transitions in Turbulent Convection.' *Proceedings of the Royal Society of London Series A* 225, no. 1161 (August): 185–195.
- . 1954b. 'The Heat Transport and Spectrum of Thermal Turbulence.' *Proceedings of the Royal Society of London Series A* 225, no. 1161 (August): 196–212.
- Mayne, N. J., I. Baraffe, D. M. Acreman, et al. 2014a. 'Using the UM dynamical cores to reproduce idealised 3-D flows.' *Geoscientific Model Development* 7, no. 6 (December): 3059–3087.
- Mayne, Nathan J., Isabelle Baraffe, David M. Acreman, et al. 2014b. 'The unified model, a fully-compressible, non-hydrostatic, deep atmosphere global circulation model, applied to hot Jupiters. ENDGame for a HD 209458b test case.' *Astronomy & Astrophysics* 561 (January): A1.
- Mayne, Nathan J., Florian Debras, Isabelle Baraffe, et al. 2017. 'Results from a set of three-dimensional numerical experiments of a hot Jupiter atmosphere.' *Astronomy & Astrophysics* 604 (August): A79.
- Meakin, Casey A., and W. David Arnett. 2010. 'Some properties of the kinetic energy flux and dissipation in turbulent stellar convection zones.' *Astrophysics and Space Science* 328, nos. 1-2 (July): 221–225.
- Melvin, Thomas, Mark Dubal, Nigel Wood, Andrew Staniforth, and Mohamed Zerroukat. 2010. 'An inherently mass-conserving iterative semi-implicit semi-Lagrangian discretization of the non-hydrostatic vertical-slice equations.' *Quarterly Journal of the Royal Meteorological Society* 136 (648): 799–814.

- Miesch, Mark S., Allan Sacha Brun, Marc L. DeRosa, and Juri Toomre. 2008. ‘Structure and Evolution of Giant Cells in Global Models of Solar Convection.’ *The Astrophysical Journal* 673, no. 1 (January): 557–575.
- Miesch, Mark S., Allan Sacha Brun, and Juri Toomre. 2006. ‘Solar Differential Rotation Influenced by Latitudinal Entropy Variations in the Tachocline.’ *The Astrophysical Journal* 641, no. 1 (April): 618–625.
- Miesch, Mark S., and Juri Toomre. 2009. ‘Turbulence, Magnetism, and Shear in Stellar Interiors.’ *Annual Review of Fluid Mechanics* 41, no. 1 (January): 317–345.
- Mura, A., P. Scarica, D. Grassi, et al. 2022. ‘Five Years of Observations of the Circumpolar Cyclones of Jupiter.’ *Journal of Geophysical Research (Planets)* 127, no. 9 (September): e07241.
- Nelson, N. J., and M. S. Miesch. 2014. ‘Generating buoyant magnetic flux ropes in solar-like convective dynamos.’ *Plasma Physics and Controlled Fusion* 56, no. 6 (June): 064004.
- Nordlund, Åke, Robert F. Stein, and Martin Asplund. 2009. ‘Solar Surface Convection.’ *Living Reviews in Solar Physics* 6, no. 1 (December): 2.
- Ogura, Yoshimitsu, and Norman A. Phillips. 1962. ‘Scale Analysis of Deep and Shallow Convection in the Atmosphere.’ *Journal of Atmospheric Sciences* 19, no. 2 (March): 173–179.
- Rast, Mark Peter. 2020. ‘Deciphering Solar Convection.’ In *Dynamics of the Sun and Stars; Honoring the Life and Work of Michael J. Thompson*, edited by Mário J. P. F. G. Monteiro, Rafael A. García, Jørgen Christensen-Dalsgaard, and Scott W. McIntosh, 57:149–161. Astrophysics and Space Science Proceedings. December.
- Ricard, Yanick, Thierry Alboussière, Stéphane Labrosse, Jezabel Curbelo, and Fabien Dubufet. 2022. ‘Fully compressible convection for planetary mantles.’ *Geophysical Journal International* 230, no. 2 (August): 932–956.
- Rincon, François, and Michel Rieutord. 2018. ‘The Sun’s supergranulation.’ *Living Reviews in Solar Physics* 15, no. 1 (September): 6.

- Rogers, Tamara M., Gary A. Glatzmaier, and S. E. Woosley. 2003. ‘Simulations of two-dimensional turbulent convection in a density-stratified fluid.’ *Physical Review E* 67 (2): 026315.
- Rossby, H. T. 1969. ‘A study of Benard convection with and without rotation.’ *Journal of Fluid Mechanics* 36 (January): 309–335.
- Sainsbury-Martinez, F., S. L. Casewell, J. D. Lothringer, M. W. Phillips, and P. Tremblin. 2021. ‘Exploring deep and hot adiabats as a potential solution to the radius inflation problem in brown dwarfs. Long-timescale models of the deep atmospheres of KELT-1b, Kepler-13Ab, and SDSS1411B.’ *Astronomy & Astrophysics* 656 (December): A128.
- Sainsbury-Martinez, F., P. Wang, S. Fromang, et al. 2019. ‘Idealised simulations of the deep atmosphere of hot Jupiters. Deep, hot adiabats as a robust solution to the radius inflation problem.’ *Astronomy & Astrophysics* 632 (December): A114.
- Salaris, Maurizio, and Santi Cassisi. 2005. *Evolution of Stars and Stellar Populations*.
- . 2017. ‘Chemical element transport in stellar evolution models.’ *Royal Society Open Science* 4, no. 8 (August): 170192.
- Schmitz, S., and A. Tilgner. 2009. ‘Heat transport in rotating convection without Ekman layers.’ *Physical Review E* 80 (1): 015305.
- Schou, J., H. M. Antia, S. Basu, et al. 1998. ‘Helioseismic Studies of Differential Rotation in the Solar Envelope by the Solar Oscillations Investigation Using the Michelson Doppler Imager.’ *The Astrophysical Journal* 505, no. 1 (September): 390–417.
- Sergeev, Denis E., F. Hugo Lambert, Nathan J. Mayne, et al. 2020. ‘Atmospheric Convection Plays a Key Role in the Climate of Tidally Locked Terrestrial Exoplanets: Insights from High-resolution Simulations.’ *The Astrophysical Journal* 894, no. 2 (May): 84.
- Showman, A. P., and T. Guillot. 2002. ‘Atmospheric circulation and tides of “51 Pegasus b-like” planets.’ *Astronomy & Astrophysics* 385 (April): 166–180.
- Showman, Adam P., and Lorenzo M. Polvani. 2011. ‘Equatorial Superrotation on Tidally Locked Exoplanets.’ *The Astrophysical Journal* 738, no. 1 (September): 71.

- Shraiman, Boris I., and Eric D. Siggia. 1990. 'Heat transport in high-Rayleigh-number convection.' *Physical Review A* 42, no. 6 (September): 3650–3653.
- . 2000. 'Scalar turbulence.' *Nature* 405, no. 6787 (June): 639–646.
- Snellen, Ignas A. G., Remco J. de Kok, Ernst J. W. de Mooij, and Simon Albrecht. 2010. 'The orbital motion, absolute mass and high-altitude winds of exoplanet HD209458b.' *Nature* 465, no. 7301 (June): 1049–1051.
- Spiegel, E. A., and G. Veronis. 1960. 'On the Boussinesq Approximation for a Compressible Fluid.' *The Astrophysical Journal* 131 (March): 442.
- Spiegel, Edward A. 1963. 'A Generalization of the Mixing-Length Theory of Turbulent Convection.' *The Astrophysical Journal* 138 (July): 216.
- Stein, R. F., and Å. Nordlund. 1998. 'Simulations of Solar Granulation. I. General Properties.' *The Astrophysical Journal* 499, no. 2 (May): 914–933.
- Stein, R. F., and A. Nordlund. 1989. 'Topology of Convection beneath the Solar Surface.' *The Astrophysical Journal Letters* 342 (July): L95.
- Stevens, Bjorn. 2005. 'Atmospheric moist convection.' *Annual Review of Earth and Planetary Sciences* 33 (1): 605–643.
- Stevenson, D. J. 1979. 'Turbulent thermal convection in the presence of rotation and a magnetic field: A heuristic theory.' *Geophysical and Astrophysical Fluid Dynamics* 12, no. 1 (January): 139–169.
- Taylor, G. I. 1923. 'Stability of a Viscous Liquid Contained between Two Rotating Cylinders.' *Philosophical Transactions of the Royal Society of London Series A* 223 (January): 289–343.
- Thorngren, Daniel, and Jonathan J. Fortney. 2019. 'Connecting Giant Planet Atmosphere and Interior Modeling: Constraints on Atmospheric Metal Enrichment.' *The Astrophysical Journal Letters* 874, no. 2 (April): L31.
- Thorngren, Daniel, Peter Gao, and Jonathan J. Fortney. 2019. 'The Intrinsic Temperature and Radiative-Conductive Boundary Depth in the Atmospheres of Hot Jupiters.' *The Astrophysical Journal Letters* 884, no. 1 (October): L6.

- Thorngren, Daniel P., and Jonathan J. Fortney. 2018. 'Bayesian Analysis of Hot-Jupiter Radius Anomalies: Evidence for Ohmic Dissipation?' *The Astronomical Journal* 155, no. 5 (May): 214.
- Tremblin, P., G. Chabrier, N. J. Mayne, et al. 2017. 'Advection of Potential Temperature in the Atmosphere of Irradiated Exoplanets: A Robust Mechanism to Explain Radius Inflation.' *The Astrophysical Journal* 841, no. 1 (May): 30.
- Vallis, Geoffrey K. 2006. *Atmospheric and Oceanic Fluid Dynamics*.
- Vasil, Geoffrey M., Keith Julien, and Nicholas A. Featherstone. 2021. 'Rotation suppresses giant-scale solar convection.' *Proceedings of the National Academy of Science* 118, no. 31 (August): e2022518118.
- Viallet, Maxime, Casey Meakin, David Arnett, and Miroslav Mocák. 2013. 'Turbulent Convection in Stellar Interiors. III. Mean-field Analysis and Stratification Effects.' *The Astrophysical Journal* 769, no. 1 (May): 1.
- Walters, D., A. J. Baran, I. Boutle, et al. 2019. 'The Met Office Unified Model Global Atmosphere 7.0/7.1 and JULES Global Land 7.0 configurations.' *Geoscientific Model Development* 12 (5): 1909–1963.
- Weiss, Lauren M., G. W. Marcy, J. Rowe, et al. 2013. 'The Relation Between Radius, Mass, and Incident Flux of Exoplanets.' In *American Astronomical Society Meeting Abstracts #221*, 221:407.05. American Astronomical Society Meeting Abstracts. January.
- Wood, Nigel, and Andrew Staniforth. 2003. 'The deep-atmosphere Euler equations with a mass-based vertical coordinate.' *Quarterly Journal of the Royal Meteorological Society* 129 (589): 1289–1300.
- Wood, Nigel, Andrew Staniforth, Andy White, et al. 2014. 'An inherently mass-conserving semi-implicit semi-Lagrangian discretization of the deep-atmosphere global non-hydrostatic equations.' *Quarterly Journal of the Royal Meteorological Society* 140, no. 682 (July): 1505–1520.

- Wyttenbach, A., D. Ehrenreich, C. Lovis, S. Udry, and F. Pepe. 2015. ‘Spectrally resolved detection of sodium in the atmosphere of HD 189733b with the HARPS spectrograph.’ *Astronomy & Astrophysics* 577 (May): A62.
- Zaleski, S. 2000. ‘The 2/7th Law in Turbulent Thermal Convection.’ In *Geophysical and Astrophysical Convection*. August.
- Zamyatina, Maria, Eric Hébrard, Benjamin Drummond, et al. 2023. ‘Observability of signatures of transport-induced chemistry in clear atmospheres of hot gas giant exoplanets.’ *Monthly Notices of the Royal Astronomical Society* 519, no. 2 (February): 3129–3153.
- Zhang, Xi, and Adam P. Showman. 2014. ‘Atmospheric Circulation of Brown Dwarfs: Jets, Vortices, and Time Variability.’ *The Astrophysical Journal Letters* 788, no. 1 (June): L6.

ProQuest Number: 30977330

INFORMATION TO ALL USERS

The quality and completeness of this reproduction is dependent on the quality  
and completeness of the copy made available to ProQuest.



Distributed by ProQuest LLC (2023).

Copyright of the Dissertation is held by the Author unless otherwise noted.

This work may be used in accordance with the terms of the Creative Commons license  
or other rights statement, as indicated in the copyright statement or in the metadata  
associated with this work. Unless otherwise specified in the copyright statement  
or the metadata, all rights are reserved by the copyright holder.

This work is protected against unauthorized copying under Title 17,  
United States Code and other applicable copyright laws.

Microform Edition where available © ProQuest LLC. No reproduction or digitization  
of the Microform Edition is authorized without permission of ProQuest LLC.

ProQuest LLC  
789 East Eisenhower Parkway  
P.O. Box 1346  
Ann Arbor, MI 48106 - 1346 USA